Laboratory and Numerical Studies of Gas Escape through Early Time Casing Fractures

Craig Andrew Hoing

Imperial College London

Department of Physics

This thesis is submitted for the degree of Doctor of Philosophy of Imperial College London and the Diploma of Imperial College

August 2020

Statement of Originality

This is to certify that, to the best of my knowledge, the content of this thesis is my own work and has not been submitted for any other degree or purpose. I certify that the intellectual content of this thesis is the product of my own work and that all the assistance received and sources used have been acknowledged and cited appropriately.

Copyright Declaration

The copyright of this thesis rests with the author. Unless otherwise indicated, its contents are licenced under a Creative Commons Attribution-Non Commercial-No Derivatives 4.0 International Licence (CC BY-NC-ND 4.0).

Under this licence, you may copy and redistribute the material in any medium or format on the condition that; you credit the author, do not use it for commercial purposes and do not distribute modified versions of the work.

When reusing or sharing this work, ensure you make the licence terms clear to others by naming the licence and linking to the licence text.

Please seek permission from the copyright holder for uses of thesis work that are not included in this licence or permitted under UK Copyright Law.

Abstract

Current accepted theory for the calculation of gas flow through narrow openings, such as fractures in weapon casings during expansion, relies on the use of ideal nozzle flow theory being applicable throughout the fracture process. The thesis initially looked to determine the acceleration phase of fragments within expanding detonation gases; however, the scope narrowed to determine the applicability of the current gas flow model. The revised scope combines numerical and experimental research to investigate the flow Mach number within narrow openings, along with any influence of internal pressure, opening width or opening length.

Numerical modelling conducted investigated internal pressures of 10 bar, 18 bar, 50 bar and 200 bar for opening diameters of 1 mm to 6 mm in 1 mm steps. Opening lengths of 5 mm, 10 mm and 20 mm were considered to determine any casing thickness effects. The modelling showed the internal pressure to have minimal effect on the flow, with the main driver being the opening diameter. In general, the flow stabilised at Mach numbers greater than unity for each case, returning Mach 1.2 for a diameter of 1 mm which increased to Mach 1.35 for diameters of 3 mm and above.

The experimental investigation measured static and stagnation pressures within the flow through a 6 mm diameter opening requiring the design, construction, and calibration of a novel miniature pressure probe. Experimental pressures were limited by the probe response with tests conducted at 8 bar and 10 bar to study flow stability. Aerodynamic blockage effects were considered and detailed analysis of the experimental data is presented, using compressible flow theory and Rayleigh supersonic pitot theory. Supplementary numerical modelling could not definitively determine detached bow shock

presence within the experimental set up used, so uncertainties in the final analyses were calculated for inappropriate use of either theory. The most conservative approach was to use compressible flow theory as this underestimated the flow Mach number should a bow shock exist.

Experimentally, the flow was approximately Mach 1.15 which gives reasonable agreement with the numerical modelling; both returning low supersonic flow. Finally, two alternative model hypotheses are presented; however, neither was developed into a working model due to experimental limitations.

Acknowledgements

Having decided to embark on the epic adventure that is a part time doctorate, I have amassed an every growing list of people and institutions I must thank.

The most obvious acknowledgement has to go to Director Technology within Defence Equipment and Support for believing enough to provide funding which has actually enabled me to undertake the research as a doctorate programme.

Two people have dedicated a great deal of time to keeping me on the right path, these being my supervisors. Both Dr Bill Proud (academic) and Dr Sam Ellis (industrial) deserve special thanks as without their time, patience and drive I may have fallen at the first (or any subsequent) hurdle.

Much of the research conducted would not have been possible without the assistance of Dr Thuy-Tien Nguyen at the Institute of Shock Physics for her time and support with the Centre for Blast Injury Studies shock tube; Mr Paul Locking for his assistance with the thermochemical calculations, and the scientific staff of AWE for giving me access to the historical papers which underpinned the research.

Finally, a huge and heartfelt thanks must go to my wife Claire, who had to endure a plethora of sleepless nights and random nonsensical ramblings throughout the many years taken to bring the research together into a coherent thesis, and to my patient children, Freya and Ethan, who have gracefully put up with me prioritising my homework over theirs and bribing them with the promise of student discount.

Contents

Statement of Originality **2**

Copyright Declaration **2**

Abstract **3**

Acknowledgements **5**

List of Figures **10**

List of Tables **19**

Abbreviations, Acronyms and Mathematical Notation **21**

Abbreviations and Acronyms 21

Mathematical Notation 23

1 Introduction **35**

1.1 Motivation and Objectives the Research 35

1.1.1 Motivation 35

1.1.2 Objectives of the Research 37

1.2 Thesis Structure 39

1.3 Publications 41

1.3.1 Conference Appearances 41

2 Background **43**

2.1 Initial Detonation Theory 45

2.2 Shock Wave - Casing Interactions 46

2.3 Casing Motion and Breakup 49

2.4 Fireball Characterisation 57

2.5 Detonation Products 67

2.5.1 Detonation Product Equations of State (EoS) 70

2.5.1.1 Jones-Wilkins-Lee (JWL) EoS 70

2.5.1.2 Becker-Kistiakowsky-Wilson (BKW) EoS 74

2.5.1.3 Other EoS 74

2.6 Metal Pushing by Detonation Products 76

2.7 Fragment Flight 85

2.8 Applicable Numerical Modelling Methods 86

2.9 Summary 87

3 Initial Global Fragment Motion **91**

3.1 Historical Experimental Evidence 91

3.2 Simple MATLAB model for fragment motion within the detonation products 97

3.2.1 Assumptions 100

3.2.2 Model Methodology 101

3.2.2.1 Initial Conditions 101

3.2.2.2 Initial Casing Particle Velocity 102

3.2.2.3 Casing Expansion: Pre-fracture 105

3.2.2.4 Casing Expansion: Post-fracture 115

3.2.3 Model Comparison with Historical Experimental Data 126

3.3 Summary 128

4 Computational Simulations of Gas Leakage 131

4.1 Initial Numerical Modelling Conducted . . . 131

4.1.1 Mesh Convergence . . . 135

4.1.2 Gas Expansion Flow Speed . . . 139

4.2 Mach Number Determination for Flow within Narrow Openings . . . 147

4.2.1 Effect of Opening Size . . . 153

4.2.2 Effect of Shock Tube Driver Pressure . . . 155

4.2.3 Effect of Opening Size to Vent Length ratio . . . 156

4.2.4 Global Flow Mach Number . . . 157

4.3 Summary . . . 159

5 Experimental Flow Determination 161

5.1 Experimental Layout . . . 161

5.1.1 CBIS Shock Tube System . . . 161

5.1.2 End Plate Hardware . . . 164

5.2 Miniature Stagnation Probe Development . . . 168

5.2.1 Miniature Probe Design . . . 168

5.2.1.1 Straight Probe Cavity Length Effects . . . 172

5.2.1.2 Shock Wave Clearing Effects . . . 174

5.2.2 Gauge Construction . . . 181

5.2.3 Gauge Functionality . . . 185

5.2.4 Analogue to Digital Output Gauge Calibration . . . 192

5.2.5 Benchmarking of Novel Gauge Response . . . 199

5.2.6 Novelty of Miniature Stagnation Probe Design . . . 200

5.3 Experimental Data Analysis . . . 201

5.3.1 Shock Tube Blockage Effect Corrections . . . 201

5.3.2 Local Flow Mach Number Determination . . . 208

5.4 Summary 224

6 New Model Hypothesis 227

6.1 Pseudo Convergent-Divergent Nozzle 227

6.2 Moving Centred Rarefaction Wave 233

6.3 Summary 238

7 Conclusions and Future Considerations 241

7.1 Summary of Thesis 241

7.2 Future Work 247

7.3 Exploitation Routes 250

Bibliography 251

APPENDICES 267

A MATLAB Function for Simple Cylindrical Case Expansion 267

B EXPLO5_V6.02 Data for RDX/Wax(88/12) 275

B.1 Brief Description of Explo5 v6.02 276

B.2 Results of Calculation for RDX/Wax 88/12 277

C AUTODYN Modelling Results: Graphs of Local Flow Mach Number 281

List of Figures

2.1 Schematic showing generic time and distance scales of event 45

2.2 Gurney Sandwich Cases 53

2.3 Plot of $v_{max} > v_{rupture}$ for varying case thickness and % aluminium 54

2.4 Fragment velocities for varying case thickness and % aluminium at 6 ft and 12 ft distances [21] 55

2.5 Maximum Fireball Diameter Curves 61

2.6 Maximum Fireball Duration Curves 62

2.7 Explosion temperature histories for 3 types of air dropped bombs [40] . . . 64

2.8 Temperature-Time history of TNT detonation products [42] 65

2.9 Temperature history measured behind blast wave from PETN [43] 66

2.10 Variation in $\sqrt{F}$ (αV) against expanding cylinder radius [79] 78

2.11 Variation in $\sqrt{F}$ (αV) against distance of travel for flat plate [79] 79

2.12 Rate of standard cylinder test expansion against expansion ratio for various explosive fills [79] 80

2.13 Rate of cylinder expansion against displacement for various casing materials [79] 81

2.14 Layout of cubical fragments surrounding cylinder [82] 82

2.15 Detonation product convergent flow concept [84] 83

3.1 Cross Section through Foulness Experimental Charge [21, 89–92] 92

3.2 Case and Gas Movement from 0.125 in Thick RDX/Wax Filled Cylinder [91] 94

3.3 Flowchart for fragment and gas motion MATLAB code 98

3.4 Intersection of RDX/Wax 88/12 and 1215 Steel Hugoniot Curves 105

3.5 Pressures and stresses 110

3.6 "Chunky" fragment drag coefficient with Mach Number [107] 125

3.7 Comparison of MATLAB model and Foulness Experimental results 127

4.1 Schematic of Model Layout for Initial Numerical Modelling Conducted . . 135

4.2 Mesh Resolution Study: Gauges 1 to 5, Flow Speed Output 137

4.3 Mesh Resolution Study: Gauges 6 to 10, Flow Speed Output 138

4.4 Mesh Resolution Study: Gauges 11 to 17, Flow Speed Output 138

4.5 Mesh Resolution Study: Gauges 18 to 24, Flow Speed Output 139

4.6 Mesh Resolution Study: Gauges 25 to 31, Flow Speed Output 139

4.7 Gas Expansion Speed - AUTODYN modelling 141

4.8 Comparison of Gas Expansion Speeds 143

4.9 Local flow speed within gap - MATLAB model 144

4.10 Local flow speed within gap - AUTODYN model 144

4.11 Local flow Mach number within gap - AUTODYN model 145

4.12 Gas Expansion Mach Numbers - AUTODYN Modelling 146

4.13 Gap Length to Gap Width Ratio Effects Model Geometry 148

4.14 Flow Mach Number for 10 bar Driver Pressure, 20 mm gap length, 1 mm gap width 150

4.15 Flow Mach Number for 10 bar Driver Pressure, 20 mm gap length, 2 mm gap width 150

4.16 Flow Mach Number for 10 bar Driver Pressure, 20 mm gap length, 3 mm gap width 151

4.17 Flow Mach Number for 10 bar Driver Pressure, 20 mm gap length, 4 mm gap width . . . 151
4.18 Flow Mach Number for 10 bar Driver Pressure, 20 mm gap length, 5 mm gap width . . . 152
4.19 Flow Mach Number for 10 bar Driver Pressure, 20 mm gap length, 6 mm gap width . . . 152
4.20 Flow Mach Number variation along Gap Length for 10 bar Driver Pressure 153
4.21 Effect of Gap Width on Local Flow Mach Number along Gap Length . . . 154
4.22 Effect of Driver Pressure on Local Flow Mach Number . . . 156
4.23 Effect of Gap Width to Length Ratio on Local Flow Mach Number . . . 158
4.24 Global Flow Mach Number variation with Driver Pressure . . . 159

5.1 Schematic of CBIS Shock Tube System [108] . . . 162
5.2 Burst Pressure with Diaphragm Thickness for CBIS Shock Tube [108] . . . 163
5.3 End Plate Specification Drawing . . . 165
5.4 Simplified Schematic for End Plate Deflection . . . 165
5.5 Reflected Pressure Coefficient against Angle of Incidence [110] . . . 167
5.6 Finished End Plate - Front View . . . 169
5.7 Finished End Plate - Top View . . . 169
5.8 FISO Optical Catheter Probe Construction [112] . . . 171
5.9 Schematic of Internal Working of Optical Gauge [112] . . . 172
5.10 Generic Stagnation Probe Model . . . 173
5.11 Effect of Cavity Length Modelling Results . . . 174
5.12 Simplification of Clearing Correction to Pressure Trace [114] . . . 175
5.13 Clearing Dimension Layout . . . 176
5.14 Gauge Layout for Soundspeed Modelling . . . 177
5.15 Direct Modelling Values of Soundspeed . . . 178

5.16 Variation of Clearing Time with Elapsed Time 179

5.17 Effect of Varying Soundspeed on Clearing Time 180

5.18 Full Needle showing Bevel Removal 182

5.19 Close Up of Needle Bevel Removal 182

5.20 FOP-LS-2FR-30 and External Protection 183

5.21 Completion of Stagnation Probe Manufacture 184

5.22 Final Completed Miniature Stagnation Pressure Probe 185

5.23 Initial Variability Tests; 4 bar driver pressure, 50 μm Mylar® single diaphragm 185

5.24 Initial Variability Tests; 4 bar driver pressure, Percentage Coefficient of Variation 187

5.25 Initial Variability Tests; 6 bar driver pressure, 75μm Mylar® single diaphragm 188

5.26 Initial Variability Tests; 6 bar driver pressure, Percentage Coefficient of Variation 188

5.27 CBIS Shock Tube Double Diaphragm Breach and Fire Control System . . 189

5.28 Initial Variability Tests; 8 bar driver pressure, 75 μm Mylar® double diaphragm 190

5.29 Initial Variability Tests; 8 bar driver pressure, Percentage Coefficient of Variation 190

5.30 Initial Variability Tests; 8 bar driver pressure, Percentage Coefficient of Variation - Detail View 191

5.31 Initial Variability Tests; 10 bar driver pressure, 75 μm Mylar® double diaphragm 191

5.32 Initial Variability Tests; 10 bar driver pressure, Percentage Coefficient of Variation 192

5.33 Static/Stagnation Probe Layout for Calibration Experiments 193

5.34 8 bar Driver Pressure Digital / Analogue Output Comparison 194

5.35 10 bar Driver Pressure Digital / Analogue Output Comparison 195

5.36 Digital And Analogue Output Comparisons - Average Traces 195

5.37 Experimental Calibration Factor ($psi\ V^{-1}$) 197

5.38 8 bar Driver Pressure Digital / Analogue Pressure Comparison 197

5.39 10 bar Driver Pressure Digital / Analogue Pressure Comparison 198

5.40 Stagnation Pressure Probe Location Hardware 203

5.41 Stagnation Pressure Probe Hardware Effects - 8 bar Driver Pressure 204

5.42 Stagnation Pressure Probe Hardware Effects - 10 bar Driver Pressure . . . 204

5.43 Static Pressure Measurements - 8 bar Driver Pressure 205

5.44 Blockage Correction Factor - 8 bar Driver Pressure, 6mm gap width 205

5.45 Static Pressure Measurements - 10 bar Driver Pressure 206

5.46 Blockage Correction Factor - 10 bar Driver Pressure, 6mm gap width . . . 206

5.47 Blockage Effects - 6mm gap width 207

5.48 Schematic of Potential Bow Shock for Supersonic Flow in Experiments . . 211

5.49 Flow Model Divergence with Mach Number 214

5.50 Close up of Flow Model Divergence with Mach Number 214

5.51 Experimental Pressure Data - 8 bar driver 215

5.52 Experimental Pressure Data - 10 bar driver, static (upper) & stagnation (lower) 216

5.53 Experimental Data - Average Measured Pressures, 8 bar driver (upper) & 10 bar driver (lower) 217

5.54 Experimental Data - Ratio of Stagnation over Static pressures, 8 bar driver (upper) & 10 bar driver (lower) 218

5.55 Experimental Data - Ratio of Stagnation over Static pressures 219

5.56 Schematic of AUTODYN Model Layout for Bow Shock Capture 219

5.57 Pressure (left) and Density (right) Contour Plots for Stagnation Probe Bow Shock Analysis 220

5.58 Experimental Analysis Errors due to Inappropriate Flow Model 221

5.59 Experimentally Determined Mach Number for 6mm gap 223

5.60 Experimentally Determined Mach Number for 6mm gap; Initial Shock Oscillation 223

5.61 Average of Experimentally Determined Mach Number for 6mm gap with Standard Deviation 224

5.62 Average of Experimentally Determined Mach Number for 6mm gap with Standard Deviation; Initial Shock Oscillation 224

6.1 Schematic Representation of Flow Re-attachment Threshold [122] 228

6.2 Schematic Representation of Pseudo Convergent-Divergent Flow Model - Early Time 229

6.3 Schematic Representation of Pseudo Convergent-Divergent Flow Model - Late Time 230

6.4 Schematic Representation of Shock Tube Flow Development 235

6.5 Schematic Representation of Centred Rarefaction Wave Development . . . 236

6.6 Experimental Pressure Trace Breakdown 237

7.1 Debris from Ruptured Diaphragm 250

C.1 10 bar driver pressure, 20 mm gap length: 1 mm gap width (upper), 2 mm gap width (middle), 3 mm gap width (lower) 283

C.2 10 bar driver pressure, 20 mm gap length: 4 mm gap width (upper), 5 mm gap width (middle), 6 mm gap width (lower) 284

C.3 18 bar driver pressure, 20 mm gap length: 1 mm gap width (upper), 2 mm gap width (middle), 3 mm gap width (lower) 285

C.4 18 bar driver pressure, 20 mm gap length: 4 mm gap width (upper), 5 mm gap width (middle), 6 mm gap width (lower) 286

C.5 50 bar driver pressure, 20 mm gap length: 1 mm gap width (upper), 2 mm gap width (middle), 3 mm gap width (lower) 287

C.6 50 bar driver pressure, 20 mm gap length: 4 mm gap width (upper), 5 mm gap width (middle), 6 mm gap width (lower) 288

C.7 200 bar driver pressure, 20 mm gap length: 1 mm gap width (upper), 2 mm gap width (middle), 3 mm gap width (lower) 289

C.8 200 bar driver pressure, 20 mm gap length: 4 mm gap width (upper), 5 mm gap width (middle), 6 mm gap width (lower) 290

C.9 18 bar driver pressure, 5 mm gap length: 1 mm gap width (upper), 2 mm gap width (middle), 3 mm gap width (lower) 291

C.10 18 bar driver pressure, 5 mm gap length: 4 mm gap width (upper), 5 mm gap width (middle), 6 mm gap width (lower) 292

C.11 18 bar driver pressure, 10 mm gap length: 1 mm gap width (upper), 2 mm gap width (middle), 3 mm gap width (lower) 293

C.12 18 bar driver pressure, 10 mm gap length: 4 mm gap width (upper), 5 mm gap width (middle), 6 mm gap width (lower) 294

C.13 Gap width effects: 10 bar driver pressure (upper), 18 bar driver pressure (lower) 295

C.14 Gap width effects: 50 bar driver pressure (upper), 200 bar driver pressure (lower) 296

C.15 Gap length effects: 1 mm gap width (upper), 2 mm gap width (middle), 3 mm gap width (lower) 297

C.16 Gap length effects: 4 mm gap width (upper), 5 mm gap width (middle), 6 mm gap width (lower) 298

List of Tables

2.1 Casing type and thickness correlation 55

2.2 Swiss Probit Values for Fireball Characterisation [35] 63

2.3 r/r_0 for gas leakage from various metals [80] 80

3.1 Foulness Experiments Explosive Composition Proportions 92

3.2 Part Reproduction of Foulness Experiments Fragment Speeds [90] 93

3.3 Explo5 v6.02 calculated parameters for RDX/Wax 88/12 104

3.4 Comparison of Initial Accelerations 115

4.1 High Resolution Mesh 136

4.2 Medium Resolution Mesh 136

4.3 Low Resolution Mesh 137

4.4 Very Low Resolution Mesh 137

4.5 Gas Expansion Speeds 141

5.1 Soundspeed Modelling Gauge Locations 177

5.2 Comparison of available pressure gauges 200

6.1 Pseudo Convergent-Divergent Nozzle Model - Experimental Flow Parameters 233

Abbreviations, Acronyms and Mathematical Notation

Abbreviations and Acronyms

AASTP	Allied Ammunition Storage and Transport Publication
ALARP	As Low As Reasonably Practicable
AWRE	Atomic Weapons Research Establishment
BKW	Becker-Kistiakowsky-Wilson (EoS)
BLEVE	Boiling Liquid Evaporating Vapour Explosion
CBIS	Centre for Blast Injury Studies
CHE	Switzerland
CHEETAH	US thermochemical code (developed by LLNL)
CHNO	Carbon-Hydrogen-Nitrogen-Oxygen
CJ	Chapman-Jouget
CPU	Central Processing Unit
CTH	US multi-material, large deformation, strong shock wave, solid mechanics code (developed by SNL)
DRES	Defence Research Establishment Suffield (Canada)
DRESTC	Joint Trials series between DRES Canada and ESTC UK
EoS	Equation of State
ESTC	Explosive Storage and Transport Committee (UK MOD)
HE	High Explosive

ITOP	International Test Operating Procedure
JCZ3	Jacobs-Cowperthwaite-Zwisler-3 (EoS)
JWL	Jones-Wilkins-Lee (EoS)
LLNL	Lawrence Livermore National Laboratory
MATLAB	Matrix laboratory (numerical computing environment
MOD	Ministry of Defence
NATO	North Atlantic Treaty Organisation
PETN	Penta-Erythritol Tetra-Nitrate
RDX	Research Department Explosive (Cyclo-Tri-Methylene-Tri-Nitramine)
SNL	Sandia National Laboratories
STP	Standard Temperature and Pressure
TMD	Theoretical Maximum Density
TNT	Tri-Nitro-Toluene
UK	United Kingdom (of Great Britain and Northern Ireland)
US	United States (of America)

Mathematical Notation

Chapter 1

a	drag factor
A	fragment cross sectional area
C_D	drag coefficient
m	mass of fragment
r	range
$\bar{v}$	average velocity
v_0	initial velocity
x	linear range
ρ_{air}	air density

Chapter 2

a	inner radius of cylinder
a_0	initial inner radius of cylinder, initial acceleration of cylinder
A	presented area of fragment
A, B, R_1, R_2	JWL EoS constant fitting parameters
c	material sound speed
C	mass of explosive charge
C_D	drag coefficient
C_e	effective charge mass
$C(S)$	JWL EoS function of entropy
D	detonation velocity; retarding force on fragment
E	energy, detonation energy per unit volume
E_0	chemical energy of detonation per unit mass
L	length of tamping cylinder
m	mass of fragment
M	mass of casing
n	number of mols of material

N	mass of tamping face
r	radius behind the shock, outer radius of cylinder
r_e	expansion radius
r_{e0}	initial outer radius of cylinder
r_i	inner radius of tamping cylinder
r_{i0}	initial inner radius of cylinder
r_o	outer radius of tamping cylinder, initial outer radius of cylinder
R	radius of fireball expansion; radius of the shock, universal gas constant
R_{max}	maximum radius of fireball
P	pressure
P_α	pressure exerted on inner casing wall (by detonation products)
P_0	effective detonation pressure (acting on inside of casing)
Pr	probit value
s	crack tip speed
s_0	initial cross sectional area of cylinder case
S	entropy per unit initial volume
S_0	initial cross sectional area of charge
t	time
T	temperature
v	final velocity of casing, current volume
v_0	initial volume
v_{case}	velocity of case
v_∞	velocity to which cylinder wall tends at late time, large expansion
V	volume, volume relative to undetonated state (JWL EoS)
W	mass of explosive charge
x	linear distance, distance from detonation front
$\ddot{x}$	second time derivative of linear distance
$\sqrt{2E}$	Gurney velocity coefficient
α, β, δ, k	constant

$\alpha, \beta, \kappa, \theta$	BKW EoS parameters
γ	adiabatic constant
Γ	Gruneison gamma
Δ	correction to thermal energy due to thermal capacity dependence on T
ϵ	specific internal energy
θ	effective charge cone base angle, angle between axial section of expanded case and longitudinal axis
μ	molecular weight of detonation products
ρ	density
ρ_0	initial density
ρ_{air}	density of air
ρ_{HE}	density of explosive
ρ_m	density of cylinder metal
ρ_{shock}	density of shock
ρ_ϕ	density of tamping material
σ_H	hoop stress
ϕ	barrel tamping mass, angle of direction of motion of case
ω	JWL EoS assumed constant parameter $(\gamma - 1)$

Chapter 3

$A_{external}$	external surface area of cylinder
$A_{fracture}$	area of fractures opened
$A_{fragment}$	presented area of fragment
$A_{fragment,external}$	external surface area of fragment
$A_{fragment,internal}$	internal surface area of fragment
$A_{fragment,x-sectional}$	cross sectional area of fragment
$A_{internal}$	internal surface area of cylinder
$A_{x-sectional}$	cross sectional area of cylinder
a	acceleration

a_1	acceleration of inner surface of cylinder
a_{10}	initial acceleration of inner surface of cylinder
a_4	fragment acceleration due to expanding detonation products direct drive on internal surface
a_{casing}	acceleration of the casing
a_{drag1}	fragment acceleration due to drag in region ahead of shock wave
a_{drag2}	fragment acceleration due to drag in region between shock wave and contact surface
a_{drag3}	fragment acceleration due to drag in region behind contact surface (once detonation products have overtaken fragments)
a_{drag4}	fragment acceleration due to detonation products escaping between fragments
$a_{fragment}$	acceleration of fragments
$a_{products_{post-rupture}}$	post rupture acceleration of gaseous detonation products
a_{total}	total fragment acceleration
C	mass of explosive charge
c	sound speed
c_0	material sound speed
c_1	atmospheric sound speed ahead of shock wave
c_2	sound speed behind expanding shock wave but ahead of contact surface
c_3	sound speed immediately outside casing but behind contact surface
c_4	driver sound speed within casing
C_D	drag coefficient
C_{D_1}	drag coefficient for fragment motion ahead of shock wave
C_{D_2}	drag coefficient for fragment motion in region between shock wave and contact surface
C_{D_3}	drag coefficient for fragment motion in region behind contact surface
C_{D_4}	drag coefficient for fragment motion due to detonation products escaping between fragments

D	detonation velocity
d	projectile reference diameter
$\bar{d}$	average diameter
$d_{average}$	average diameter of cylinder
$d_{external}$	external diameter of cylinder
$d_{internal}$	internal diameter of cylinder
F	force
F_4	unbalanced force in region of expanding detonation products direct drive on internal surface
$F_{external}$	force acting on the cylinder external surface
$F_{internal}$	force acting on the cylinder internal surface
$F_{material}$	force acting within the material
K	strength coefficient
L	Lagrangian; cylinder length
M	mass of metal casing
m	mass of projectile
$\bar{m}$	average fragment mass
$\dot{m}$	mass flow rate
m_1	mass of gaseous detonation products within casing prior to venting
m_2	mass of gaseous detonation products within casing post venting
m_f	mass of fragment
m_{gas}	mass of gaseous detonation products
m_{lost}	mass of gaseous detonation products lost through venting
n	number of dimensions (1, 2, 3); strain hardening exponent
$n_{fragment}$	number of fragments generated
P	pressure
P_0	initial pressure
P_1	pressure of gaseous detonation products within casing prior to venting; atmospheric pressure ahead of shock wave

P_2	pressure of gaseous detonation products within casing post venting; pressure behind expanding shock wave but ahead of contact surface
P_3	pressure immediately outside casing but behind contact surface
P_4	driver pressure within casing, pressure on fragment internal surface due to expanding detonation products direct drive
P_{atmos}	atmospheric pressure
P_{CJ}	Chapman Jouget pressure
P_{DP}	pressure due to detonation products
$P_{external}$	external pressure
$P_{internal}$	internal pressure
$P_{transmural}$	transmural pressure, $P_{transmural} = P_{internal} - P_{external}$
$\hat{r}$	increasing radial direction vector
$\bar{r}$	average radius
$\dot{r}$	first time derivative of radial expansion
$\ddot{r}$	second time derivative of radial expansion
$\ddot{r}_4$	second time derivative of radial expansion in region of expanding detonation products direct drive on internal surface
$\ddot{r}_{drag1}$	second time derivative of radial expansion for fragment motion ahead of shock wave
$\ddot{r}_{drag2}$	second time derivative of radial expansion due to drag effects for fragment motion in region between shock wave and contact surface
$\ddot{r}_{drag3}$	second time derivative of radial expansion due to drag effects for fragment motion in region behind contact surface
$\ddot{r}_{drag4}$	second time derivative of radial expansion due to drag effects from detonation products escaping between fragments
r_1	inner radius of cylinder
r_{10}	initial inner radius of cylinder
r_2	outer radius of cylinder
r_{20}	initial outer radius of cylinder

$r_{contactsurface}$	radius of contact surface
$r_{external}$	external radius of cylinder
$r_{internal}$	internal radius of cylinder
s	experimentally determined parameter
s_{casing}	expansion of the casing
$s_{products_{post-rupture}}$	post rupture expansion of gaseous detonation products
T	kinetic energy
t	time; thickness of cylinder
$t_{rupture}$	time of casing rupture
U	potential energy
U_s	shock speed
u_2	particle speed behind expanding shock wave but ahead of contact surface
u_3	particle speed immediately outside casing but behind contact surface
u_p	material particle speed
V	volume
$V_{internal}$	internal volume of cylinder
V_0	initial volume
V_C	volume of explosive charge
V_M	volume of metal casing
v	projectile speed
v_1	velocity of inner surface of cylinder
v_{10}	initial velocity of inner surface of cylinder
v_{casing}	velocity of the casing
$v_{fragment}$	velocity of the fragment
v_{gas}	velocity of gaseous detonation products
$v_{products_{post-rupture}}$	post rupture velocity of gaseous detonation products
W_x	range direction component of wind speed
W_r	radial component of wind speed
w	constant, such that $w^2 = r_2^2 - r_1^2 = r_{20}^2 - r_{10}^2$

$w_{fracture}$	width of casing fracture
x	linear distance
x_0	initial position
$\dot{x}$	first time derivative of linear distance
$\ddot{x}$	second time derivative of linear distance
δ	small increment in associated variable
δt	timestep length
ϵ	true strain
γ	adiabatic constant
γ_1	adiabatic constant of atmosphere ahead of shock wave
γ_2	adiabatic constant behind expanding shock wave but ahead of contact surface
γ_3	adiabatic constant immediately outside casing but behind contact surface
γ_4	driver adiabatic constant within casing
ρ_1	density of gaseous detonation products within casing prior to venting; atmospheric density ahead of shock wave
ρ_2	density of gaseous detonation products within casing post venting; density behind expanding shock wave but ahead of contact surface
ρ_3	density immediately outside casing but behind contact surface
ρ_4	driver density within casing
ρ	material density
ρ_m	casing metal density
ρ_0	initial density
σ_{flow}	flow stress
σ_H	hoop stress

Chapter 4

c	sound speed
r_{case}	radial expansion of casing
r_{gas}	radial expansion of gaseous detonation products
$\dot{r}$	first time derivative of radial expansion
$\dot{r}_{gas}$	first time derivative of radial expansion of gaseous detonation products
$\ddot{r}$	second time derivative of radial expansion
P	pressure
P_0	reference pressure
t	time
γ	adiabatic constant
ϵ	specific internal energy
ρ	density
ρ_0	reference density

Chapter 5

a	outer radius of circular annular endplate; sonic velocity within reflected pressure region; acceleration
b	inner radius of circular annular endplate
$CV_{\%}$	percentage coefficient of variation
C_1, C_4	plate constant
D	flexural rigidity of circular annular endplate
d_{gauge}	diameter of stagnation probe
d_{vent}	diameter of venting opening
E	Young's modulus of elasticity
G	larger of height or half width of target face
k	calibration factor
L_{11}, L_{14}	plate loading constant
M	Mach number

M_1	flow Mach number upstream of shock wave
M_2	flow Mach number downstream of shock wave
$M_{compressible}$	flow Mach number calculated using compressible flow theory
$M_{Rayleigh}$	flow Mach number calculated using Rayleigh Supersonic Pitot Theory
N	number of values in sample of population
P	pressure
P_s	static pressure
$P_{s_{corrected}}$	static pressure corrected for blockage effects
$P_{s_{measured}}$	static pressure as measured
P_T	stagnation (total) pressure
P_{S_1}	static pressure upstream of shock wave
P_{S_2}	static pressure downstream of shock wave
P_{T_2}	stagnation (total) pressure downstream of shock wave
q	uniformly distributed pressure; dynamic pressure
R	ratio S/G
r	radius of cylinder
r_0	inner radius to which uniformly distributed pressure is applied
S	smaller of structure height or half width of target face; distance travelled
s	standard deviation
t	annular plate thickness; time
t_c	clearing time
u	initial speed
u_∞	freestream flow speed
V	analogue voltage signal
x	individual result
$\bar{x}$	mean value of results
y_b	final deflection of circular annular endplate
β	blockage factor
γ	adiabatic constant

ρ_1	density upstream of shock wave
ρ_2	density downstream of shock wave
ρ_∞	freestream density
ρ_S	static density
ρ_T	stagnation (total) density
ν	Poisson's ratio

Chapter 6

A	area
A_3	cross sectional area of region 3
A_{3a}	cross sectional area of region 3a
A_{3b}	cross sectional area of region 3b
d_0	orifice diameter
h_0	orifice channel height
M	Mach number
M_3	Mach number of flow in region 3
M_{3a}	Mach number of flow in region 3a
M_{3b}	Mach number of flow in region 3b
M_4	Mach number of flow in region 4
M_x	Mach number of flow in region x
$\dot{m}$	mass flow rate
P_0	reference pressure
P_{3a}	pressure in region 3a
P_4	pressure in region 4
u	local flow speed
γ	adiabatic constant
ρ	density
ρ_0	reference density

Chapter 1

Introduction

1.1 Motivation and Objectives the Research

1.1.1 Motivation

The underlying driver for this research is the need to ensure the risk to personnel (both military and civilian) is reduced to As Low As Reasonably Practicable (ALARP) during ammunition and munitions storage, transport, loading, unloading and processing. Technology and manufacturing techniques are progressing and the development of munitions with longer anticipated life cycles are becoming ever more commonplace, however the majority of any munition's life is spent within a relatively benign storage environment.

The storage phase can be either within UK based masonry or concrete facilities, or potentially ISO containers / earth covered field storage facilities during out of area operations. Regardless of which, the UK Ministry of Defence Explosives Regulations [1] dictates a minimum distance to the inner surface of the storage facility walls of 500 mm to prevent flash over from lightning strikes, allow natural ventilation and give room for manual inspection of the munitions.

This minimum distance to the wall is not large enough to ensure that any fragments formed have exited the detonation product cloud prior to impacting the walls; nor is it large enough to guarantee the formation of discrete fragments as predicted by either arena

trials or statistical based theories. The pressure loading from such fragments impacting the storage facility walls are calculated based on an assumption that the fragments are predictable and discrete, and are still travelling at their initial launch speeds as the air gap traversed is short.

The estimation of fragment masses and the fragment mass angular distribution is generally developed based on fragments collected within prescribed logarithmic mass bands and angular zones around the arena. The data gathered requires correction to account for the recovery arena shape, height and standoff distance before being fitted to a statistical distribution for use in fast running engineering models, and for comparison to existing data from historical sources.

The estimation of the initial speed of fragments generated from a munition detonation is determined by following the guidelines laid down in the current edition of The International Test Operations Procedure for determining weapon fragment spatial distributions [2]. The methodology uses an arena layout surrounding the munition with witness packs to collect the fragments produced. These witness packs have their front faces instrumented to record the time of arrival of the fragments, thus giving an average speed of the fragments across the arena radius. The initial speed is then calculated as a function of the recorded average speed

$$v_0 = \frac{\bar{v}(e^{\frac{ar}{m^{1/3}}} - 1)}{\frac{ar}{m^{1/3}}} \tag{1.1}$$

This method rigidly implies an instantaneous jump of the fragment to the launch speed followed by deceleration of the fragment throughout its trajectory, the flight of which is wholly within an ideal gas at Standard Temperature and Pressure (STP).

As with the fragment mass angular distribution, the calculated launch (or initial) speeds can be averaged across each angular band with each band being used to construct the full angular distribution of initial fragment speed from nose to tail of the weapon under test.

An alternative method for determining the fragment initial speed is to use high speed

video photography of a selection of fragments to determine fragment retardation data. This is usually gathered for mid to far range fragment flight (i.e. 10's to 100's of charge initial diameters into the ballistic flight phase) from the source. This retardation data can then be used to reverse extrapolate from the measured instantaneous speed on the high speed video evidence back to an initial launch speed at time zero. This can be done by applying standard aerodynamic relations [3]

$$v = v_0 e^{\frac{-C_D A \rho_{air}}{2m} x} \tag{1.2}$$

Neither of these methods takes account of the detonation product / fireball effects (temperature, density, flow rate, etc.); they employ simple aerodynamic drag laws with an invariant adiabatic constant of 1.4 to reverse calculate the initial fragment speed.

In reality this will not be the case and although any deviations from this assumption of early time fragment motion may not be significant for long-range interactions there is no evidence that the same can be said for close in interactions. This is especially true for those where the target is either within or close to the edge of the detonation product cloud / fireball expansion.

1.1.2 Objectives of the Research

The aim of the research was originally to develop a model of the acceleration phase of the fragments within the expanding detonation product cloud. This was very quickly overtaken by the need to investigate the more fundamental aspect of the applicability of the current and generally accepted gas leakage model, as during the numerical modelling of an idealised venting scenario the results returned evidence that the current accepted gas leakage model did not hold for any of the scenarios investigated. For venting openings of 1 mm diameter or more, the research conducted clearly showed the flow within the vent opening to be at Mach numbers greater than unity. The accepted concept of the flow within the vent following ideal nozzle theory and thus being limited to sonic speeds is clearly not applicable in these cases.

The revised aim of this research is therefore to determine the limits of applicability of the current gas leakage model and where possible to determine a more generally applicable model.

This aim will be realised by meeting the following objectives throughout the research:

- Determine the limits of applicability of the current gas leakage model
  - Develop an original fast running engineering model of available historical experimental data
    - Apply current gas leakage model to venting phase
    - Determine the level of agreement between the current gas leakage model and the experimental evidence
  - Conduct original numerical simulations to investigate the gas flow through openings within an idealised munition casing fracture
  - Investigate phenomenological effects based on original numerical simulations
    - effect of opening size
    - effect of driver pressure
    - effects of opening size to casing thickness ratio
- Conduct original shock tube experiments to investigate gas flow through small openings
  - Use original numerical simulations to plan effective experimental series
  - Develop original and novel diagnostic hardware to measure gas flow parameters within small openings
    - Generate original optimised designs using bespoke numerical simulations and novel application of existing shock wave clearing theory
    - Test, calibrate and field original design in experimental series
    - Generate bespoke blockage correction factors using original experimental data

    - Apply existing flow theories to analyse experimental data for supersonic gas flows in small idealised openings

- Propose new gas leakage model based on original experimental data.

  - Investigate levels of applicability of proposed new models

1.2 Thesis Structure

This chapter gives an introduction to the what, why and how of the research.

Chapter 2 gives a brief review of available literature within related topics including the initial interaction of the casing material with the detonation induced shock wave followed by the motion and breakup of explosively driven metal, the generation and characterisation of detonation products and fireballs, metal pushing through detonation product expansion and subsequent fragment flight.

Each area reviewed adds to the background of the research but compilation of historical experimental data, relating directly to the acceleration of the casing material through the expansion of the gaseous detonation products both at fracture and post-fracture, is limited. The available data is briefly reviewed within Chapter 2 but is examined in more detail later in the thesis.

Chapter 3 introduces a simplified original MATLAB model developed during the research to replicate historical data generated from explosively driven cylinder tests.

The model developed covers the interaction of the detonation induced shock wave with the meta cylinder and the subsequent expansion of the metal cylinder casing up to and beyond the point of rupture. Post rupture the internal driving pressure is reduced by the leakage of detonation products through the growing cracks. Alongside the tracking of fragment motion, the expansion of the detonation products is also studied, including the application of ideal nozzle flow within the venting gap caused by the casing fracture.

The pre-fracture casing expansion initial acceleration from the original MATLAB model is compared to a high fidelity equation of motion and the levels of agreement as-

sessed. Post casing fracture, the casing gaseous detonation product expansions generated by the model are compared directly to the output of the historical experiment.

Chapter 4 uses high fidelity numerical simulation software to run a series of original scenarios to determine the applicability of the gas flow methodology within the MATLAB modelling. The outcome of this study led to the narrowing of the thesis scope to research high pressure gas flow through narrow openings.

Further numerical modelling is used to investigate any effects driven by the opening size of the fracture, the gas pressure within the casing and any potential effect due to combinations of the opening size to the vent length (casing thickness).

Chapter 5 comprises the main section of the research. The experimental phase layout is discussed, including original hardware design to enable a specific numerical modelling scenario to be realised experimentally. Discussion of the re-purposing of commercially available rodent catheter probes into an original and novel design for a miniature probe to measure static and stagnation pressures is included, along with details of the construction method applied and the calibration of the probes for shock tube use.

Detailed analysis of the experimental data is undertaken with the outcome being compared with the numerical modelling and the research hypothesis.

Chapter 6 introduces two original gas leakage model concepts, based on a novel application of nozzle and shock tube flows, with their applicability demonstrated; however neither concept is fully developed at this stage due to a lack of data across multiple scenarios.

Chapter 7 summarises the thesis giving concise conclusions of the research linking back to the stated aims and objectives, along with details of expected exploitation routes. Suggestions for future work are made to enable improvements to the experimental and numerical aspects of the research, and to generate further data required to underpin new and alternative models for the gas leakage.

Finally, details of the original MATLAB function developed, the thermochemical output used to develop the reacted explosive JWL equation of state, and extensive output

from the numerical modelling conducted, are included in separate appendices at the end of the thesis for completeness.

1.3 Publications

1.3.1 Conference Appearances

- **The Effects of Expanding Detonation Products on Early Time Fragment Flight: Early Stage Assessment**

  C Hoing. Group of Experts on Mitigation Systems, UK. January 2015. *Presentation*

- **Flame Grilled Fragments: Post Casing Breakup Fragment Acceleration Update**

  C Hoing. Group of Experts on Mitigation Systems, UK. January 2016. *Presentation*

- **Further Investigation of the Post Casing Fracture Fragment Acceleration: Early Time Nozzle Flow through Casing Fractures**

  C Hoing, M Hutchinson, W G Proud. 24^{th} International Symposium on the Military Aspects of Blast and Shock, Halifax, Nova Scotia, Canada. September 2016. *Presentation, Paper in proceedings*

- **Post Casing Fracture Fragment Acceleration: Early Time Nozzle Flow Through Casing Fractures. Research Update**

  C Hoing. Science and Technology Division Seminar, Defence Ordnance Safety Group, UK. May 2017. *Presentation*

- **Miniature Optical Stagnation Probe Development**

  C Hoing. Group of Experts on Mitigation Systems, UK. January 2018. *Presentation*

Chapter 2

Background

Detonation of an explosive charge surrounded by a casing material will, in simple terms, accelerate and fracture the casing material into many small high-speed fragments. The detailed timelines for the event are complex but of fundamental importance to gaining a full understanding of both the generation, and effects, of these fast moving fragments.

To simplify to a general case the initial investigation will be limited and will not include reactive casing materials; non-ideal, enhanced or aluminised explosives; non-detonative event fireballs or multiple coalescing fireballs.

Pearson [4] gives a breakdown of the casing expansion and fragmentation behaviour from first motion to target impact categorising the motion into four phases, however it is necessary to consider an additional phase before any physical motion of the casing is detected:

- Phase 0: Shock propagation through casing but no expansion. Local flaw sites initiate crack propagation.
- Phase 1: Elastic-plastic expansion but no fractures
- Phase 2: Plastic expansion to opening of fractures but no gas leakage
- Phase 3: Further case expansion with major fragmentation. Leakage of gas products. Fragment flight through product cloud.
- Phase 4: Ballistic flight of fragments to target.

An indication of the distance and time-scales required to assess the effects of interest

are combined with the phase breakdown expanded from Pearson in Figure 2.1 below. This gives a schematic break down of the major processes involved in the production of fragments from a cylindrical cased charge detonation.

The time and distance scales in Figure 2.1 are a generic approximation with R_{case} being the initial radius of the cylinder case material. Actual values will vary depending on system parameters such as geometry, energetic and case materials, case thickness, etc. The portion of the process under interest for this study is highlighted in red and clearly gives an indication of the potential challenges faced to develop theories and gather experimental data within the indicated time and distance scales.

Pearson also discusses work conducted by Waggener [5] which used multi-flash radiography to determine fragment velocities from a cylindrical warhead within the detonation product cloud. From the study, although Waggener observed a maximum fragment velocity within the cloud of approximately 95% of the calculated Gurney velocity for the configuration tested, the data generated was limited to only two individual times (between 130 μs and 450 μs post initiation). This gave a coarse estimation of a single average velocity.

Waggener appears to have not conducted enough tests to return a reasonable fidelity to the results, which would otherwise have offered an indication of the acceleration phase of the fragments.

Although the work conducted by Waggener appears to give an excellent starting point, it is worth spending a little time reviewing work conducted within the other portions of the process as these may have some bearing on the final direction of the research. Other aspects not shown in Figure 2.1, including metal plate acceleration, should be considered for the same reason.

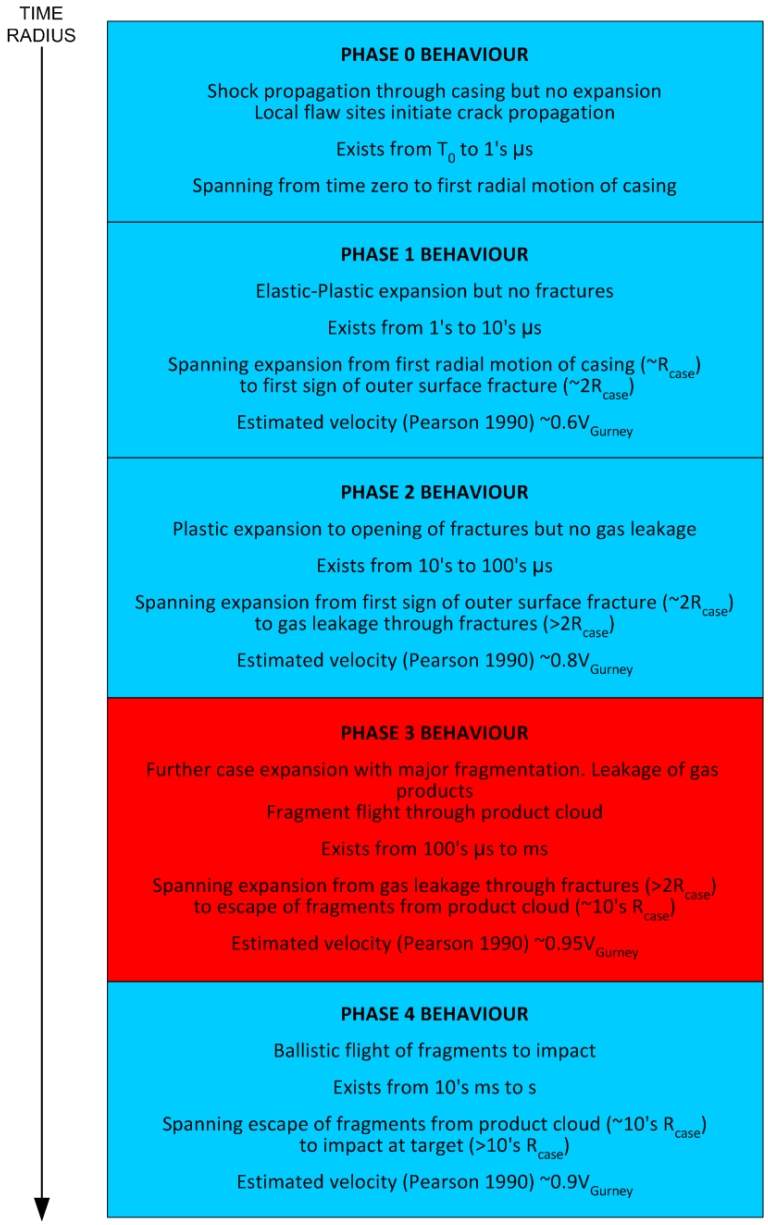


Figure 2.1: Schematic showing generic time and distance scales of event

2.1 Initial Detonation Theory

To understand the generation of fireballs and their properties, it is necessary to briefly look at the detonics within the system. Explosives have been in use for centuries, however detailed study of the detonative processes did not start until the late nineteenth century.

The work of early western pioneers of the modern detonation theory including Vielle, Berthelot, Mallard, Dixon, Chapman, Jouguet, Rankine and Hugoniot as well as the contribution from Russian pioneers, including Mikelson, is well summarised by Lee [6].

The historical research by Lee reviews the seminal works for detonation theory but does not cover the topic of casing acceleration, break up and the subsequent gas leakage. These topics began to gather more momentum with the desire to better understand, and ultimately improve the characteristics of weaponised systems.

2.2 Shock Wave - Casing Interactions

In the initial few microseconds after detonation of the explosive, the detonation wave interacts with the casing material and transmits a shock wave into the casing material as well generating a reflected Hugoniot adiabat running back into the detonation products. The strength of the transmitted shock wave depends on the shock impedance matching and can be calculated using shock Hugoniots for each material involved with a similar technique being employed to calculate the strength of subsequent internally reflected shock waves reverberating within the casing.

Prior to any movement of bulk material, the shock wave runs through and interacts with flaws and voids within the casing material. Under the compressive loading from the shock wave, the voids collapse leading to tensile cracking with microcracks nucleating at the intersections of slip lines. These microcracks then grow along the slip lines generally normal to the applied compression during unloading. Nemat-Nasser & Chang [7] showed that the crack growth was dependent on the initial void size, rate of loading and the fracture toughness of the material. They also showed the resistance of the voids collapsing into cracks under compressive loading increases with an increasing loading rate, however once the void has collapsed the amount of cracking generated during unloading increases with an increasing loading rate.

In Split Hopkinson Bar compression tests, it can be seen that unloading only covers a few microseconds at most, making the crack growth process very fast compared to the bulk material expansion that follows. At very high strain rates, Nemat-Nasser & Chang showed that recrystallisation can occur at the crack tips along with the tensile cracking

in pure copper, mild steel and pure iron.

As with metals, shock induced cracking within rock is a widely researched subject for mining and blasting with substantial progress being made in the development and application of numerical simulation methods; however, even as recently as 2015, there was no robust numerical model which could accurately simulate gas flow within cracks in rocks [8], although over time different researchers have employed different numerical modelling methods and techniques to progress the situation.

Lanari & Fakhimi conducted numerical simulations to isolate the effects of the shock wave loading from the gas induced damage by modelling an explosive charge within a bore hole. The explosive charge was modelled both with and without a copper lining to isolate the shock wave effects from those of the shock wave and gas penetration combined. From this they were able to confirm that the majority of internal cracks were formed through the shock wave interaction with internal flaws, whilst the gas penetration was mainly responsible for the fragment separation. This was confirmed experimentally by Brinkmann [9] who showed that the rock fragmentation break out is controlled by the gas with the strain wave loading controlling the fragmentation sizes. Further research by Banadaki [10], amongst others, reiterates this position and also shows how the initial material microstructure and internal defects have a substantial effect on the fractures and fragmentation produced.

Along with this, Lanari & Fakhimi [8] showed an increase in internal damage of the rock sample as the compressive shock wave reflected off the free edge of the sample is transmitted as a tensile wave back into the sample. This phenomenon would also occur within a weapon metallic casing. From the study conducted by Lanari & Fakhimi, it was also seen that increasing the strength of the rock sample reduced the overall number of cracks produced and dramatically reduced the time taken to produce the initial phase of internal cracking. It can be postulated that this observation suggests the shock wave induced internal damage to a metallic weapon casing would generate a lower number of internal cracks within a very short timeframe; potentially the first few microseconds or

less.

Fracture mechanics lectures, for example by Eindhoven University of Technology [11], show that cracks only grow if the tip stress exceeds the fracture toughness of the material. Energy balance arguments show that the crack tip speed under dynamic loading conditions often sit within the range

$$0.2 < \frac{s}{c} < 0.4$$

where s is the crack tip speed and c is the material sound speed. Generally an approximation of $\frac{s}{c} \approx 0.38$ is acceptable for estimating the crack tip speed from material properties; however, experimental data has shown that the actual value can be lower due to energy dissipation during crack growth.

For a steel cylinder surrounding an explosive charge, as in the historical trials conducted by James *et al* discussed in more detail later, a rough order of magnitude estimate of the expected significant speeds can be developed:

- Detonation velocity of explosive, circa 8 $mm\ \mu s^{-1}$
- Dynamic loading shock velocity, circa 5 $mm\ \mu s^{-1}$ (based on the sound speed of steel)
- Crack tip speed, circa 2 $mm\ \mu s^{-1}$ (based on the generic approximation $\frac{s}{c} \approx 0.38$)

As previously mentioned, the crack usually propagates in a direction normal to the loading stress wave. In this case the dynamic loading is from the shock wave imparted into the steel casing by the detonation wave running the length of the cylinder, due to the single end initiation. From this the dynamic loading shock wave is also running the length of the cylinder and thus it would be expected that cracking would appear at flaw sites running through the thickness of the cylinder. It can be seen that for a cylinder of approximately 3 mm thickness, it would take less than 2 μs from loading for individual cracks to be completely through thickness.

As the material properties, including flaw site locations and fracture toughness, are not identical at all locations but statistically distributed throughout the material, different degrees of internal cracking will be distributed throughout the material; with some cracks propagating through thickness and other, often nearby, cracks will arrest after only a short distance.

This rough estimation of relative speeds and timeframes illustrates that the majority of internal damage would be generated within the first microsecond following the arrival of the dynamic shock wave loading at the flaw site; during which time the bulk expansion of the casing has not yet begun.

2.3 Casing Motion and Breakup

The concept of surrounding an explosive charge with a metal casing to produce fragments upon detonation has been around for some considerable time: the earliest serious (Western) study into the prediction of the casing motion and break up is attributed to Mott, Gurney and Taylor. It is obvious that wartime research by scientists and engineers from Germany and Russia would have been conducted along similar lines; however, the difficulty in locating and accessing such historical literature makes a comparison between approaches across the entire field unfeasible at this stage. The publication of contemporary research in scientific journals eases the situation greatly.

Initial studies conducted by Mott concentrated on the development of a theoretical thesis for the statistical distribution generated from the natural fragmentation of cylindrical style weapons [12–15]. Mott investigated the distribution of masses and sizes of fragments generated by the detonation of a limited number of in-service (at the time) weapons. He used data gathered from outside his own sphere of work, including distribution laws for some crushed materials, and extended the concept to two and three dimensions. He applied similar distribution laws to his own material before comparing them against available experimental data. Underlying assumptions within the work are

not documented and some aspects of the improved theory are not compared against the experimental data, but are reported as being limited to only the cylindrical portions of the shell [15].

When investigating the velocity relationships for the fragmentation developed, Mott looked to Taylor in the first instance. Within his earlier work [16], Taylor makes the assumption that the radial motion of the detonation gases is substantially less than the longitudinal motion (i.e. following the direction of the detonation wave). From this assumption, he infers that the radial motion of the gases can therefore be neglected and the standard Bernoulli Equation may be used to calculate the subsequent motion of the gas.

Taylor also calculates the velocity of the weapon case material and shows that for a trinitrotoluene (TNT) filled charge only approximately 25% of the available energy is given to the casing at a radius such that the casing has expanded by 12% of its original radius ($R/R_0 = 1.12$). He continues to show that in order to get the efficiency to 50% of the available energy being given to the expanding casing it would have to remain intact until an expansion of 90% has been reached ($R/R_0 = 1.90$).

Within this work Taylor conducts limited comparisons with experimental data captured by Payman; although Taylor doesn't reference any experimental set-up or analysis documentation he does state that the experiments are not suitable due to the cylinder used being short, having heavy confining end caps which will induce internal reflections, and the explosive fill material being different. Given these extreme caveats (different tube design and explosive fill), the comparison between Taylor's theory and the experiments still returns a reasonable agreement of 1190 ms^{-1} (Taylor) c.f. 1360 ms^{-1} (Payman).

Taylor uses his theory of the motion of the expanding gases within a tube to determine the fragment velocities and direction at the point of casing break up. He does not use this knowledge to investigate the gas leakage nor the fragment velocity profile post fracture. Taylor introduces the concept that the velocities of the casing and fragments at the

point of break up cannot be assumed to be equal. Indeed, he shows this using test results from multiple experiments using different materials and some scored (non-naturally fragmenting) shells which break up at different expansion ratios. Some of this relies on unpublished references.

Mott uses this knowledge within his study [12]; however some of the experimental data he uses shows the casing velocity exceeding that of the resulting fragments. Given the contradictory nature of the data and the unexplained origin of this contradiction, Mott dismissed it in favour of the theoretical values. In addition, some of his data shows small fragments of very high velocity being recovered; this is dismissed as probably acquired from the expanding gases after break-up and again (unfortunately) does not warrant further investigation.

Mott corroborates Taylor's premise that the velocity of the fragments need not be equal to the velocity of the casing at break up using unpublished experimental data. He suggests that the experimental data shows the pressure applied from the explosive onto the inner face of the casing continues to affect the expansion of the casing even after break up has occurred. Although he is suggesting that the final velocity of the fragments may be affected by the complete pressure history seen by each fragment throughout the expansion and beyond fracture, Mott limits the dependence of the fragment sizes on their velocity only to the influence of the moment of break up and not their full history to that point.

The research conducted by Taylor was also the starting point for further experimental investigations of the expansion and fracturing of cylinders [17]. Here Allison and Schriempf present results that suggest the cylinders are fracturing well before the usually assumed 100% expansion of the radius but no discussion is made of this point. It is unclear why the cylinders may have fractured early and why the authors failed to discuss this point. They suggest the observed data fits well with Taylor's theorem at large radii but again there is no discussion concerning the degree of fit between the experiment and the theory for very small radii. It is clear from the work presented, and the discussion on the measurement

methods employed, that although experimental care was taken, the data is of limited fidelity purely due to the mechanics of positioning pin probes at varying radii around the cylinder, with a positional variation of 0.002 inch giving a temporal variation of 0.006 μs.

Probably the most widely used theory for the motion of the casing and the fragments produced post fracture is that credited to Gurney [18]. This work only concentrates on cylindrical and spherical cases but is claimed to be applicable to munitions ranging in size from grenades, through large artillery shells, to aircraft bombs.

Gurney's original expression has been quoted by numerous authors, including Cooper [19,20] in a simplified form relating the mass of casing (M [kg]) and the mass of explosive (C [kg]) in a dimensionless load factor (M/C):

$$\frac{v}{\sqrt{2E}} = \begin{cases} \left(\frac{M}{C} + \frac{1}{2}\right)^{-\frac{1}{2}} & \text{for cylindrical charges} \\ \left(\frac{M}{C} + \frac{3}{5}\right)^{-\frac{1}{2}} & \text{for spherical charges} \end{cases} \tag{2.1}$$

where v is the final velocity of the casing $[ms^{-1}]$ and $\sqrt{2E}$ is the Gurney velocity coefficient $[ms^{-1}]$, giving a dimensionless velocity $(v/\sqrt{2E})$.

In their explanation of the extension to other geometries [19], Cooper and Kurowski credit JE Kennedy for the introduction of similar equations to the symmetric, asymmetric and open faced sandwich cases; although no citation is given for the work of Kennedy (or anyone else) which led to this extension of Gurney's work.

Figure 2.2 gives basic sketches of examples of each sandwich case; (A) Symmetric (B) Asymmetric (C) Open Sandwich.

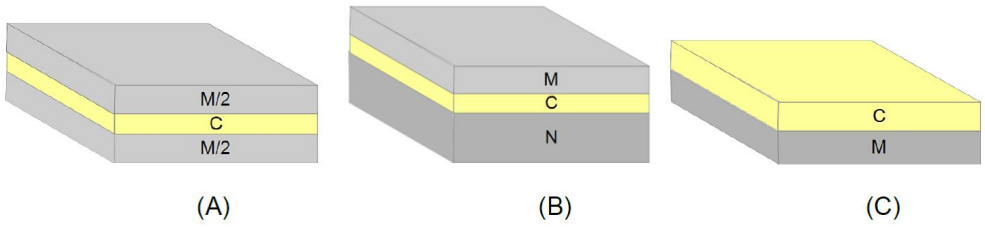


Figure 2.2: Gurney Sandwich Cases

The equations for the cases quoted by Cooper and Kurowski being shown in Equations 2.2

$$\frac{v}{\sqrt{2E}} = \begin{cases} \left(\frac{M}{C} + \frac{1}{3}\right)^{-\frac{1}{2}} & \text{for symmetric sandwich charges} \\ \left(\frac{(1+2\frac{M}{C})^2+1}{6(1+\frac{M}{C})} + \frac{M}{C}\right)^{-\frac{1}{2}} & \text{for open face sandwich charges} \\ \left(\frac{1+A^3}{3(1+A)} + \frac{N}{C}A^2 + \frac{M}{C}\right)^{-\frac{1}{2}} & \text{for asymmetric sandwich charges} \end{cases} \tag{2.2}$$

where M [kg] is the mass of the casing and C [kg] is the mass of the charge as per the cylindrical and spherical geometry cases. For the asymmetric sandwich case, additional terms are included as given by Equation 2.3 below:

$$A = \frac{1 + 2\frac{M}{C}}{1 + 2\frac{N}{C}} \quad \text{with N = mass of tamping face} \tag{2.3}$$

From Figure 2.2, it can be seen that the mass of the casing (M) includes both faces for the symmetrical sandwich.

The Gurney velocity coefficient ($\sqrt{2E}$) depends on the explosive material used and can be estimated by taking one-third of the detonation velocity (D/3); according to Cooper and Kurowski this estimation gives a reasonable agreement with experiment, usually to within 7%.

The concept that the maximum fragment velocity reached is not equal to the velocity measured at the point of break up is clearly supported by experimental findings [21]. In this study, Denny *et al* considered the effects of casing thickness and the proportion of

aluminium introduced into the energetic material. Plotting their data allows the surface plot shown in Figure 2.3 to be constructed which clearly shows $v_{max} > v_{rupture}$ (the data points are labelled with the surface plot being constructed through interpolation).

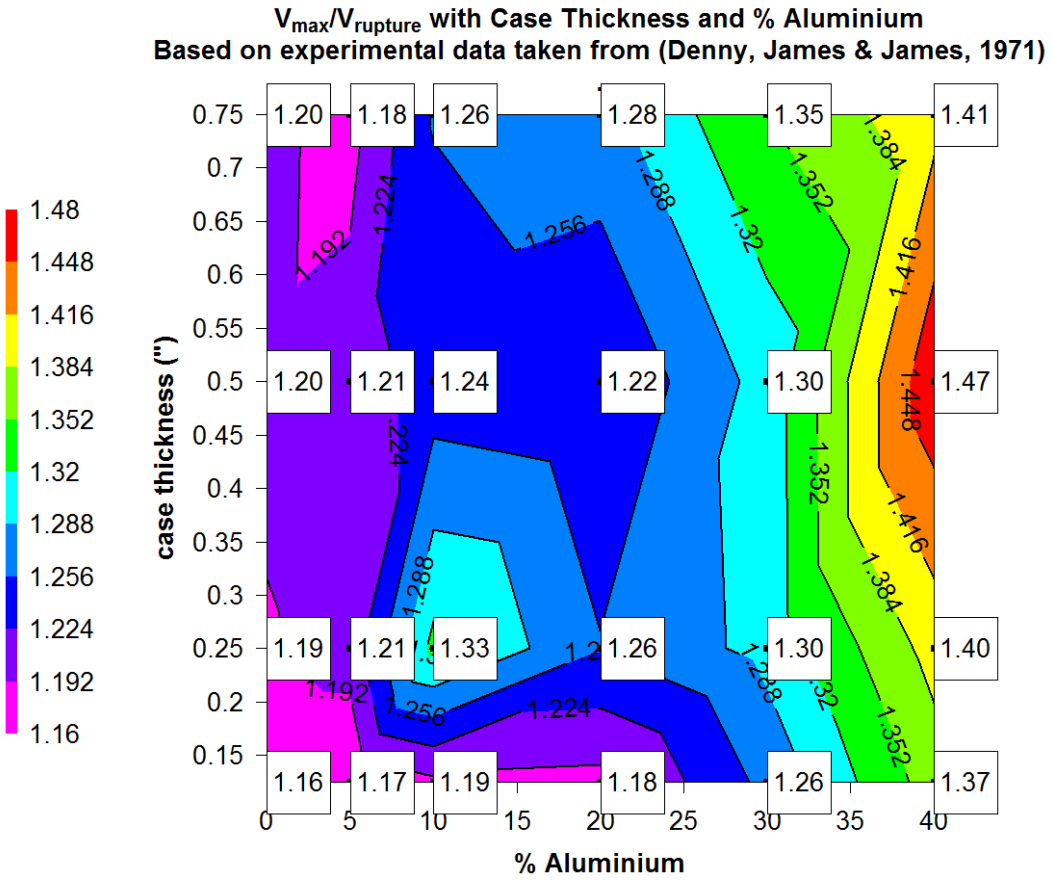


Figure 2.3: Plot of $v_{max} > v_{rupture}$ for varying case thickness and % aluminium

Denny *et al* present data showing that for 40% aluminium inclusion, the velocity of the fragments measured at a range of 12 ft is greater than that measured at a range of 6 ft from the centre of the initial charge. The authors explain extra impetus provided to the fragments by the presence of a much larger fireball due to the 40% aluminium inclusion.

Figure 2.4 [21] below shows the measured fragment velocities (based on high-speed video measurements) as analysed by Denny *et al*. The effect of the higher percentage aluminium content can clearly be seen for each case thickness with the velocity at 12 ft being greater than that at 6 ft for all but the case with Type A (0.125 in) casing. A greater effect may be from the casing type (thickness) as it can be seen that the overall difference in data sets between 6 ft and 12 ft decreases as the casing thickness increases.

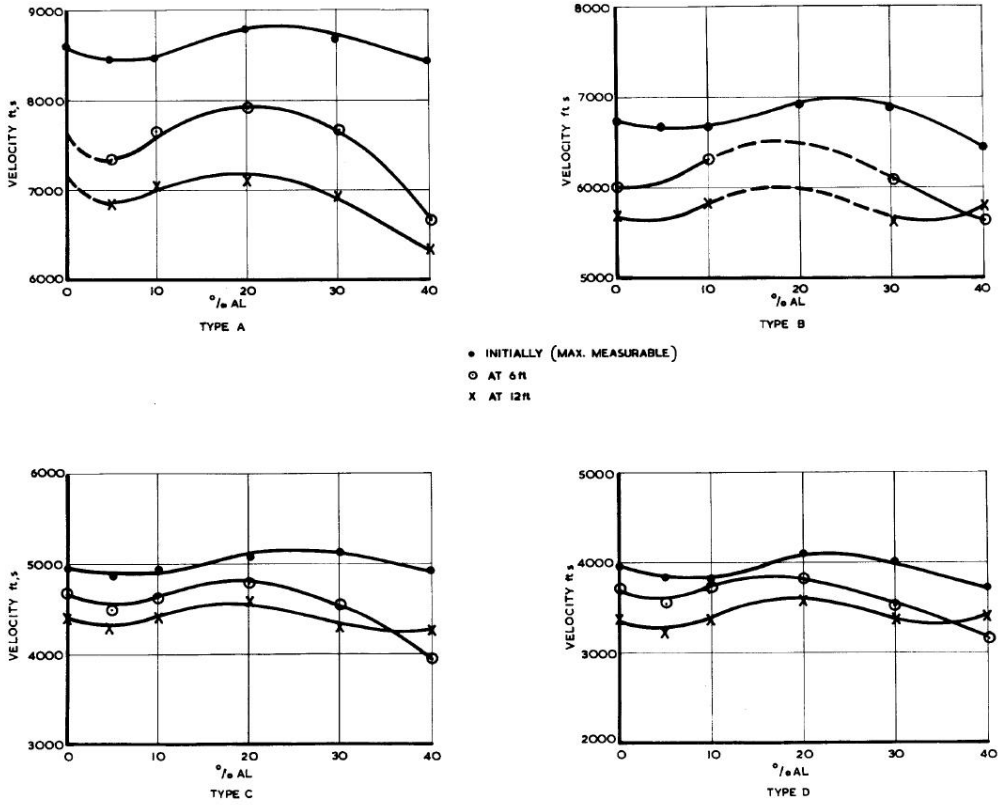


Figure 2.4: Fragment velocities for varying case thickness and % aluminium at 6 ft and 12 ft distances [21]

The reported casing type thicknesses are summarised in Table 2.1 below.

Casing Type	**Casing Thickness (nominal) [in]**
A	0.125
B	0.250
C	0.500
D	0.750

Table 2.1: Casing type and thickness correlation

Al-Hassani, with varying co researchers, looked at both spherical and tubular configurations [22, 23] conducting analyses to predict fragment velocity and the conditions for the radius of complete fracture. He found that even for spherical casings the conditions at complete fracture were similar to that reported by Taylor relating to tubular bombs.

Al-Hassani investigated the influence on fragment velocity and fracture strain determined by the charge radii, casing wall thickness and tensile strength. He noted that for

tubular casings with end detonation there is a non-uniform distribution of forces acting along the wall leading to an axial extrusion coupled with the radial expansion. He favours a spherical casing with a central detonation point as the symmetrical stress system is more amenable to associated theoretical analyses. He theorises that under these conditions a quasi-static expansion may show similar crack propagation results as in a dynamic expansion as both systems are under extremely high pressures. In his investigation of the tensile strength effects [22], Al-Hassani shows that as the tensile strength of the casing material increases the corresponding radius of complete fracture decreases.

During work on the spherical system [22], Al-Hassani and Johnson show that the speed of the radial crack propagation is far faster than the radial expansion velocity of the casing. They adopted a fracture mechanics approach to the problem and postulated a fracture toughness parameter showing a relationship exists between the hoop stress exhibited at failure, the crack opening displacement, and the crack length.

The approach, however, is shown to be applicable only in cases where the stresses and strains at the crack tip are under plane strain conditions. Since each element in the casing expansion is shown to be subjected to a tri-axial stress / strain system, they show that the adopted fracture mechanics approach is not appropriate.

Al-Hassani and Johnson also show that for a thick walled sphere, theory matched that shown for tubular bombs by Taylor. That is to say, the casing expands under pressure from the detonation products until, due to the gaseous product expansion, the internal pressure reduces to a value equal to the tensile strength of the casing material.

One of the earliest attempts to numerically model the interaction of the expanding casing with the gaseous detonation products [24] was the development of the BASIC 2D time dependent model. This treated the metal casing as a series of discretised mass points, with the gas products treated as Lagrangian with the provision for slippage at the metal boundary included. The interior gas dynamics used the concept of artificial viscosity.

The majority of the work looking at casing expansion and fragment development has

been undertaken on a single test item in a configuration where the expansion is not affected by proximity to the ground, structures or other test items.

Alongside the work conducted in the investigation of the fragmentation properties produced by cylindrical and spherical cased charges, work has been conducted for several decades looking at the metal pushing characteristics of the detonation products. This work was often related to the derivation of the fragment speeds from each system, but some was conducted to understand the acceleration of flyer plates etc. that would be used in material modelling experiments.

2.4 Fireball Characterisation

Before any real effort can be made to ascertain the effects of the fireball on the fragment motion within it, some degree of understanding of the environment seen by the fragment must be gained. At the very early time, this can be expected to be extremely harsh; with high temperatures, densities and degrees of turbulence.

It is not only the detonation of high explosives that can create these regimes. The accidental explosion of large rocket motors, such as that of the Ariane-5 rocket may also be of interest. Surzhikov [25] uses a simplified approach assuming that the propellant forms only water vapour as its product and that this is formed instantly. He does however look closely at the turbulent mixing that occurs.

In the development of his model, Surzhikov compares different turbulent mixing methodologies and recommends one for use in computational models. In studying the actual problem, the applicability of the data (to the problem of high explosive fireballs) must be questioned as the oxygen-hydrogen propellant explosion fireball was calculated to exist for approximately 20 s, develop from an initial radius of 100 m out to around 500 m, and reach a maximum temperature of less than 3000 K.

Similarly, Novozhilov [26] looks at Reynolds-averaged Navier-Stokes based compu-

tational methods for fireballs formed from vapour cloud explosions and boiling liquid expanding vapour explosions (BLEVEs). His study concludes that the fireball dynamics are able to be predicted rather well, however once again the time and temperature scales studied are not wholly helpful for high explosive fireballs in the very early stages of development.

In his thesis [27], Steward points out the chaotic nature of the expansion phase of the fireball and highlights that although some features may be reproducible within laboratory conditions, these features quickly become highly variable at munition scale in the real atmosphere. However, he does isolate some features within the first 10 ms or so of the fireball evolution that show more reproducibility than later time features which may be affected by afterburning with the atmosphere. This said, these are not enough to comfortably predict the behaviour of the fireball with any degree of confidence.

As described by Balakrishnan & Menon [28], the contact surface (between detonation products and the compressed atmospheric air trailing the primary blast shock wave) is propelled outwards by the expanding detonation products. The density discontinuity across the contact surface leads to any perturbations growing unstable and turbulent mixing being initiated; these perturbations can originate either at a molecular scale within the donor charge or, more usually, as a result of surface roughness on the charge itself. The study conducted by Balakrishnan is primarily concerned with the effects on (and of) aluminium particles within the charge and subsequent fireball, but the conclusion relating to the afterburn energy release may be significant.

Late time release of energy through afterburning was seen to have an effect on the flow field trailing the primary blast shock wave. The turbulent mixing within the flow field increased the afterburning; this led to observation of an effect within the flow field itself.

The effect of the rapid expansion of the detonation products has since been looked at using a spherical shock tube to isolate the interfacial mixing [29]. Mankbadi uses

a series of numerical calculations to view different methodologies for both unperturbed and perturbed conditions to isolate the instability of the expanding contact surface. The results of the numerical calculations were compared to theory and the effects of certain parameters, such as adiabatic index, viscosity, Reynolds number and thermal diffusion were explained. It was found that some parameters tended to stabilise the contact surface (under certain conditions) whilst other parameters destabilised the surface leading to a highly complex flow field within the turbulent fireball.

From this brief review of research conducted looking at the stability of the expanding contact interface and the flow field within the fireball behind the primary blast wave, it is unlikely that any detailed predictive modelling of the flow field and the effects on the fragmentation will be achievable. A simplified approach with an experimental phase looking at any effect measured on a consistent fragment within the flow field will return data to answer the research intent. It may even return an insight into the actual flow field and the reciprocal effects exhibited by it on the fragment.

The evidence of afterburning causing an increase in the complexity of the flow field can be used to determine the potential condensed-phase high explosive to use for the experimental phase. An energetic material exhibiting as close to oxygen balance as possible would be preferred to limit the degree of afterburning seen; unfortunately this may not be possible in practice. The explosive material used will be characterised and the potential degree of afterburning incorporated within the analysis.

Most early work conducted to determine the maximum diameter and duration of the fireball concentrates on the phenomena generated by nuclear weapon detonations [30–33] and although of interest, they are often of only limited applicability due to the extreme regimes generated.

That said, from this early work on nuclear fireballs, some approaches are potentially applicable to conventional high explosive systems. Porzel [31] gives a general expression

for the radius of fireball expansion as

$$R \approx kt^{0.4} \tag{2.4}$$

where R is the radius of the fireball, k is a constant and t is the time in question.

Unfortunately, no units are quoted for the expression however, given the date of the work it is reasonable to assume that some form of imperial units would have been used. Based on work conducted by Fuchs, Porzel suggests the above expression is suspect due to variations in the adiabatic constant not being accounted for.

Porzel states that the strong shock theory used may be potentially inapplicable within the first few metres due to radiative effects. He quotes, for strong shocks

$$\frac{\rho_{shock}}{\rho_0} = \frac{(\gamma + 1)}{(\gamma - 1)} \tag{2.5}$$

and also that when the shock is at radius R with a density of ρ_{shock} then at a radius r behind the shock

$$\rho = \rho_0 \left(\frac{r}{R}\right)^{\frac{6}{\gamma - 1}} \tag{2.6}$$

These expressions are based on the assumption that the air immediately ahead of the shock is at ambient conditions. Porzel argues that this assumption may not hold due to spectral radiative effects from the edge of the fireball. Although Porzel was considering the extreme case of the atomic fireball, the effect may still be present (at a much less dramatic level) for conventional HE so should potentially be considered in the analysis.

The characterisation of fireballs from non-nuclear high explosive detonations, in the simplest terms of maximum radius, duration and temperature appears to generate some considerable uncertainty. Indeed, even within the current NATO Allied Ammunition Storage and Transport Publication on explosive effects and consequence tools, it is difficult to find agreement between the contributing nations as to the appropriate method of estimation [34, 35].

Figure 2.5 and Figure 2.6 show the level of (dis)agreement on the maximum diameter and duration of fireballs from high explosives. Included in the graphs are similar curves from other sources [36,37]. In both these Figures the yellow band highlights the spread of results across the Swiss (CHE) model within the confidence level interval of 5% to 95%.

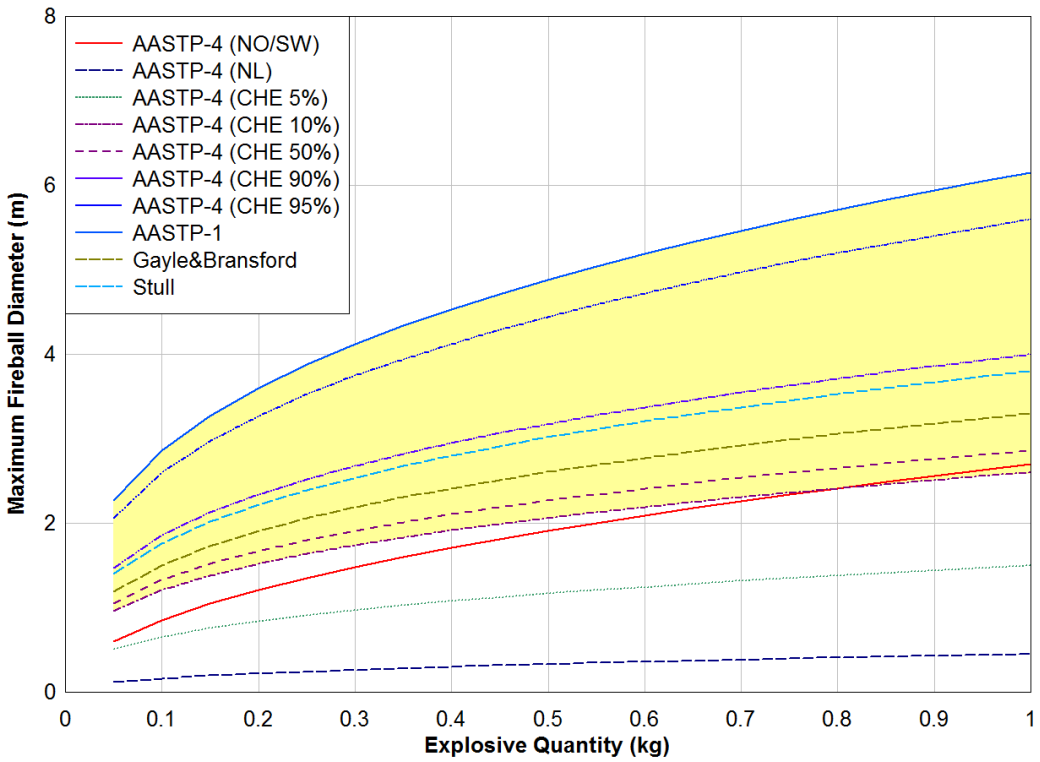


Figure 2.5: Maximum Fireball Diameter Curves

The applicability of some of these curves, as plotted in Figure 2.5 and Figure 2.6, limited to a charge regime of <1 kg explosive mass, is questionable since they are plotted for charge masses of hundreds of kilograms, or even tonnes, in the source documentation. The use of these curves is intended as an initial guide, and should be supplemented with numerical modelling to inform experimental diagnostic placement and ranging.

Work conducted jointly by the Defence Research Establishment Suffield (DRES) and the Explosive Storage and Transport Committee (ESTC) on the DRESTC trials series, allowed Laidlaw [38] to construct a simple formula for the fireball radius.

$$R = 5W^{\frac{1}{3}} \tag{2.7}$$

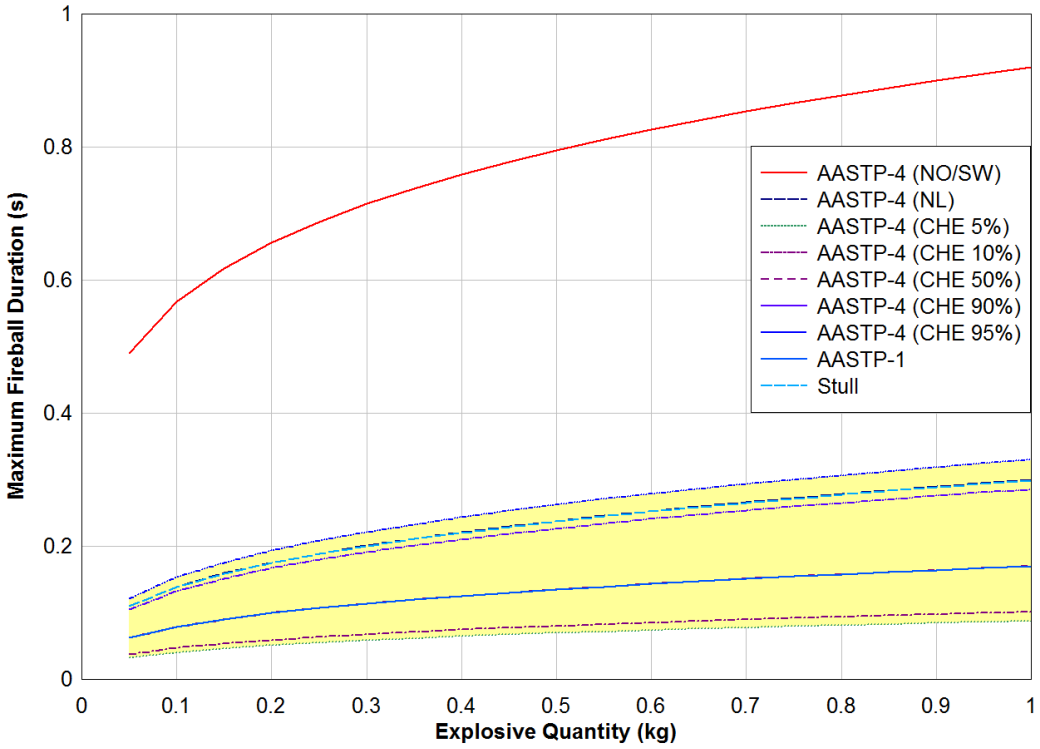


Figure 2.6: Maximum Fireball Duration Curves

where R is the fireball radius [ft] and W is the charge mass [lb]. When converted to metric units with R [m] and W [kg], the expression becomes

$$R = 1.53W^{\frac{1}{3}} \tag{2.8}$$

The source equations behind Figure 2.5 are given (Equation 2.9 to Equation 2.11) and can be compared with that from the DRESTC trials (Equation 2.8).

The equations and symbols used have been adjusted from the original layout to reflect those used in the DRESTC equation. Each equation has been rewritten such that W is the mass of explosive [kg] and R is the radius of fireball [m]. In Equation 2.11, Pr is a probit value as shown in Table 2.2 [35] and depends on the percentage confidence level required.

$$R_{max} = \begin{cases} 1.35W^{0.5} & \text{for W} < 7 \text{ kg (Norway/Sweden)} \\ 1.9W^{0.325} & \text{for W} > 7 \text{ kg (Norway/Sweden)} \end{cases} \tag{2.9}$$

$$R_{max} = 0.9W^{0.44} \quad \text{(Netherlands)} \tag{2.10}$$

$$R_{max} = 2W^{\frac{1}{3}}10^{(0.114(Pr-5))} \quad \text{(Switzerland)} \tag{2.11}$$

%	0	1	2	3	4	5	6	7	8	9
0		2.67	2.95	3.12	3.25	3.36	3.45	3.52	3.59	3.66
10	3.72	3.77	3.82	3.87	3.92	3.96	4.01	4.05	4.08	4.12
20	4.16	4.19	4.23	4.26	4.29	4.33	4.36	4.39	4.42	4.45
30	4.48	4.50	4.53	4.56	4.59	4.61	4.64	4.67	4.69	4.72
40	4.75	4.77	4.80	4.82	4.85	4.87	4.90	4.92	4.95	4.97
50	5.00	5.03	5.05	5.08	5.10	5.13	5.15	5.18	5.20	5.23
60	5.25	5.28	5.31	5.33	5.36	5.39	5.41	5.44	5.47	5.50
70	5.52	5.55	5.58	5.61	5.64	5.67	5.71	5.74	5.77	5.81
80	5.84	5.88	5.92	5.95	5.99	6.04	6.08	6.13	6.18	6.23
90	6.28	6.34	6.41	6.48	6.55	6.64	6.75	6.88	7.05	7.33

Table 2.2: Swiss Probit Values for Fireball Characterisation [35]

The formula used by the Netherlands includes a safety factor of 2 within the multiplier for dealing with bulges in the fireball shape. This is reminiscent of fireball perturbations reported by Patterson [39].

This simple comparison shows the level of ambiguity and variability behind the basic phenomenon of fireball maximum radius. This makes the use of engineering approaches, like those shown above, unreliable at this stage for accurate prediction of the fireball characteristics.

Alongside the work conducted in looking at the instabilities and turbulent growth within the fireball, research conducted to understand the temperature history throughout the lifetime of the fireball is of great importance.

Orson [40] studied the infrared signatures from a number of air launched ordnance detonations. The temperature histories were well characterised by a grey body with continuously decreasing temperature from a maximum of around 1600 K and a characteristic

decay time of 1 s to 4 s. Figure 2.7 below shows the temperature histories for three different air dropped bombs.

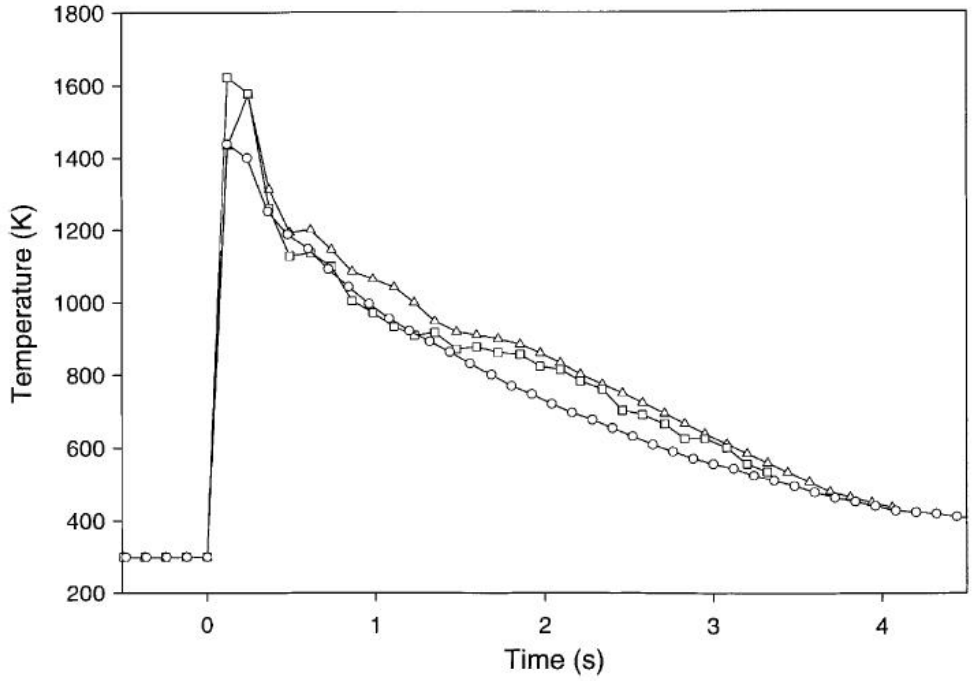


Figure 2.7: Explosion temperature histories for 3 types of air dropped bombs [40]

The same series of air dropped bomb trials was analysed by Gross & Perram [41]. They found the temperature dropped from a maximum of near 1800 K to ambient conditions in about 3 s to 5 s. Although the differences between the results presented by Orson and those of Gross appear minimal and within potential experimental error, it does show the potential variability of analysis methodologies employed.

Kato *et al.* [42] studied the detonation temperatures of various solid and liquid explosives using a four-colour pyrometer. During these studies they measured the temperature history of the detonation products created from tri-nitro-toluene (TNT) charges of different initial densities. For one density the measurements were compared to calculations. Although the calculational values returned may not have been in close agreement to the test results, the general form of the curve agrees very well.

The experimental and calculational curves are shown in Figure 2.8.

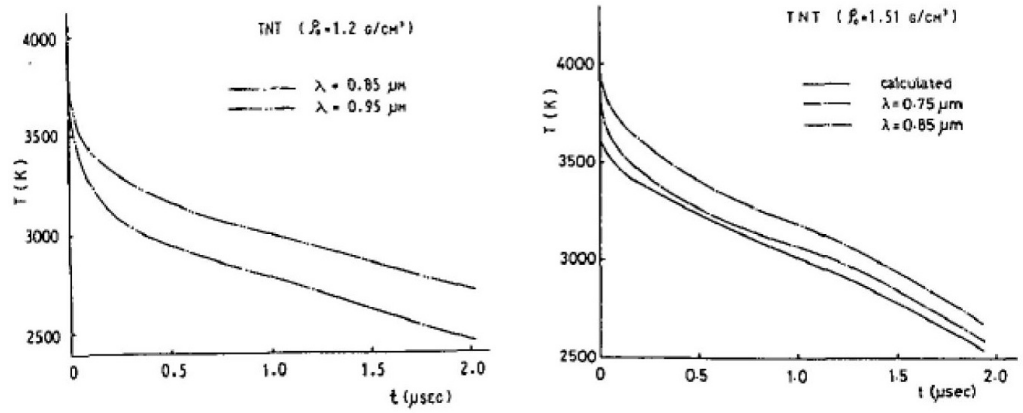


Figure 2.8: Temperature-Time history of TNT detonation products [42]

The temperature history measured for TNT by Kato differs wildly from the temperature histories measured by Orsen *et al* for the air dropped munitions. Kato discusses the effect of transparent anvils on artificially raising the temperature due to shock reflections from the higher impedance anvils, however this may not be the sole reason for such gross discrepancies in both initial temperature and decay time.

Koch *et al.* [43] show evidence of the measurement of the temperature of the gas behind the blast wave from varying small charges. The temperature history from a small pentaerythritol tetranitrate (PETN) donor charge is shown in Figure 2.9.

The maximum temperature recorded agrees well with those shown in Figure 2.7; however, the decay times shown in Figure 2.7 to Figure 2.9 disagree by orders of magnitude across each graph. Further study of the raw data and experimental layout would be required to ascertain the reasons for the differences which may include measurements taken of different phenomena. It is unclear, for example, whether the results presented by Koch *et al* were taken ahead of, or behind, the expanding contact surface.

Kato used laboratory scale charges to measure the detonation temperature of the material rather than the temperature history of the free field expanding fireball. This shows the potential flaw in using a theoretical (or even experimental) detonation temperature for the free field fireball initial temperature.

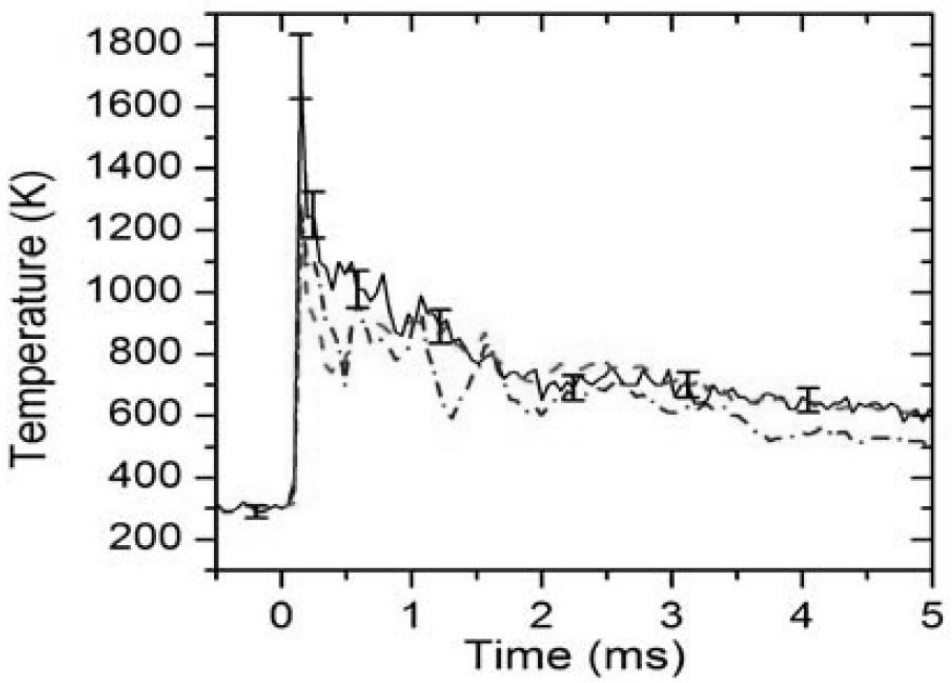


Figure 2.9: Temperature history measured behind blast wave from PETN [43]

However, the temperature regime shown by Kato is similar to the early time fireball maximum temperature of approximately 2900 K reported by Lewis *et al.* [44]. This maximum temperature is shown to agree relatively well with the 3150 K returned by theoretical measurements.

Most of the measurements of the temperature of fireballs have been conducted using spectroscopic methods which often only penetrate a few centimetres into the optically dense product cloud. Lebel *et al.* [45] developed a fibre optic based method capable of measuring temperatures close in to the explosive charge, thus gaining a measurement from deep within the detonation product cloud. Using this method, Lebel reports temperatures of between 1600 K and 1900 K for Detasheet-C explosive charges. This agrees well with the values reported by Orsen and Koch *et al.*

From this brief review of the expected maximum temperature, it appears that distinct differences are seen depending on how and where within the flow field measurements are taken. An in depth review of the actual experimental layouts and data gathered would be required to account for all the differences in experimental results reported.

2.5 Detonation Products

Although during the expansion of the detonation products the adiabatic constant is expected to vary over time with changing temperature and pressure, most of the published research in this area simplifies the problem by assuming an invariant adiabatic constant throughout the entire expansion phase.

Work conducted on the determination of the adiabatic constant of the detonation products for Composition B [17], produced a suitable description of the products using a polytropic equation with the adiabatic constant (γ) set at 2.77. The products were treated as an adiabatically expanding polytropic gas to allow the use of Bernoulli's theorem for fluids.

Although the main objective of his work was fragment velocity and spread angle management, in his study of PETN [46] Porter uses a gamma gas law equation of state for the detonation products with an invariant adiabatic constant

$$E = \frac{PV}{(\gamma - 1)} \tag{2.12}$$

where the adiabatic constant is defined as

$$\gamma = \left(\frac{D^2}{(2E_0) + 1} \right)^{\frac{1}{2}} \tag{2.13}$$

with D being the detonation velocity [ms^{-1}] and E_0 being the chemical energy of detonation per unit mass of explosive [Jkg^{-1}]. By taking the values for PETN of D = 8350 ms^{-1} and E_0 = 5794 x 10^3 Jkg^{-1}, Porter estimates the adiabatic constant for the detonation products of PETN as being 2.64.

During work on tubular bombs [22], Al-Hassani assumed an isentropic expansion of the detonation products within the derivation of the approximation for the pressure exerted

on the inner casing wall by the products, P_α [Pa]

$$P_\alpha = P_0 \left(\frac{a}{a_0} \right)^{-2\gamma} \tag{2.14}$$

with P_0 being the effective detonation pressure acting on the inside of the casing [Pa] when $a = a_0$, where a is the inner radius of the cylinder [m] and the subscript 0 relates to the initial conditions.

During this work, Al-Hassani clearly states that the adiabatic constant for the products is not invariant throughout the expansion and for TNT typically starts at a value around 3.4 and drops to roughly 1.9 by the time the density of the products has reached one-quarter of the initial density. Al-Hassani concludes that using an adiabatic constant of 3 is a reasonable approximation for a system that demonstrates a moderate expansion to fracture.

Following this Al-Hassani [22] states that for non-TNT explosives the adiabatic constant can be as high as 5 in the very early stages of expansion. The final value of 1.9 appears to remain unchanged however. He again concludes that taking a constant value of 3 is a reasonable approximation.

Having said that most papers employ an invariant adiabatic constant, Kornhauser [47] uses a variable adiabatic constant; however he shows that, for an expansion of less than twice the initial radius, the use of a variable adiabatic constant does not give any real benefits over using a constant value of 2.85. It is unclear whether the data for this observation is based on that collected for the close in radii, or simply collected outside the region in question and back calculated. Within the same paper, Kornhauser discusses different models and the errors in each are assessed against experimental data; however, no error estimates for the experimental data have been included.

In a simplification of a variable adiabatic constant case Kozorezov and Sergeev [48] use a three stage expansion isentrope for the detonation products, with each stage employing

a different constant exponent. This can be visualised by assigning two transition points (1 and 2) within the expansion such that

$$P_0 V_0^{\alpha} = P_1 V_1^{\alpha}; P_1 V_1^{\beta} = P_2 V_2^{\beta}; P_2 V_2^{\delta} = P V^{\delta} \tag{2.15}$$

where the subscript 0 relates to the detonation front, and the lack of subscript denotes the energy similarity zone or Sadovskii region (>10 to 12 charge radii for spherical and >20 to 30 charge radii for cylindrical geometries).

Using this approximation (and assuming the expansion isentrope for the detonation products is known), the authors conducted a theoretical study of the effects of the charge being initiated in a non-air atmosphere and of the effects of the initial explosive charge density. They also looked at the influence of the choice of the transition points (and exponent values) for the three stage isentrope, and found that keeping the transition points within the following limits:

$$P_1 = (11.7 \pm 4.0) \text{ GPa}$$
$$98 \leq P_2 \leq 294 \text{ MPa}$$
$$\alpha = 3; \beta = 2; \delta = 1.14$$

gave results indicating, to a first approximation, that the three-stage expansion isentrope could be generalised for most organic high explosive charges.

Popel [49] also recognised that the detonation products cannot be treated as an ideal gas and introduced a correction factor into the calculation for a high and a low value of the adiabatic constant. Although the application of this correction appears to be arbitrary, the method used describes the shock damping experienced in experiments reasonably well for the higher value of the adiabatic constant ($\gamma = 3$).

The fundamental work by Jones and Miller, suggesting the use of an invariant value of 3 for the adiabatic constant, is discussed by Dehn [50]. Within this discussion, Dehn

shows how Jones and Miller calculated the adiabatic constant throughout the entire expansion process from directly behind the detonation front through to the final expanded product cloud. The values calculated range from 3.36 at detonation pressures down to approximately 1.20 at near atmospheric conditions, concluding that a suitable effective value for metal pushing applications "ought" to be 3. Although no mathematical justification for this statement is given, Dehn does give graphical representations of how the detonation product gas density and velocity varies with expansion giving an indication of the function shape.

Numerical solutions for the motion of the detonation products have been conducted for many years despite a lack of computing capability in the early days. Kashirskii *et al.* [51] solved the gas dynamics equations for a cylinder of pentolite expanding into a vacuum. Although the calculation only used a grid of 50 x 30 cells and neglected the casing material, a reasonable indication of the direction of the detonation product expansion from an end initiated open cylinder was presented. The authors did not explicitly solve for the velocity of the cloud edge but presented some rather course diagrams of position with time.

2.5.1 Detonation Product Equations of State (EoS)

As well as numerous approaches to dealing with the adiabatic constant, many different equations of state (EoS) exist to describe the detonation products generated from high explosives. These range from the application of the simple ideal gas EoS through to the widely used Jones-Wilkins-Lee (JWL) EoS, and some more exotic equations as well.

2.5.1.1 Jones-Wilkins-Lee (JWL) EoS

The commonly used JWL EoS is popular as the equation is empirical and the data either exists for most common explosives or is relatively simple to obtain through well-characterised experiments. The JWL EoS has been described by a number of researchers including Elek [52], Lee [53], Kwak [54], Nagayama [55], Huson [56], Polk [57], Alhus-

san [58], Hutchinson [59], and Nagayama [60], however there are no definitive documents available from either of the attributed three which has led to the equation being presented in a variety of different forms. Whatever form the equation of state takes, as it is based on a significant amount of empirical data, it is not possible to discount any of the versions used [61].

A common version of the equation is based on a family of isentropes, such that

$$P(S,V) = Ae^{-R_1 V} + Be^{-R_2 V} + C(S)V^{-(\omega+1)} \tag{2.16}$$

with P being pressure, S being entropy per unit initial volume ($\frac{s}{v_0}$), and V being the volume relative to the undetonated state ($\frac{v}{v_0}$). A, B, R_1, and R_2 are constant fitting parameters and ω is an assumed constant parameter based on the material, $\omega = \gamma - 1$. The function $C(S)$ is dependent on the entropy, S.

With the equation in this form, the first term on the right hand side describes the behaviour at very high pressure and low expansion ratios, the second term describes the intermediate pressure zone and the third term describes the behaviour at low pressures and large expansion ratios.

While A and B have dimensions of pressure, the parameters R_1,R_2 and ω are dimensionless and all subject to the constraints [62]

$$R_1 > R_2 > 0 \quad ; \quad \omega > 0$$

$$A > B > 0 \quad \text{for explosive products}$$

$$A > -B > 0 \quad \text{for reactants}$$

Although the entropy-volume form of the EoS is a common form, the most widely used form for simulations involving explosive detonation and work conducted by the detonation products is the pressure-energy form. This form is often referred to as the Grüneisen EoS

form of the JWL equation

$$P(E,V) = A\left(1 - \frac{\omega}{R_1 V}\right)e^{-R_1 V} + B\left(1 - \frac{\omega}{R_2 V}\right)e^{-R_2 V} + \frac{\omega}{V}E \tag{2.17}$$

where E is the detonation energy per unit volume [63].

It should be noted that the JWL EoS is not meant for use in low temperature simulations [62] and in the case of large expansions, such that $v >> v_0$, the EoS limits to an Ideal Gas EoS.

As mentioned previously, the parameters for the JWL EoS are empirically derived; primarily through the use and analysis of cylinder tests employing a cylinder of explosive surrounding by an open ended copper tube. The explosive is detonated from one end and the copper tube expansion is recorded (either using multiple probes or high speed photographic methods). Analysis of the copper expansion returns the relevant JWL parameters for the explosive under test.

Historically the methodologies involved in the measurement and analysis of the copper expansion has been discussed by Taylor [16] and Hill [64] amongst others. Taylor gives the shape of the case,

$$x = \int_{r_0}^{r} \frac{dr}{tan\theta}$$

such that θ is the angle between an axial section of the expanded case and the axis at a distance x from the detonation front where $\frac{dr}{dx} = tan\ \theta$, r_0 is the initial outer cylinder radius and r is the outer radius at the time of measurement.

Using the perspective of a fixed observer frame of reference Taylor shows that the velocity of the case can be shown as

$$v_{case} = U\left((1 - cos\ \theta)^2 + sin^2\ \theta\ \right)^{\frac{1}{2}} \tag{2.18}$$

whilst the direction of motion of the case is at an angle such that

$$tan\ \phi = \frac{1 - cos\ \theta}{sin\ \theta} = tan\ \frac{1}{2}\theta \tag{2.19}$$

thus $\phi = \frac{1}{2}\theta$ where positive ϕ is forward of the radial direction.

It can also be found that the angle of fragment projection satisfies the relationship

$$\frac{v_{frag}}{D} = 2sin\ \frac{1}{2}\theta$$

More recently Sutton *et al* [65] revisited the analysis of the data to fit directly to the cylinder wall expansion velocity rather than the expansion radius, such that

$$r_e - r_{e0} = \frac{v_\infty t g(t)}{2\frac{v_\infty}{a_0} g'(0) + g(t)} \tag{2.20}$$

where

$$a_0 = \frac{4 S_0 P_{CJ}}{\rho_m s_0 (r_{i0} + r_{e0})} \quad ; \quad g(t) = (1+t)^{\sigma_H} - 1$$

and S_0 is the initial cross sectional area of the explosive charge, s_0 is the initial cross sectional area of the copper cylinder, ρ_m is the density of the cylinder, r_{i0} is the initial inner radius and r_{e0} the initial outer radius of the cylinder respectively, v_∞ is the velocity to which the cylinder wall tends to at late time and large expansion, a_0 is the initial acceleration of the cylinder and σ_H is the hoop stress exerted on the cylinder.

Extension of the analysis to include application of a data fit in the form of the JWL EoS to the analytical isentropes, such that

$$P(V_r) = Ae^{-R_1 V_r} + Be^{-R_2 V_r} + CV_r^{-(1+\omega)} \tag{2.21}$$

where V_r relates to the Rayleigh line.

Thus the radially expanding velocity profile is used to calculate the pressure of the

detonation products, the Chapman-Jouget pressure and the JWL parameters.

2.5.1.2 Becker-Kistiakowsky-Wilson (BKW) EoS

An alternative to JWL EoS is the Becker-Kistiakowsky-Wilson (BKW) EoS, derived to describe the fluid component of the detonation products. The EoS is a simple equation based on the virial EoS with a repulsive potential applied, and relates the pressure as a function of the number of moles

$$\frac{PV}{nRT} = 1 + xe^{\beta x} \tag{2.22}$$

where

$$x = \frac{k}{V(T+\theta)^{\alpha}}$$

with $k = \kappa \sum_i n_i k_i$ and $n_i = \sum_i n_i$.

Although the BKW EoS is very versatile due to the variability available in the values of the parameters α, β, κ and θ, this versatility is offset by a lack of physical interpretation in the equation.

The BKW parameters are not as easily derived and require some iterative fitting of experimental data to optimise the equation [66]. For quite a long time, the BKW EoS validity has been questioned [67] and this has been expounded by a lack of experimental verification. Indeed, Souers & Kury [68] have shown that the BKW EoS does not accurately predict the output of the simple cylinder test, unlike the JWL EoS as previously shown.

2.5.1.3 Other EoS

Even with the shortcomings of the BKW EoS, it is still popular with some developers of thermochemical codes [69], [70], [71], [72] along with the theoretically developed

Jacobs-Cowperthwaite-Zwisler-3 (JCZ3) EoS. The JCZ3 EoS uses the exponential six intermolecular potential function to desribe interactions between molecules and is used within some thermochemical equilibrium codes, primarily those for use with complex elemental compositions [71], [72], [73], [74], [75]. Finally there are more recently developed equations such as the Kuznetsov-Shvedov [58], Rice-Walsh type [60], modified van der Waals based [76] and a three phase EoS to account for carbon within the detonation products [77].

Kuznetsov-Shvedov Equations of State for detonation products are readily available, though some materials less so than for the JWL equations. One such example of the Kuznetsov-Shvedov EoS is that for the detonation products of RDX, limited to a density less than 2.3 gcm^{-3}.

$$P\ [bar] = (15.4\rho^3 - 12.6\rho^2).10^3 + \frac{10}{3}\rho T\Psi \tag{2.23}$$

$$\varepsilon\ [Jkg^{-1}] = (0.77\rho^2 - 1.26\rho) + \frac{10^{-3}}{3}\frac{T\Psi}{\Gamma} + 10^{-10}\Delta \tag{2.24}$$

where P is pressure, ρ is density and ε is the specific internal energy of the detonation products.

Within Equation 2.23 and Equation 2.24 other variables are defined as

$$\Psi = 1 + \frac{2.7\tau + 15\tau^4}{1 + 2.6\tau^4} \quad ; \quad \Delta = \frac{1.76RT\theta}{\mu(e^\theta - 1)}\left(1 - \frac{\theta e^\theta}{(e^\theta - 1)}\right) \tag{2.25}$$

From this brief review, it can be seen that many equations of state are available for the detonation products; however, it is not clear what the overall differences in predictive output are. Should it be possible to substitute varying EoS for the explosives into the numerical software packages available a simple comparison of each EoS used will be possible; the percentage difference in casing or plate motion between each EoS can then be defined. In the absence of such a study, the JWL EoS will be used within this research as, being the most widely used generally, it is the easiest EoS to gain either experimental,

theoretical or numerically simulated data for.

2.6 Metal Pushing by Detonation Products

Early work on the acceleration of metal by detonation products was conducted by Gurney [18] where he developed his fragment velocity equations for cylindrical charges. These were then extended by Kennedy to cover spherical and sandwich geometries as discussed by Cooper and Kurowski [19].

Cooper [20] further developed the concept with the use of an effective charge mass rather than the complete explosive mass for cases of non-infinite geometries where edge effects will be significant. This effective charge mass (C_e) is simply the mass of explosive contained within a cone with base diameter equal to that of the cylindrical charge and having a base angle of 60°. Should the cylinder aspect ratio render the cone apex to be outside the bounds of the charge cylinder, a truncated cone is used to calculate the effective charge mass.

Cooper states that the 60° angle for non-tamped cylinders is based on numerous experimental observations where the side losses from the expanding gases exert zero pressure onto the accelerating plate. These experiments are unreferenced.

Cooper does discuss the work conducted by Benham in deriving an equation for the effective charge cone base angle for a barrel tamped cylinder of explosives.

$$\theta = 90 - 30/\sqrt{((2\phi/C + 1))} \tag{2.26}$$

where ϕ is the barrel tamping mass [kg], C is the charge mass [kg] and θ is the effective charge base angle [°].

For simple cylinders, the barrel tamping mass can be calculated using

$$\phi = \pi(r_o^2 - r_i^2)L\rho_\phi \tag{2.27}$$

with r_o and r_i being the outer and inner radii of the tamping cylinder [m] respectively, L being the length of the cylinder [m] and ρ_ϕ being the density of the tamping material [kg/m^3].

Similarly the total charge mass can be calculated using

$$C = \pi r_i^2 L\rho_{HE} \tag{2.28}$$

with r_i and L as above, and ρ_{HE} being the density of the explosive [kg/m^3]

Charron [78] uses a different cone angle for his effective charge in certain cases and continues to investigate the effective mass cone angle and the effect of this on the resulting calculated fragment velocity. He compares calculations to a considerably limited selection of experimental data.

This concept is particularly applicable where non-fragmenting flyer plates are considered, and can easily be verified through high fidelity numerical studies or relatively simple experimental tests.

During similar work to develop the Mott, Gurney and Taylor approaches Tucker [79] investigated both the effect of the expansion of the detonation products on the casing until the point of fracture and (separately) the effects of the gaseous detonation products escaping past the fragments post fracture. He concludes that the contribution from the escaping detonation products appears to be negligible and concentrates mainly on the pre-fracture regime, simply assuming that the escaping detonation products will only serve to assist in keeping the fragments at their initial velocity until the air drag acting on them becomes significant.

Within this work Tucker presents evidence for the effect of the detonation products

adiabatic constant on the resulting case velocity; finding that for r/r_0 close to unity, the assumed (or chosen) value of the adiabatic constant used has no real effect. This is seen in Figure 2.10, which shows $\sqrt{F}$ against r/r_0, where $\sqrt{F}$ is proportional to the velocity (the full derivation for this is given by Tucker).

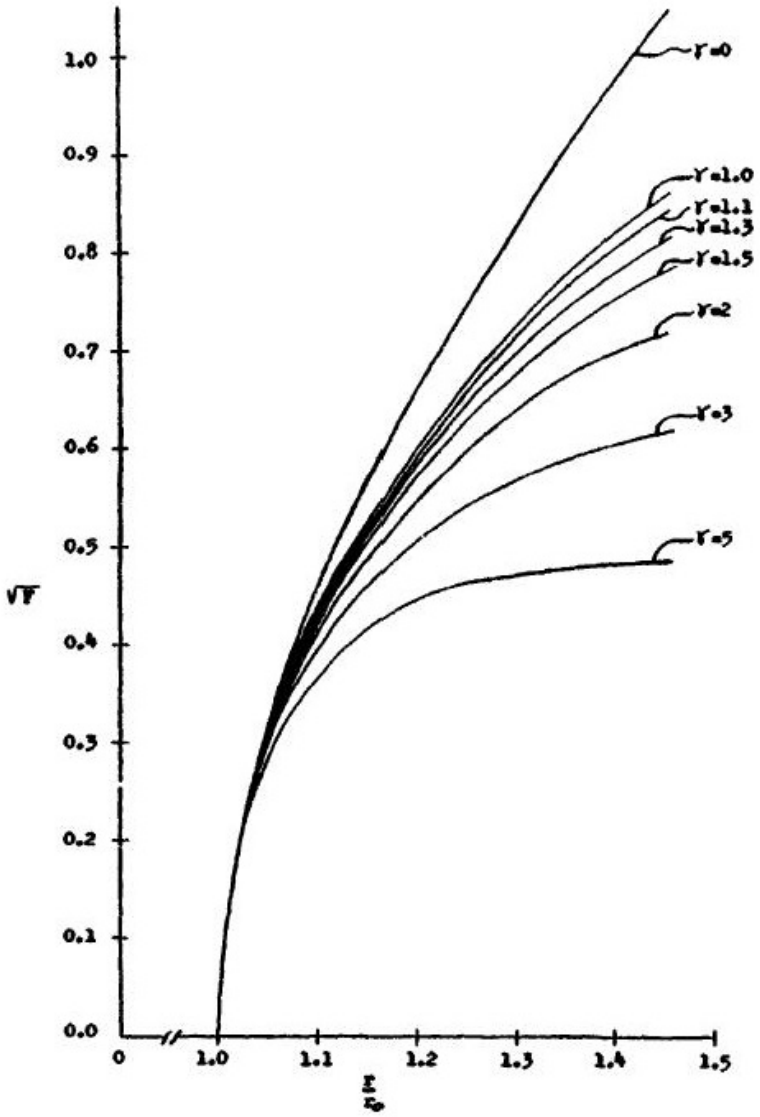


Figure 2.10: Variation in $\sqrt{F}$ (αV) against expanding cylinder radius [79]

The scale of the graph and lack of gridlines makes accurate derivation of actual values difficult; however a reasonable estimation of the point where the curves diverge from each other and the effect of the adiabatic constant becomes noticeable is $r/r_0 > 1.1$ (possibly even as low as $r/r_0 > 1.07$ for γ=5). The effect is significant by $r/r_0 = 1.5$ and thus can be assumed to be significant at the radius of complete fragmentation.

Figure 2.11 shows the same effect for a flat plate accelerated by the expanding products. Although the effect of the value of the adiabatic constant is not as obvious as for the expanding cylinder, it is still possible to see a rather significant effect by $x/x_0 = 1.5$.

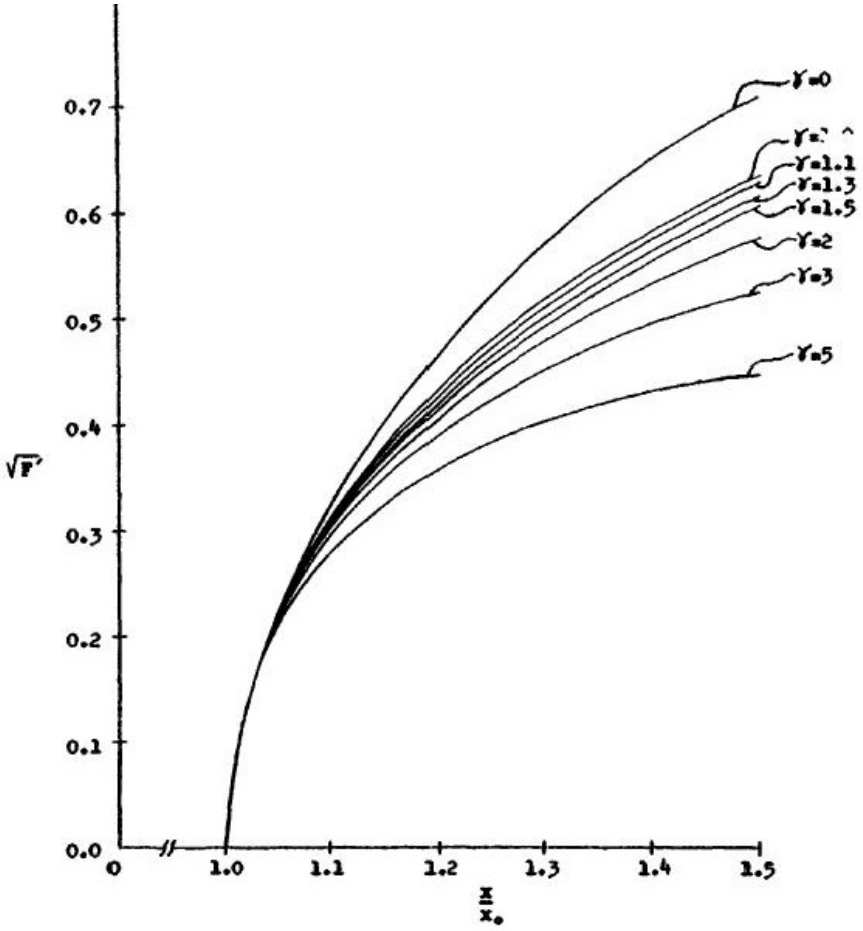


Figure 2.11: Variation in $\sqrt{F}$ (αV) against distance of travel for flat plate [79]

This appears to be at odds with Tuckers observations that the effect of the expanding gaseous products is negligible.

Observation of gas leakage from experimental tests has been reported by Karpp and Predebon [80] for different metals, with a considerable spread of r/r_0 values returned. The values quoted by Karpp are given Table 2.3.

The values reported show the effect of the material properties on the casing break up radius; however the accepted average $r/r_0 = 2$ for casing fragmentation to occur lies firmly within the values quoted with only aluminium being considerably different ($\sim 50\%$ greater).

Metal	r/r_0 **for gas leakage**
Steels with various HE	1.6 - 2.1
Copper	2.4
Aluminium	3.2

Table 2.3: r/r_0 for gas leakage from various metals [80]

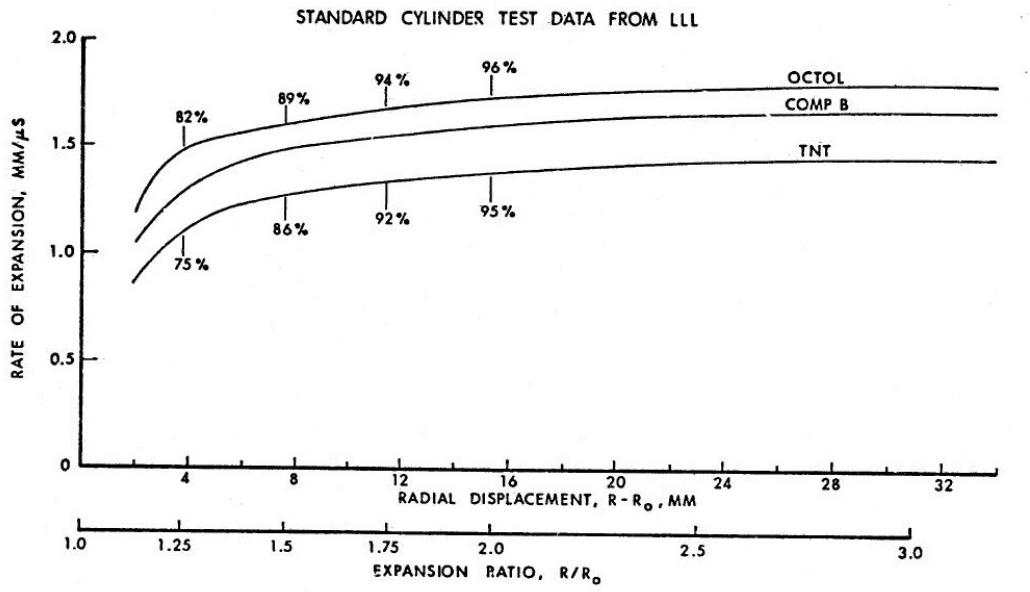


Figure 2.12: Rate of standard cylinder test expansion against expansion ratio for various explosive fills [79]

Karpp also shows graphically the effects of different explosive fills on a standard cylinder test and argues that for a TNT charge approximately 92% of the final velocity of the casing is reached by r/r_0 of 1.75. Figure 2.12 clearly demonstrates this along with the increase in the expansion rate by moving to a more energetic explosive (such as Comp B or Octol).

Figure 2.13 shows the effect of changing material (for the same explosive fill) on the rate of cylinder expansion with radial displacement. In general, the differences seen between the metals are not considerable, however aluminium was not included within this comparison. This may support the development of the general rule of thumb for the expansion ratio at which most metallic cylinders fracture.

Although the majority of the casing expansion rate has been achieved by r/r_0 of

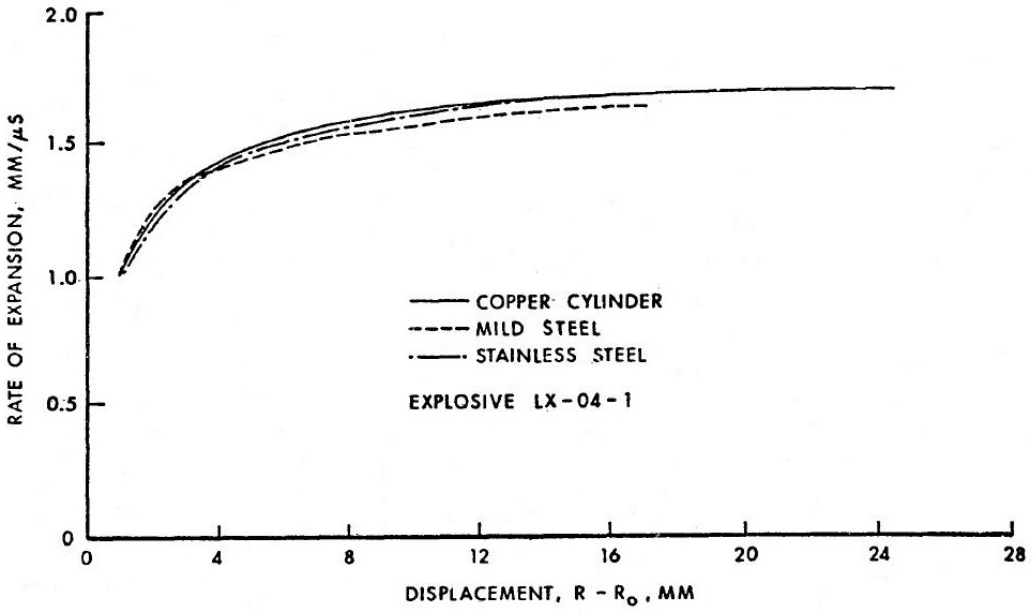


Figure 2.13: Rate of cylinder expansion against displacement for various casing materials [79]

approximately 1.75, Karpp and Predebon firmly believed that in order to achieve accurate fragment velocity predictions it is necessary to include gas leakage effects within the time dependant calculational schemes.

A simplification on the natural fragmentation of the expanding casing is to have the explosive driving an array of preformed cuboidal fragments. A series of experiments conducted using steel cubical fragments surrounding a cylinder of explosives, conducted by Predebon *et al.* [81], show that the calculated Gurney velocity for such a configuration (assuming a continuous casing) dramatically overestimates the final fragment velocity.

Development of a discrete fragment numerical model employing an ideal nozzle based gas leakage calculation generated very good agreement with the experimental data. This highlights the importance of the gas leakage model.

O'Donoghue *et al.* [82] built upon the previous work of Predebon *et al.* conducting a predominantly numerical analysis with some supporting experimental data. From this study, O'Donoghue illustrates that for cubical fragments placed in contact around a cylindrical charge there is obviously a small gap between the cubes at their outer surface, as

shown in Figure 2.14.

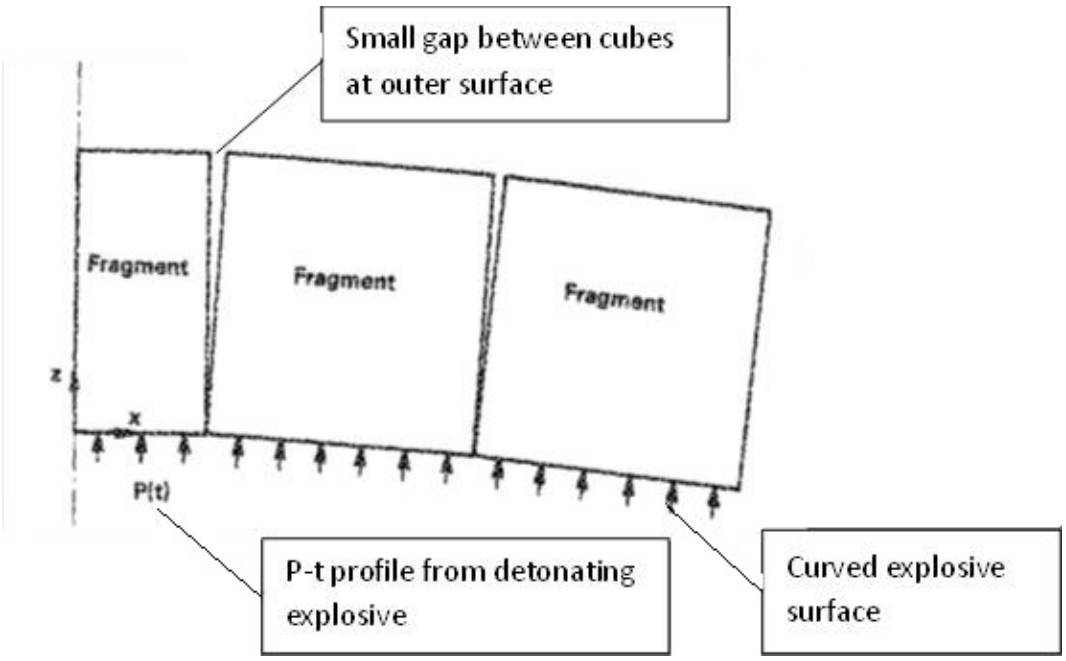


Figure 2.14: Layout of cubical fragments surrounding cylinder [82]

From the calculations and experiments conducted, O'Donoghue found that the outer gap closes under shock action before reopening due to shock reflection from the free surface. This closing action results in a delay in gas leakage and a greater drive being applied to the fragments by the expanding gas. Evidence of this phenomenon, isolated by numerical simulations, was observed experimentally using soft capture of the fragments and inspecting the cube surfaces. Surface damage, similar to that seen in explosive welding, was found suggesting the impact of the cubes as the gap closed on launch.

A further simplification of the problem of accelerating metal with detonation products can be found by looking at explosively driven flyer plates.

Trofimov [83] illustrates a simple method for accelerating flyer plates using a plane detonation wave impacting the rear side of a full diameter plate. Although he accounts for charge edge effects, there is no discussion of detonation products wrap around. He does discuss the drive on the plate from the detonation products and assumes a polytropic equation for the gases.

Trofimov ignores the breakdown of the polytropic nature with pressure below several

kilobars because as the pressure in the detonation products reaches this value the flyer plate acceleration has all but ceased. He actually takes a value of 6.7 kbar (0.67 MPa) at the interface between the detonation products and the plate as the point where acceleration finishes.

Rather than using a simple planar detonation wave to drive the flyer plate, an alternative method is introduced by Bing-Sheng and Fu-Qian [84]. Here Bing-Sheng and Fu-Qian use a convergent flow of detonation products to launch the flyer plate. The configuration, shown in Figure 2.15, is reminiscent of a miniaturised gas gun in principle though it uses high explosive rather than a driving gas.

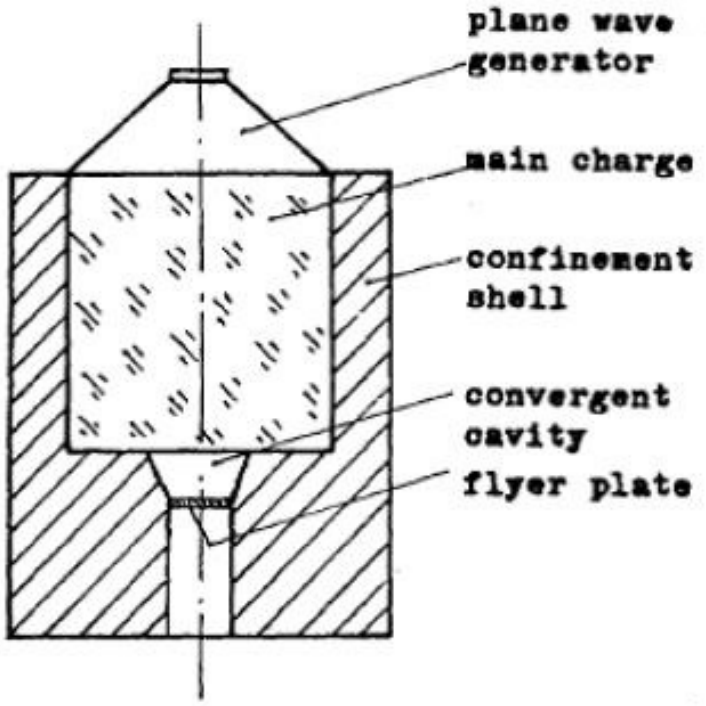


Figure 2.15: Detonation product convergent flow concept [84]

Although Bing-Sheng and Fu-Qian claim the device can return higher flyer plate velocities than the standard plane wave lens in contact with the plate (as used by Trofimov amongst others), the sensitivity to the geometrical parameters surrounding the convergent cavity may make the system rather troublesome to manufacture.

From sample results presented, the donor explosive charge is given dimensions of 200 mm diameter by 400 mm length. Although the actual dimensions of the flyer plate

are not given, it can be assumed from the diagram that the diameter of the flyer plate will be rather small and potentially limited by the confinement material of the system (unless confinement shell fragmentation is not a problem within the facility used). Any benefits of such a design may therefore be outweighed by the limited sample size, difficulty of manufacture and potential fragmentation problem.

An alternative method for increasing the terminal velocity of explosively driven plates is that of using backing plates [85]. This method gives a detailed analytical approach to the shock wave interaction and motion of both plates. The paper assumes that the explosive charge is detonated normally over one surface, both plates are incompressible and the detonation products obey a simple gas law with an invariant adiabatic constant of 3.

Hoskin and Lambourn [85] compare their findings with those from the accepted Gurney asymmetric sandwich theory for the two extremes of infinite and zero mass backing plate. The comparison is shown to be reasonable, however for the single plate case it is claimed the Gurney approach underestimates the energy transfer to thin plates. The explanation given being that Gurney neglects the momentum of the detonation products which appears sound.

The final conclusions of the study are that the effect of a backing plate is only really seen if one (or both) plates are heavy (relative to the mass of explosive) and large flight distances are required.

From this simple review, it appears that for any flyer plate work there is little benefit to be gained from using elaborate methods of increasing the plate velocity over the simple plane detonation wave driving a single plate method. However, as mentioned previously, cognisance should be taken of the effective charge mass concept (*e.g.* as described by Cooper [19]) in an attempt to limit the explosive mass required.

2.7 Fragment Flight

A quick study of the aerodynamics associated with the ballistic flight of fragmentation returns a multitude of literature. It can, however be quickly ascertained that the majority (if not entirety) of this material restricts itself to the free flight of fragments through predominantly still air at ambient conditions.

The ballistic trajectory of the fragments and the retardation during flight through still air can be calculated following the methods presented by (amongst others) Janzon [3].

Both Janzon and the International Test Operating Procedure (ITOP) for the static testing of high explosive munitions for obtaining fragment spatial distributions [2] use the same basic equation of motion (simplified into one dimension) of

$$m\ddot{x} = -D = -\frac{1}{2}\rho_{air} C_D A x^2 \tag{2.29}$$

where m is the fragment mass [kg], x is the linear distance travelled by the fragment [m], ρ_{air} is the density of the air being travelled through [kg/m^3], C_D is the drag coefficient [dimensionless] and A is the presented area of the fragment in the direction of flight [m^2]. $\dot{x}$ and $\ddot{x}$ are the first and second time derivatives of the linear distance respectively.

Although differences in approaches are apparent, the ITOP approach relates the initial fragment velocity to the measured average fragment velocity whereas Janzon relates the initial fragment velocity to the instantaneous fragment velocity as some point in its trajectory; these methods assume a constant drag acting during flight through a standard atmosphere. No account is taken of the fireball nor its effect on either the fragment drag characteristics or the atmospheric conditions.

2.8 Applicable Numerical Modelling Methods

Numerical modelling techniques exist that can be applied to parts, or all, of the fragment generation through high explosive detonation. A number of commercial packages are available that can be used to model all the different aspects of the problem, from shock and detonation wave propagation through gas and casing expansion to the casing mechanical failure and fragment generation. These multiphysics packages often require specialist high performance computer hardware, which can run into many thousands of pounds, and require many hours of computational time to complete the simulation. It is often more efficient, and both financially and computationally cheaper, to use multiple software packages employing multiple computational techniques to complete a full simulation. Within most research, it is often only necessary to build a partial model, or model part of the scenario, to study an in depth portion of the problem in question.

Depending on the problem, or part of the problem to be modelled, it is often necessary to use different numerical solvers to complete the simulation. The most widely used of these are Eulerian and Langrangian meshed solvers, and the Smoothed Particle Hydrodynamics (SPH) meshless solver. Both Eulerian and Lagrangian meshed solvers track the motion of material during the calculation. The Eulerian solver utilises fixed, often rectangular or square, cells through which all materials move, compared with the Lagrangian solver which utilises a moving grid, of triangular, tetrahedral or hexahedral cells, which tracks and deforms with each material.

Lagrangian meshes can become highly distorted, requiring user intervention to delete cells or remesh areas to reduce the distortion. This can often be avoided by using a Lagrangian based meshless solver, such as SPH. Although often computationally more expensive than more conventional meshed methods, as the calculation is based on the interaction of a node with each of it's neighbours and doesn't require connections, as in the meshed methods, large deformations can be modelled without the mesh tangling / deformation problems. For SPH calculations the state variables calculated at each time

step are held within the nodes, as compared to being held within the cells of a meshed solver.

The solvers and methods mentioned above can be used to model either 2-dimensional or 3-dimensional problems, depending on the scenario to be modelled and the computational hardware capabilities. Examples of available software packages employing these methods are LS-DYNA and ANSYS AUTODYN, and fragmentation modelling often uses a mixture of both Eulerian and Lagrangian solvers known as Arbitrary Lagrangian-Eulerian (ALE) which automatically combines the best features of both. An example of this can be seen in the 3-dimensional LS-DYNA modelling conducted by Chen [86]. Often 3-dimensional problems are too large to compute in full so, where possible, rotational symmetry is used [87]. Ugrčic [88] uses rotational symmetry in his AUTODYN modelling of a 105mm artillery shell which also employs a coupled Euler-Lagrangian mesh, where the HE products and surrounding air are modelled in an Eulerian mesh which has a two-way feedback with the Lagrangian mesh used for the metal casing.

2.9 Summary

From this brief review of some of the available literature, it is clear that as the research objectives of the thesis tightened, areas of the background reviewed change in significance:

- Extensive literature exists covering the interaction of shockwaves with internal flaws, in both metal weapon casing and rocks, forming microcracks and pre-weakening the material.
- The majority of available research on weapon fragmentation refers to the casing breakup and natural fragment generation from cylindrical style weapon casings.
- Fragment flight studies concentrate on free air retardation effects.
- Gas leakage models are reported as important for the correct estimation of the initial

fragment velocity profile but very little experimental data exists to validate against during this early time motion.

- For initial planning purposes, the use of an invariant adiabatic constant for the detonation products will suffice and simplify the calculations considerably. Introduction of a variable adiabatic constant may be necessary during the analysis phase.

- The overall effect of using different detonation product equations of state within calculations is not clear.

- Numerical modelling methods exist which can be used to simulate either part, or all, of the weapon casing expansion and break up. Different solvers may be required to isolate the gas leakage through casing fractures.

Initially the placement of the research was within a late stage of the expansion, well beyond the point of fracture of the expanding cylinder. Planned experiments would concentrate on the free flight of fully formed discrete fragments within the expanding gas cloud, and any mensurable acceleration. This approach would have required deeper research into the effects of the fireball expansion, from macroscale flow speed and temperature effects down to the influence of the initial microcracking within the casing, and the statistical manner of the casing breakup. Localised hotspots in the gas expansion through early time, microscale, statistical aspects would have to be averaged through conducting a large number of identical experiments, as prediction of their position and intensity would not be possible making it impossible to account for them during individual experimental data analysis.

As the research narrowed to concentrate on the gas flow through casing fractures, and the applicability of the current model for this, the shift in emphasis of the background literature reviewed was significant. Beyond the influence of the material properties for the gaseous detonation products, such as equation of state, the influence of the details of the fracture may dominate the flow. With this, the emphasis shifted to a need to understand the fracture process in its entirety. This included from the interaction of the

transmitted shockwave through the casing material with flaw sites, the process involved in the generation of internal microcracks, through to the casing fracture at these sites under macro expansion.

Any microscale artefacts on the surface of the fracture may have a measurable effect on the flow. At this stage in the research, however, a simplified ideal fracture surface was studied, reducing the need to fully research the effects of any surface artefacts. This would make an ideal topic for a follow up thesis, or research package.

Chapter 3

Initial Global Fragment Motion

3.1 Historical Experimental Evidence

Historically, the majority of research conducted has concentrated on the metal fracture and initial metal drive, however Waggener [5] also includes observations on the effects of the expanding detonation products on the motion of the fragments post casing breakup. Although his research employs either pre-fragmented or pre-scored casings, the observations are consistent with only a difference in magnitude being seen. Waggener observes the in-flight fragments being affected in both the direction and speed of flight, with different magnitudes of effect seen at the initiation and non-initiation ends of a cylindrical charge initiated at one end; the speed of the fragments near the non-initiation end of the cylinder is affected more than those fragments near the initiating end of the cylinder. Unfortunately, Waggener does not offer any evidence to substantiate his hypothesis.

The most comprehensively reported historical experimental evidence for the continued acceleration of casing fragments post rupture is contained within a series of reports generated by Bishop, Denny, James and James from AWRE Foulness [21, 89–92]. The experimental campaign covers a series of tests involving the explosively driven expansion of BS970 EN1A steel cylinders of varying thickness: 0.125 in, 0.25 in, 0.5 in, 0.75 in. The

most consistent cylinder component dimensions across the series were an internal length of 17.5 inch and an internal diameter of 3.15 inch. The cylinders used flanges at each end; however, these are not considered during the analyses.

Six explosive compositions were tested, RDX/Wax 88/12 and five different RDX/Wax/Poly-iso-butylene/aluminium compositions, each being supplied as ten pellets dimensioned to give a smooth fit within the cylinder. The charges were initiated using a No.8 electric detonator and CE primer. The charge / casing configuration can be seen as reproduced from [21, 89–92] in Figure 3.1. This Figure also indicates the Type code given by the experimenters for the different cylinder wall thicknesses.

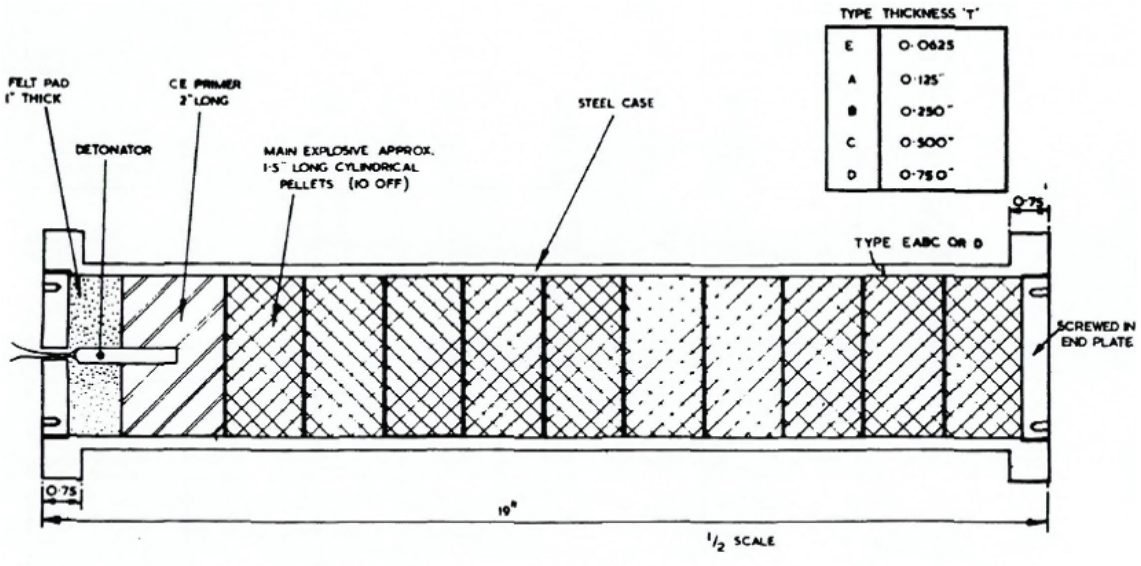


Figure 3.1: Cross Section through Foulness Experimental Charge [21, 89–92]

The composition proportions used are summarised in Table 3.1

	RDX	**Wax**	**PIB**	**Al**
0% Al	88.0	12.0	0.0	0.0
5% Al	84.6	8.4	2.0	5.0
10% Al	80.1	7.9	2.0	10.0
20% Al	71.0	7.0	2.0	20.0
30% Al	61.9	6.1	2.0	30.0
40% Al	52.8	5.2	2.0	40.0

Table 3.1: Foulness Experiments Explosive Composition Proportions

Bishop and James [90] present evidence of the measured experimental fragment speeds at the point of rupture, at 6 ft and 12 ft range and also the maximum speed measured during the experiments. For all case thicknesses and all aluminium content levels it can be seen that the speed of the fragments at 6 ft range is consistently greater than that measured at the point of rupture; this indicates a phase of continued fragment acceleration within the expanding detonation product cloud. It can also be seen from the evidence presented that this continued acceleration stops at a range somewhere between 6 ft and 12 ft as the recorded fragment speed has reduced by 12 ft range, signifying that the fragment has most likely entered a ballistic trajectory by this stage and is subject to drag effects. From Bishop & James [90] it can be seen that the average charge mass for the 0% Al experiments is approximately 116 oz (3.29 kg), which gives an expected maximum fireball radius of between 8 ft and 10 ft, depending on which equation is used, which fits with the fragment speed data and postulated reasoning presented.

The reported values for the fragment speeds for the RDX/Wax 88/12 (0% Al) is reproduced from Bishop & James [90] in Table 3.2 below.

RDX/Wax (0% Al)	**Fragment Speed Measured [ft/s]**			
Case Thickness [in]	**Rupture**	**Maximum**	**6 ft**	**12 ft**
0.125	7400	8600	7600*	7150*
0.25	5650	6720	6000	5700
0.50	4110	4930	4700	4400
0.75	3280	3940	3730	3400

* interpolated

Table 3.2: Part Reproduction of Foulness Experiments Fragment Speeds [90]

Within the reporting of the experimental campaign [91], the comparative expansions of the casing pre and post fracture, and the escaping gaseous detonation products, are shown graphically for the RDX/Wax 88/12 (0% Al) charge with 0.125 inch case thickness. This graphical figure is reproduced in Figure 3.2.

The expansion curves reported are based on a least squares fit of the composite data

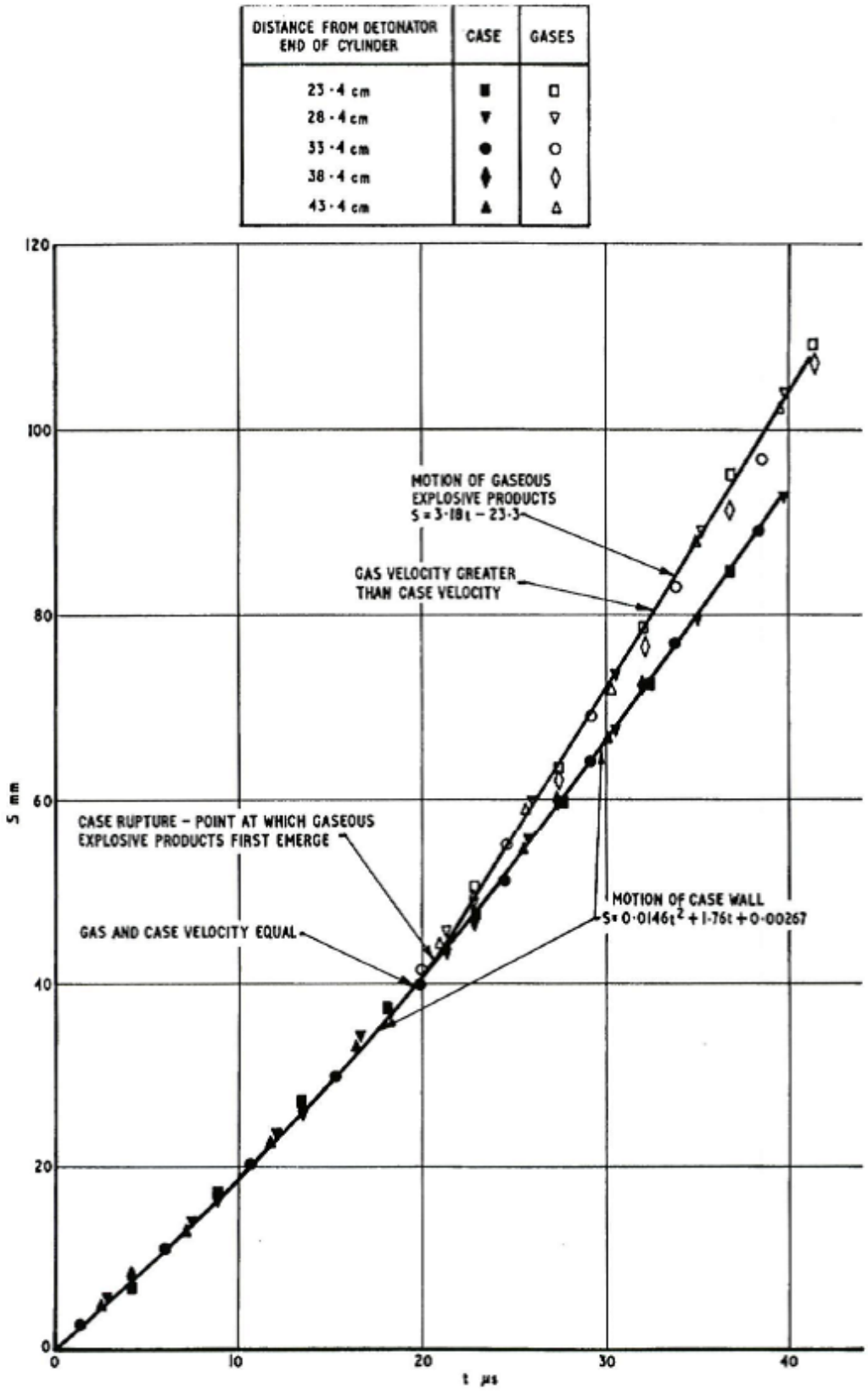


Figure 3.2: Case and Gas Movement from 0.125 in Thick RDX/Wax Filled Cylinder [91]

generated from five recorded positions along the cylinder (measured from the initiation end); the corresponding time reported along the abscissa is the time from the arrival of the detonation wave at each specific reporting point.

Inspection of Figure 3.2 shows that within the timeframe of the recorded data, the expansion of the casing (both pre and post fracture) has been estimated by a quadratic curve, which artificially constrains the casing to a constant acceleration throughout the experiment.

$$s_{casing} = 0.0146t^2 + 1.76t + 0.00267 \quad [mm] \tag{3.1}$$

Differentiation of the position curve gives the speed of the casing

$$v_{casing} = 0.0292t + 1.76 \quad [mm\ \mu s^{-1}] \tag{3.2}$$

Further differentiation of the speed curve gives the acceleration of the casing

$$a_{casing} = 0.0292 \quad [mm\ \mu s^{-2}] \tag{3.3}$$

This suggests that the drive given to the fragments from the escaping gaseous detonation products is the same as that given to the casing pre-rupture,i.e. no additional drive from the expanding products. This may hold for the timeframe over which the experimental measurements were taken; however if the original data files were available it would be useful to apply separate curve fits to the casing data pre and post rupture. This may suggest different expansion characteristics between the two cases, however any such effect may be masked within the uncertainties of the experimental methods employed.

Pre-rupture the gaseous detonation products are reported as having an expansion speed equal to the casing; this is reasonable given the requirement for the gaseous products to be driving the casing expansion and the non-porous character of the steel casing. The post rupture expansion of the gaseous detonation products, however, has been estimated

in Figure 3.2 with a linear curve fit, which in turn constrains the gaseous detonation products to a constant speed post rupture.

$$s_{products_{post-rupture}} = 3.18t - 23.3 \quad [mm] \tag{3.4}$$

As seen above, differentiation of the position curve gives the speed of the gaseous products post rupture

$$v_{products_{post-rupture}} = 3.18 \quad [mm\ \mu s^{-1}] \tag{3.5}$$

Further differentiation of the speed curve gives the acceleration of the post rupture gaseous products

$$a_{products_{post-rupture}} = 0 \quad [mm\ \mu s^{-2}] \tag{3.6}$$

As the expansion of the gaseous products is identical to that of the casing until the point of rupture, it is obvious that the time of casing rupture can be calculated by equating Equations 3.1 and 3.4, such that

$$s_{products_{post-rupture}} = s_{casing} \tag{3.7}$$

This leads to the quadratic equation

$$0.0146t^2 - 1.42t + 23.30267 = 0 \tag{3.8}$$

which can be solved to determine $t_{rupture} = 20.904\ \mu s$.

Using this, simply substitute $t_{rupture}$ into Equation 3.2 to determine the casing velocity at rupture as being approximately 2.37 $mm\ \mu s^{-1}$ (7775 ft/s) which is approximately 5% higher than the measured velocity reproduced in Table 3.2.

Again, the artificial constraint of the gaseous expansion does not match the evidence gathered at a later time, although it is consistent with the constraint of the post rupture casing fragment motion reported within Figure 3.2. This suggests a potential deficiency

within the accuracy of the available diagnostics for the measurement of the casing and gaseous product expansion both pre and post rupture; a more accurate positional measurement and measurement over a longer timeframe may have returned evidence of a change in casing motion at (or around) the point of rupture.

As mentioned earlier in this section, the evidence presented by the series of Foulness experiments is currently the most comprehensive available. The experiment using a 0.125 in casing wall thickness with RDX/Wax 88/12 charge will be used for the verification and validation of a simple model to determine the motion of the fragment post rupture under the influence of the expanding detonation products.

3.2 Simple MATLAB model for fragment motion within the detonation products

From the brief discussion within Chapter 2, it can be envisioned that use can be made of a fully coupled Euler-Lagrange 3-dimensional model such as within AUTODYN or LS-DYNA. Although possible, the use of such a model is complex in mesh generation, and requires detailed and accurate materials models for every material used within the model. These levels of complexity also make the use of such models computationally expensive often taking days or weeks to run to completion, depending on the cell resolution and final elapsed time required. This makes such models less than optimal for conducting sensitivity studies given the long turn around required for each scenario. Initial study of the single historical experiment discussed in Section 3.1 could be conducted using the fully coupled AUTODYN model, however as the final intention was to model all the experiments from the series, incorporating the effects of aluminium on the fragment motion, a fast running simplified engineering model development was undertaken.

A simple model, written in MATLAB, has been developed by the author to replicate a single experiment undertaken by James *et al* in the early 1970's (described above). The

replicated experiment used a RDX/Wax (88/12) charge surrounded by a 0.125 in steel case. This experiment was chosen to replicate in the simple MATLAB model due to it being a baseline test with no aluminium within the charge formulation, thus making the physics easier with no late time energy being added through chemical reactions involving aluminium combustion, and as seen in the previous section James [91] reports velocity - time curves for the case and the escaping detonation products.

The MATLAB code listing is included at Appendix A of this thesis, however for ease of visualisation, a flow chart is included in Figure 3.3. This separates the code into either a defined MATLAB model step, an external software calculation, internal MATLAB data manipulation or the application of existing theory, often in a novel way.

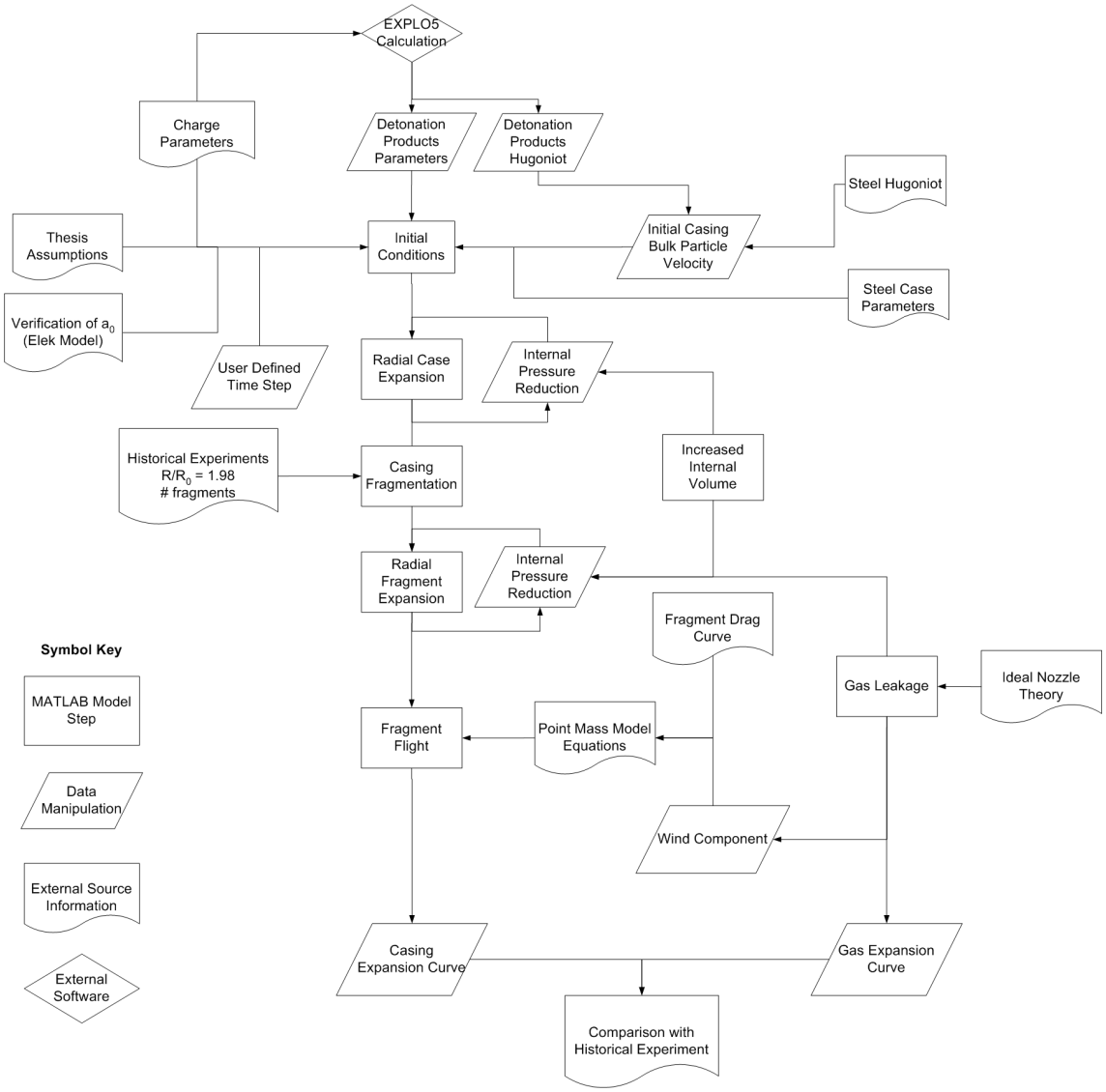


Figure 3.3: Flowchart for fragment and gas motion MATLAB code

From the flow chart, it can be seen that use is made of the Explo5 thermochemical software to generate the detonation product parameters and Hugoniot data which, coupled with the charge parameters, casing parameters, casing steel Hugoniot, and simplifying assumptions forms the initial conditions for the expansion calculations.

Verification of the initial conditions is through a simple comparison of the initial acceleration of the casing, calculated by the MATLAB code, with that calculated using a method with higher fidelity and less simplifying assumptions. The comparison is given in Section 3.2.2.3.

Through a user defined timestep, the iterative calculation of the expanding case and the reduction in drive pressure is conducted through simple physics applied in a novel way. Historical experimental evidence is used to dictate the expansion ratio for casing fracture, beyond which the iterative calculation factors in a pressure reduction through gas leakage as well as the continued pressure reduction due to increasing volume. The volume is taken as that of an unfractured case of the same radius, and the area for gas leakage is the difference of the internal surface area of such a cylinder and the total area of all fragments; the number of fragments being fixed by the historical experimental evidence and the area of the fragments being taken as the cylinder area at fracture. The originality in the method of calculation of the gas leakage area enables its simplicity to reduce the calculational burden within the model.

The mass flow of detonation products through the fractures in the casing is calculated using the accepted gas leakage model, namely ideal nozzle flow. Further originality, however, is incorporated with the use of the standard shock tube equations to calculate flow and shock wave parameters ahead of the casing based on the output of the ideal nozzle flow within the casing fracture. Additional originality is included in the approach by using these flow parameters as the tail wind component within a point mass model trajectory calculation for the fragments, using an external source for the Mach number based drag curve.

The expansion of both the gaseous detonation products and the fragments are tracked within the MATLAB model, and finally compared to the reported historical experimental expansion evidence.

3.2.1 Assumptions

Without the use of high performance computing platforms and large advanced hydrocode models, several simplifying assumptions are necessary to enable an estimation of the casing and gaseous detonation products velocities to be made.

1. Within the cylindrical geometry only radial expansion is accounted for. No effort is made to model the axial expansion of the cylinder.

2. All the high explosive charge converts to detonation products (gaseous and solid) instantaneously. This assumption removes the progressive expansion of the cylinder as the detonation wave progresses along the cylinder length. Under this assumption the radial expansion of the cylinder is equal regardless of axial position along the cylinder.

3. The internal pressure created by the conversion of the high explosives to (mainly) gaseous detonation products generates internal forces leading to radial expansion of the cylinder. As previously mentioned, axial expansion due to internal pressure acting on the end plates of the cylinder is not accounted for.

4. The total number of fragments recovered from the experiment is given by James [91] and the MATLAB model is constrained to generate this number of fragments in total.

5. The mass of each fragment is assumed to be the average fragment mass, generated by dividing the mass of the cylindrical casing by the total number of fragments produced. This fragment mass is kept constant throughout the simulation.

6. Each fragment is assumed to be square in planform.

7. The radial expansion ratio at which the casing fractures to produce fragmentation is given by James [91] and the MATLAB model is constrained to fracture at this radial expansion ratio.

8. The density of the casing material is unchanged by the action of the initial shock wave interaction and expansion process.

9. The expansion can be deemed as quasi-static adiabatic.

3.2.2 Model Methodology

The MATLAB model simulates the expansion of the experimental cylinder by applying basic principles and iteratively stepping forward through time using a (user) fixed timestep value.

3.2.2.1 Initial Conditions

Initially the external conditions and physical properties of the test cylinder and associated materials are established. These could be generated through a user input script, however as the model is only investigating a single experimental set up at this stage the values are "hard wired" into the code listing.

- The charge and casing masses, volumes and surface areas are subsequently calculated. The casing and charge masses are conserved throughout the simulation, however the volumes and both internal and external surface areas are changed at each timestep calculation.

The instantaneous production of detonation products is calculated using an external software package "Explo5 v6.02" available from OZM Research. The detonation product

characteristics calculated by Explo5 v6.02 are given in Appendix B. A brief description of Explo5 v6.02 is also given in Appendix B with more detailed calculations of detonation parameters being given by researchers such as Suceska [93].

- This data was used to give the volume of solidus detonation product formed, which was accounted for in the calculation of the internal pressure generated by the gaseous detonation products formed.

3.2.2.2 Initial Casing Particle Velocity

The detonation wave interacts with the cylinder casing as it passes through the explosive, setting a shockwave running through the thickness of the casing material. This shockwave motion increases the internal pressure and particle velocity of the casing material, such that the casing can be assumed to immediately accelerate up to some initial speed, dictated by the material properties of the detonation products and steel casing. The material properties in question are the shock equation of state for each material, thus allowing the end state to be calculated using the Shock Hugoniot data for each material.

Following the conservation laws allows the locus of states to be described by the Hugoniot curve

$$U_s = c_0 + su_p \tag{3.9}$$

$$P = \rho U_s u_p \tag{3.10}$$

where U_s is the shock speed $[ms^{-1}]$, c_0 is the material sound speed $[ms^{-1}]$, u_p is the material particle speed $[ms^{-1}]$, ρ is the material density $[kg\ m^{-3}]$, P is the pressure $[Pa]$ and s is an experimentally determined parameter. Equation 3.9 and Equation 3.10 can be combined to give a description within shock pressure - particle velocity (P - u_p) space.

$$P = \rho s u_p^2 + \rho c_0 u_p \tag{3.11}$$

The Hugoniot curve for the gaseous detonation products was generated from the output of the Explo5 v6.02 calculation. Plotting the Hugoniot curve for the reacted explosive (gaseous detonation products) and conducting a simple curve fit generated the following equations depending on the percentage of the explosive density compared with the Theoretical Maximum Density (TMD):

$$98\%\ \text{TMD} : P = 2.772u_p^2 + 2.797u_p + 9.216 \tag{3.12}$$

$$100\%\ \text{TMD} : P = 2.834u_p^2 + 2.990u_p + 9.582 \tag{3.13}$$

It can be seen that the curves for the reacted explosive contain an extra term offsetting the curve from the origin by an amount corresponding to chemical energy released during the detonation reaction.

The material properties for the steel casing used in the experiments is listed by James [91], and this has been compared to modern steels with Hugoniot data available within literature. A close approximation of the material properties for the original steel used within James' experiments are those for 1215 steel, as reported by Brar and Rosenberg [94]. The 1215 steel has been used to calculate the initial speed of the casing prior to the acceleration under the influence of the expanding gaseous detonation products held within the unfractured casing volume.

$$1215\ \text{Steel} : P = -0.6211u_p^2 + 36.944u_p \tag{3.14}$$

To calculate the particle velocity imparted into the bulk steel of the casing, it is first necessary to reflect the Hugoniot curves for the explosive products about the particle velocity corresponding with the Chapman Jouget Pressure of the detonation process, P_{CJ}. The calculated parameters, from Explo5 v6.02, can be seen in Table 3.3.

The P_{CJ} values can be used to calculate the corresponding particle velocity ($u_{p_{CJ}}$)

TMD [%]	$P_{CJ}[GPa]$	$D_{CJ}[m/s]$	γ_{CJ}
98%	23.531	7885.72	3.325
100%	24.72	8030.75	3.357

Table 3.3: Explo5 v6.02 calculated parameters for RDX/Wax 88/12

about which to reflect the curves, or these values can be estimated directly.

$$u_p = \frac{D}{\gamma + 1} \tag{3.15}$$

Using either of these methods gives corresponding particle velocities of 1.8233 $mm\ \mu s^{-1}$ (98% TMD) and 1.8432 $mm\ \mu s^{-1}$ (100% TMD). Reflecting each reacted explosive Hugoniot about the appropriate particle velocity gives:

$$98\%\ \text{TMD} : P^* = 2.772u_p^2 - 23.0126u_p + 56.2756 \tag{3.16}$$

$$100\%\ \text{TMD} : P^* = 2.834u_p^2 - 23.8823u_p + 59.1129 \tag{3.17}$$

The bulk particle velocity imparted into the steel casing is calculated by intersecting the reflected reacted explosive Hugoniot curves (Equation 3.16 and Equation 3.17) with the Hugoniot curve for the 1215 Steel (Equation 3.14). Completing this returns particle velocities of 0.995 $mm\ \mu s^{-1}$ and 1.032 $mm\ \mu s^{-1}$ for 98% TMD and 100% TMD explosive respectively; a range of 0.037 $mm\ \mu s^{-1}$. Graphical illustration of the Hugoniot curves can be seen in Figure 3.4.

Although explosive pressing is well controlled, it is possible that some variation of the explosive density may occur and as such it is reasonable to estimate the explosive as having a density of 98% TMD with uncertainty between 100% and 96% TMD; this suggests an initial casing bulk particle speed, $v_{10} = 995 \pm 37\ ms^{-1}$.

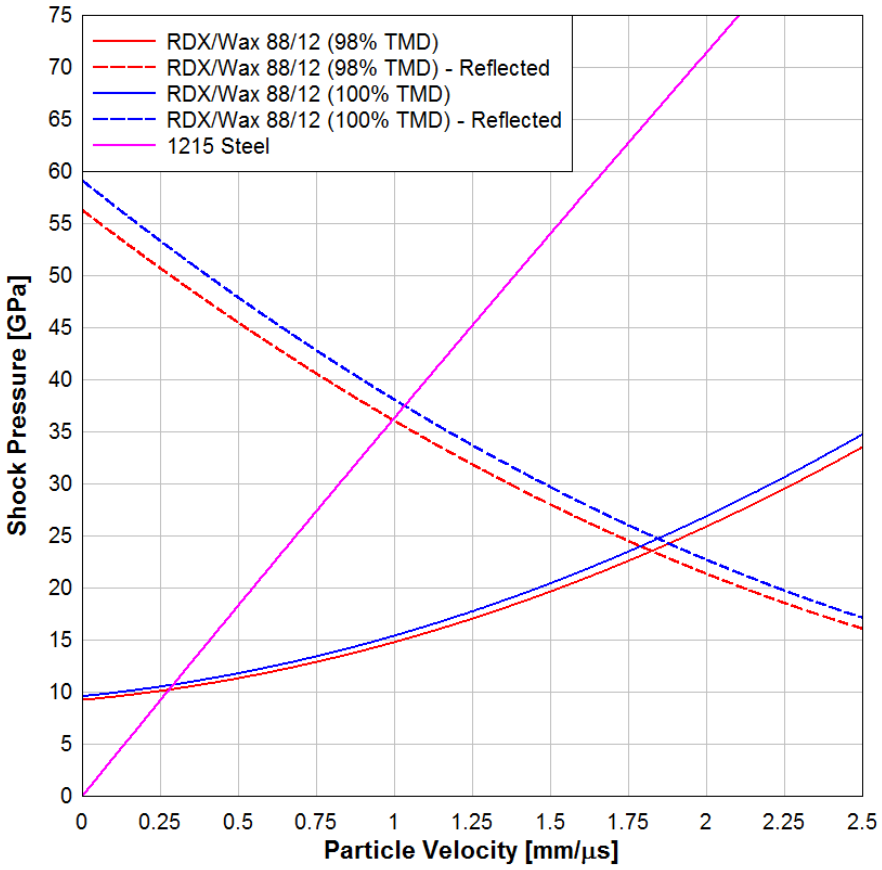


Figure 3.4: Intersection of RDX/Wax 88/12 and 1215 Steel Hugoniot Curves

3.2.2.3 Casing Expansion: Pre-fracture

Once the initial casing particle velocity has been applied to the bulk casing material, the casing is accelerated further by the unbalanced forces generated between the detonation products (acting on the internal casing surface), the surrounding atmosphere (acting on the external casing surface) and the circumferential stresses generated (acting through the material around the circumferential directions to resist expansion).

Work has been conducted previously by different researchers to develop non-hydrocode high fidelity Lagrangian models for the acceleration of metal by explosive action. Flis [95] developed single degree of freedom systems into a cylindrical case before applying Lagrange's Equation.

$$\frac{d}{dt}\left(\frac{\delta L}{\delta \dot{x}}\right) - \frac{\delta L}{\delta x} = 0 \tag{3.18}$$

with the Lagrangian, L = T - U, being the difference in kinetic (T) and potential (U) energies. Flis presents the kinetic energy (per unit planar area) of the system as

$$T = \frac{1}{2}M\dot{x}^2 + \frac{1}{2}\int_{gas} v_{gas}^2 dm_{gas} = \left(\frac{1}{2}M + \frac{1}{6}C\right)\dot{x}^2 \tag{3.19}$$

and the potential energy (per unit area) of the system as

$$U = -\int PdV = -\int P_0\left(\frac{V_0}{V}\right)^{\gamma} dV = \frac{P_0 C}{\rho_0(\gamma-1)}\left(\frac{x_0}{x}\right)^{\gamma-1} \tag{3.20}$$

which, when applied to Lagrange's Equation yielded the equation of motion

$$\left(M + \frac{C}{3}\right)\ddot{x} = P_0\left(\frac{x_0}{x}\right)^{\gamma} \tag{3.21}$$

This equation of motion was integrated to give the metal speed as a function of x,

$$\dot{x} = \left\{\frac{2P_0}{\rho_0(\gamma-1)\left(\frac{M}{C}+\frac{1}{3}\right)}\left[1 - \left(\frac{x_0}{x}\right)^{\gamma-1}\right]\right\}^{\frac{1}{2}} \tag{3.22}$$

Flis continued to generalise the Lagrangian for n dimensions, such that

$$L = \frac{1}{2}\left(M + \frac{n}{n+2}C\right)\dot{x}^2 - \frac{P_0 C}{\rho_0(\gamma-1)}\left(\frac{x_0}{x}\right)^{n(\gamma-1)} \tag{3.23}$$

where the explosive mass, $C = \begin{cases} \rho_0 x_0 \quad \text{for n} = 1 \\ \pi \rho_0 x_0^2 \text{ for n} = 2 \\ \frac{4}{3}\pi \rho_0 x_0^2 \text{ for n} = 3 \end{cases}$

and $x_0 = \begin{cases} \text{explosive thickness for n} = 1 \\ \text{explosive radius for n} = 2, 3 \end{cases}$

Application of Lagrange's principle to Equation 3.23 allowed the more generalised equation of motion to be developed,

$$\left(M + \frac{n}{n+2}C\right)\ddot{x} = \frac{nP_0C}{\rho_0 x_0}\left(\frac{x_0}{x}\right)^{n(\gamma-1)+1} \tag{3.24}$$

which in turn was integrated and rearranged to give

$$\dot{x} = \left\{\frac{2P_0}{\rho_0(\gamma-1)\left(\frac{M}{C} + \frac{n}{n+2}\right)}\left[1 - \left(\frac{x_0}{x}\right)^{n(\gamma-1)}\right]\right\}^{\frac{1}{2}} \tag{3.25}$$

Elek [96, 97] took this approach further and generated the high fidelity equation of motion;

$$\left[\frac{M}{C}\frac{r_1^2}{w^2}\ln\left(1 + \frac{w^2}{r_1^2}\right) + \frac{1}{2}\right]a_1 + \frac{M}{C}\frac{v_1^2}{r_1}\left[\frac{r_1^2}{w^2}\ln\left(1 + \frac{w^2}{r_1^2}\right) - \frac{r_1^2}{w^2 + r_1^2}\right]$$

$$= \frac{2r_1}{\rho_0 r_{10}^2}P(r_1) - \frac{\sigma_H}{\rho_0}\frac{w^2}{r_{10}^2}\frac{1}{\sqrt{w^2 + r_1^2}} \tag{3.26}$$

with;

$$\frac{M}{C} = \frac{\rho_m w^2}{\rho_0 r_{10}^2} \tag{3.27}$$

$$\Rightarrow w^2 = \frac{M}{C}\frac{\rho_0 r_{10}^2}{\rho_m} \tag{3.28}$$

Substituting for w^2 into the high fidelity equation of motion gave

$$\left(\frac{a_1\rho_m r_1^2 + v_1^2 r_1 \rho_m}{\rho_0 r_{10}^2}\right) \ln\left(1 + \frac{M\rho_0 r_{10}^2}{C\rho_m r_1^2}\right) + \frac{a_1}{2} - \frac{v_1^2 r_1 \rho_m M}{M\rho_0 r_{10}^2 + C\rho_m r_1^2}$$

$$= \frac{2r_1}{\rho_0 r_{10}^2} P(r_1) - \frac{M\sigma_H}{C\rho_m}\left(\frac{C\rho_m}{M\rho_0 r_{10}^2 + C\rho_m r_1^2}\right)^{\frac{1}{2}} \tag{3.29}$$

Undoubtedly the implementation of such a high fidelity equation of motion into a predictive model would be complicated and numerically expensive in CPU time, potentially making it difficult to justify. As the model being developed within this research is envisioned as a fast running approximation capable of replicating the trials conducted at Foulness to within the experimental uncertainties, a simpler representation of the motion is sought.

Other disciplines have similar requirements for cylinder wall expansion. Although not metallic cylinders, significant research has been conducted in trying to predict and avoid arterial aneurysm through increased blood pressure [98–101]. White and Hollier [98] devised a relatively simple model of the arterial wall expansion based on the transmural pressure and resistive hoop stress generated. Although the model assumed infinitesimally thin arterial walls, the methodology could be expanded to approach cases akin to the thin wall approximation in standard engineering texts.

The cylinder used within the Foulness tests, although not infinitesimally thin, constitutes a thin wall cylinder, especially in the Type A configuration modelled.

Adherence to conservation of mass principles dictates that as the cylinder expands radially the annular thickness must reduce to maintain a constant volume and, through the constant density assumption, mass.

By constraining the number of fragments generated it is possible to define the average fragment mass (as highlighted within the assumptions section), which in turn can be used to calculate the average fragment volume based on the constant material density

assumption. Using the constrained fragment numbers also allows the internal and external surface areas of the average fragment to be calculated.

The internal force is calculated by using the internal pressure of the detonation products (calculated at each timestep) and the time dependant internal surface area of the average fragment. Similarly, the external force is calculated using the surrounding atmospheric pressure and the time dependent external surface area of the average fragment. Both the internal and external surface areas are time dependent as the cylindrical casing is expanded radially at each timestep. As the density of the casing material is assumed unchanged by the action of the initial shock wave and the expansion process, conservation of mass results in an increase in both internal and external surface areas leading to a thinning of the casing thickness (overall volume of the casing remains constant throughout the expansion phase), and thus the average fragment grows very slightly in surface area but reduces in thickness with every timestep.

Combining the forces acting on the cylinder allows the unbalanced force to be calculated from the summation of the internal force driving the cylinder wall outwards and the external force and the hoop stress based material force both of which resist the outward motion. Starting with the simple definition of pressure being the force per unit area and rearranging gives

$$F_{internal} = P_{internal} A_{internal}(\hat{r})$$

$$F_{external} = P_{external} A_{external}(-\hat{r})$$

$$F_{material} = \sigma_H A_{x-sectional}(-\hat{r})$$

As the force on an object is proportional to the rate of change of its momentum [102], a simplistic Newtonian mechanics approach allows the acceleration of each fragment to be isolated. As the casing has not fractured each fragment is still linked to its adjacent neighbouring fragments, which are accelerated by an equal amount in their respective

radial direction.

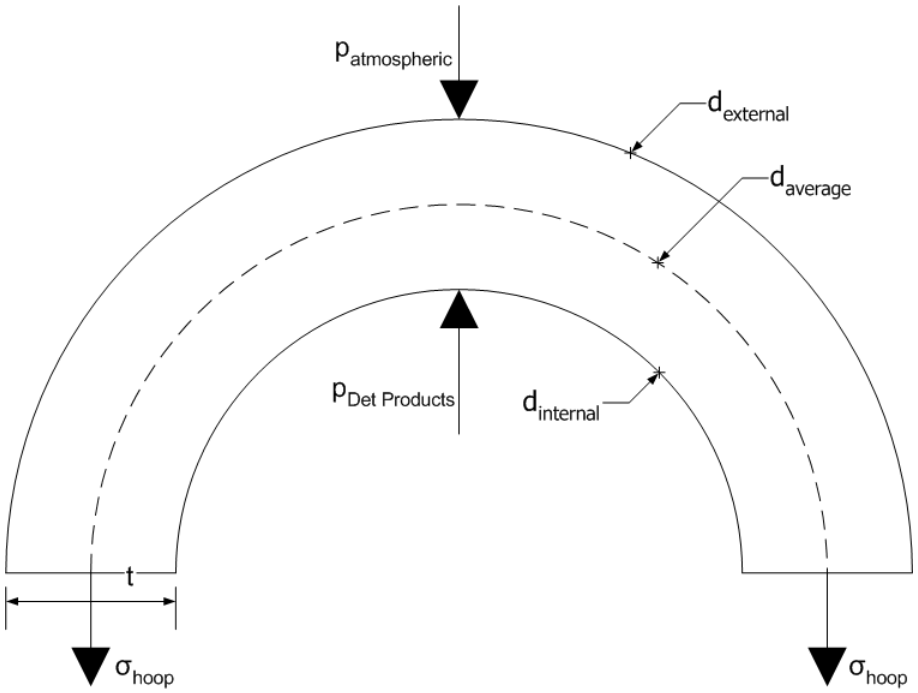


Figure 3.5: Pressures and stresses

$$F = ma \Rightarrow a = \frac{F}{m}$$

$$a_{fragment} = \frac{F_{internal} + F_{external} + F_{material}}{\bar{m}_{fragment}} \tag{3.30}$$

$$a_{fragment} = \frac{P_{internal}A_{internal}(\hat{r}) + P_{external}A_{external}(-\hat{r}) + \sigma_H A_{x-sectional}(-\hat{r})}{\bar{m}_{fragment}} \tag{3.31}$$

since $P_{internal} = P_{DP}$ and $P_{external} = P_{atmos}$, with P_{DP} being the pressure of the detonation products at each timestep $[Pa]$ and P_{atmos} being the external atmospheric pressure $[Pa]$.

$$a_{fragment} = \left(\frac{P_{DP}A_{fragment,internal} - P_{atmos}A_{fragment,external} - \sigma_H A_{fragment,x-sectional}}{\bar{m}_{fragment}} \right) (\hat{r}) \tag{3.32}$$

As all the fragments are still joined within the unfractured casing at this stage,

$$A_{fragment,internal} = \pi d_{internal} L$$

$$A_{fragment,external} = \pi d_{external} L$$

$$A_{fragment,x-sectional} = 2tL$$

where L is the length of the cylinder $[m]$ and t is the casing thickness $[m]$, thus from the thin walled assumption of

$$\sigma_H = \frac{P\bar{r}}{t} = \frac{P\bar{d}}{2t}$$

where $\bar{r}$ is the average radius $[m]$ and $\bar{d}$ is the average diameter $[m]$

$$a_{fragment} = \left(\frac{P_{DP}\pi d_{internal} L - P_{atmos}\pi d_{external} L - \frac{P_{transmural}\,\bar{d}}{2t}\, 2tL}{\bar{m}_{fragment}} \right) (\hat{r}) \tag{3.33}$$

Since $P_{transmural}$ is the difference between the internal and the external pressures, with $P_{external} << P_{internal}$ at this stage it is reasonable to make the simplifying assumption that $P_{transmural} \approx P_{internal}$. Thus Equation 3.33 can be simplified to

$$a_{fragment} = \left(\frac{\left[P_{DP}\pi d_{internal} - P_{atmos}\pi d_{external} - P_{DP}\,\bar{d}\right] L}{\bar{m}_{fragment}} \right) (\hat{r}) \tag{3.34}$$

with $\bar{d} = (d_{internal} + t)$.

This radial acceleration is then applied across all fragments for the duration of the timestep, with the velocity of the fragments being recalculated at the end of each timestep in question.

$$v_{fragment} = u_{fragment} + a_{fragment}\,\delta t$$

$$v_{fragment,i} = v_{fragment,i-1} + a_{fragment,i}\,\delta t \tag{3.35}$$

Similarly for the internal surface radial positions

$$r_{internal,i} = v_{fragment,i-1}\delta t + \frac{1}{2}a_{fragment,i}(\delta t)^2 + r_{internal,i-1} \tag{3.36}$$

The parameter compared to the experimental results is the external casing position during expansion, and this is found by simply applying the cylindrical geometry to get

$$r_{external,i} = \sqrt{r_{internal,i}^2 + \frac{m}{\pi\rho L}} \tag{3.37}$$

As the internal radius of the casing increases with each timestep, it is obvious that both the internal surface area and internal volume also increase with each timestep. As the mass of the detonation products does not change with each timestep pre-casing fracture (as there is no physical route for mass escape) this leads to a reduction of the internal pressure driving the expansion.

From the assumption that the cylinder expands uniformly within the radial direction, with no progressive expansion along the length of the cylinder, it can be seen that the internal surface area of the cylinder within any given timestep is

$$A_{internal,i} = 2\pi r_{internal,i}L \tag{3.38}$$

Similarly, the internal volume of the cylinder within any given timestep is given by:

$$V_{internal,i} = \pi r_{internal,i}^2 L \tag{3.39}$$

where L is the length of the cylinder.

Even though the timescale of each timestep is extremely short in standard engineering terms, it is assumed that the expansion of the detonation products within the cylinder is

quasi-static adiabatic and as such

$$PV^{\gamma} = constant \tag{3.40}$$

thus it can be seen that

$$P_i = \frac{P_{i-1}V_{i-1}^{\gamma}}{V_i^{\gamma}} \tag{3.41}$$

Coupling this with the assumption of no axial expansion within this simplistic model, and thus $\delta L = 0$:

$$\frac{V_i}{V_{i-1}} = \frac{\pi r_i^2 L}{\pi r_{i-1}^2 L} = \left(\frac{r_i}{r_{i-1}}\right)^2$$

$$P_i = P_{i-1}\left(\frac{r_{i-1}}{r_i}\right)^{2\gamma} \tag{3.42}$$

This procedure is repeated for successive timesteps until the casing expansion ratio, $\left(\frac{\text{current casing radius}}{\text{initial casing radius}}\right)$, is as per the constrained value from the experimental evidence. Once this is reached, the fragment surface areas and thicknesses are frozen and do not change during subsequent timestep calculations. Further expansion of the casing leads to the generation of openings between the fragments which allows the escape of detonation products.

As a check of the fidelity of the simple method developed, an extension of the method devised by Elek to calculate the initial acceleration has been undertaken, with the results being compared to those calculated using the proposed MATLAB model.

Setting the initial conditions within Equation 3.29 such that $r_1 = r_{10}; v_1 = v_{10}; a_1 = a_{10}$ allows the initial conditions equation of motion to be derived.

$$\left[\left(\frac{a_{10}\rho_m}{\rho_0} + \frac{v_{10}^2\rho_m}{\rho_0 r_{10}}\right)\ln\left(1 + \frac{M\rho_0}{C\rho_m}\right) + \frac{a_{10}}{2} - \frac{v_{10}^2\rho_m M}{r_{10}(M\rho_0 + C\rho_m)}\right](\hat{\mathbf{r}})$$

$$= \left[\frac{2}{\rho_0 r_{10}}p(r_{10}) - \frac{M\sigma_{flow}}{C\rho_m r_{10}}\left(\frac{C\rho_m}{M\rho_0 + C\rho_m}\right)^{\frac{1}{2}}\right](\hat{\mathbf{r}}) \tag{3.43}$$

The flow stress, $\sigma_{flow} = K\epsilon^n$, is defined by Groover [103] as "the instantaneous value

of stress that is required to just continue deforming the material during any operation". Groover also defines the Mean Flow Stress as being "the average value of the stress over the stress-strain curve from the beginning of the strain to the final (maximum) value that occurs during deformation". In this situation the mean flow stress can be equated to the average value of the yield strength (onset of plastic deformation) and the ultimate strength of the material (onset of fracture), which for the material under consideration here gives a mean flow stress of approximately 400 MPa.

Hutchinson [104] shows that the initial internal pressure due to the detonation products is approximately 42% of the Chapman Jouget detonation pressure, $P(r_{10}) = 0.42p_{CJ}$ thus

$$P_{CJ,98\%TMD} = 23.531\ [GPa] \rightarrow P(r_{10})_{98\%TMD} = 9.9E9\ [Pa]$$

$$P_{CJ,100\%TMD} = 24.72\ [GPa] \rightarrow P(r_{10})_{100\%TMD} = 10.4E9\ [Pa]$$

Simple algebraic manipulation of Equation 3.43 along with substitution for these values of σ_{flow} and $p(r_{10})$, along with the numerical values corresponding to the experimental cylinder used during the Foulness tests [21, 89–92]

$$r_{10} = 0.04\ [m]; v_{10} = 995 \pm 37\ [ms^{-1}]; \rho_0 = 1636\ [kgm^{-3}]; \rho_m = 7850\ [kgm^{-3}]$$

$$V_C = 0.0019\ [m^3]; V_M = 0.00032\ [m^3]; C = 3.108\ [kg]; M = 2.512\ [kg]$$

allows the initial acceleration of the cylinder casing to be calculated.

Doing this, and conducting a similar exercise with the proposed simple MATLAB model, gives an initial acceleration a_{10} for each case that can be seen in Table 3.4

No uncertainty values are calculated within each density case for the simple MATLAB model due to their being no reliance on the initial velocity of the casing, however there is still a difference of approximately 5% depending on the density of the explosive against the calculation based on Elek's method.

MODEL USED	TMD [%]	$\mathbf{a_{10}}$ [$\mathbf{m/s^2}$]	UNCERTAINTY
Elek (High Fidelity)	98	2.41E8	3%
	100	2.53E8	3%
Hoing (Low Fidelity)	98	2.55E8	–
	100	2.68E8	–

Table 3.4: Comparison of Initial Accelerations

Comparing the two methods used shows the proposed simple MATLAB method to be overestimating the initial acceleration by an order of 6% based on the values returned by Elek's high fidelity method. Given the reduction in fidelity and complexity of the proposed MATLAB method, coupled with the corresponding ease of coding and speed of calculation, this difference between the two methods is acceptable and probably within most experimental measurement uncertainty at the time the Foulness tests were conducted.

It is expected that the proposed MATLAB methodology will diverge from the time dependent results that would be calculated using Elek's method. However, given the overall timeframe of the pre-fracture phase, and the expected uncertainty in the experimental results, this divergence is acceptable for the purposes of this comparison.

3.2.2.4 Casing Expansion: Post-fracture

Once the predetermined fracture expansion radius is reached, any further expansion serves to open the fractures between fragments. The internal surface area of the cylinder is increased as discussed in the pre-fracture expansion section, however, once the critical radius for fracture is reached the surface area of each fragment is frozen.

$$A_{fragment_{critical}} = \frac{m_{casing}}{n_{fragments}\rho_{casing}[r_{external_{critical}} - r_{internal_{critical}}]} \tag{3.44}$$

where

$$r_{external_{critical}} = r_{external_{initial}} \left(\frac{r_{external}}{r_{external_{initial}}} \right)_{critical}$$

$$r_{internal_{critical}} = \sqrt{r^2_{external_{critical}} - \frac{m_{casing}}{\rho_{casing}\ \pi\ l_{casing}}}$$

Thus during the post fracture phase, the frozen fragment surface area can be seen to be

$$A_{fragment_{frozen}} = A_{fragment_{critical}}$$

As the casing internal surface area continues to be calculated every timestep, it is trivial to determine the area of the fractures opened within each timestep as being

$$A_{fracture,i} = A_{internal,i} - (A_{fragment_{frozen}}\ n_{fragment}) \tag{3.45}$$

To simplify the calculation, no account of the energy lost in fracturing the casing material is taken.

After fracture has occurred the pressure reduction due to mass of detonation products lost through the fractures is calculated first, followed by the reduction in pressure due to continued casing expansion.

Numerous gas leakage models have been independently developed and employed over the years, however they all appear to be based on ideal nozzle theory.

The gas leakage model suggested by Karpp [80], based on ideal nozzle theory, isolated the maximum rate of flow. A comparison of modelling results (for the model with gas leakage included) and experimental data showed good agreement for a variety of explosive fills and charge mass to casing mass ratios.

Similarly the gas leakage model used by O'Donoghue [82] is based on the premise of ideal nozzle flow passing the maximum mass flow rate.

The ideal nozzle theory methodology has been independently progressed by Hutchinson and Price [59]. In their investigation into the problem Hutchinson and Price adopt both analytical and numerical approaches to the problem.

The analytical approach makes several simplifying assumptions regarding the system geometry and properties, namely;

- The geometry is perfectly cylindrical
- All the explosive material is consumed instantaneously and produces gases internal to the casing that are ideal and at uniform pressure and density. The gas density being initially equal to that of the condensed phase explosive material.
- Gas expansion is adiabatic and no wave phenomena are present internal to the casing (quasi steady state approach)
- The casing fractures with simple edges that do not impart viscous drag on the gas flow.
- The fragments produced remain radially aligned and do not start to tumble.

The numerical approach uses the Sandia National Laboratories developed Eulerian code CTH with standard equations of state for each material, including a JWL equation of state for the explosive. The explosive was approximated using the nearest equivalent with an available material model as the original explosive used in the experiments [21] was not available within CTH. The numerical approach allowed for wave phenomena within the gas internal to the casing.

Hutchinson and Price compare their results with experimental data and conclude that although the final velocity reached by casing fragments is less than the expected Gurney velocity this is not due to prompt gas leakage. Indeed, they argue that competing factors, such as casing expansion and fracture opening serve to limit the peak flow rate of gaseous products leaking through the cracks.

Hutchinson and Price conclude that the analytical and numerical approaches undertaken do not give exact numerical agreement (even as to the order of magnitude) for the physical processes; however, they do stress that the approaches support the same general conclusion, i.e.:

- The gas pressure at casing fracture is extremely high but the gas leakage is limited.
- The leakage rate increases as the casing expands and the cracks grow, however this competes with the drop in gas pressure due to its continued adiabatic expansion.
- The gas flow rate therefore reaches a peak before being reduced (and stopped) as it catches and mixes with the shock compressed ambient air ahead of it.

Hutchinson and Price close by suggesting a repeat of historical experimental work in this area with modern diagnostics could give a detailed explanation of the physical processes at work during the casing expansion and gas leakage phases.

Applying the current accepted gas leakage model, based on ideal nozzle flow [59, 80], and assuming the maximum rate of gas leakage occurs when the flow through the fracture is sonic,

$$\dot{m}_i = A_{fracture,i} \sqrt{\gamma_4 \ \rho_{4_{i-1}} \ P_{4_{i-1}}} \left(\frac{2}{\gamma_4 + 1} \right)^{\frac{\gamma_4 + 1}{2(\gamma_4 - 1)}} \tag{3.46}$$

coupled with the user defined timestep for the iterative calculations, δt, gives the mass of gaseous products lost per iteration,

$$m_{lost,i} = \dot{m}_i \ \delta t \tag{3.47}$$

which is deducted from the remaining mass of gaseous detonation products.

Taking m_1 as being the mass of gaseous products within the casing envelope immediately prior to the venting iteration, and m_2 as the mass of gaseous products within the casing envelope immediately after venting has occurred, it can be deduced that

$$m_{2,i} = m_{1,i} - m_{lost,i} \tag{3.48}$$

and it can be seen that as time progresses

$$m_{1,i} = m_{2,i-1}$$

Similarly, taking p_1 as being the pressure of the gaseous products within the casing envelope immediately prior to the venting iteration and p_2 being the pressure immediately after the venting iteration, it is possible to adapt the simple adiabatic equation

$$\frac{P_{1,i}}{P_{2,i}} = \left(\frac{\rho_{1,i}}{\rho_{2,i}}\right)^{\gamma} \tag{3.49}$$

to account for any change in mass, such that the volume remains constant to give

$$\frac{P_{1,i}}{P_{2,i}} = \left(\frac{m_{1,i}}{m_{2,i}}\right)^{\gamma} \tag{3.50}$$

and finally

$$P_{2,i} = P_{1,i}\left(\frac{m_{1,i} - \dot{m}_i\,\delta t}{m_{1,i}}\right)^{\gamma} \tag{3.51}$$

and, likewise, it can be seen that as time progresses

$$P_{1,i} = P_{2,i-1}$$

This internal gaseous products pressure is then subjected to the same treatment under continued casing expansion as shown in the section covering pre-fracture expansion, with the exception that the fracture area must be recalculated within each timestep to enable the variation of gas leakage with expansion to be calculated. It can be seen that

$$A_{fracture,i} = w_{fracture,i}L \tag{3.52}$$

where $w_{fracture,i}$ is the width of the fracture at the start of timestep i.

As per high speed flow through any orifice, the escaping flow will continue downstream for a measurable distance before it begins to slow and diverge. For this reason, and the extremely short timeframes under consideration, it can be assumed that the flow is constrained within a non-physical shock tube. Thus the standard shock tube flow equations may be employed to calculate the expected initial shock strength and other

associated flow phenomena.

Taking the opening of the fractures as being akin to the failure of the shock tube diaphragm allows the region within the casing to be designated as the driver region, and subsequently labelled subscript 4. The region immediately outwith the casing can be compared to that within the driven region but still behind the expanding contact surface, labelled subscript 3. Although the region ahead of the expanding detonation product cloud has been acted on by an initial expanding shock wave, resulting from the initial detonation wave transmitting through the casing wall into the surrounding atmosphere, this shock wave is not strong enough to significantly displace the immediate surroundings within the timeframe under consideration. The significant blast shock wave will be generated by the expansion of the detonation products.

Using the conditions within the detonation products immediately prior to casing fracture allows an initial value of P_4 to be determined, with P_1 taken as standard atmospheric pressure. Using these conditions, with known calculated values of P_4, ρ_4, γ_4, P_1, ρ_1, and γ_1 allows the local speeds of sound in the driver and driven gases to be calculated simply by using

$$c = \sqrt{\frac{\gamma P}{\rho}} \tag{3.53}$$

The associated ratio of driver to driven section pressure can be used with the standard shock tube equations [105] to calculate the initial shock strength, $\frac{P_2}{P_1}$.

$$\frac{P_4}{P_1} = \frac{P_2}{P_1}\left[1 - \left(\frac{(\gamma_4 - 1)\left(\frac{c_1}{c_4}\right)\left(\frac{P_2}{P_1} - 1\right)}{\sqrt{\left(2\gamma_1\left(2\gamma_1 + (\gamma_1 + 1)\left(\frac{P_2}{P_1} - 1\right)\right)\right)}}\right)\right]^{-\frac{2\gamma_4}{(\gamma_4 - 1)}} \tag{3.54}$$

The form of Equation 3.54 is such that it must be solved using an iterative, numerical method. Within the MATLAB code, Equation 3.54 is rearranged to enable use of the

"fzero" command to find the root of the non-linear function. This is done by supplying an initial guess for the value of $\frac{P_2}{P_1}$, which is then varied iteratively to enable the value of $\frac{P_4}{P_1}$ to be approached. The default cut-off values used to terminate the iterations, in both variable and function values, is 1 x 10^{-4}.

Once the pressure behind the expanding shock wave, P_2, is calculated it is possible to calculate the remaining associated parameters [105]. The shock speed, U_s, can be calculated using

$$U_s = c_1 \sqrt{\frac{\gamma_1 + 1}{2\gamma_1}\left(\frac{P_2}{P_1} - 1\right) + 1} \tag{3.55}$$

and the associated speed of the induced mass motion of the gas through which the shock moves, assuming the gas was stagnant prior to shock action, can be found applying

$$u_p = U_s \left(1 - \frac{\rho_1}{\rho_2}\right) \tag{3.56}$$

Using the isentropic relations

$$\frac{P_3}{P_4} = \left(\frac{\rho_3}{\rho_4}\right)^{\gamma_4}; \quad \frac{P_1}{P_2} = \left(\frac{\rho_1}{\rho_2}\right)^{\gamma_1} \tag{3.57}$$

along with the assumption that there is no mixing of the detonation products and the surrounding air at this stage, gives the contact surface moving at the speed of the gas behind the shock wave with $u_3 = u_2 = u_p$ and $P_3 = P_2$. Simple substitution and algebraic manipulation yields

$$u_p = u_3 = \frac{2c_4}{\gamma_4 - 1}\left(1 - \left(\frac{P_3}{P_4}\right)^{\frac{\gamma_4 - 1}{2\gamma_4}}\right) \tag{3.58}$$

Equation 3.58 is used to determine the speed of expansion of the gaseous detonation

products immediately outside the casing.

The effect of this gas flow through the casing fractures on the newly formed fragments can be found by taking a standard point mass model equation for range [106] and assuming expansion in the radial direction only, no elevation or azimuthal drift effects are accounted for at this stage.

$$\frac{d^2x}{dt^2} = -\frac{\pi\rho d^2 C_D}{8m} v(\frac{dx}{dt} - W_x) \tag{3.59}$$

where d is the reference diameter of the projectile $[m]$ (such that the cross sectional area is given by $\pi d^2/4$), v is the projectile speed $[ms^{-1}]$, and W_x is the range direction component of the wind speed $[ms^{-1}]$.

Adapting Equation 3.59 to account for the radial expansion and the fragment presented surface area, allows a generalised fragment equation of motion to be written

$$\ddot{r} = -\frac{\rho A_{fragment} C_D}{2m} \dot{r}(\dot{r} - W_r) \tag{3.60}$$

In the MATLAB model, the acceleration seen by the fragments can be found from the summation of the individual accelerations acting due to the unbalanced forces from the expanding detonation product direct drive acting on the rear surface of the fragments, the indirect drive from the drag acting on the fragments as the detonation products flow through the fractures, and the resistance due to the drag acting on the fragments from the atmosphere into which the fragments are moving.

$$a_{total} = a_4 + a_{drag4} + a_{drag3} + a_{drag2} + a_{drag1} \tag{3.61}$$

At each stage the acceleration linked to the regions through which the fragment is not travelling can be seen to be zero.

The acceleration due to the direct action of the detonation products can be calculated in a similar way to that pre-fracture, with the force F_4 adjusted to account for the loss of internal pressure with gas mass flow through the fractures and continued radial expansion of the fractured cylinder.

$$a_4 = \ddot{r}_4 = \frac{F_4}{m_f} = \frac{P_4 A_{fragment,internal}}{m_f}(\hat{r}) \tag{3.62}$$

To calculate the indirect drive from the drag due to the flow through the cracks, and since the MATLAB model is using the current accepted gas leakage flow model which limits the maximum flow rate using ideal nozzle flow, the flow speed of the gas through the fracture is the local sound speed of the gas, c_4, in a stationary fragment frame of reference. Converting to a moving fragment frame of reference gives a flow speed of $W_r = (c_4 + \dot{r})$. Thus applying the point mass model with a wind speed

$$a_{drag4} = \ddot{r}_{drag4} = -\frac{\rho_4 A_{fragment,internal} C_{D_4}}{2\bar{m}_f}\dot{r}(\dot{r} - (c_4 + \dot{r}))(\hat{r}) \tag{3.63}$$

so

$$\ddot{r}_{drag4} = \frac{\rho_4 A_{fragment,internal} C_{D_4}}{2\bar{m}_f}\dot{r}c_4(\hat{r}) \tag{3.64}$$

For motion into Region 3, where the detonation products have overtaken, and are travelling ahead of the fragment, it can be visualised that the drag on the fragment could be either positive, zero, or negative depending on the relative speeds of the fragment and gas flow. For this, it can be seen that if a simplification is made such that $\dot{r}$ and W_r are both positive in an expanding radial direction then since $W_r = u_3$ in region 3

$$a_{drag3} = \ddot{r}_{drag3} = -\frac{\rho_3 A_{fragment,external} C_{D_3}}{2\bar{m}_f}\dot{r}(\dot{r} - u_3)(\hat{r}) \tag{3.65}$$

Similar treatment for Region 2, where the fragment has passed through the contact surface but is still travelling within air that has a mass motion due to the previous passage of the shock wave such that $W_r = u_2$, gives

$$a_{drag2} = \ddot{r}_{drag2} = -\frac{\rho_2 A_{fragment,external} C_{D_2}}{2\bar{m}_f} \dot{r}(\dot{r} - u_2)(\hat{r}) \tag{3.66}$$

Finally, once the fragment catches the decelerating shock wave and passes through it into Region 1, it can be assumed that no external wind effects are present (flight into still air) and thus $W_r = 0$

$$a_{drag1} = \ddot{r}_{drag1} = -\frac{\rho_1 A_{fragment,external} C_{D_1}}{2\bar{m}_f} \dot{r}^2(\hat{r}) \tag{3.67}$$

Hence it can be seen that whilst Equation 3.64 is of a slightly different format to Equations 3.65 to 3.67, due to the use of the internal fragment area and the local flow speeds, the equations relating the fragment acceleration to drag effects can be grouped.

$$\ddot{r}_{drag\varepsilon} = -\alpha \dot{r}^2 (1 - \beta) \tag{3.68}$$

where $\varepsilon = 4, 3, 2, 1$ with

$$\alpha = \frac{\rho_\varepsilon A_{fragment} C_{D\varepsilon}}{2\bar{m}_f}$$

$$\beta = \frac{W_{r\varepsilon}}{\dot{r}}$$

and

$$W_{r\epsilon} = \begin{cases} u_4 = c_4 + \dot{r} & \varepsilon = 4 \\ u_3 = u_2 = u_p & \varepsilon = 3, 2 \quad \text{as per Equation 3.58} \\ u_1 = 0 & \varepsilon = 1 \end{cases}$$

It can also be seen that

$$\ddot{r} = \begin{cases} +ve, & \beta > 1, \quad W_r > \dot{r} \\ 0, & \beta = 1, \quad W_r = \dot{r} \\ -ve, & \beta < 1, \quad W_r < \dot{r} \end{cases}$$

During the calculations within the MATLAB model, the drag coefficient, C_D, used is that for a "chunky" metal fragment taken from the US trajectory calculation software package Traj_Can [107] and applied as a C_D-Mach table with simple linear interpolation between the data points.

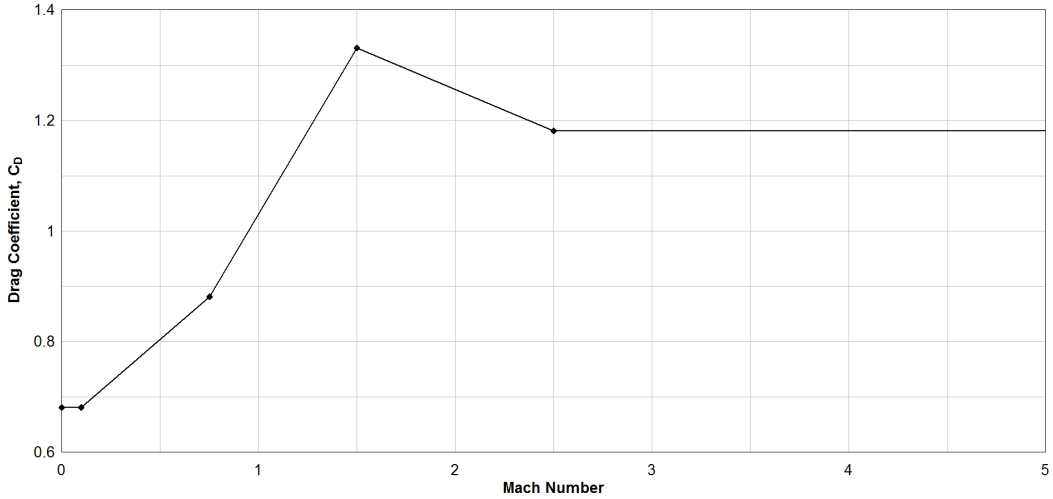


Figure 3.6: "Chunky" fragment drag coefficient with Mach Number [107]

Applying this with the gas speeds for each region derived earlier from the shock tube equations allows the radial motion of the fragments to be estimated. As seen previously, within region 3, behind the contact surface, Equation 3.61 applies whereas in the region ahead of the contact surface but still behind the shock wave, region 2, the acceleration seen by the fragment relates only to the retardation of it's flight by the slower moving air through which it travels, a_{drag2}. Likewise once the fragments have caught and overtaken the shockwave they are moving through essentially still air and as such only see the effects of a_{drag1}.

At this stage of development, however, the simplified model will concentrate on the

early time fragment motion within the regime behind the expanding contact surface only. Thus we make use of Equation 3.61 and its application within each timestep such that

$$v_i = v_{i-1} + a_{total}\delta t \tag{3.69}$$

and

$$r_{external,i} = r_{external,i-1} + v_{i-1}\delta t + \frac{1}{2}a_{total}\delta t^2 \tag{3.70}$$

where δt is the user defined timestep for the MATLAB model.

The position of the contact surface is tracked using Equation 3.58 such that

$$r_{contactsurface,i} = r_{contactsurface,i-1} + v_{3,i-1}\delta t \tag{3.71}$$

where both parameters can be compared to the experimental results as per the pre-fracture case.

It can be envisioned that eventually the remaining internal pressure becomes too low to sustain any positive acceleration on the fragments, either by direct drive or "tailwind" drag. This scenario is modelled by the transition between regions of interest, but requires a rather lengthy cut off time to be selected by the user.

As the MATLAB model has been developed solely for use within this research package, it is possible to output any of the stored variables calculated to assess the appropriateness of the approach employed. Constraining the input parameters closely to the experimental setup used by Denny *et al.* [21, 89–92] allows the simplified approach to be compared directly to the experimental evidence gathered.

3.2.3 Model Comparison with Historical Experimental Data

Output from the MATLAB model can be generated from any of the calculated parameters, however the primary outputs generated are the local flow speed of the gaseous detonation

products immediately external to the casing, and the casing fragment speed.

Initial comparisons with the Foulness experimental results show obvious differences between the modelled and experimental results. These can be seen in Figure 3.7 where the experimental results are reproduced [21] whereas the modelled results are based on Equation 3.37 for the casing and gas motion prior to casing fracture. The modelled motion of the casing and gas post casing fracture are based on Equation 3.70 and Equation 3.71 respectively.

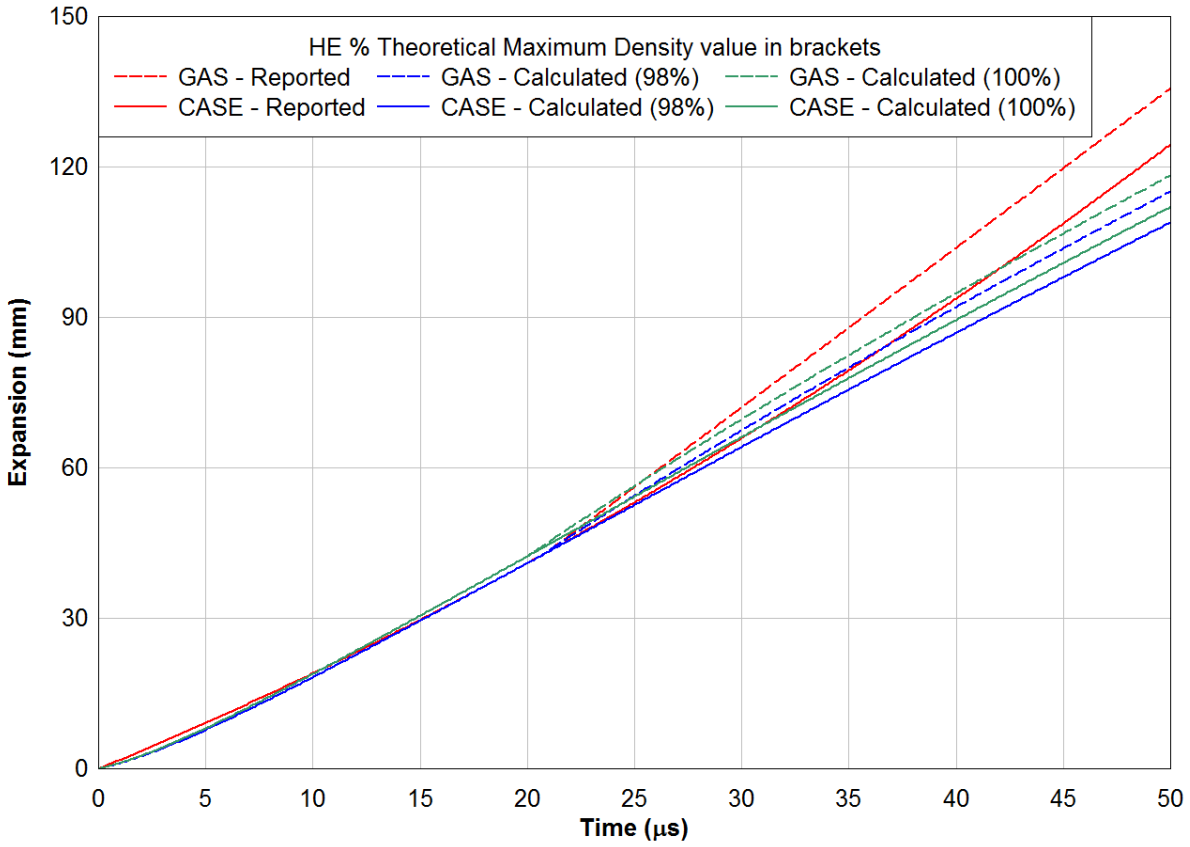


Figure 3.7: Comparison of MATLAB model and Foulness Experimental results

A graphical comparison of the results is shown in Figure 3.7 where the effective change in initial casing speed due to the density of the explosive can be clearly seen. The difference between the experimental casing speed and the modelled casing speed driven by 100% TMD RDX/Wax can be clearly seen, which is most probably down to the physical limitations in casting explosives approaching 100% TMD. The curves generated by the model using the data calculated for an explosive with 98% TMD show a remarkable

agreement to the pre-fracture experimental casing expansion curve. The difference in the graphs occurs post fracture, where the model can be seen to lag behind the experimental curves even for the case with 100% TMD.

The sets of curves diverge greatly as time increases, however the act of fitting simple linear and polynomial curves to the gas expansion and casing expansion experimental results by James *et al.* introduces non physical behaviour which negates the validity of extrapolating the experimental data beyond it's original limits.

Upon further investigation of the comparison of the gaseous detonation product expansion it can be seen that the modelled results immediately lag behind the experimental results. This is potentially due to the methodology used to calculate gas speeds within the model, but may also be due to limitations with the experimental analysis.

Use has been made of high fidelity numerical modelling to assess the effect of the expansion external to the casing on the speed of the gaseous products to determine the applicability of the use of the general shock tube equation in this configuration.

3.3 Summary

The simple model developed to investigate the post rupture fragment acceleration showed a remarkable level of agreement with the casing motion pre-rupture, given the simplifying assumptions and the non complex physics used during that phase of motion. By fixing the fracture radius of the casing to that observed in the Foulness experiments, it was not possible to ascertain any information regarding the ability of the model to predict the point within the expansion phase where fracture would occur, which equally means that the model is unable to predict the casing speed at fracture for any other experimental data that may become available.

The results of the model for the motion of the gaseous products disagree with the experimental observations, however this may be explained. The modelled flow ahead

of the fragment relies on the applicability of both the ideal nozzle assumption limiting the flow within the fracture to being locally sonic, and also on the applicability of the general shock tube equations in this scenario. Should either of these assumptions not be applicable, the gas flow speed will be dramatically affected. This led to the need to employ complex numerical modelling to the flow in order to determine the level of applicability of the modelling methodologies employed.

The use of this complex numerical modelling is discussed in the following chapter, however it can be noted here that the results highlighted a potential shortcoming in the use of the ideal nozzle flow assumption for flow expansion through the cracks in the expanding casing [59, 80, 82].

This finding led to the re-scoping of the research hypothesis to move from investigating the global motion of the fragments within the expanding gaseous detonation products cloud to concentrate on the gaseous detonation product flow through the cracks within the casing and the potential development of an updated flow model for use within a more complex predictive capability.

Chapter 4

Computational Simulations of Gas Leakage

4.1 Initial Numerical Modelling Conducted

Chapter 2 introduced the concept of numerical methods being applicable to the calculation of the scenario under consideration and prior to development of the MATLAB model in the previous chapter, it was noted that commercial simulation packages are available that would model the entire scenario.

The modelling conducted during the research may undoubtedly have been more representative of physical flow regimes by using a computational fluid dynamics (CFD) package with turbulent flow capabilities, such as Fluent or Star-CCM+, however the limitations of time and available resources dictated the use of software with existing researcher proficiency levels. The AUTODYN software package used is a transient dynamics, multi solver package primarily used for the response from short duration severe loadings such as impact, high pressure phenomena or explosions. Complex material models are included and cover all phases of materials and interactions between these. Gas flow calculations within AUTODYN are conducted using the same fluid dynamic equations as CFD pack-

ages, however these are limited to use within a generic Eulerian solver and do not include complex turbulent flow capabilities.

Placement of numerical gauge points at relevant points within the model enables the measurement of numerous parameters, and thus some derived parameters, at these points. Measureable parameters include pressure, density, material velocity and material sound-speed allowing derived parameters such as Mach number to be deduced. The difficulty can be in the placement of gauge points in the areas of interest; however unlike physical gauges the numerical gauges do not interfere with the material or its motion as so large numbers of gauge points can be incorporated within a single calculation. The problem then becomes one of data management.

Ideally a 3-dimensional calculation would include all components with accurate material models, including a stochastic distribution within the strength and failure models to ensure pseudo-random material fracture. If the material strength is constant across the entire bulk of the material, and the failure point is also constant, then the material will fail in every cell all at the same time which is not entirely realistic. To avoid this, a statistical distribution within the strength model can be applied to enable different areas of the material to behave slightly differently, as in reality due to uncertainties introduced within the manufacturing process. Likewise, a similar approach to the failure model also guarantees that cells containing the material fail at different times, representing the inclusion of a number of flaw sites within the material. This approach also has the benefit of enabling some form of Monte Carlo parameter / sensitivity analysis to be conducted if needed, although at a high computational cost.

Modelling the casing with such a stochastic approach, and placement of gauge points moving within the material would also enable tracking of the initial shockwave through the casing material, measurement of the bulk internal particle velocity, and tracking of internal stress relief waves as the fracture and fragmentation process proceeds. This would require a very fine mesh to give the resolution required, which would increase the computational burden.

Using an Eulerian mesh to model the detonation products, with a JWL equation of state, and the surrounding air would enable the flow of high pressure detonation products through any fractures modelled within the casing. Use of a Lagrangian mesh for the casing material would enable significant deformation of the casing to occur, including fracture and even the formation of discrete fragments; however some form of mesh management may be required to avoid run errors due to excessive mesh distortion or mesh entanglement. To enable the drive of the casing material from the internal pressure exerted from the detonation products a fully coupled Eulerian-Lagrangian model will be required with information being fed from the Eulerian mesh to the Lagrangian to enable casing motion, and similar information being fed back from the Lagrangian mesh to the Eulerian to update gas boundary positions, etc.

Obviously, the flow of gaseous detonation products through the developing fractures will be influenced by the fracture growth rate and the surface roughness within the fracture. The limitations of the surface within each fracture will depend on the through thickness mesh resolution used within the casing material as well as the mesh resolution used around the circumference of the casing cylinder. The higher the mesh resolution, the smaller any surface artefacts can exist within the model. To avoid the use of 3-dimensional mesh resolutions so small as to make the overall cell count prohibitively high for modelling the full lifecycle to discrete fragments in flight, the study of the effect of the surface condition on the gas flow through the fractures would be better studied in a separate series of more controlled models. These could be 3-dimensional, or 2-dimensional to enable higher resolution for the same overall number of cells, and could be used to determine the effect of surface features on the boundary layer and bulk gas flows. Aspects of the boundary layer flow may, however, be better studied using a more conventional computational fluid dynamics package, with turbulence models included.

As described earlier in Section 2.2, the fracture growth initially starts at one of the flaw sites and develops quickly. To capture the details of the fracture growth, the calculational timestep needs to be very small which links with the dimensions of the smallest cell size

within the calculational mesh.

Using these methods, a 3-dimensional model of the experimental setup will return general development of the casing fractures and associated fragmentation along with the mass flow of gaseous detonation products. Specific 2-dimensional, or targeted 3-dimensional, partial models will enable details of the effects of surface artefacts on the flow to be isolated and develop an understanding of the significance of different flow parameters.

The use of ANSYS AUTODYN will enable both 2-dimensional and 3-dimensional modelling with large cell domain numbers to be used; the computational run time required for each simulation will be dictated by the hardware available. At the time of the numerical phase of the research, computational hardware and remote access licencing issues denied the use of the full, commercially available version of the AUTODYN software. This, unfortunately, limited the research to using the student version of the ANSYS AUTODYN software, running on a Dell Precision M3800 laptop with 16 GB RAM installed.

The student version of AUTODYN has full functionality across all aspects including solvers, materials models, strength and failure models, however it is limited to a maximum of 32,000 cells per model. To maximise the available details within the developed model, it was run using 2D axial symmetry with an Eulerian solver for the gas flow region and appropriate boundary conditions to simulate inner surfaces of the developing crack, and the open expansion region external to the casing.

Given the limitation on the number of cells available within each model, it is necessary to determine the minimum number of cells required for a converged solution. To simplify the model used each model involved a static gap width which was varied between models. Each gap width was modelled against a variety of driver pressures.

A schematic diagram of the model used to calculate the flow properties within and external to the gap representing the crack in the casing is shown in Figure 4.1, with the green lines around the expansion region indicating the location of the Flow Out boundary condition used.

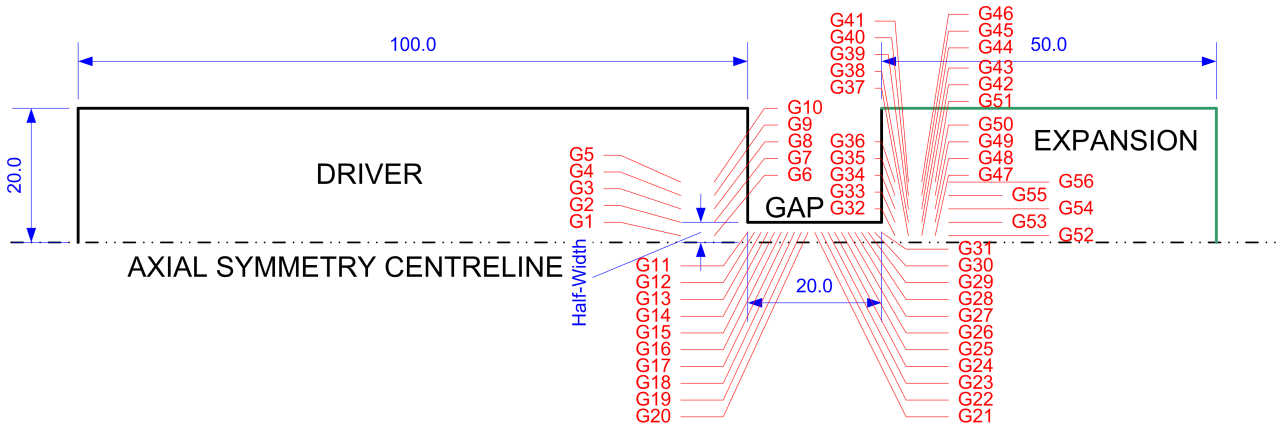


Figure 4.1: Schematic of Model Layout for Initial Numerical Modelling Conducted

4.1.1 Mesh Convergence

As mentioned above, before AUTODYN numerical modelling could be used to determine the flow within the casing crack and immediately external to the casing, any effects introduced by the generation of the model meshing had to be established. This was done by investigating the effects of four different mesh resolutions on an 18 bar high pressure air driver with 6 mm gap width and 20 mm gap length.

The high pressure air for the mesh convergence study driver used an arbitrary pressure of 18 bar which was kept constant across all mesh resolutions. It employed a simple ideal gas equation of state within the Eulerian solver, with a reference density of 1.225 kgm^{-3} and an adiabatic constant of 1.4.

From the isentropic flow equation

$$\frac{P}{P_0} = \left(\frac{\rho}{\rho_0}\right)^{\gamma} \tag{4.1}$$

it was possible to calculate the density of the air within the driver section at 18 bar as being 9.557 kgm^{-3}. It was then possible to calculate the specific internal energy of the driver section for inclusion within the AUTODYN model;

$$e = \frac{P}{\rho(\gamma - 1)} \tag{4.2}$$

which returned a specific internal energy of 470859 Jkg^{-1}.

As mentioned, four different mesh resolutions were tested to determine if convergence on a stable output could be achieved. The details of these meshes are summarised in Table 4.1 to Table 4.4. Each model was run on the same laptop to remove any potential platform vagaries.

SECTION	**I DIRECTION**	**J DIRECTION**	**TOTAL CELLS**
DRIVER	100 cells: RHS 10mm = 50 cells @ 0.2mm, remaining 90mm = 50 cells varying	100 cells: lower 5mm = 50 cells @ 0.1mm, remaining 15mm = 50 cells varying	10,000
GAP	200 cells @ 0.1mm	30 cells @ 0.1mm	6,000
EXPANSION	100 cells: LHS 10mm = 50 cells @ 0.2mm, remaining 40mm = 50 cells varying	100 cells: lower 5mm = 50 cells @ 0.1mm, remaining 15mm = 50 cells varying	10,000
TOTAL GEOMETRY			26,000

Table 4.1: High Resolution Mesh

SECTION	**I DIRECTION**	**J DIRECTION**	**TOTAL CELLS**
DRIVER	100 cells: RHS 10mm = 50 cells @ 0.2mm, remaining 90mm = 50 cells varying	75 cells: lower 5mm = 25 cells @ 0.2mm, remaining 15mm = 50 cells varying	7,500
GAP	100 cells @ 0.2mm	15 cells @ 0.2mm	1,500
EXPANSION	75 cells: LHS 10mm = 50 cells @ 0.2mm, remaining 40mm = 25 cells varying	75 cells: lower 5mm = 25 cells @ 0.2mm, remaining 15mm = 50 cells varying	5,625
TOTAL GEOMETRY			14,625

Table 4.2: Medium Resolution Mesh

Convergence of the results may be highlighted by comparing the sets of results from each of the four mesh resolutions modelled. The speed of the gas flow within the gap was chosen as the most relevant parameter, and was used as the output for comparison.

SECTION	I DIRECTION	J DIRECTION	TOTAL CELLS
DRIVER	90 cells: RHS 10mm = 40 cells @ 0.25mm, remaining 90mm = 50 cells varying	50 cells: lower 5mm = 20 cells @ 0.25mm, remaining 15mm = 30 cells varying	4,500
GAP	80 cells @ 0.25mm	12 cells @ 0.25mm	960
EXPANSION	60 cells: LHS 10mm = 40 cells @ 0.25mm, remaining 40mm = 20 cells varying	50 cells: lower 5mm = 20 cells @ 0.25mm, remaining 15mm = 30 cells varying	3,000
TOTAL GEOMETRY			8,460

Table 4.3: Low Resolution Mesh

SECTION	I DIRECTION	J DIRECTION	TOTAL CELLS
DRIVER	200 cells @ 0.5mm	40 cells @ 0.5mm	8,000
GAP	40 cells @ 0.5mm	6 cells @ 0.5mm	240
EXPANSION	100 cells @ 0.5mm	40 cells @ 0.5mm	4,000
TOTAL GEOMETRY			12,240

Table 4.4: Very Low Resolution Mesh

Given the number of numerical gauge points deployed within the gap and the number of resolution scenarios modelled, it was necessary to split the results across multiple graphs for clarity. The graphs can be seen in Figure 4.2 to Figure 4.6.

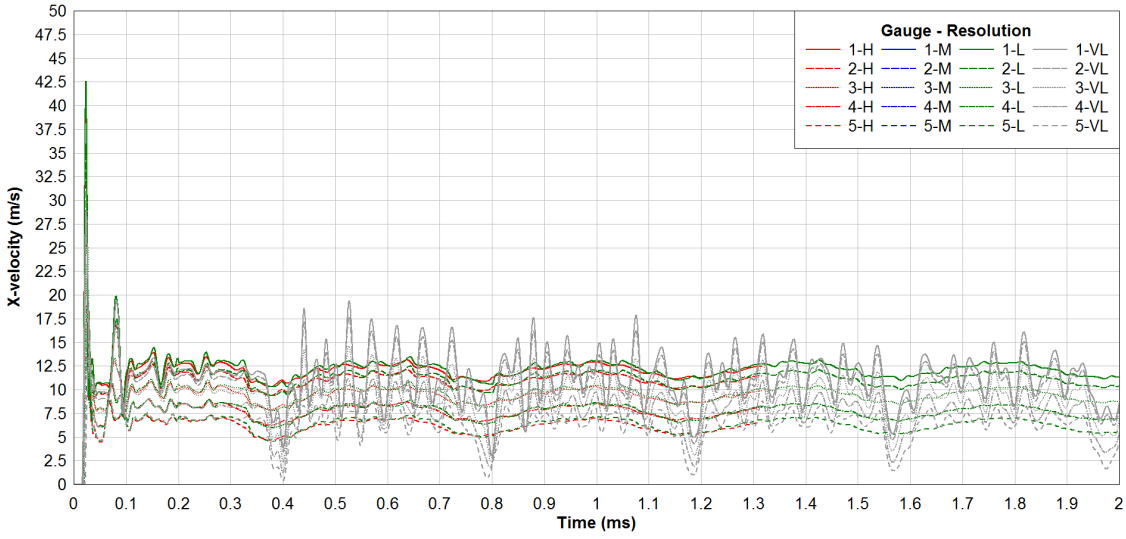


Figure 4.2: Mesh Resolution Study: Gauges 1 to 5, Flow Speed Output

Investigation of the actual numerical values returned by each mesh resolution showed

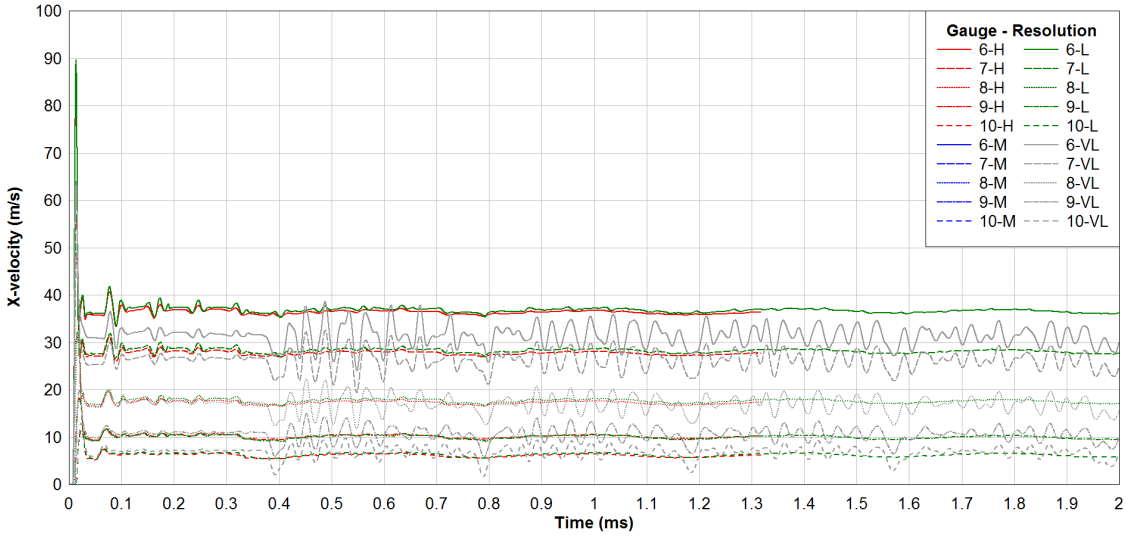


Figure 4.3: Mesh Resolution Study: Gauges 6 to 10, Flow Speed Output

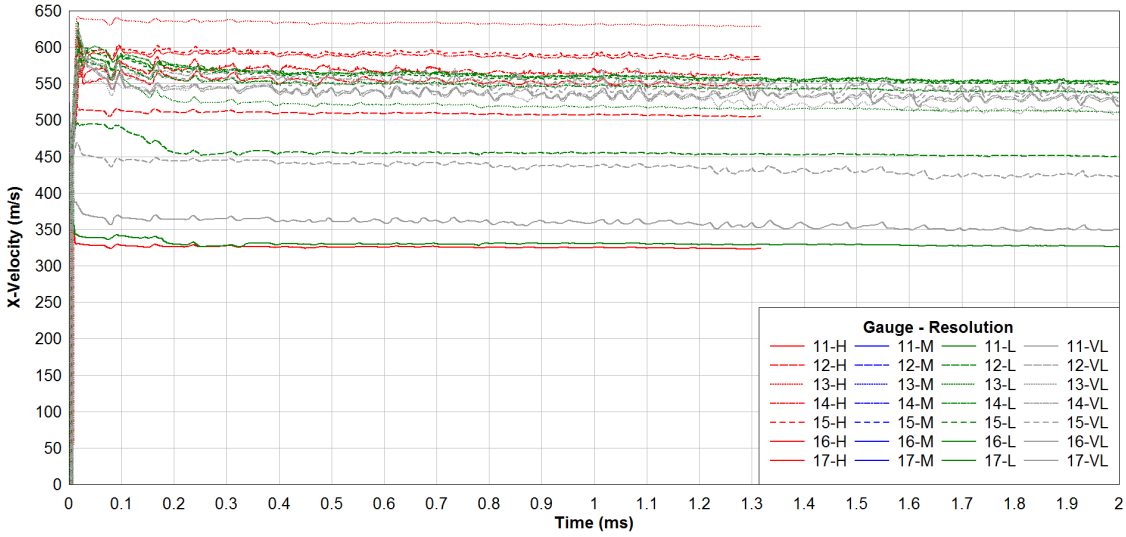


Figure 4.4: Mesh Resolution Study: Gauges 11 to 17, Flow Speed Output

very close agreement between the medium and low resolution cases, with the results for the medium mesh resolution (blue) lying coincident with the results for the low mesh resolution (green) within Figures 4.2 to 4.6; however the spread of results indicates complete convergence is not available at these mesh resolutions. This, coupled with the cell count limitation of the student version of the AUTODYN software, suggested it was reasonable to use the highest resolution of mesh for the detailed investigation of the flow.

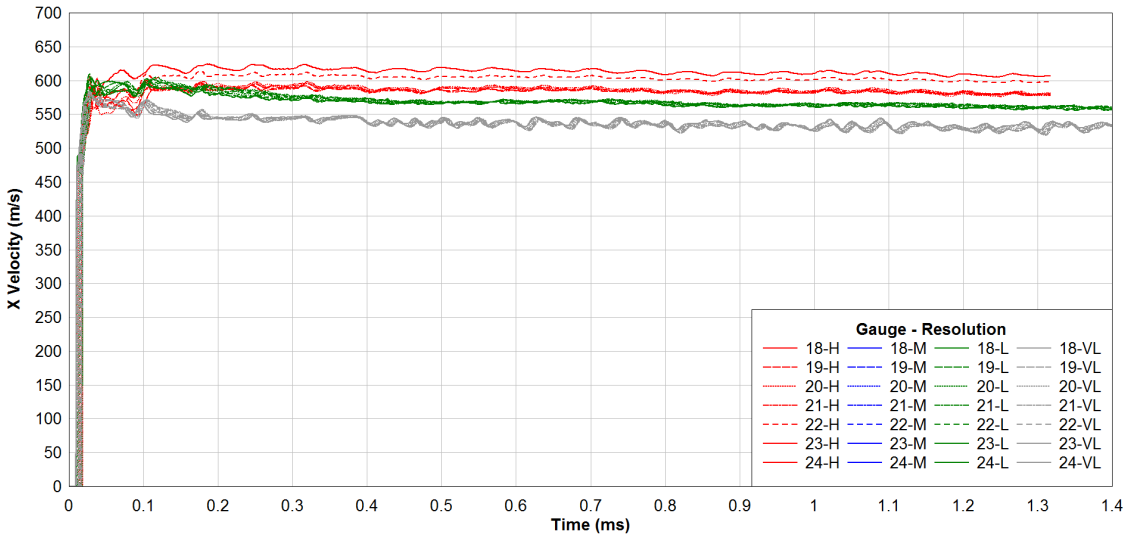


Figure 4.5: Mesh Resolution Study: Gauges 18 to 24, Flow Speed Output

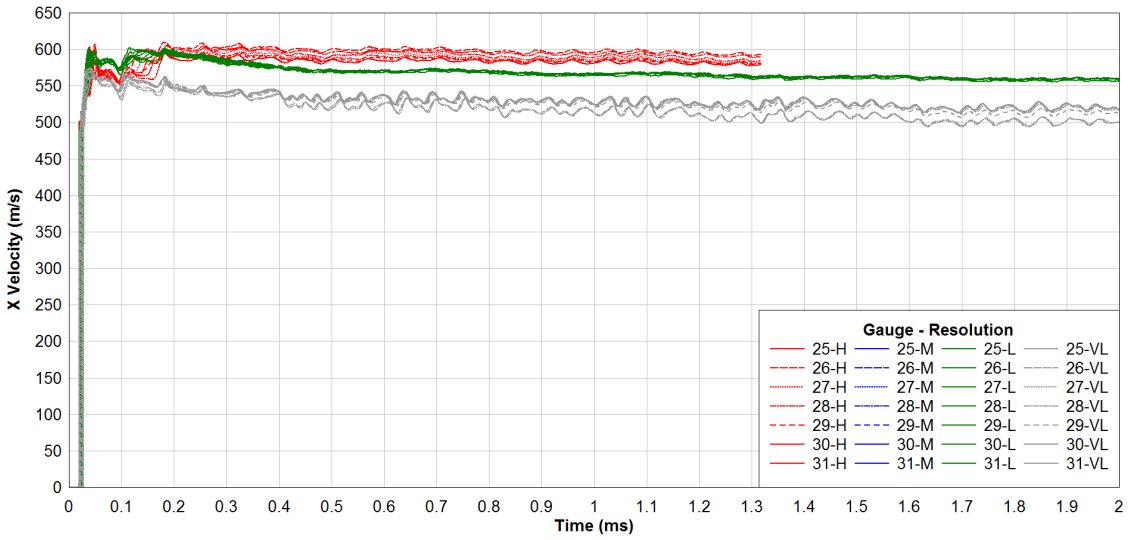


Figure 4.6: Mesh Resolution Study: Gauges 25 to 31, Flow Speed Output

4.1.2 Gas Expansion Flow Speed

As mentioned in the previous chapter, the developed MATLAB model returned values for the post fracture gas and casing speeds based on the general shock tube equations and the effects of a tail wind within a point mass model. The gas flow through the gap was based on the ideal nozzle flow assumption applied within a static fragment frame of reference which was translated to a general frame of reference by the simple summation with the fragment speed. The gas flow ahead of the fragment was based on the application of flow stream lines creating a non-physical shock tube immediately ahead of the fracture, such that the

shock tube equations could be applied to determine the flow speeds behind the initial shock wave and the expanding contact surface. The thickness of the casing was ignored in this simplistic model, with the non-physical shock tube extending an indeterminate length downstream of the fracture. Eventually the gas flow ahead of the fragment will expand such that the non-physical shock tube analogy is not applicable, with each non-physical shock tube having expanded in diameter to conjoin with its nearest neighbours.

From the MATLAB model it was found that the internal pressure of the gaseous detonation products within the cylinder at the point of rupture was approximately 460 bar. This was coupled with the results of the Explo5 calculation (Appendix B), Equation 4.1 and Equation 4.2 to estimate the density and specific energy of the detonation products at this point. This was used to develop a simple material model for the gaseous detonation products for inclusion within the driver section of the AUTODYN model.

To determine the applicability of the MATLAB model, the AUTODYN numerical model with a 1 mm gap opening was used, as this was the closest modelled scenario to that of a recently opened fracture. The AUTODYN model layout in Figure 4.1 uses a static frame of reference, with the gas flow speeds within the gap and immediately external to the casing being calculated. In order to avoid any potential issues with translating the AUTODYN model into a general frame of reference, a comparison of the gas flow speeds with those calculated by the MATLAB model, within the static frame of reference, was conducted.

Within Figure 4.7, G30 and G31 are the final two gauges within the gap whereas G32 and G37 are part of the line of gauges within the expansion zone running 1 mm from, and parallel to, the symmetry axis.

Details of the AUTODYN generated flow speeds are given in Table 4.5, which clearly shows the gas flow speed increasing with distance from the outer face. The values in Table 4.5 actually show the flow starts to accelerate before reaching the outer face of the gap, however this phenomenon is not included within the MATLAB model which has the gas

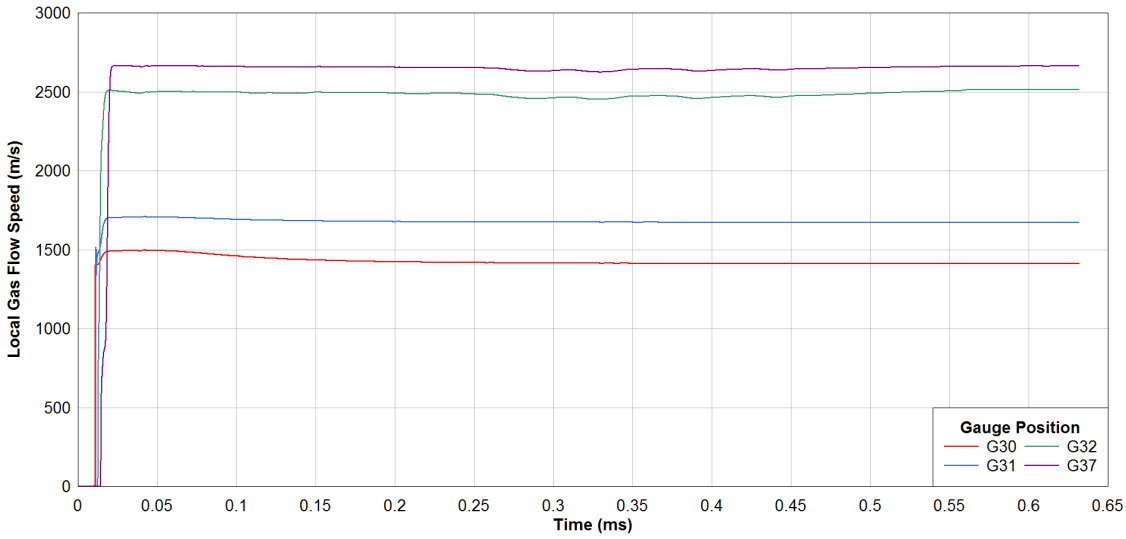


Figure 4.7: Gas Expansion Speed - AUTODYN modelling

flow within the gap limited to the local sonic speed for the full length of the gap.

GAUGE	**LOCATION**	**X mm** (from external face)	**Y mm** (from symmetry plane)	$V_{plateau}$ **mm/μs**
G30	GAP	-1.0	0.25	1.415
G31	GAP	0.0	0.25	1.675
G32	EXPANSION	2.0	1.0	2.487
G37	EXPANSION	4.0	1.0	2.653

Table 4.5: Gas Expansion Speeds

Using the output of the MATLAB model, with the time of rupture set to 20.9 μs as per the Foulness experiments, it is possible to conduct simple curve fits to derive the following relationships for the case expansion

$$r_{case}\ [mm] = \begin{cases} 0.0195t^2 + 1.726t - 0.9801 & \text{pre-rupture} \\ -0.0044t^2 + 2.58t - 9.053 & \text{post rupture} \end{cases} \tag{4.3}$$

and a similar quadratic curve fit for the detonation product gases post rupture

$$r_{gas}\ [mm] = -0.00632t^2 + 2.87t - 12.86 \tag{4.4}$$

Pre-rupture, the detonation product gases follow the same curve as the casing as no leakage can occur through the unfractured metal and it was assumed the gases remain in contact with the inner face giving internal pressure drive to the casing.

Differentiating the MATLAB expansion curves allowed simple speed-time curves to be generated. These curves are constrained to a simple linear fit, giving constant acceleration, as the original expansion curves were constrained to a quadratic fit.

$$\dot{r}\ [mm/\mu s] = \begin{cases} 0.039t + 1.726 & \text{case pre-rupture} \\ -0.0088t + 2.58 & \text{case post rupture} \\ -0.0126t + 2.87 & \text{gas post rupture} \end{cases} \tag{4.5}$$

Rearranging the gas post-rupture case within Equation 4.5 and substituting back into Equation 4.4 to eliminate t allowed a gas expansion curve to be generated, where $r_{gas} = f(\dot{r}_{gas})$

$$r_{gas} = -39.809\dot{r}_{gas}^2 + 0.723\dot{r}_{gas} + 312.964 \tag{4.6}$$

which was plotted against the AUTODYN generated points as per in Table 4.5. This comparison is shown in Figure 4.8.

Figure 4.8 could be interpreted as showing that although the MATLAB model grossly oversimplifies the situation, the two models appear to converge onto a common plateau speed. It should be noted however that the limited range of data from the AUTODYN model does not allow any confidence to be placed on the convergence.

It can be seen that using the current assumption of ideal nozzle flow linked to the general shock tube equations returns expansion curves within the MATLAB model such that further differentiation shows both the fragments and the expanding gases to be decelerating with time from the point of rupture.

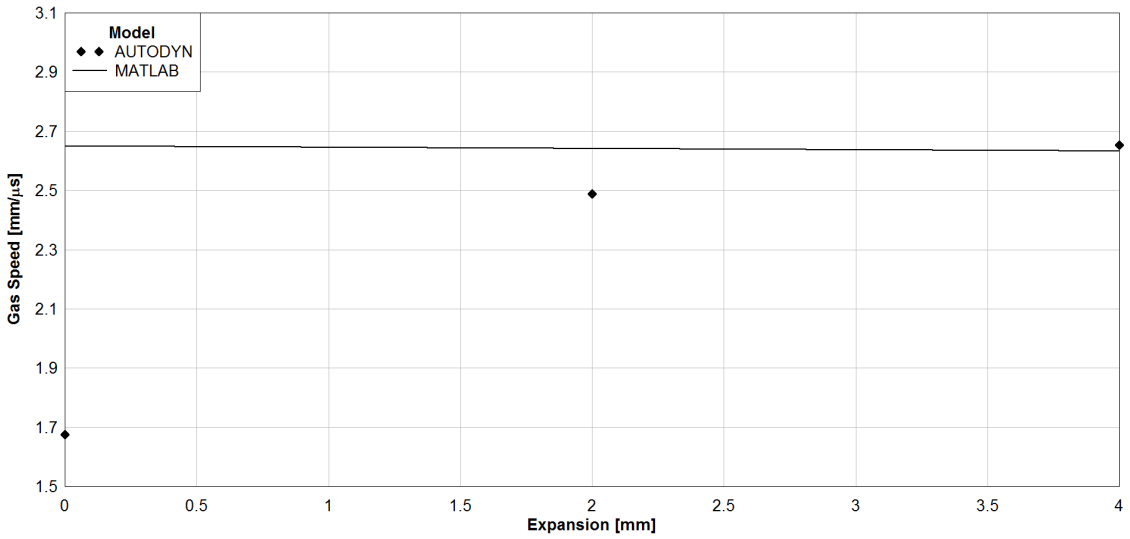


Figure 4.8: Comparison of Gas Expansion Speeds

A quick comparison of the second derivatives of the expansion curves

$$\ddot{r}\ [mm/\mu s] = \begin{cases} 0.039 & \text{case pre-rupture} \\ -0.0088 & \text{case post rupture} \\ -0.0126 & \text{gas post rupture} \end{cases} \tag{4.7}$$

confirms this and shows the gases to be slowing at a quicker rate than the fragments. This is to be expected, however the MATLAB model returns no evidence of the continued fragment acceleration immediately post rupture (and out to at least 6 ft) as indicated by the Foulness experimental data, which may be due to the oversimplification constraining the curve fits and driving a constant acceleration throughout the expansion. It may, however, be indicative that the MATLAB approach may not be applicable for the prediction of fragment speeds within the regime of interest.

As the MATLAB model assumes the maximum mass flow rate is generated using the ideal nozzle flow, and thus constrains the flow within the gap to be the local sonic value, use of the definition of sound speed

$$c = \sqrt{\frac{\gamma P}{\rho}} \tag{4.8}$$

returns the values shown in Figure 4.9

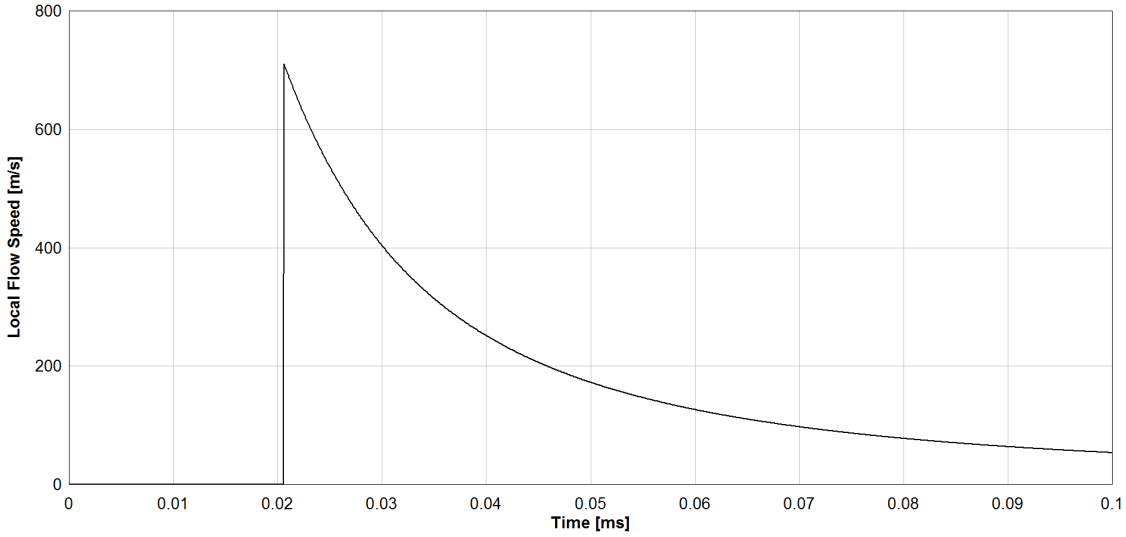


Figure 4.9: Local flow speed within gap - MATLAB model

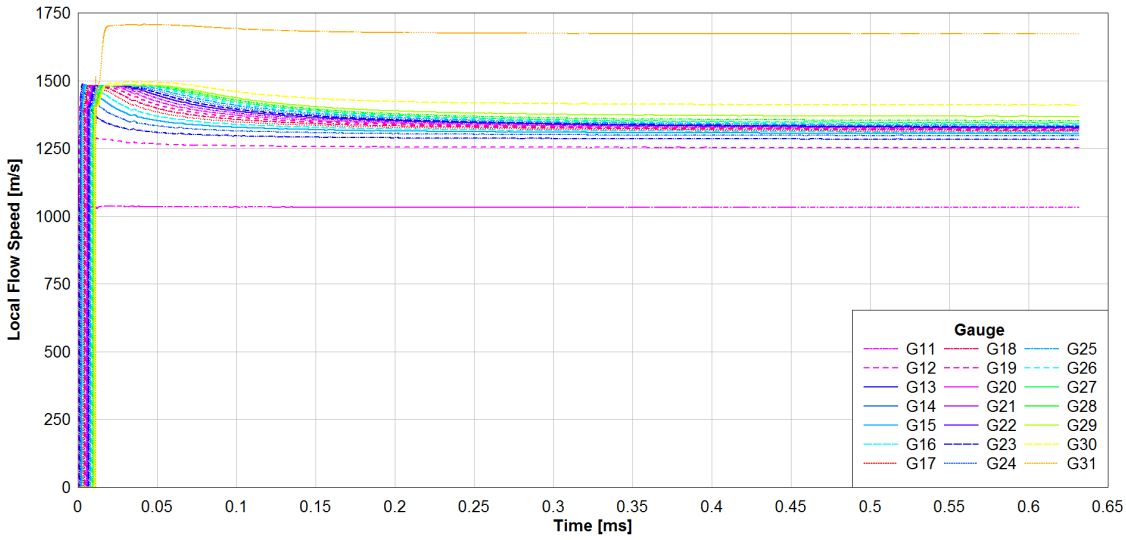


Figure 4.10: Local flow speed within gap - AUTODYN model

Comparing this with the flow speeds returned by multiple numerical gauge points along the gap length within the AUTODYN modelling, as shown in Figure 4.10, it can be seen that there is a dramatic difference between the two Figures. The AUTODYN modelling returns an unconstrained flow speed showing that, although a slight increase in speed can be expected along the length of the gap (from approximately 1250 ms^{-1} to 1400 ms^{-1}), the overall trend is reasonably consistent along the length with the flow being almost twice the speed to that predicted using the MATLAB model. Taking the local pressure and density values calculated during the AUTODYN modelling allowed the

variation of Mach number along the gap length to be developed. This is shown in Figure 4.11.

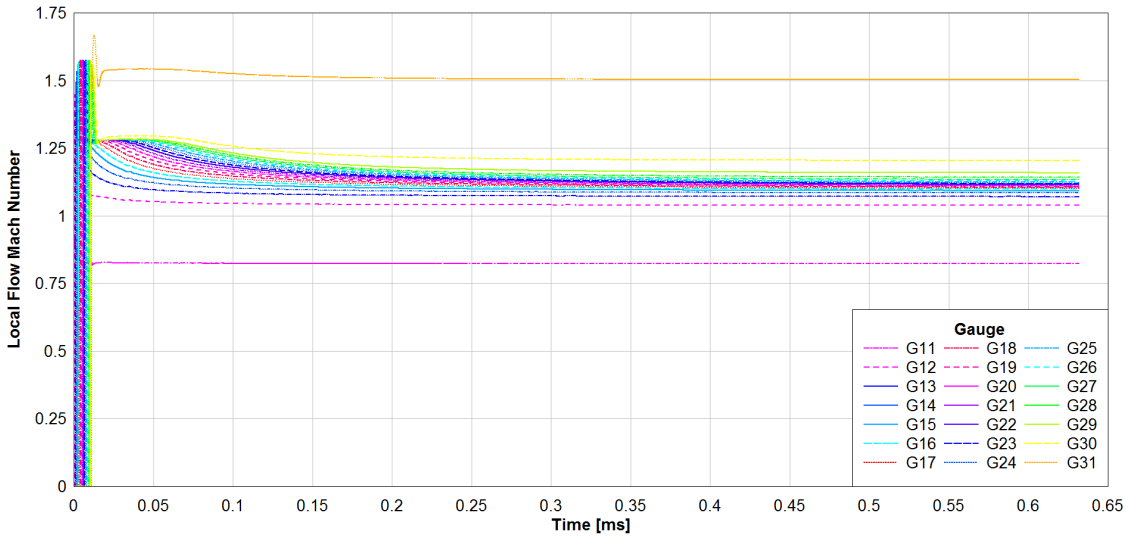


Figure 4.11: Local flow Mach number within gap - AUTODYN model

Gauge 31 sits level with the outer face of the gap and both the local flow speed and Mach number for this gauge can be seen to be higher than the values returned for the other gauge points within the gap (especially those for Gauge 11 which sits at the inner face of the gap and sees subsonic flow). The increased flow speed returned by Gauge 31 is shown within Figure 4.7 and also Table 4.5, which indicates the start of the flow expansion at the outer face of the gap. Figure 4.12 shows this flow expansion in terms of Mach number. Again G30 and G31 are the final two gauges within the opening whilst G32 and G37 are part of the line of gauges within the expansion region, being 2 mm and 4 mm from the outer face respectively.

From this it can be seen that although the difference in local flow speeds between the models is of the order of a factor of two, the difference in flow Mach numbers is not. However, it can be seen that the Mach numbers generated by the AUTODYN modelling are generally greater than unity for the flow within the gap. This suggests the fundamental assumption of the flow being constrained to the local sonic speed appears to be unjustified.

The evidence generated here and seen within the AUTODYN modelling does not fit with the application of the ideal nozzle flow for the escape of expanding gaseous products

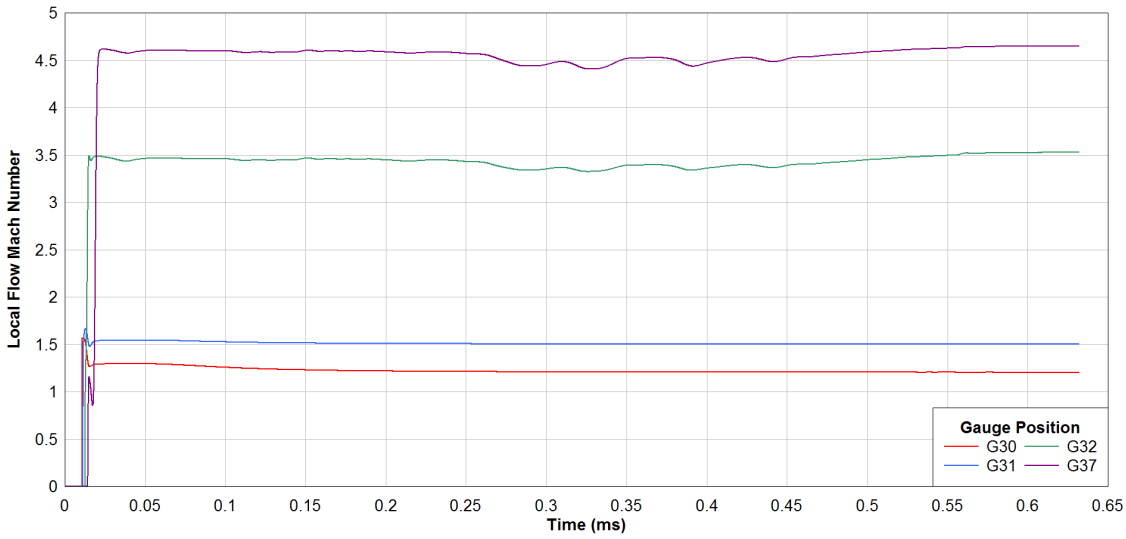


Figure 4.12: Gas Expansion Mach Numbers - AUTODYN Modelling

through cracks within the casing. It was for this reason that the scope of the research hypothesis was changed, as mentioned previously in Section 3.2.4. The narrowed scope of the research concentrates on the flow characteristics of high pressure gas escaping from narrow through thickness openings and the consequences for the range of applicability of the current accepted model assumption.

In order to develop the hypothesis along a combined numerical and experimental route, it was necessary to reflect the model geometry in any potential physical experiments. Use of the Centre for Blast Injury Studies (CBIS) shock tube gave an ideal match to the axial symmetry employed by the AUTODYN modelling, however it requires the use of high pressure air (or helium) up to a maximum driver pressure of 18 bar to be used and would thus require the output of the numerical modelling to include a comparison of flow properties within the gap for scenarios driven by both detonation products at 460 bar and air at a range of driver pressures below the operating limit of the CBIS shock tube.

4.2 Mach Number Determination for Flow within Narrow Openings

The escape of high pressure gas through narrow openings is a complex scenario with many inter-related aspects which may be extremely difficult to investigate independently. Indeed the opening of the vent width will enable an increase in mass flow rate to be generated which will, in turn, increase the reduction of driver pressure gas mass and thus driver pressure for a static volume. At this stage it is unclear as to whether conditions may exist so that the flow aerodynamically chokes within the venting gap at some time, thus limiting the upper flow rate to Mach 1.0, or whether the flow is free to reach supersonic levels throughout the fracture process. Should the flow be unchoked, there may be a fine balance between the effects of increased gap width and the subsequent reduction of driver pressure from the increased mass flow rate, and the effects of this on the local flow are to be determined.

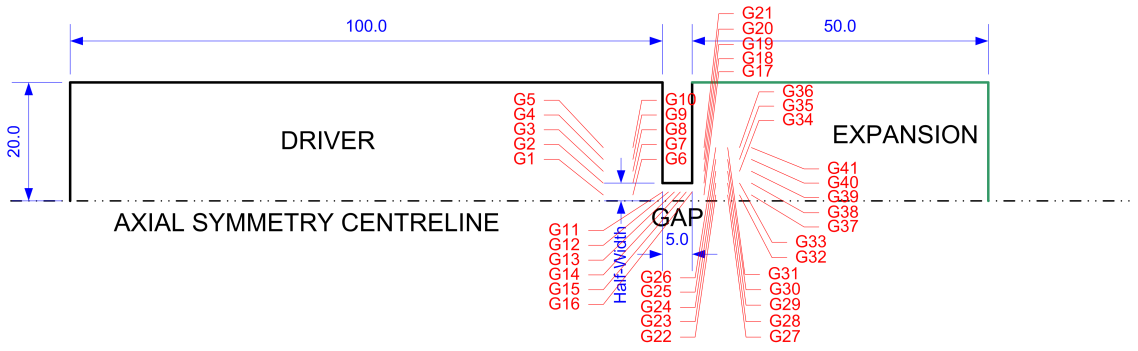
Although the majority of weapon casing thicknesses are not too dissimilar, it is also necessary to determine the effects on the flow of changing the opening length through which the gas flows. Changes in the opening length may lead to the inability of the flow to generate stable conditions, or may affect the flow by increasing the significance of any edge effects that may propagate from the external free edges of the gap.

The results of the numerical modelling were used to investigate the effects of the driver pressure, the opening width and the opening width to length (casing thickness) ratios, which are described in the following sections.

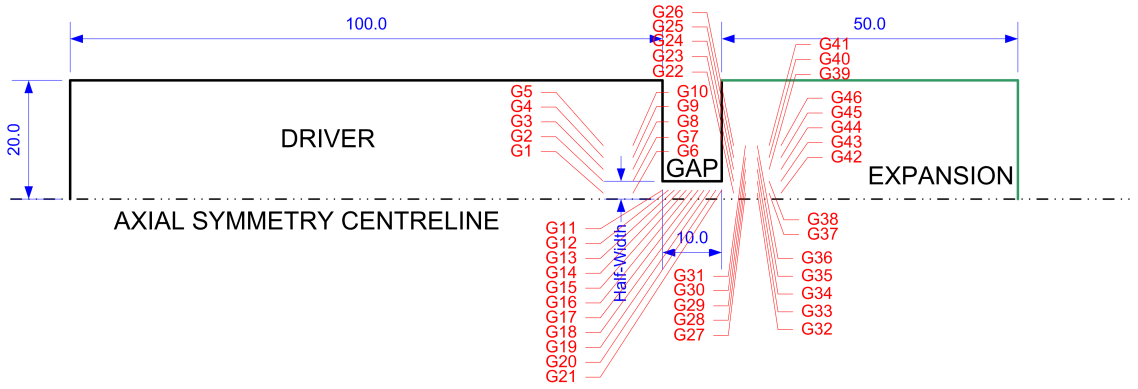
To simplify the approach such that an experimental characterisation of the flow could be determined, it was necessary to model the dynamically expanding crack width as a series of static openings. The models used the same layout as shown in Figure 4.1; however to investigate any potential effects due to the gap length to width ratio it was necessary to repeat some of the modelling with different gap lengths. The gap lengths chosen were

5 mm and 10 mm, which would supplement the existing 20 mm gap length numerical data such that it is possible to compare scenarios with physically different gap lengths and widths, but identical length to width ratios.

The model geometry and gauge locations for this supplementary investigation are shown in Figure 4.13. The green walls of the Expansion Section again signifies the use of flow out boundaries to simulate the laboratory beyond the confines of the shock tube end plate used in the experimental campaign.



A:5 mm gap length



B:10 mm gap length

Figure 4.13: Gap Length to Gap Width Ratio Effects Model Geometry

As mentioned previously, it was necessary to model scenarios using driver pressures that were both lower and higher than the maximum operating pressure of the experimental shock tube to be used. The development of a novel diagnostic capability was required to enable measurement of the stagnation pressure within the venting flow, and this will be reported fully within the Experimental Flow Determination chapter of this thesis; however, a scenario was required to enable direct comparison of the experimental and

numerical results. It was therefore necessary to model one scenario at a driver pressure of 10 bar, corresponding to the maximum pressure measurable by the novel diagnostic, whilst the other driver pressures were more arbitrary and chosen as 18 bar (maximum operating pressure of the Centre for Blast Injury Studies shock tube), 50 bar and 200 bar.

Each modelled scenario returned time based data for several key flow parameters at each gauge location; using the parameters of absolute flow velocity and local material sonic velocity (based on the local fluid pressure and density), it was straightforward to convert the data recorded into Mach number variation with time for each gauge point within each modelled scenario. As with most numerical investigations, it was possible to generate huge numbers of data traces which could quickly become unmanageable. Each model included data points within the driver and expansion sections of the model geometry, although these were mainly used as a global check of the repeatability of the models across each scenario. For this section of the numerical analysis, it is purely the gauge points within the gap section of each scenario that are of interest. Even limiting the data recorded to that within the venting gap, still returned in excess of 900 individual gauge location traces which needed to be managed such that the data could be presented in a reasonable fashion. The data was grouped by modelled scenario such that each gauge location trace was grouped by driver pressure, gap width and gap length.

This returned Local Flow Mach Number against Time plots as shown in Figure 4.14 to Figure 4.19, for the case with 10 bar driver pressure, 20 mm gap length and gap widths of 1 mm to 6 mm respectively. Similar plots were produced for driver pressures of 18 bar, 50 bar and 200 bar which are included in Appendix C for completeness, but are not be reproduced within the main text of the thesis.

To enable the data to be presented in an understandable format, it was necessary to conduct further data processing. Inspection of the graphs in Figure 4.14 to Figure 4.19, and within Appendix C, shows the data for each scenario to demonstrate some complex early time behaviour which is probably due to turbulent features in the early time flow before the flow Mach numbers appear to stabilise and become relatively time-

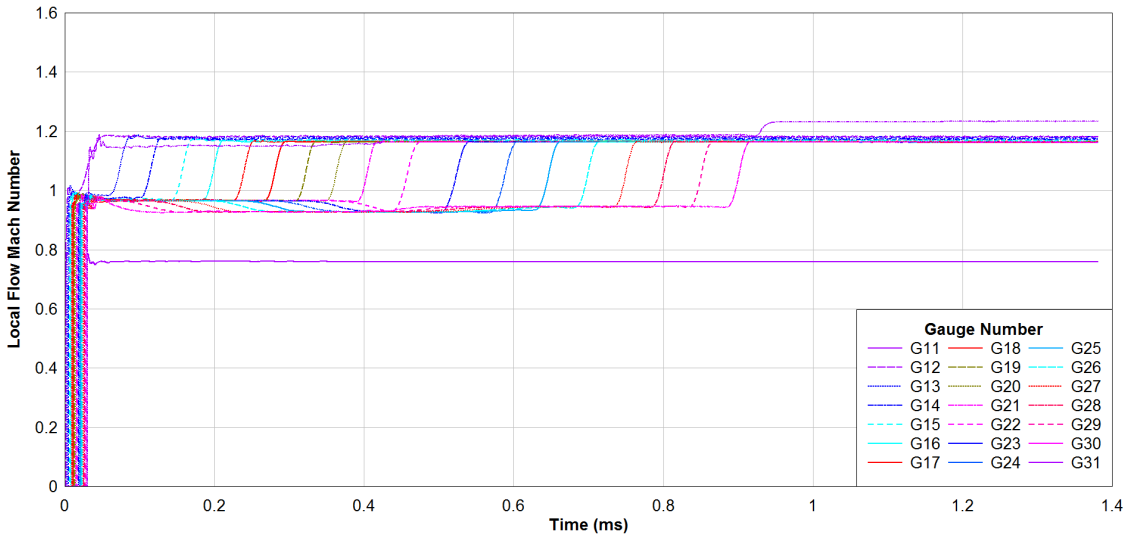


Figure 4.14: Flow Mach Number for 10 bar Driver Pressure, 20 mm gap length, 1 mm gap width

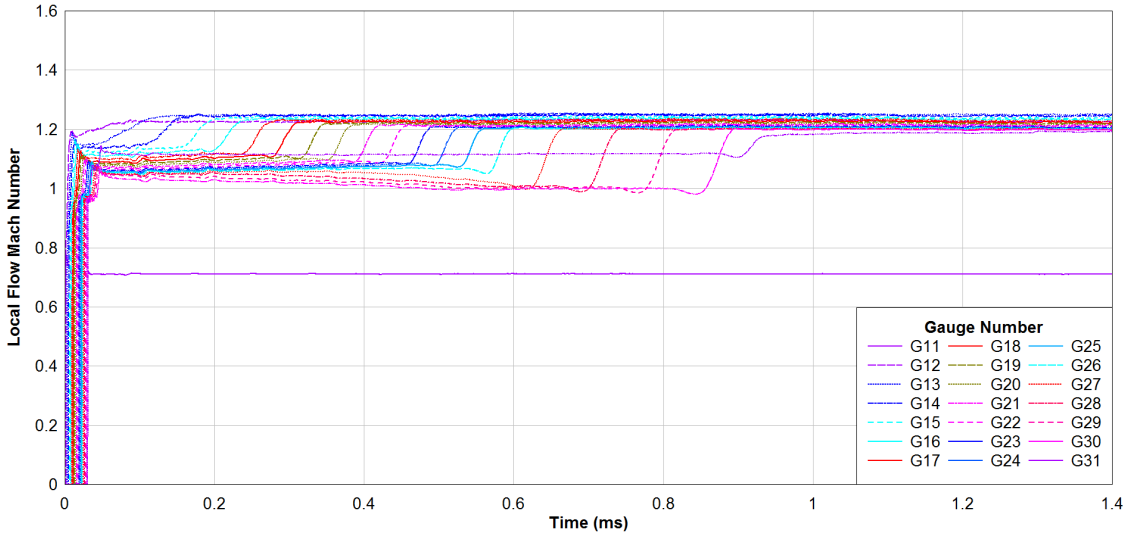


Figure 4.15: Flow Mach Number for 10 bar Driver Pressure, 20 mm gap length, 2 mm gap width

independent. Given the expected differences in measurement timescales between the numerical modelling and the shock tube experiments conducted, this very early complex behaviour was not expected to have any implications on the experimental results and was discounted at this stage of the research. A comparison of the results was made such that general flow regimes could be determined for each gap. For this reason, it was reasonable to generate a time averaged flow Mach number from within the plateau region exhibited in each case.

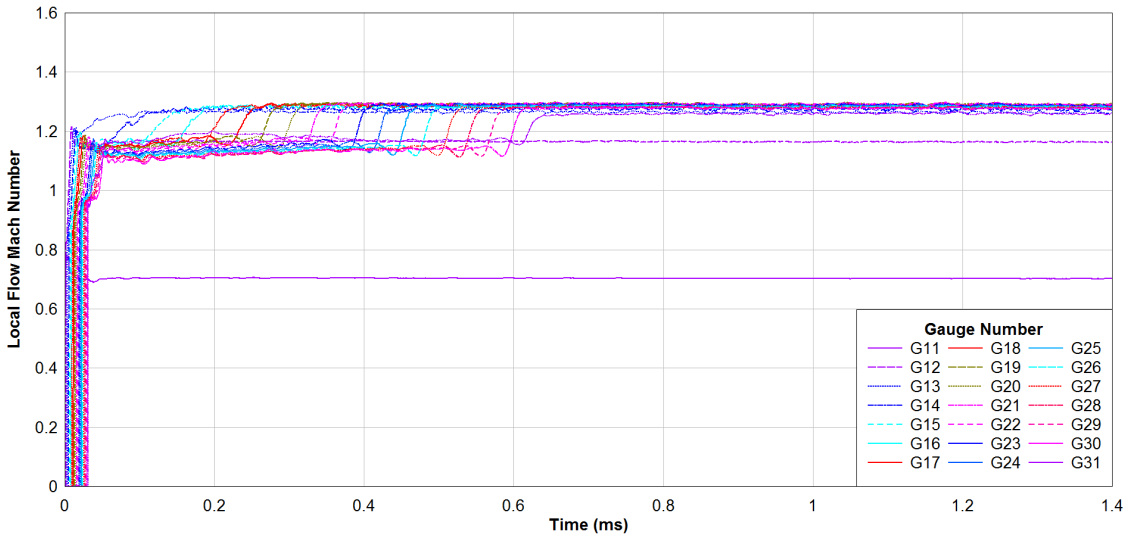


Figure 4.16: Flow Mach Number for 10 bar Driver Pressure, 20 mm gap length, 3 mm gap width

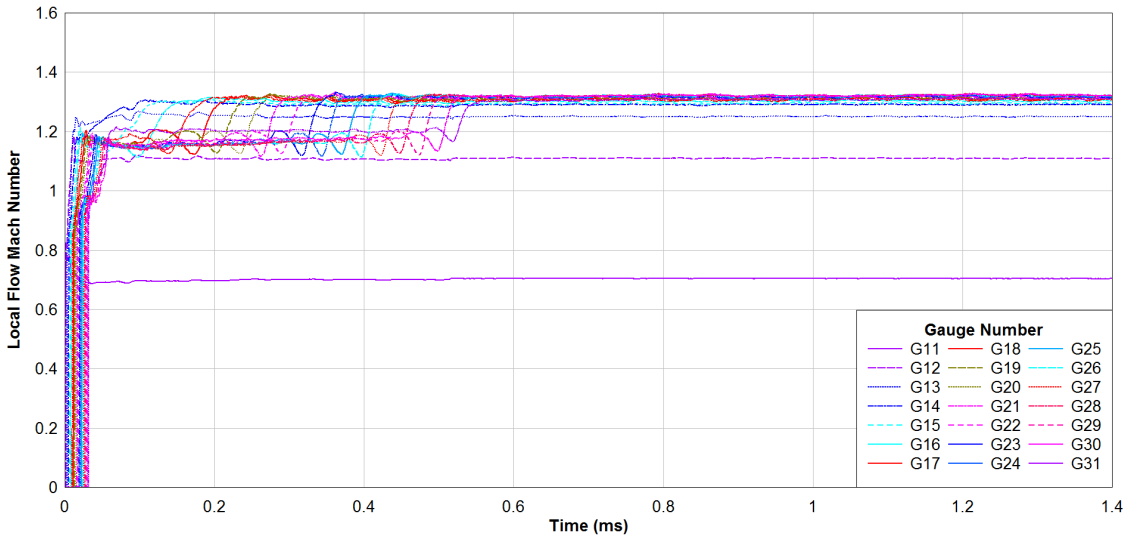


Figure 4.17: Flow Mach Number for 10 bar Driver Pressure, 20 mm gap length, 4 mm gap width

The time averaged flow for the 10 bar driver pressure case is shown in Figure 4.20, which clearly shows a gap width effect; however, this will be discussed further in the coming sections.

To enable reasonable data recovery, the experimental campaign within this research needed to be conducted using no greater than 10 bar driver pressure, coupled with a gap width and length of 6 mm and 20 mm respectively. The trace within Figure 4.20 corresponding to this case shows the local flow Mach number to take a short distance

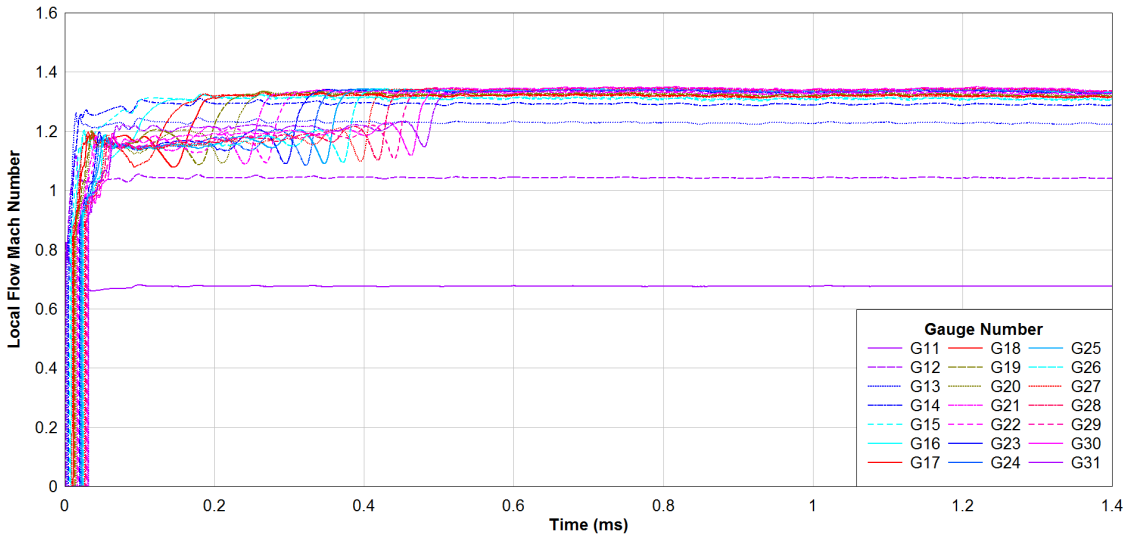


Figure 4.18: Flow Mach Number for 10 bar Driver Pressure, 20 mm gap length, 5 mm gap width

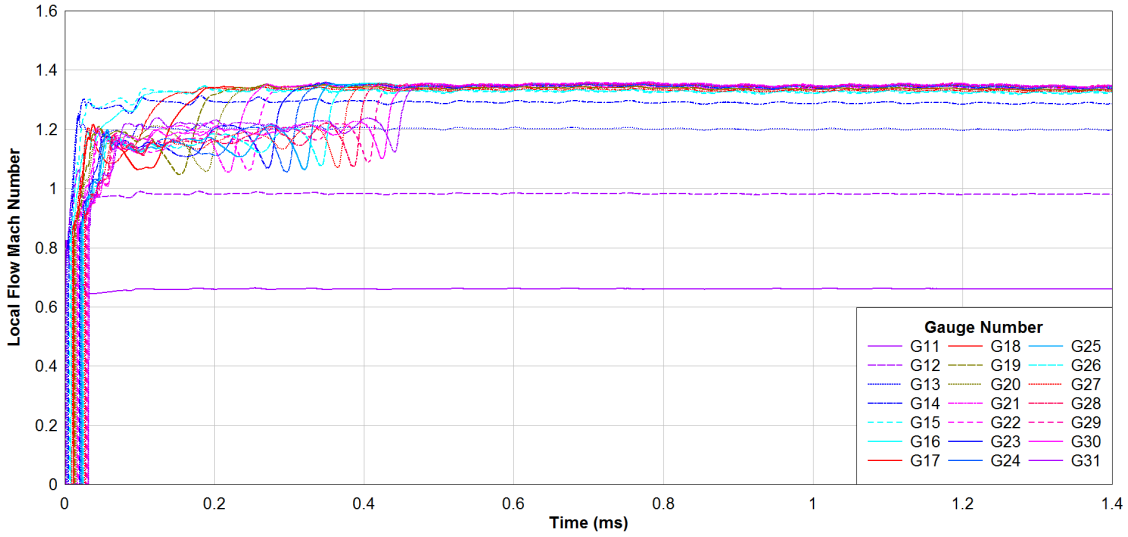


Figure 4.19: Flow Mach Number for 10 bar Driver Pressure, 20 mm gap length, 6 mm gap width

to fully accelerate up to a steady state final Mach number in the region of Mach 1.3. This particular numerical case was compared to the experimental campaign results, and is discussed in a later section.

Should it be necessary to experimentally determine the effects of the early time complex flow behaviour, this should be conducted outside the bounds of this research thesis.

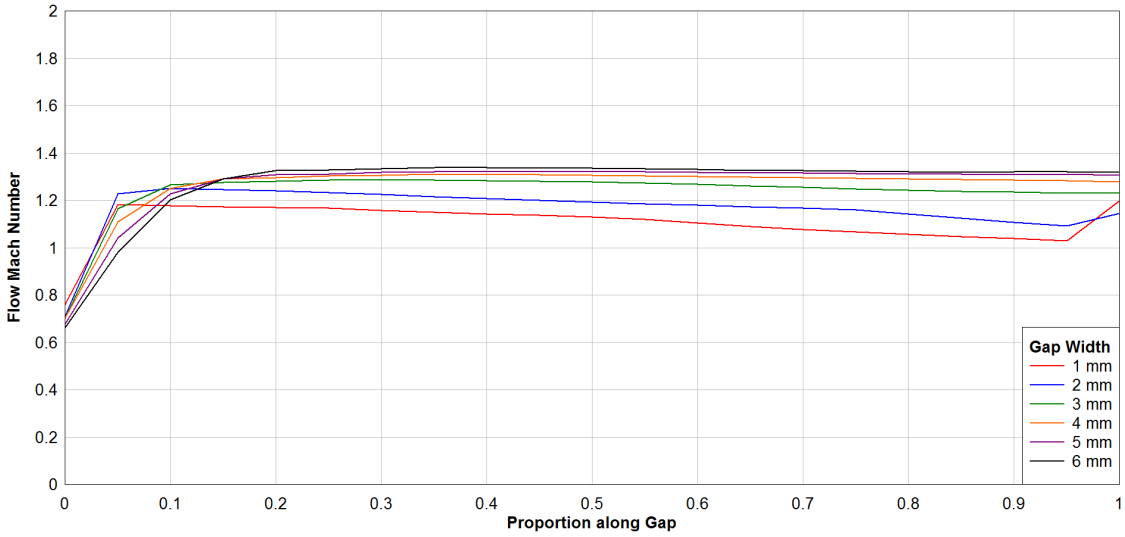


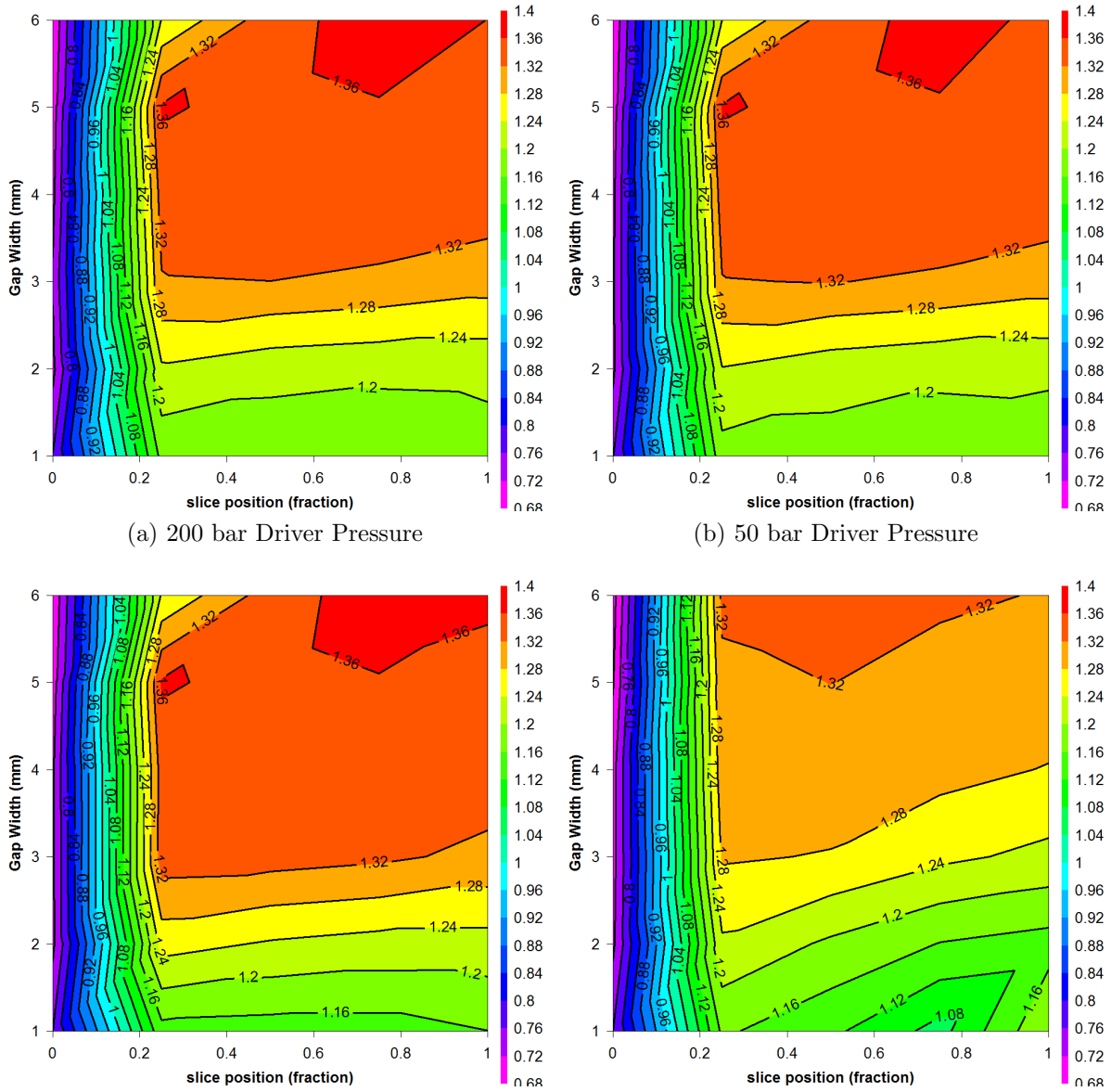
Figure 4.20: Flow Mach Number variation along Gap Length for 10 bar Driver Pressure

4.2.1 Effect of Opening Size

It is reasonable to postulate that any variation in gap width, through which the gas vents, will have a large effect on the flow speed of the venting gas. To investigate any effects of the gap opening width, it was necessary to ensure all other parameters were kept invariant; although it was possible to combine the results of several independent analyses, plotted in Appendix C, into surface plots as seen in Figure 4.21.

Although only one gap length scenario is included, from Figure 4.21 it can be seen that for each driver pressure case the gap width has no effect on the local flow Mach number for the initial quarter of the gap length. This is signified by the vertical iso-Mach lines indicating that any change in gap width has no visible effect on the flow Mach number at a given location. Closer inspection of the initial quarter of the gap length, from slice position 0 to 0.25, reveals that the closeness of the iso-Mach lines shows the flow number is increasing rapidly along this section of the vent. The rise is slightly less rapid in the 10 bar driver pressure case than the others, with the 10 bar case reaching approximately Mach 1.28 compared with Mach 1.32 to Mach 1.34 for the others.

Beyond the initial quarter of the gap length it can be seen that for all the driver pressure cases, except the 10 bar case, the slice position has very little effect. At this



(a) 200 bar Driver Pressure

(b) 50 bar Driver Pressure

(c) 18 bar Driver Pressure

(d) 10 bar Driver Pressure

Figure 4.21: Effect of Gap Width on Local Flow Mach Number along Gap Length

stage it is the gap width which is the driving factor for change in flow Mach number up to a gap width of 3 mm. Gap widths greater than 3 mm seem to exhibit fairly stable flow Mach numbers with the exception of a couple of high flow rate areas in the 5 mm to 6 mm gap range. The angle of the iso-Mach lines in the 10 bar driver pressure case show that even for the slice positions further downstream into the gap, the position still has some influence over the flow as well as the gap width effect similar to the other driver pressures.

It would appear that for high pressure drivers exhibited within a weapon scenario the

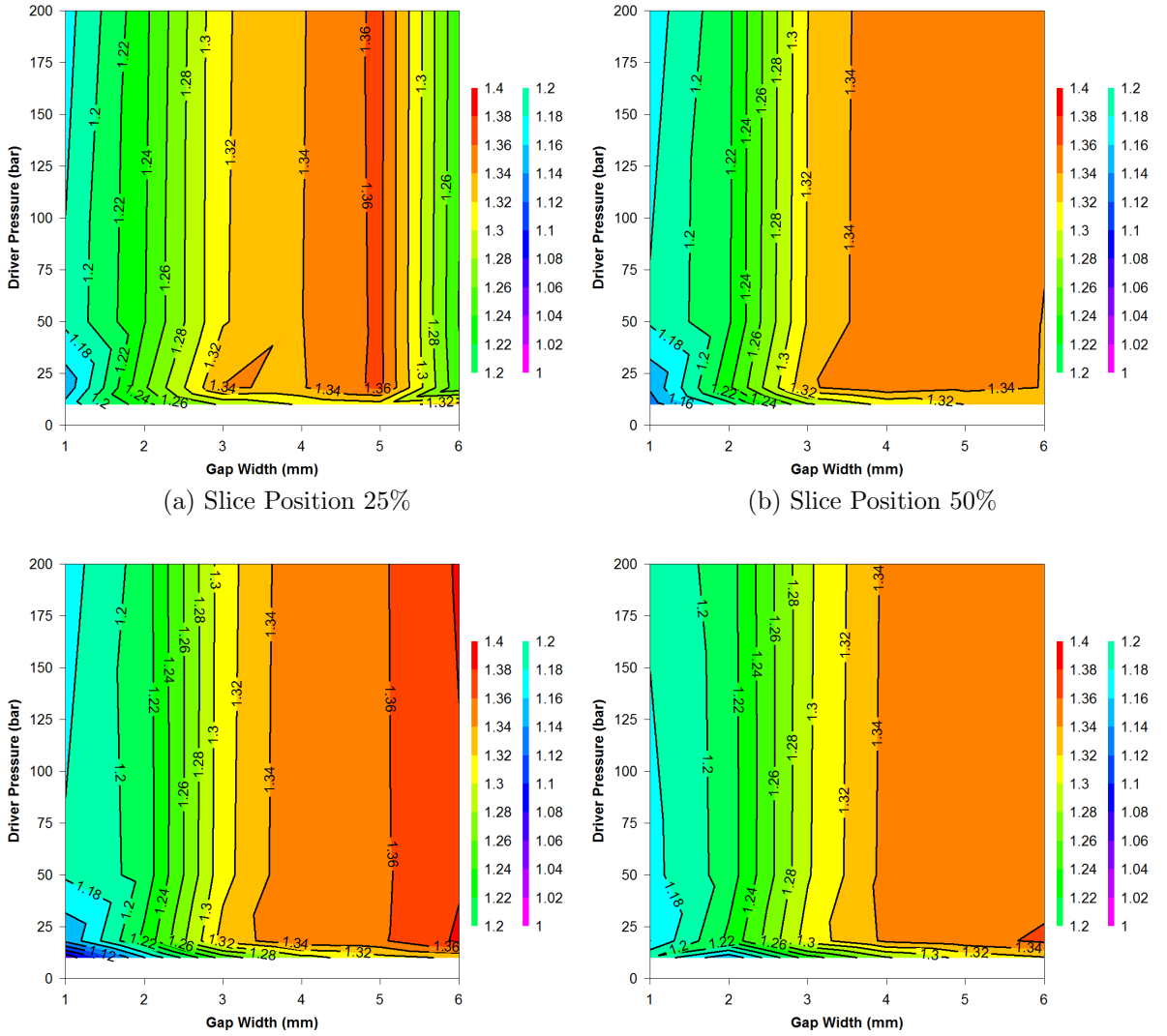
flow Mach number would be fairly stable along the length of the gap (through casing thickness) once beyond the initial inner quarter of the thickness. The expanding gap width would lead to an increase in Mach number up to a maximum value slightly over Mach 1.3; some local hotspots, however, may exhibit higher Mach number flow as the gap increases.

4.2.2 Effect of Shock Tube Driver Pressure

Initially the parameter with greatest influence on the flow within the gap could be hypothesised to be the driver pressure as, assuming the flow does not aerodynamically choke within the gap, it is reasonable to estimate that a greater driver pressure could produce an increased flow speed within the venting gap.

Plots of the derived time averaged flow Mach number against the variation in driver pressure are given in Appendix C; however this produced data in a format which made it difficult to determine the effect without looking across each gap width. To enable a more general effect of varying the driver pressure to be determined, a series of surface plots have been developed as shown in Figure 4.22.

Although Figure 4.22 essentially reports the same data as Figure 4.21, it does so in such a way as to show that, except for relatively low driver pressures (*i.e.* below 50 bar), the driver pressure has very little effect on the flow Mach number reached. Again, as mentioned in the previous section, an increase in the flow Mach number for larger opening values at a position of approximately 75% along the gap length can be seen. This is echoed by a similar feature in the graph for 25% gap length, however in this case the flow Mach number peaks at a gap width of approximately 5 mm before reducing as the gap width approaches 6 mm. This may be an indication that for gaps greater than 6 mm the postulated venting phenomena may not wholly apply with the flow in the gap eventually becoming subsonic as the gap continues to widen to values beyond those of interest within this research thesis.



(a) Slice Position 25%

(b) Slice Position 50%

(c) Slice Position 75%

(d) Slice Position 100%

Figure 4.22: Effect of Gap Width on Local Flow Mach Number

4.2.3 Effect of Opening Size to Vent Length ratio

Having determined any effect on the flow Mach number for changes in the gap width and driver pressures, given a single gap length scenario, it was necessary to investigate the effect of the gap length or the ratio of the gap length to the gap width on the flow Mach number. For this study the driver pressure was arbitrarily set at 18 bar. The data is given in Appendix C, with a summary surface plot presented in Figure 4.23.

Looking across all the slice proportions with Figure 4.23, the flow at the input opening slice position fraction 0.0 shows a wholly subsonic flow regardless of gap width or gap

length. Apart from some deviation within the range of gap widths between 2 mm and 4 mm, there appears to be no effect of changing the gap length on the flow Mach number. The horizontal iso-Mach lines indicate the gap width on the ordinate axis as the major effector on the flow Mach number.

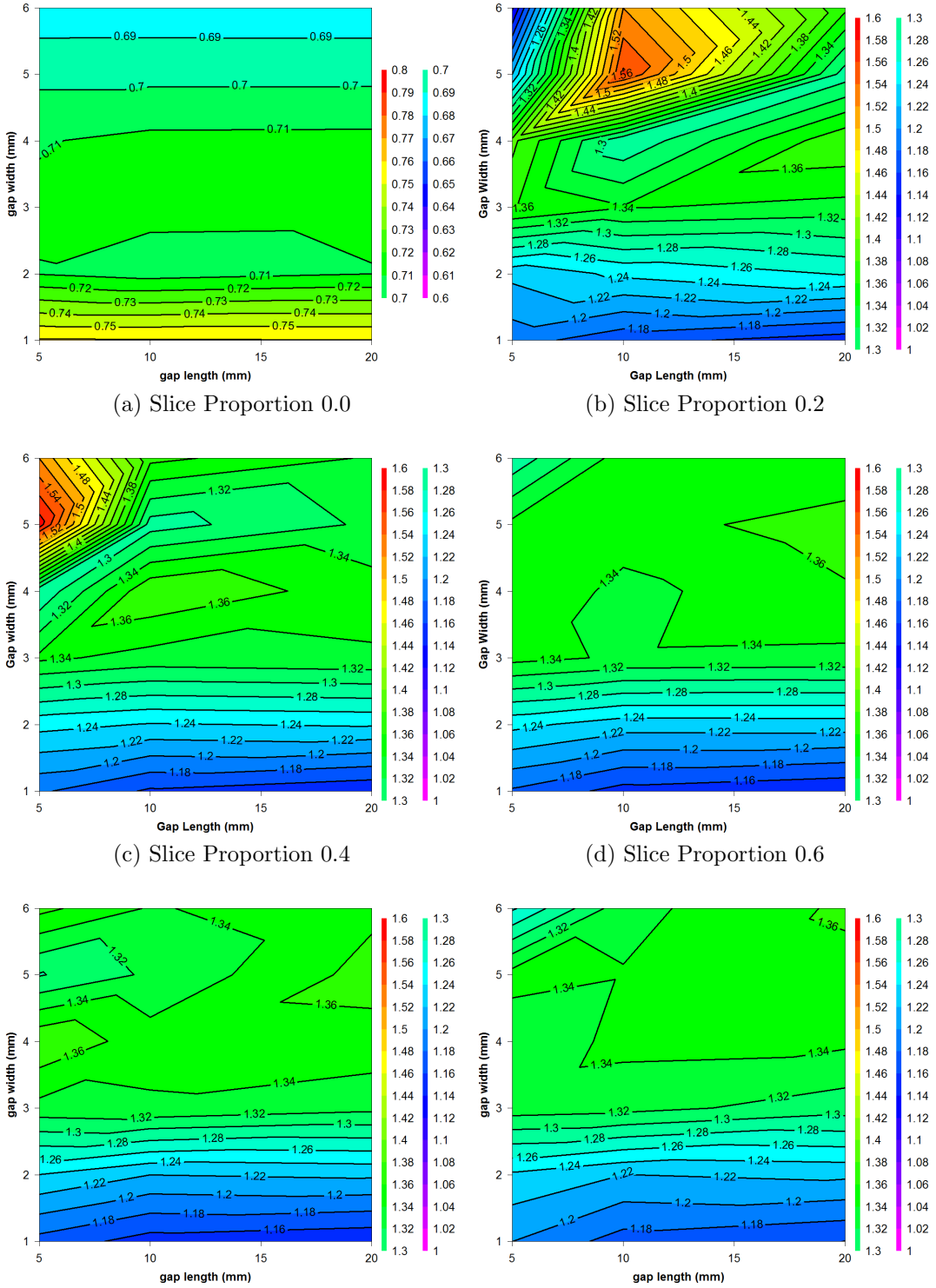
From the remaining slice proportions in Figure 4.23, it can be seen that for a gap width less than 3 mm there is no evident change in flow Mach number for a change in gap length; again as indicated by horizontal iso-Mach lines. For slice position fractions 0.2 and above it is clear that increasing the gap width to 3 mm shows an increase in flow Mach number up to approximately Mach 1.34. Gap widths greater than 3 mm show a much slower increase in flow Mach number with gap width and indicate the development of an effect on the flow Mach number from a change in gap length. This is signified by the angled iso-Mach lines. For slice positions towards the inner half of the gap length (slice position fractions 0.2 and 0.4) it can be seen that more complex flow behaviours appear, signified by the iso-Mach line structure.

4.2.4 Global Flow Mach Number

Taking the data processing a step further it is possible to generate a single plot showing the global flow Mach number, where the flow shown in Figure 4.20 and corresponding analysis for higher driver pressure cases, has been averaged along the length of the gap.

Doing this gives a plot of the global flow Mach number against gap width, for a 20 mm gap length, as shown in Figure 4.24. It can be seen that the simplified global flow appears to be relatively independent of driver pressure for all cases modelled except the 10 bar driver pressure case, which shadows the trends shown by the other curves but at a consistently lower Mach number.

The reason for this departure of the 10 bar driver pressure case is not fully understood at this time, but a reasonable comparison of the numerical and experimental results with a 10 bar driver pressure will give confidence that the numerical results for the higher



(a) Slice Proportion 0.0

(b) Slice Proportion 0.2

(c) Slice Proportion 0.4

(d) Slice Proportion 0.6

(e) Slice Proportion 0.8

(f) Slice Proportion 1.0

Figure 4.23: Effect of Gap Width to Length Ratio on Local Flow Mach Number

driver pressures give usable estimates of the true flow. With this in mind, it appears that any flow through the widening cracks within an expanding weapon casing would remain supersonic well into the expansion and formation of discrete fragments.

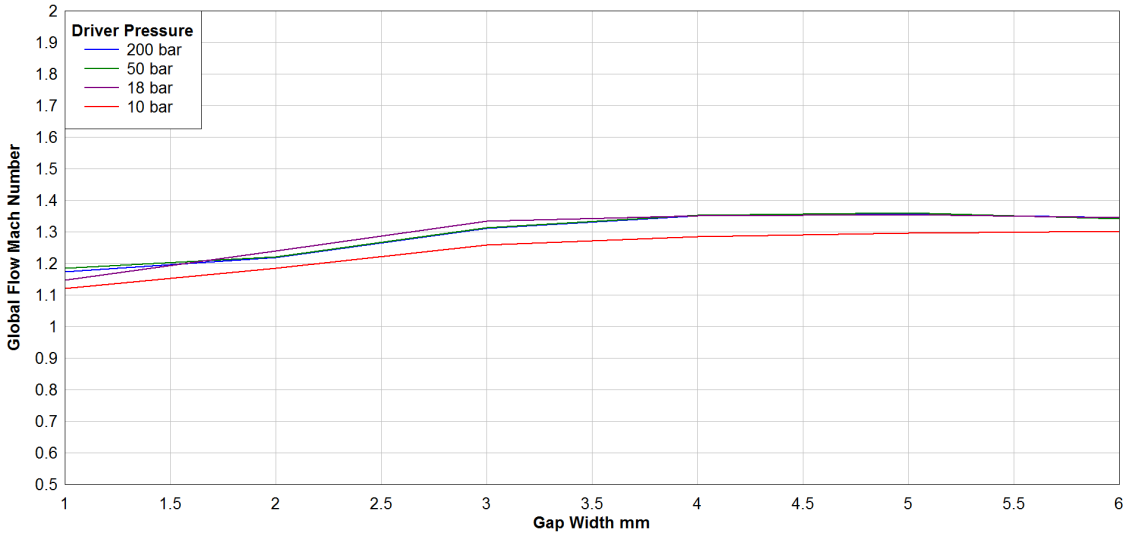


Figure 4.24: Global Flow Mach Number variation with Driver Pressure

4.3 Summary

Initial computational simulations conducted using a simple material model for the detonation products showed that the MATLAB model returned a reasonable comparison to the high fidelity modelling for the gas flow speeds external to the casing; although major differences were found within the first millimetre or so. This comparison is caveated however as the high fidelity modelling results were based on a very sparse data set. During the comparison, it was seen that the flow within the gap was not well described by the MATLAB model, and this brought the underlying ideal nozzle flow assumption into question. This in turn led to a change in scope of the research to concentrate on the flow within the narrow gap and the applicability of the underlying assumption currently used.

Further high fidelity modelling was undertaken using air as the driver gas, at pressures which could easily be replicated experimentally using the CBIS shock tube. This showed that the ideal nozzle flow assumption failed to hold in the majority of cases modelled with this reduced driver pressure.

This modelling campaign also concluded that within the initial quarter of the gap length, the gap opening width has no influence on the flow Mach number. Beyond this position the gap opening width has a strong influence on the flow.

For all but the lowest driver pressures modelled, the shock tube driver pressure was seen to have no influence on the flow at any given location within the gap; gap width and position along the gap being the influencing factors.

A brief study of any influence from the gap width to length ratio showed the gap length to have no influence below gap widths of 3mm, with the flow becoming complex for gap widths greater than this value.

Overall the high fidelity modelling showed an insight into the flow structure within the gap which enabled the experimental set up to be optimised. The regime for the driver pressure available from the CBIS shock tube behaved in a similar manner to the high pressure regimes akin to explosively driven scenarios, and so any results obtained, either experimentally or numerically, could be read across into the "real world".

Chapter 5

Experimental Flow Determination

5.1 Experimental Layout

5.1.1 CBIS Shock Tube System

The shock tube system employed during the experimental phase of the research was the 60 mm bore tube housed within The Royal British Legion (TRBL) Centre for Blast Injury Studies (CBIS) laboratory within Imperial College London. The design, build and commissioning of the shock tube is described in detail by Nguyen [108], however for completeness the salient points shall be repeated here.

The shock tube is of stainless steel design and predominantly air driven, although provision can be made should helium be required as the driver gas. It consists of three 1.22 m length tubes with one being used as the driver section and if used at full length, as per the experiments conducted here, the other two give a driven section of approximately 2.44 m (not accounting for the minimal difference due to the inclusion of a gasket at the mid point joint within the driven section). A schematic of the shock tube system has been taken from Nguyen [108] as is reproduced in Figure 5.1.

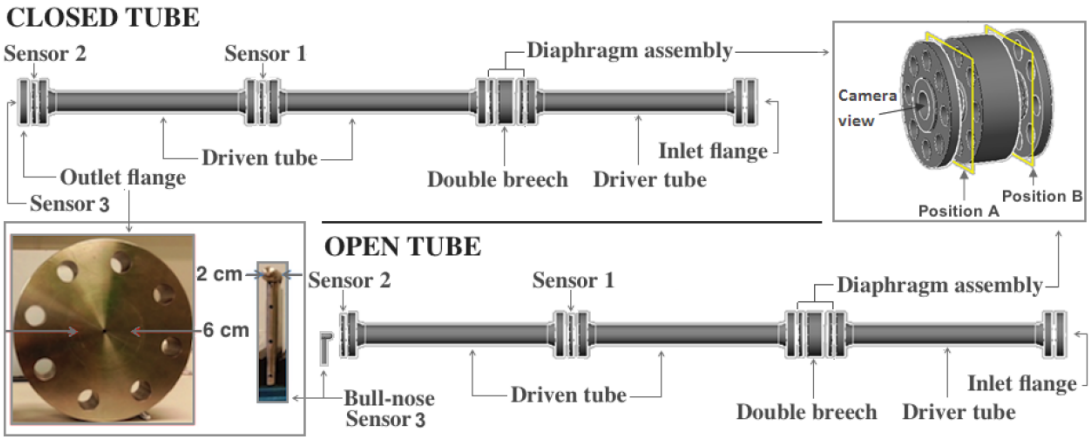


Figure 5.1: Schematic of CBIS Shock Tube System [108]

The shock tube was designed to be used up to a maximum safe driver pressure charge of 18 bar with either a single or double diaphragm configuration, depending on the driver pressure requirements. For lower driver pressure requirements, a single diaphragm may be used, however a double diaphragm setup should be used for higher driver pressures to avoid the need for excessively thick single diaphragm materials.

To use a single diaphragm setup, a thin sheet of aluminium or Mylar®, 10 cm square in dimension, is carefully placed at Position A within the inset of Figure 5.1 to form a sealed driver unit. The driver section is then charged until the material of the diaphragm fractures under load and a shock wave is generated travelling along the driven section of the shock tube. This method can suffer from batch to batch variation of material properties within the diaphragm material.

The use of a double diaphragm setup is used for driver pressures in excess of the material fracture pressure employing similar 10 cm square sheets of either thin aluminium or Mylar ® at both Position A and Position B, shown in the inset of Figure 5.1. The volume between the two diaphragms is initially charged to approximately half the required driver pressure, remaining below the fracture pressure of the diaphragm material. The volume of the driver section beyond Position B is then charged to the required pressure and sealed from the high pressure air source; i.e. if the required driver pressure is P, it can be seen that by labelling the section of the driver section between Position A and

Position B as being part of the breach

Section	Driven Section	Breach	Driver Section
Pressure	Atmospheric	0.5 P	P

Although the required driver pressure is greater than the fracture pressure of the diaphragm material used, both diaphragms remain intact as the differential pressure over each is approximately half the driver pressure, which should be well below the material fracture pressure.

When the air within the breach section, between the two diaphragms, is rapidly removed the diaphragm material at Position B is suddenly subjected to the full driver pressure and instantaneously fractures under the load. This full driver pressure load is then transferred onto the diaphragm at position A which itself fractures, generating a shock wave which travels along the driven section. The benefit of the double diaphragm setup can be seen to be more control over the actual driver pressure generated, removing any batch to batch variation within the diaphragm material.

Part of the extensive commissioning work conducted by Nguyen [108] was to generate relationships between the expected fracture, or burst pressure, and the diaphragm material thickness for both aluminium and Mylar®. The results of this are shown in Figure 5.2 which has again been taken directly from [108].

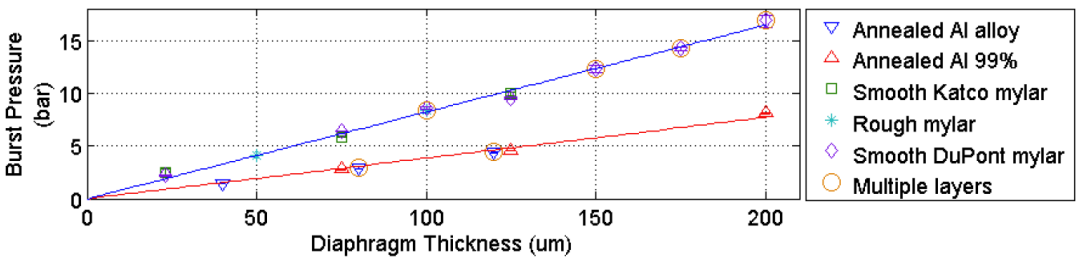


Figure 5.2: Burst Pressure with Diaphragm Thickness for CBIS Shock Tube [108]

From Figure 5.2 it can be seen that a 75 μm thick Mylar® sheet is expected to fracture at approximately 6 bar differential pressure. This material and thickness was chosen for the later stages of the experimental campaign as it could be used within a

single diaphragm setup at 6 bar driver pressure, or within a double diaphragm setup to generate either 8 bar or 10 bar driver pressures. Early stage initial investigations for the diagnostics used single diaphragms of 50 μm thickness Mylar® to generate approximately 4 bar driver pressures. More detail of each setup used is given later within the relevant section describing the experimental work undertaken to ascertain gauge functionality and the final data gathering.

5.1.2 End Plate Hardware

The experimental campaign required the design and manufacture of an end plate, such that the 2D modelling cases with a gap diameter of 6 mm and a gap length of 20 mm could be replicated. This simple design was completed with a 1.1 mm hole drilled radially to allow the fielding of a static pressure probe. This will be discussed further in the following section.

The end plate design not only had to enable the measurement of the required experimental data with minimal interference to the flow, but also withstand the forces each firing subjected it to without displaying excessive elastic deformation during each test, or any residual plastic deformation post test.

The Imperial College London Physics Workshops constructed the end plate to the authors design, as shown in Figure 5.3. The plate was cut from stock aluminium alloy and CNC machined to final form employing a general surface roughness finish, Ra, of 3.2 μm, and a tolerance on all holes of -0.0 / +0.1 mm. Before the choice of aluminium alloy (6062-T6) could be accepted, a series of engineering calculations were required to determine any relevant deflections.

The maximum deflection calculation used was as per that for an annular circular plate with fixed outer edges and free inner edges subjected to a constant loading across the entire plate from Roarks Formula for Stress and Strain [109]. A simplified schematic layout of the system for a circular annular plate with fixed outer edges and free inner

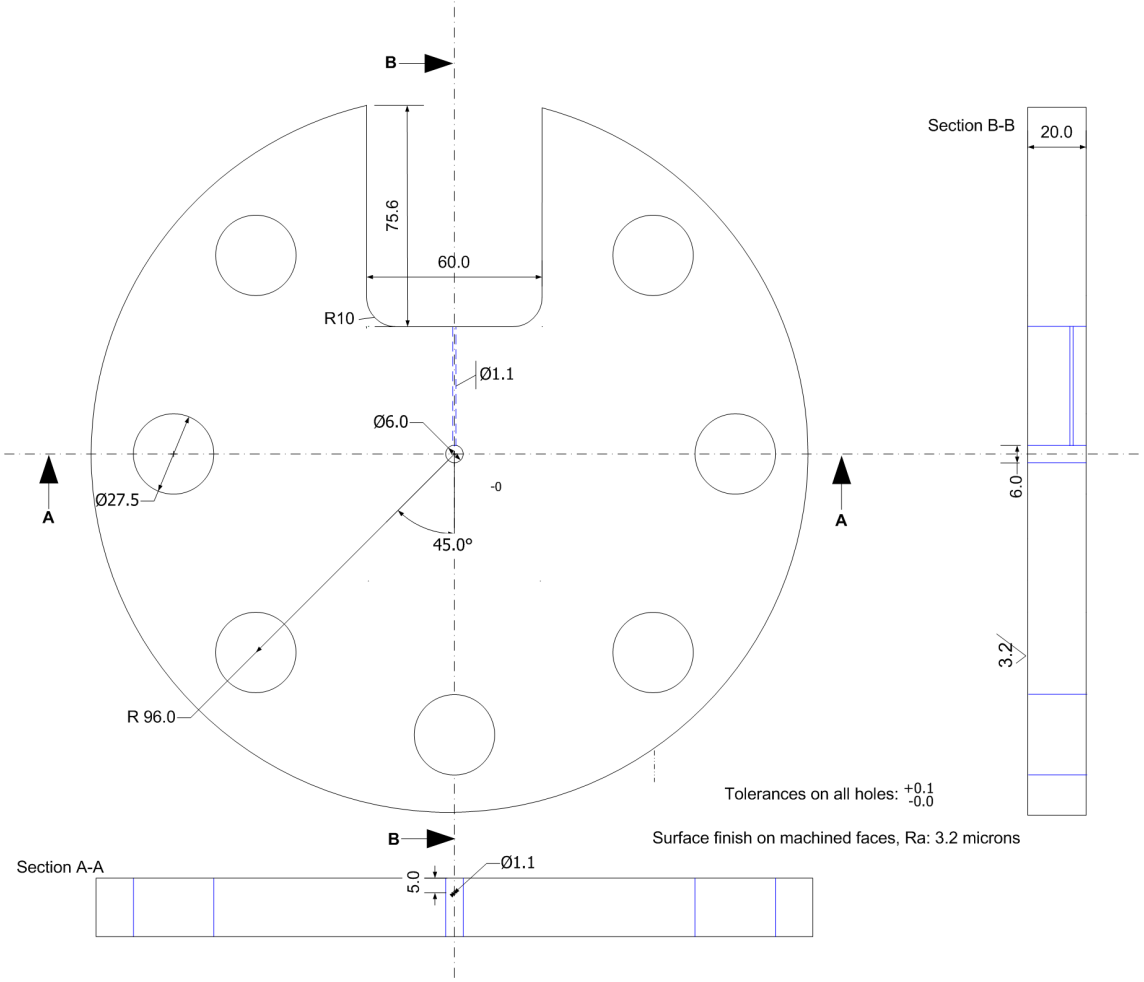


Figure 5.3: End Plate Specification Drawing

edges, loaded over a portion of the surface, is shown in Figure 5.4; where a and b are the outer and inner radii of the plate respectively [m], q is a uniformly distributed pressure [Pa] applied over the portion from r_0 to a. For the case considered here, the loading is applied to the entire face of the annular plate, such that r_0 is equal to b.

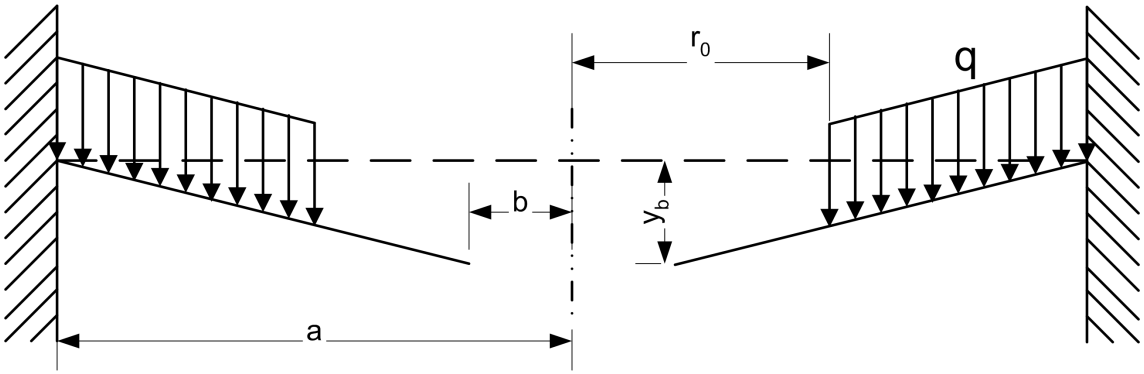


Figure 5.4: Simplified Schematic for End Plate Deflection

To use the equations within Roarks Formula for Stress and Strain [109], it was neces-

sary to determine some intermediate stages prior to the calculation of the final deflection which is given by

$$y_b = \frac{-qa^4}{D}\left(\frac{C_1 L_{14}}{C_4} - L_{11}\right) \tag{5.1}$$

The flexural rigidity, D [Nm], is calculated using

$$D = \frac{Et^3}{12\left(1-\nu^2\right)} \tag{5.2}$$

where E is the Youngs modulus of elasticity $[Nm^{-2}]$, t is the plate thickness [m], and ν is the Poissons ratio for the material. Using $E = 69$ GPa and $\nu = 0.33$ (both for aluminium) with a plate thickness of 20 mm, gives a flexural rigidity of 51621.6 Nm.

The other intermediate steps are the calculation of

$$C_1 = \frac{1+\nu}{2}\frac{b}{a}\ln\frac{a}{b} + \frac{1-\nu}{4}\left(\frac{a}{b} - \frac{b}{a}\right)$$

$$C_4 = \frac{1}{2}\left[\left(1+\nu\right)\frac{b}{a} + \left(1+\nu\right)\frac{a}{b}\right]$$

$$L_{14} = \frac{1}{16}\left[1 - \left(\frac{r_0}{a}\right)^4 - 4\left(\frac{r_0}{a}\right)^2 \ln\frac{a}{r_0}\right]$$

$$L_{11} = \frac{1}{64}\left[1 + 4\left(\frac{r_0}{a}\right)^2 - 5\left(\frac{r_0}{a}\right)^4 - 4\left(\frac{r_0}{a}\right)^2\left[2 + \left(\frac{r_0}{a}\right)^2\right]\ln\frac{a}{r_0}\right]$$

which combine with the output of Equation 5.2 to complete the calculation of Equation 5.1 to give the final deflection.

It is obvious that the uniform loading experienced by the plate will have a significant effect on the final deflection and must be carefully considered. For the experimental phase of the research, the shock tube will be run at a maximum driver pressure of 10 bar; however, the maximum achievable safe driver pressure is 18 bar and the deflection calculations

will be conducted against this value such that if necessary the plate could be used at the highest pressure. Although the driver pressure taken is 18 bar (261 psi) it is necessary to estimate the reflected pressure that the plate will see and use this value for the uniform pressure loading. The reflected pressure generated is affected by the angle of incidence with the reflecting surface as shown in Figure 5.5 [110].

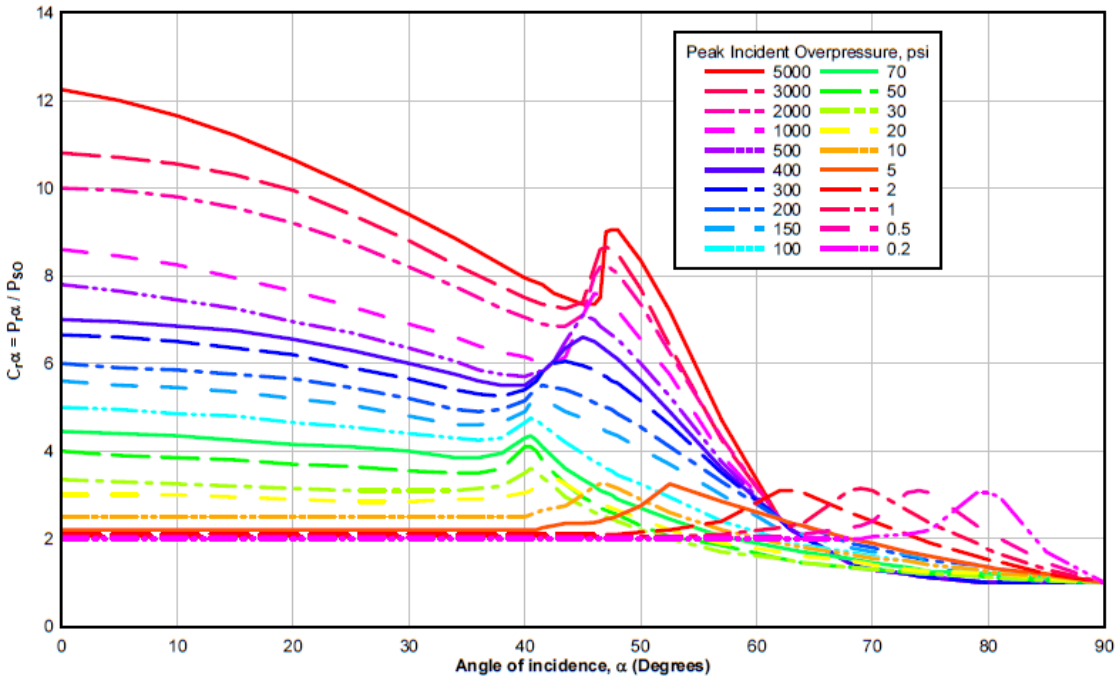


Figure 5.5: Reflected Pressure Coefficient against Angle of Incidence [110]

As the end plate will be mounted on the shock tube such that it is normal to the direction of travel of the planar shock wave generated, there is thus a zero degree angle of incidence between the shock front and the end plate inner face. Interpolating between the curves for an incident overpressure of 200 psi and 300 psi allows an estimation of the reflected pressure coefficient $C_{r\alpha}$ for 261 psi to be made; giving a $C_{r\alpha}$ at zero degrees incidence of approximately 6.25. This can then be used to generate the reflected pressure expected, which was estimated at 1631 psi or 112.5 bar.

Continuing the calculation of the deflection using a uniform pressure loading, q, of 112.5 bar on a plate of 20 mm thickness with an inner radius of 3 mm, an outer radius of 30 mm and a flexural rigidity of 51621 Nm, where the loading is applied across the entire face ($r_0 = b$ in Figure 5.4) gives a final deflection of approximately 0.003 mm.

As the expected experimental maximum reflected pressure is below the 12.5 MPa (112.5 bar) used in the calculations, which itself is well below the Youngs Modulus of the material (69 GPa), it was assumed that the deflection calculated remains within the elastic regime and no permanent plastic deformation is caused during the deflection phase. Thus the aluminium end plate is acceptable for use within the experimental phase of the research.

In this particular case, given the physical thickness of the plate and the relatively low levels of loading to be applied, the anticipated displacement of the end plate was small and non-permanent which meant the small displacement theory [109] could be used as shown. Had the anticipated deformation been larger, or permanent, or had the method applied returned unexplained values, it would have been necessary to use a Finite Element Analysis (FEA) non-linear model to simulate the full deformation history of the plate under load.

The finished end plate configuration can be seen front on in Figure 5.6 and from above in Figure 5.7. The static pressure hole (1.1 mm diameter) is visible within Figure 5.7.

5.2 Miniature Stagnation Probe Development

5.2.1 Miniature Probe Design

Given the physical dimensions of the vent opening through which the flow has to be measured, conventional off the shelf stagnation probe designs are not small enough to give accurate measures of the flow properties; indeed some designs are physically too large to fit within the vent opening and take any measurements of interest.

To overcome this, it was necessary to design and build a bespoke miniature stagnation probe for use within the shock tube experiments. Given the limited space available regarding hardware location in and around the gap, and the fragility of any probe design



Figure 5.6: Finished End Plate - Front View

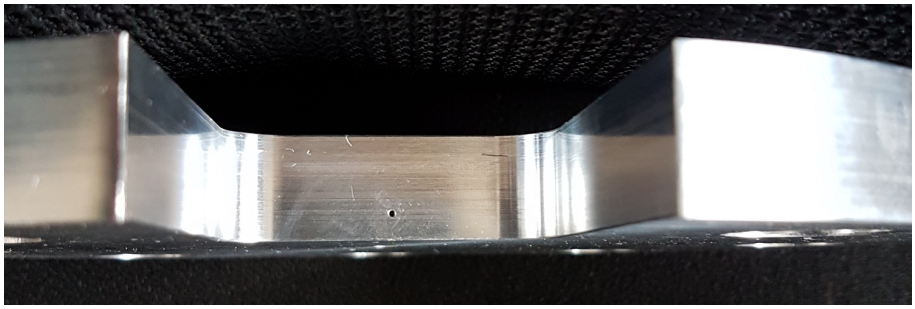


Figure 5.7: Finished End Plate - Top View

given the physical dimensions required, the simplest design for a miniature pressure probe was pursued.

The external diameter of the gauge had to be kept as small as possible to minimise the blockage effects within the shock tube experiments. The dimensional limitations for the build of a protected pressure gauge therefore required specialised equipment and thin wall cylindrical external protection. The limitations on the wall thickness of the external protection made it extremely difficult for anything other than a straight probe design to

be constructed, to avoid damaging the external protection during shaping, at this stage.

Although a straight tube gauge undoubtedly introduced simplifications into the manufacturing process, it did however introduce complications into the mounting method necessary to avoid complete blockage of the exiting flow. Following a successful straight probe design, it could be envisioned that pursuance of a design with a curved section within the probe length will reduce any external hardware effects on the flow, as the gauge can be fixed in position outside the vent path of the experiment.

Josey *et al* [111] developed a reasonably miniature stagnation-pitot gauge using semiconductor piezoresistive medical catheter probes; however, even this design was physically too large to be used in this research. Some models of the piezoresistive catheter probes would be physically small enough for use within the planned shock tube experimental campaign, however the limited pressure response and side facing transducer makes them unsuitable for the stagnation probe design under consideration.

A brief review of commercially available miniature probes returned a selection of rodent catheter optical pressure probes with external diameters of 2 French (c.666 μm), 0.9 French (c.300 μm), or 0.5 French (c.167 μm) and all with front facing sensor position. The majority however reported usable pressure ranges limited to 300 mmHg (0.4 bar); although this pressure range is adequate for the intended life science purposes such as ureter, arterial or venal blood, intradiscal, intramedullary, or intracranial pressures it is far too limited for measurement of stagnation pressures within the shock tube.

One rodent catheter optical pressure gauge (FISO FOP-LS-2FR-30) did, however, have a working pressure range up to 10 bar; although this maximum pressure fell short of the ideal test pressure range as shown by the previous numerical modelling, and the maximum working pressure of the shock tube (18 bar), it allowed a tolerable firing pressure to enable the research to move forward.

The FOP-LS-2FR-30 has an external diameter of 2 French (c.666 μm) which is adequate for use with the larger vent diameters studied, although too large for use with the

smaller 1 mm to 3 mm vent diameters due to excessive blockage effects negating any testing at these scales. Indeed, even with thin wall external protection the overall diameter of the finished stagnation probe would be of the order of the 1 mm vent diameter.

The FOP-LS-2FR-30 probe is a complete optical unit using a fabry-perot cavity and fibre optics with no electronic components within the measurement element or the connection to the signal processing unit; this precludes the need for any shielding to limit interference from any external electromagnetic or radio frequency source, thus removing the need for a potentially bulky component of the finished gauge.

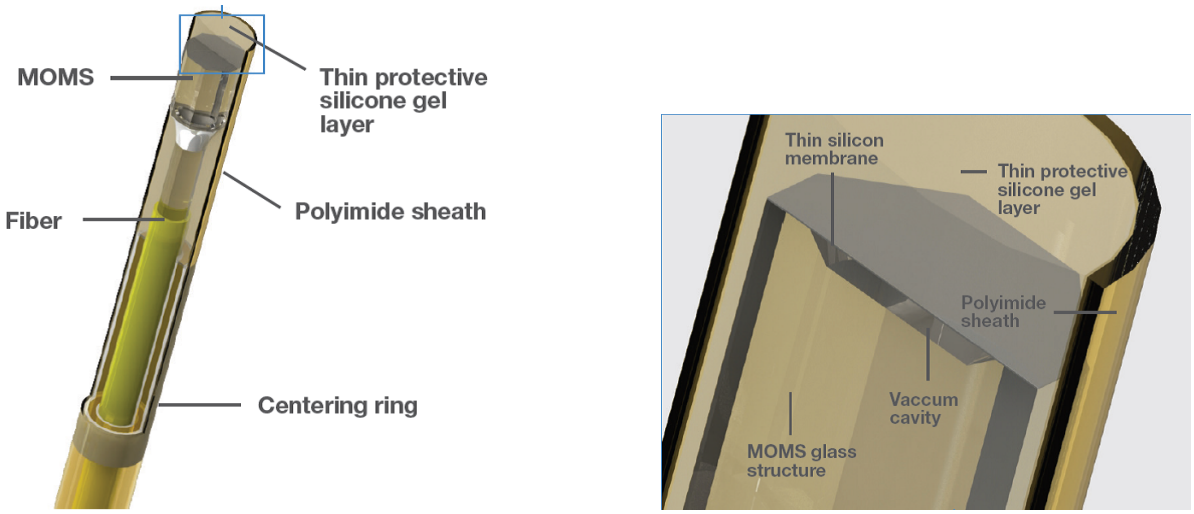


Figure 5.8: FISO Optical Catheter Probe Construction [112]

Figure 5.8 shows the general construction of the optical rodent catheter gauge, with a close up of the Micro Optical Mechanical System (MOMS) unit shown in the right hand figure. The gauge was purchased as a sealed unit, without any repair or re-calibration option.

From Figure 5.8, it can be seen that the sensor unit employs a deformable membrane ahead of a vacuum cavity, such that as an external pressure signal is applied to the unit this membrane deflects and reduces the cavity length, as shown in Figure 5.9.

The rate and amount of deflection shown by the membrane has been calibrated by the manufacturer, with the information stored within the connector linking the pressure transducer to the laser conditioning unit. The data acquisition software [112] interrogates

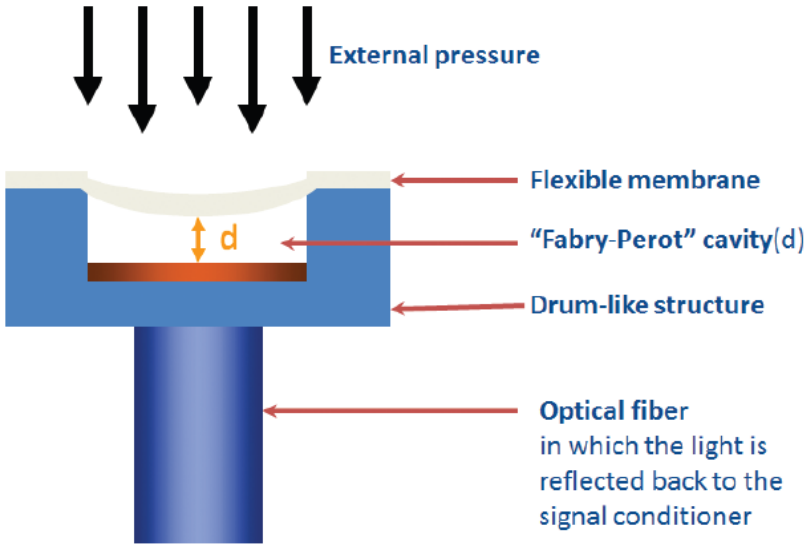


Figure 5.9: Schematic of Internal Working of Optical Gauge [112]

the laser conditioning unit, and the output is one of pressure directly.

Limitations in the acquisition rate are discussed in a later section; however it may be possible to overcome these by employing a non standard conditioning unit and data acquisition system, although this may introduce other complexities including the need to recalibrate the pressure transducer.

5.2.1.1 Straight Probe Cavity Length Effects

With the basic design of the miniature probe finalised, it was necessary to assess any potential effects from the length of the cavity used to enable the flow to be brought to rest. Initial thoughts revolved around the standard concept of a long cavity length compared to the diameter of the overall probe. Use of numerical modelling allowed the cavity length to be varied and the stagnation pressure recorded at the front of a dummy gauge block to be compared to that calculated based on the free field flow some distance away from the gauge (to minimise the effects of the gauge on the local flow).

Varying the cavity length between 20 mm and 0 mm within the numerical model allowed the design of the gauge to be optimised. Each model used followed the generalised

layout shown in Figure 5.10, with variation only within the cavity length ahead of the gauge block.

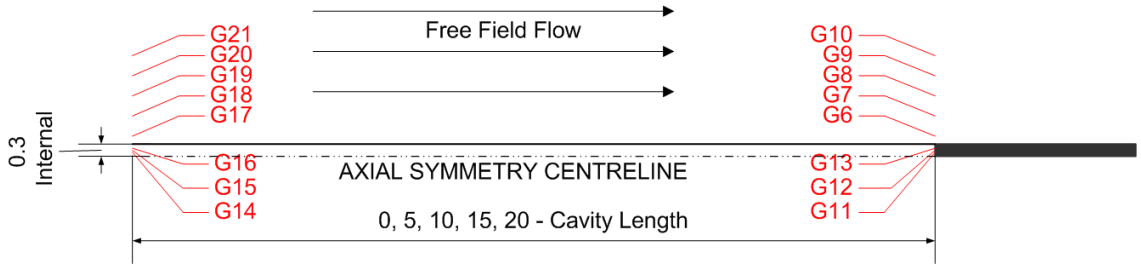


Figure 5.10: Generic Stagnation Probe Model

The results of the modelling can be seen in Figure 5.11. The "measured" traces shown in these Figures are derived from the average of the results of gauge points G11 to G13, as shown in Figure 5.10, whereas the "calculated" traces are taken from the results of gauge points G9 and G10.

The AUTODYN model used cannot output the stagnation pressure at a point directly, but returns other flow parameters that was used to infer the stagnation conditions, such as the free field static pressure, the local density and the local flow speed. These parameters were used to calculate the dynamic pressure at the point of interest, and then the stagnation pressure by using

$$p_{stagnation} = p_{static} + q \tag{5.3}$$

where

$$q = \frac{1}{2}\rho_{\infty}u_{\infty}^{2}$$

Inspection of Figure 5.11 shows that for each case with a non zero cavity length some form of oscillation can be seen in the traces. Whether this would be a physical artefact of any probe constructed with a straight cavity, or whether this is a numerical artefact of the modelling conducted, would only be found if such a probe design was built and tested; if the oscillation was physical this would require potentially complex algorithm development to filter the oscillations during the experimental data analysis. The non-zero cavity cases

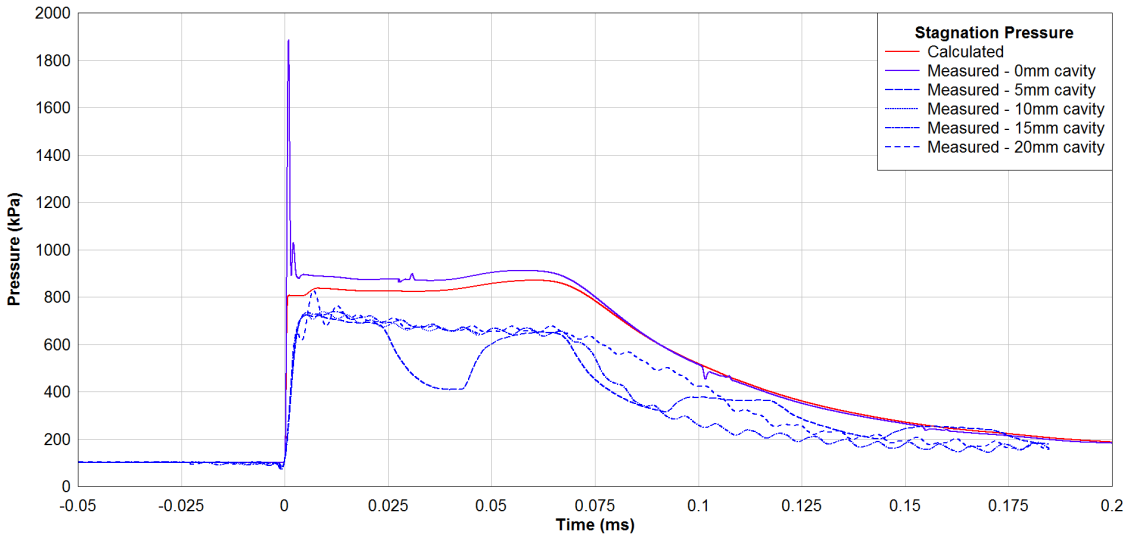


Figure 5.11: Effect of Cavity Length Modelling Results

also returned measured pressure profiles which appear to be significantly lower than those calculated from the free field flow parameters.

It can also be seen in Figure 5.11 that the measured trace for the zero cavity case shows a large spike of pressure which very quickly reduces to a level very similar to the calculated stagnation pressure. As there is no cavity ahead of the measurement element of the probe it is essentially acting as a miniature reflected pressure gauge, which is the high pressure reading at the adjusted time zero for this case. A standard reflected pressure gauge would be embedded flush in the face of a much larger structure to enable the reflected pressure to be measured over a period of time before blast wave clearing effects affect the recorded trace. This is not the case here, and the clearing effects are used to enable the probe design rather than limit it.

5.2.1.2 Shock Wave Clearing Effects

Although blast wave clearing effects are usually applied to the measurement of reflected pressure on the front walls of large scale test cubicles or structures, there is no physical reason why the same theory cannot be applied to smaller scale scenarios. This blast wave clearing phenomenon is described fully by the United States Department of Defense (US

DoD) [110], and by authors such as Kinney & Graham [113]; however it is described succinctly by Rigby [114].

It is well understood that for a flat surface placed perpendicular to the trajectory of an advancing plane shock wave, thus parallel to the shock front, the full reflected pressure will be seen across the surface. This reflected pressure will be reduced over time and space, as a relieving expansion wave propagates inwards from the outer edge, until the surface sees the stagnation pressure associated with the mass air flow behind the shock wave. Rigby simplified the graphical representation of this, which is reproduced in Figure 5.12.

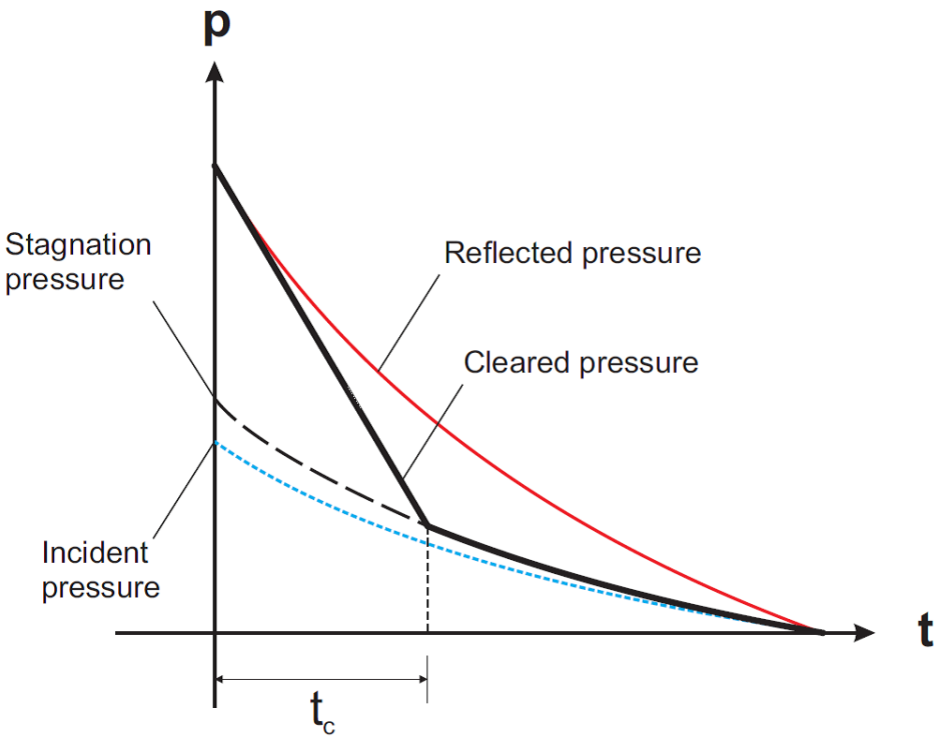


Figure 5.12: Simplification of Clearing Correction to Pressure Trace [114]

The method as explained by Kinney & Graham [113] considers only the smaller face dimension, S [m], described as the smaller of either the structure height or half width of the front face. This is referred to as the 2-dimensional clearing time,

$$t_c = \frac{3S}{a} \tag{5.4}$$

where a is the sonic velocity within the reflected pressure region $[ms^{-1}]$.

An alternative method, which considers both the height and width dimensions in the analysis is found in the United Facilities Criteria document generated by the US DoD [110] and gives the clearing time as

$$t_c = \frac{4S}{(1+R)a} \tag{5.5}$$

again as above; a is the sonic velocity in the reflected pressure region, S is smaller of either the height or half width of the target face [m], however R is the ratio S/G where G is the larger of either the height or half width of the target face [m]. This method is referred to as the 3-dimensional clearing time.

In the case of the application here, it can be seen that the cross section of the probe is circular, thus this coupled with the lack of a ground plane clearly gives a 2-dimensional case where the height and half width of the reflecting surface are equal to the cylinder radius, such that $r = H = \frac{W}{2}$ as shown in Figure 5.13

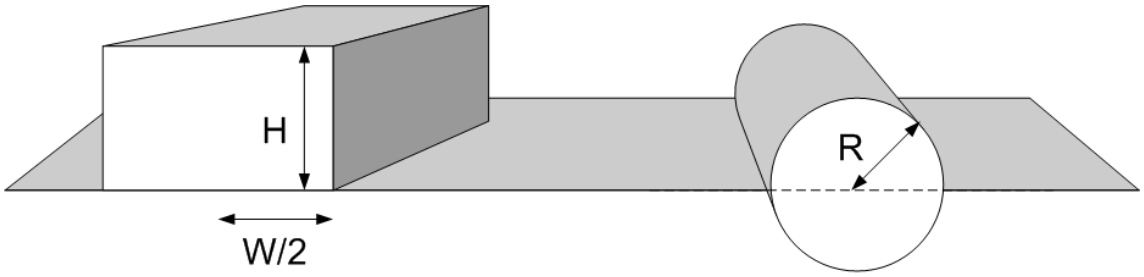


Figure 5.13: Clearing Dimension Layout

Thus it is reasonable to apply the 2-dimensional case as given by Equation 5.4, with S set to the outer radius of the probe.

Doing this required the calculation of the sonic velocity in the reflected region. Re-running the zero length cavity probe numerical model with additional gauge points immediately ahead of the gauge block, as seen in Figure 5.14, allowed direct output of the local sound speed to be obtained.

For completeness, the coordinates of each gauge point in Figure 5.14 are given in Table 5.1.

Using the direct measurement of the soundspeed at gauge points G19 to G24 allowed

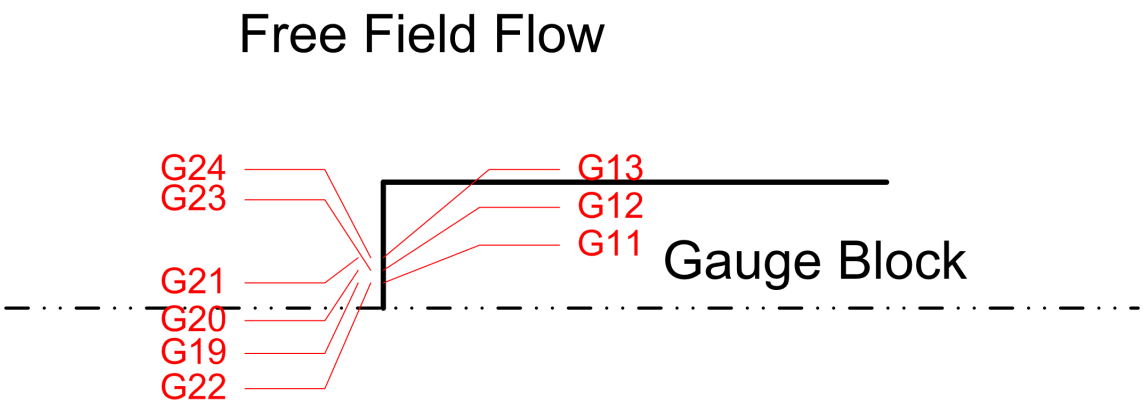


Figure 5.14: Gauge Layout for Soundspeed Modelling

GAUGE POINT	x [mm]	y [mm]	NOTE
G11	75.00	0.1	On face of Gauge Block
G12	75.00	0.15	
G13	75.00	0.2	
G19	74.90	0.1	In fluid ahead of Gauge Block
G20	74.90	0.15	
G21	74.90	0.2	
G22	74.95	0.1	
G23	74.95	0.15	
G24	74.95	0.2	

Table 5.1: Soundspeed Modelling Gauge Locations

the speed-time traces shown in Figure 5.15 to be constructed. All six gauge point curves lie coincident and are covered by the line showing the average value across all gauge points. The values can easily be verified using the local static pressure and flow density to calculate the soundspeed at each point.

From Figure 5.15 it can be seen that the soundspeed varies with time, reaching a maximum value of 564.2 m/s before reducing and reaching a relatively stable plateau value of 493.1 m/s. Using these values, along with the external dimensions of the probe, gave clearing times of 0.00266 ms and 0.00304 ms for the maximum and plateau soundspeeds respectively.

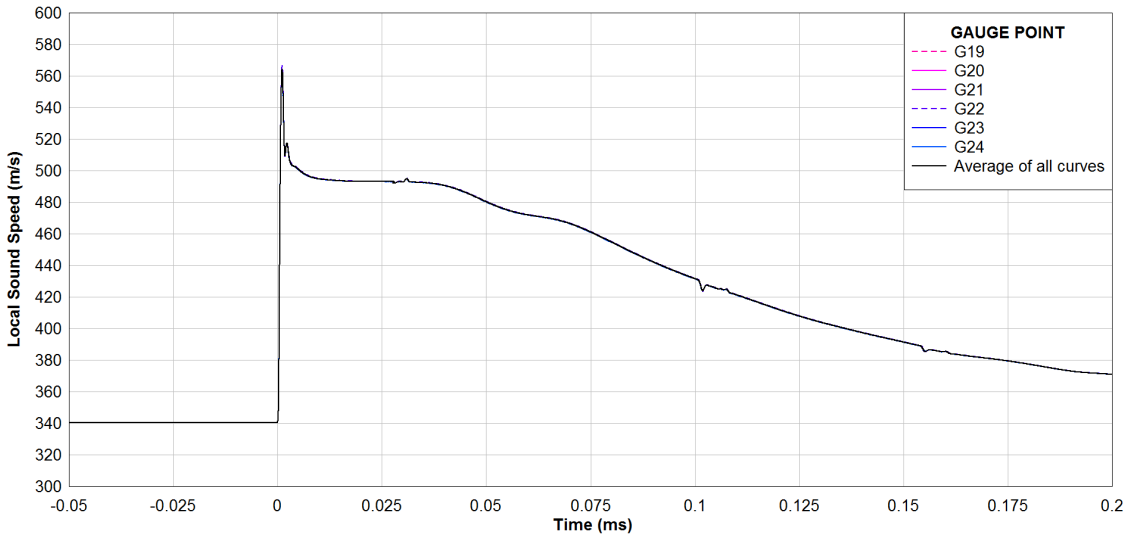


Figure 5.15: Direct Modelling Values of Soundspeed

The "measured" value for the clearing time, taken as the time for the pressure to reach the start of the plateau region thus reducing the pressure to the stagnation value generated by the stable flow behind the initial shockwave, was estimated to be approximately 0.00339 ms.

This shows a reasonable agreement between the measured time for the pressure to reach a stable value and the calculated clearing time; however, during the time interval whilst the clearing is occurring, the local sound speed in the flow ahead of the gauge block is varying significantly.

To account for this time variation in sound speed, the clearing time was recalculated, as shown in Figure 5.16.

The reference line in Figure 5.16 shows the locus of times where the clearing time is equal to the elapsed time, thus any position north of this reference line does not make physical sense as the calculated clearing time is greater than the elapsed time and so clearing of the probe face would not be complete. From this it can be seen that the minimum time required to complete the clearing process is approximately 0.003 ms using this method. A fundamental flaw in this method may exist as the clearing time variation is a calculation of the time taken to clear the probe face given the value of the soundspeed

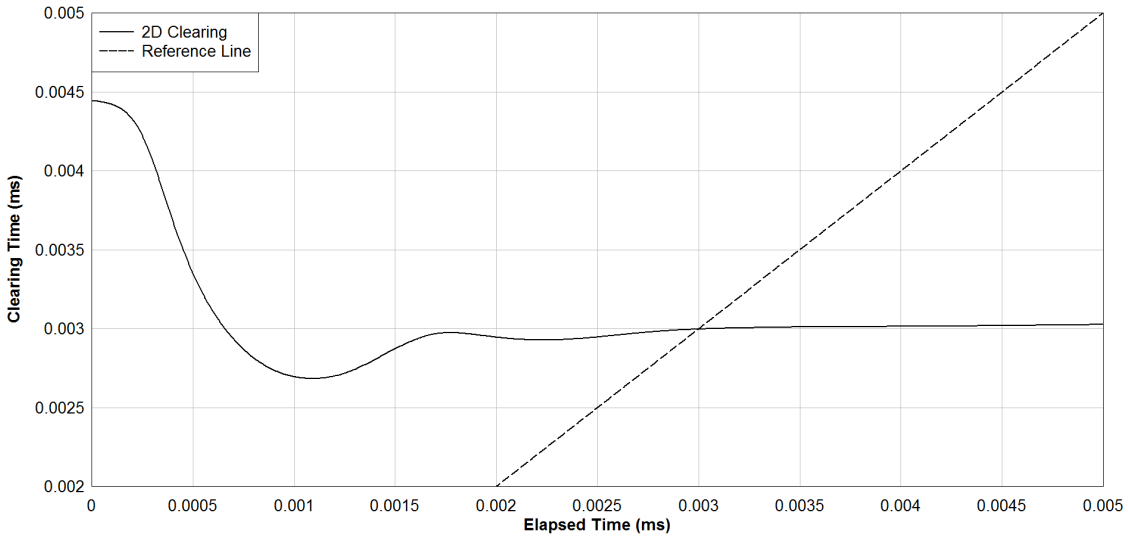


Figure 5.16: Variation of Clearing Time with Elapsed Time

at that particular instant in time; this method does not recalculate to account for dynamic changes in soundspeed with time.

To account for this phenomenon, it was assumed that the relieving expansion wave was travelling at the local speed of sound following simple Newtonian mechanical theory, such that the distance travelled by the wavefront obeys

$$S = ut + \frac{1}{2}at^2 \tag{5.6}$$

where S is the distance travelled [m] in time t [s] and a is the acceleration $[ms^{-2}]$ within that timestep.

Using the values for the modelled soundspeed with a returned timestep of the order of 5 μs allowed the rate of change of soundspeed to be calculated, and thus the distance travelled per timestep and eventually the cumulative distance travelled by the relief wave front. The time zero for calculation of the cumulative distance travelled by the relief wave was taken as the time at which the initial reflected pressure is seen, which can be related to the peak in sound speed immediately ahead of the probe face. This can be seen clearly in Figure 5.17.

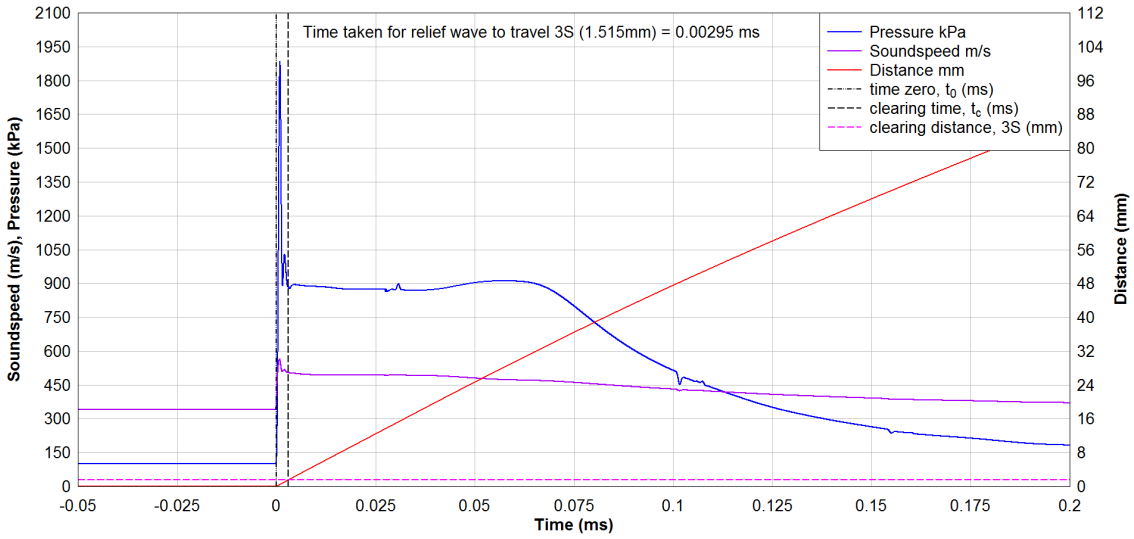


Figure 5.17: Effect of Varying Soundspeed on Clearing Time

Plotting the cumulative distance against time allowed the time for the relief wave to travel three times the gauge radius ($3S$), again assuming the wave travels at the local sonic speed, to be calculated. This is shown by the reference line, labelled t_c in Figure 5.17 and its crossing through the point where the distance travelled curve meets the $3S$ distance reference line. Using this method of incorporating the dynamic variation of the local sound speed returned a clearing time of 0.00295 ms, which can be seen to coincide reasonably well with the end of the peak (including the smaller secondary peak) and the start of the plateau region.

From this short analysis, it can be determined that the zero cavity gauge design may see a very short reflected pressure peak which will quickly reduce to the local stagnation pressure of the flow within which the gauge is placed. The time for the reduction in measured pressure down to the stagnation value is relatively short given the minimal physical dimensions of the gauge design, however it could be shortened further by reducing the overall diameter of the gauge.

It should be noted that the overall duration of the plateau region is extremely short when compared to the expected duration created by the escaping flow in the shock tube experiments as the model was required to use a much smaller driver section given the limitation on the number of cells available through the student version of the ANSYS

AUTODYN software. This is not expected to affect the response time for the clearing wave as the gauge was modelled at the correct diameter within a high pressure flow.

5.2.2 Gauge Construction

Given the resources available, a compromise was found between quality of components used, time taken for manufacture and the cost of hardware development for the construction of the stagnation pressure probes. The purchase of the FISO Technologies Inc. FOP-LS-2FR-30 optical rodent catheter pressure sensors were funded and facilitated by the MOD, whilst the physical construction of each gauge was conducted by the author within the laboratory.

The nominal external diameter of the FOP-LS-2FR-30 sensor unit is 2 French, which equates to 666 μm (0.67 mm). This gave the minimum internal diameter constraint of any external protection used, which also needed an external diameter as small as reasonably possible to reduce the blockage effects when it is employed within the experimental set up. To this end, 19 Gauge regular wall hypodermic needles have a minimum internal diameter of 0.648 mm and an external diameter range of between 1.030 mm and 1.100 mm, with thin walled needles having the same external dimensions but a minimum internal diameter of 0.750 mm to enable greater flow rates without increasing the external needle size [115].

The initial step in the build was to ensure the FOP-LS-2FR-30 unit would fit inside a 19 Gauge hypodermic needle, and this was successfully tested by carefully feeding the gauge through from the syringe end of the needle; a quick test of the fibre post this exercise confirmed no damage and the build was continued.

The standard bevel on a hypodermic needle enables easy use within the original design parameters for injection in a medical setting, however it was not required for the design of the stagnation pressure probe. Investigation was made of the best method to remove the bevel and all attempts to saw or cut the bevel away resulted in catastrophic damage to the resulting end of the needle. Only careful use of fine wet and dry abrasive paper enabled

the bevel to be removed without damage to the remaining needle. A small amount of burring was seen which was carefully removed using the bevelled point of a second 19 Gauge needle.

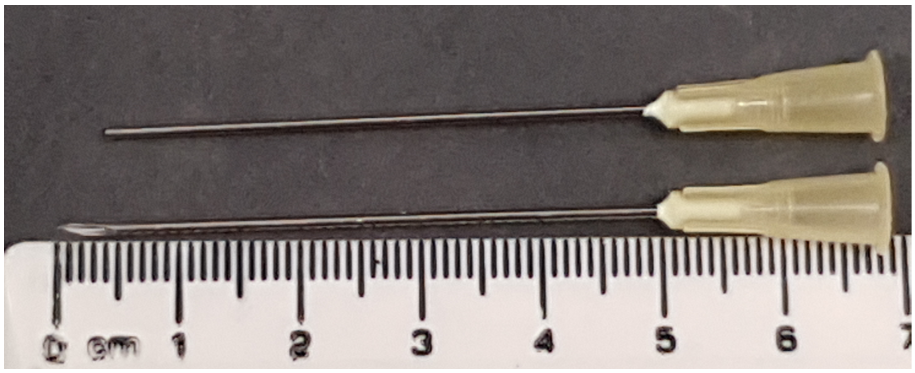


Figure 5.18: Full Needle showing Bevel Removal

Figure 5.18 shows the full extent of the 19 Gauge hypodermic needle and the associated fraction of the length taken by the bevel. The removal of the bevel shortened the needle by approximately 5 mm but this still left ample to form a usable external protective tube to protect the pressure sensor and the delicate fibre optic. Figure 5.19 shows a close up view of the bevel and the resulting tube end after removal.



Figure 5.19: Close Up of Needle Bevel Removal

With the sharp bevel removed from the end of the hypodermic needle, the next phase of the probe build schedule was to fix the sensor in place such that it was flush with the end of the protective tube. Figure 5.20 shows the FOP-LS-2FR-30 unit alongside

the completed external protective tube prior to final assembly of the stagnation pressure gauge.

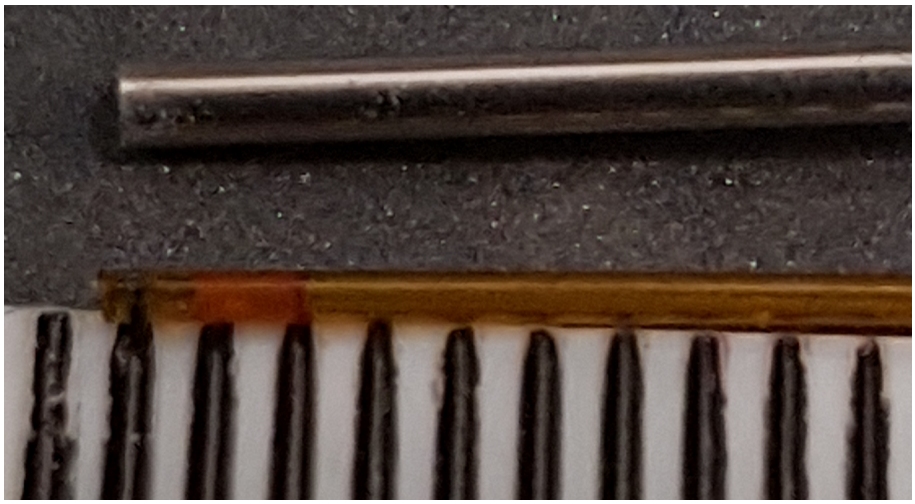


Figure 5.20: FOP-LS-2FR-30 and External Protection

Simple mechanical stabilisation was used to hold the external protective tube vertical and slightly above the surface of the cleaned workbench, with the syringe lock end of the tube uppermost. The FOP-LS-2FR-30 unit was carefully hand lowered into the tube using the syringe lock mechanism as a guide; the sensor was very carefully lowered through the tube and proud of the end to rest in contact with the workbench surface (a thin piece of white card was used to protect the sensor from any residue or debris that remained on the workbench surface). The external protective tube was slowly lowered to be in contact with the white card, thus ensuring the co-location of both the end of the sensor and the protective tube; the syringe lock was then carefully filled with two part fast hardening adhesive using a small plastic syringe. Figure 5.21 shows the finished stagnation gauge held in the vertical aspect to allow the two part adhesive to cure. Once the two part adhesive had fully cured, a laser test was conducted to ensure no damage to the fibre optic had occurred during construction.

Prototype gauges were tested within the shock tube using low pressure driver fills and although the resulting pressure trace measurements were encouraging the trailing fibre optic suffered catastrophic damage due to whipping which resulted in the complete failure of the probe. To prevent this from reoccurring during the higher pressure driver



Figure 5.21: Completion of Stagnation Probe Manufacture

fill experiments a length of heat shrink electrical insulation tubing was fed along the fibre optic prior to it being fed into the external protective tube. The insulation material was carefully shrunk using a domestic hairdryer, but was still oversized compared to the fibre optic. It was held in place with the two part adhesive at the syringe lock and allowed to move freely along the rest of the length of the insulation. A laser test confirmed no damage to the fibre optic during this additional stage of construction and further shock tube tests showed the heat shrink insulation tubing to give adequate protection to the fibre optic whilst not affecting the deployability of the gauge as a whole.

The final constructed version of the miniature stagnation pressure probe is shown in Figure 5.22.

This construction methodology, although reasonably "Heath Robinson" in nature, produced a number of gauges robust enough to take forwards for testing. Ideally more controlled manufacturing methods, such as laser cutting, laser welding and specialist thin

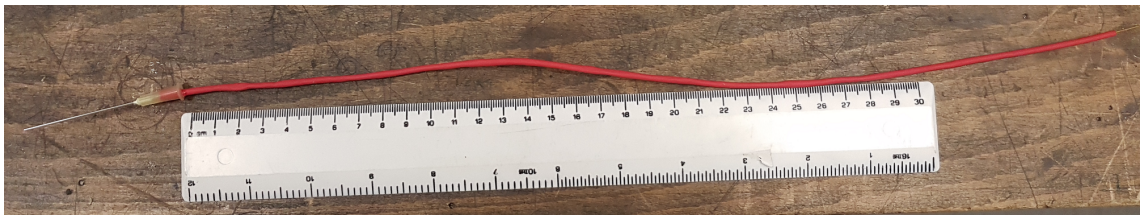


Figure 5.22: Final Completed Miniature Stagnation Pressure Probe

walled bending techniques, could be employed to make more reproducible gauges to enable further research to be continued.

5.2.3 Gauge Functionality

Initial low pressure tests were conducted to evaluate the functionality of the developed miniature optical pressure gauges. These initial tests used the simplest layout of the CBIS shock tube with the full 60 mm diameter bore being used in an open configuration. The initial low pressure tests used a single 50 μm thickness Mylar® diaphragm; from Figure 5.2 it can be seen that this thickness of Mylar® diaphragm returns a burst pressure of approximately 4 bar. The resulting driver pressures are shown in brackets within the legend of Figure 5.23; varying between 3.7 bar and 3.9 bar for an identical experimental set up.

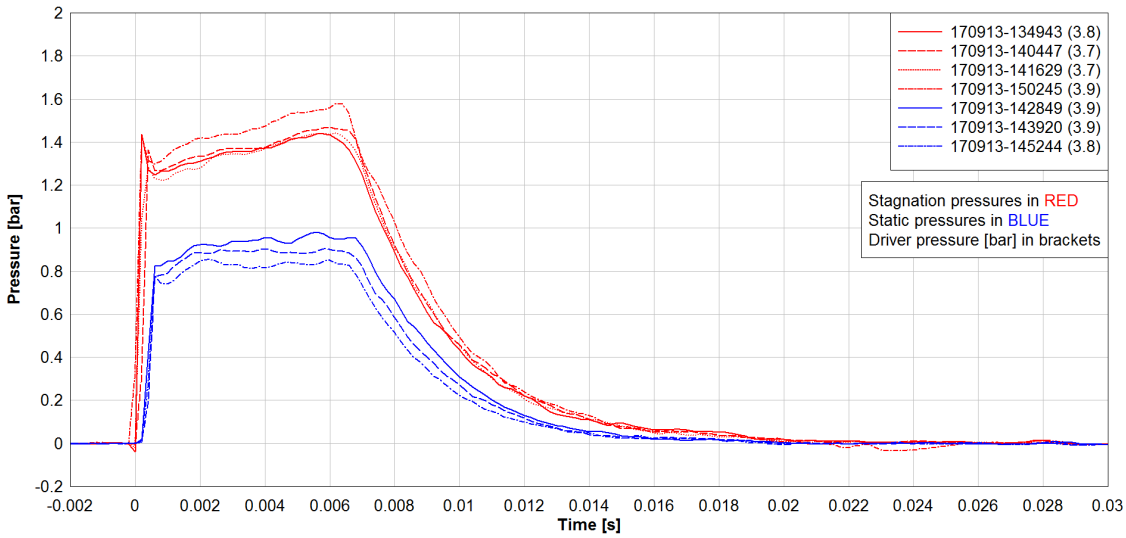


Figure 5.23: Initial Variability Tests; 4 bar driver pressure, 50 μm Mylar® single diaphragm

It can be seen from Figure 5.23 that the low pressure single diaphragm tests show a reasonable amount of variability in measured pressures; however, the details of the shape of each trace can be seen to be similar, reporting stagnation and static pressures respectively. The spread of measured values is most likely due to the variation in the driver pressure resulting from the single diaphragm set up. As mentioned previously, the use of a single diaphragm set up leads to greater variability of driver pressures due to the burst pressures being determined by the inherent failure properties of the material which can be influenced by inter-batch variations of material properties, inter- and intra-batch variations of the actual material thickness or damage to the particular Mylar® sheet used. This variability in material properties can be all but removed by using a double diaphragm set up.

The variability between traces can be expressed in terms of the precision of the results. Often confused with accuracy, the precision of results is a measure of how close the measured results are to each other; as compared to how close the measured values are to the true value. The precision displayed by varying sets of independent results can be compared using the percentage coefficient of variation. As the level of precision increases, the percentage coefficient of variation decreases such that a data set which has consistently identical results should have a coefficient of variation of exactly zero percent.

The percentage coefficient of variation can be expressed as

$$CV_{\%} = 100\left(\frac{s}{\bar{x}}\right) \tag{5.7}$$

where $\bar{x}$ is the mean value of the results and s is the standard deviation of the results. As the number of experiments undertaken is finite and obviously not the totality of the potential data set for each experimental set up, the coefficient of variation is calculated using the sample mean and the standard deviation of a sample of the total population (rather than the standard deviation of the population as a whole), thus

$$s = \sqrt{\frac{1}{N-1}\sum_{i=1}^{N}(x_i - \bar{x})^2} \tag{5.8}$$

Calculating the percentage coefficient of variation for the static pressure and stagnation pressure results with a nominally 4 bar driver pressure allows Figure 5.24 to be constructed.

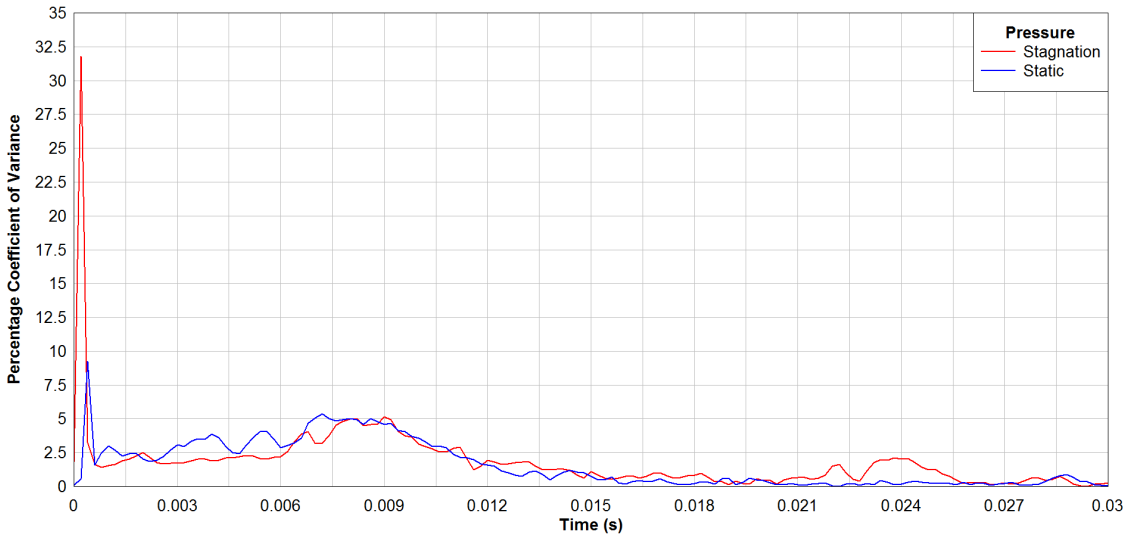


Figure 5.24: Initial Variability Tests; 4 bar driver pressure, Percentage Coefficient of Variation

Apart from the peak close to time zero, which is most likely a result of small variations within the analysed estimation of the time of arrival of the initial pressure increase, the majority of the traces show a value equal to or below 5%. This level of coefficient of variation is anecdotally very good.

The next step was to continue the functionality testing at a higher driver pressure, still using a single diaphragm set up. Figure 5.2 shows a 75 μm Mylar® single diaphragm which could be expected to produce a driver pressure of approximately 6 bar, again subject to the material property variability associated with the single diaphragm set up. Conducting a similar series of tests using the open shock tube configuration, 60 mm output bore and a 75 μm Mylar® single diaphragm returned the static pressure output traces shown in Figure 5.25.

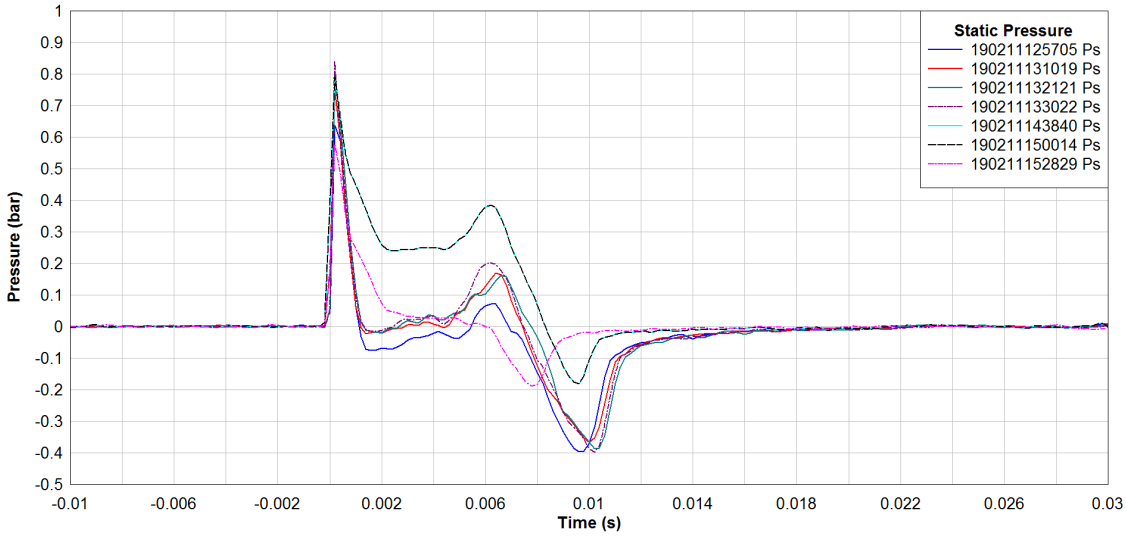


Figure 5.25: Initial Variability Tests; 6 bar driver pressure, 75μm Mylar® single diaphragm

The use of the single diaphragm set up led to variations in the returned driver pressures between 5.5 bar and approximately 6.2 bar, which is again most likely to be due to variations in the 75 μm Mylar® sheet properties, including thickness variations around the quoted nominal thickness. The resulting level of variation seen within these traces is much higher than that returned by the initial low pressure tests, with the coefficient of variation for the 6 bar experiments, shown clearly in Figure 5.26, being far in excess of the anecdotal 5% level for usable precision.

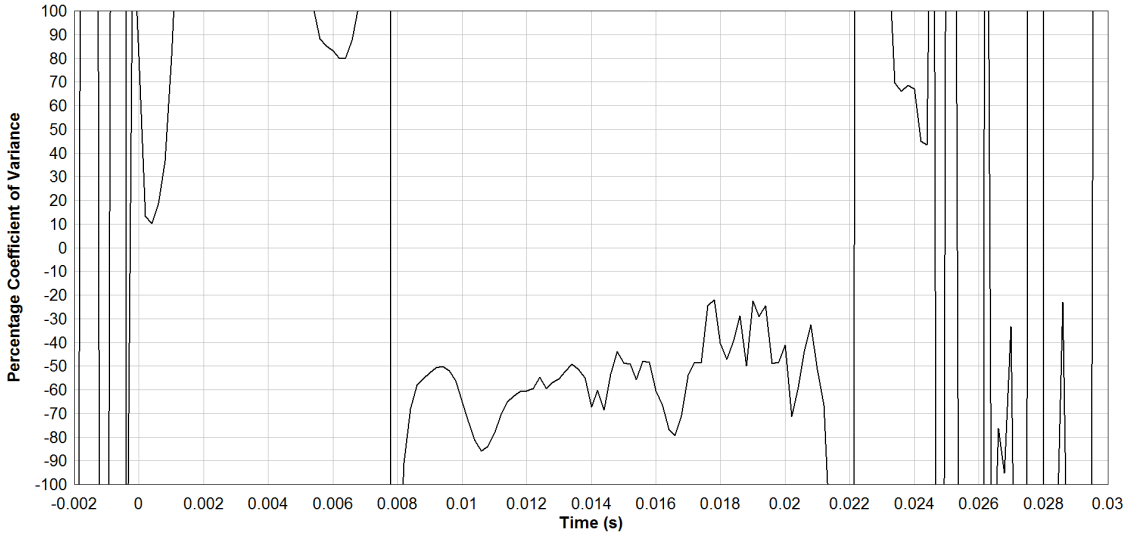


Figure 5.26: Initial Variability Tests; 6 bar driver pressure, Percentage Coefficient of Variation

Employing a double diaphragm set up, each of 75 μm Mylar®, allows driver pressures of 8.0 bar and 10.0 bar to be consistently achieved. This increased consistency is in part due to the double diaphragm set up removing any material based variability experienced with the single diaphragm set up, coupled with the CBIS shock tube firing control system enabling the driver pressure to be set and controlled to within 0.01 bar. The double diaphragm breach and firing control system are shown in Figure 5.27.

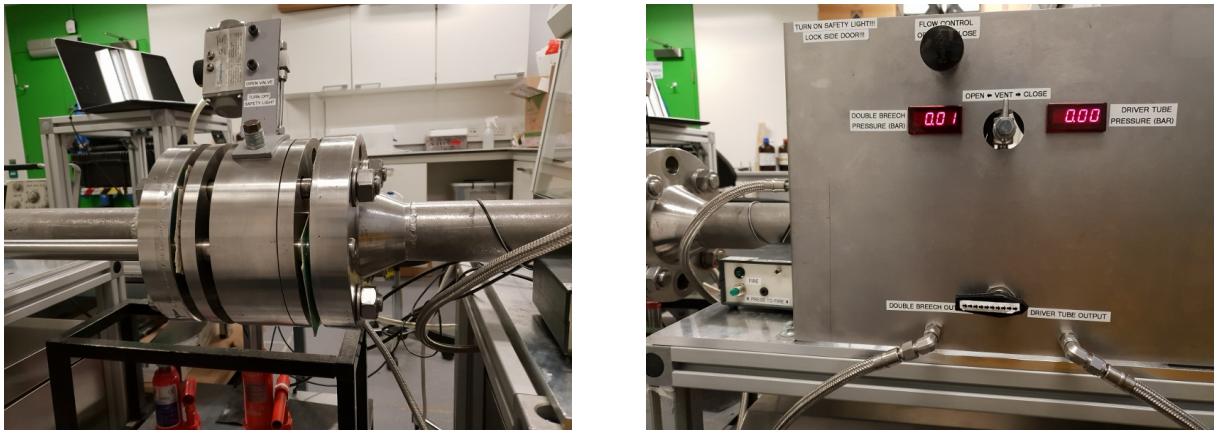


Figure 5.27: CBIS Shock Tube Double Diaphragm Breach and Fire Control System

The levels of variation in the static pressure output traces for driver pressures of 8 bar and 10 bar can be seen in Figure 5.28 and Figure 5.31 respectively. Use of the double diaphragm set up removes the majority of the variability, and the percentage coefficient of variation for each driver pressure are shown in Figure 5.29 and Figure 5.32. Figure 5.28 and Figure 5.31 also show traces for the measured stagnation pressure; which show an excellent level of consistency between firings, with the percentage coefficient of variation for the stagnation pressure curves shown in Figure 5.29, Figure 5.30 and Figure 5.32.

It can be seen that the trace for 190212144102 Pt shows a dramatic deviation from the expected shape, based on the other three traces, and this can be attributed to the stagnation probe being blown out of its holder and thus being removed from the flow during the experiment. Removing the 190212144102 Pt trace from the analysis means the percentage coefficient of variation for the 10 bar stagnation pressure results is based on three experiments only; however, it can be seen from Figure 5.32 that these remaining traces return a very good level of precision reflected by the coefficient of variation barely

peaking over 2.5% except for the initial peak.

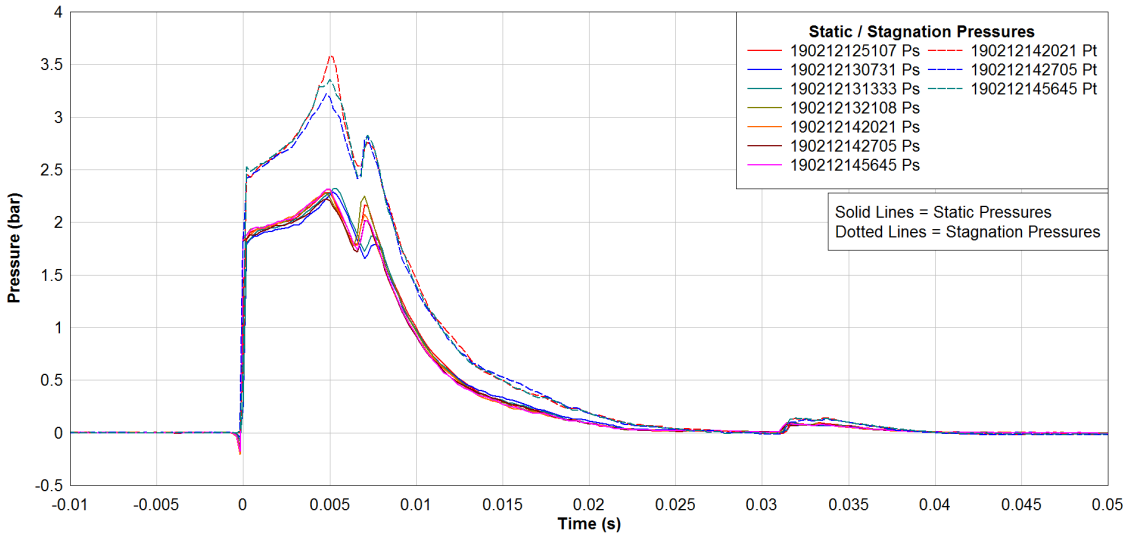


Figure 5.28: Initial Variability Tests; 8 bar driver pressure, 75 μm Mylar® double diaphragm

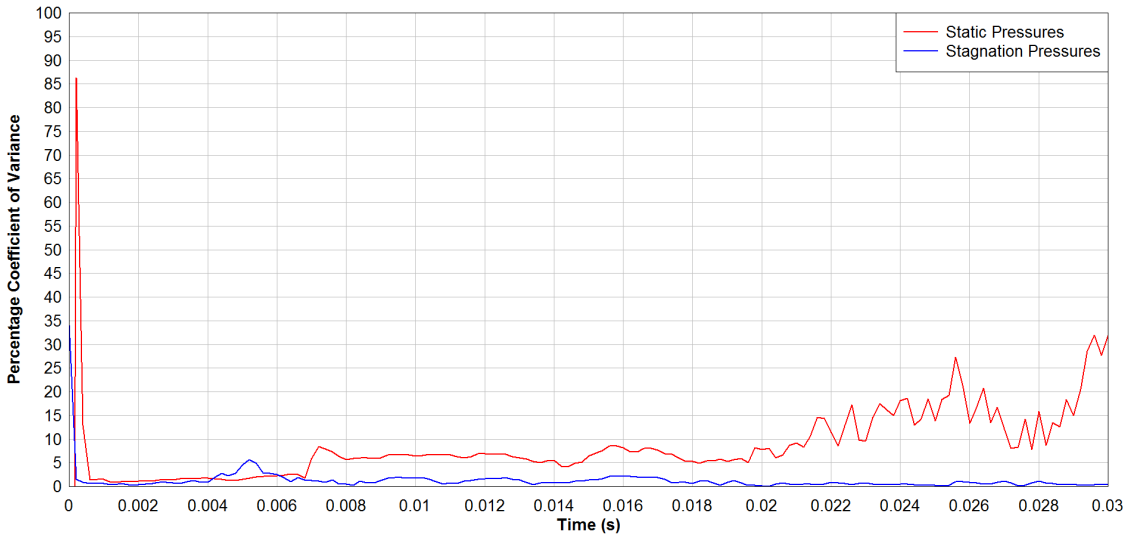


Figure 5.29: Initial Variability Tests; 8 bar driver pressure, Percentage Coefficient of Variation

Similarly the static pressure results, based on 8 experiments, returns a similar coefficient of variation which peaks at approximately 2.5% maximum. These levels of precision indicate that although the number of repeatable experiments used may be lower than usually preferred, the level of precision returned by the experimental set up and the CBIS shock tube is high enough to enable a reduced number of available experiments to return reliable and usable results.

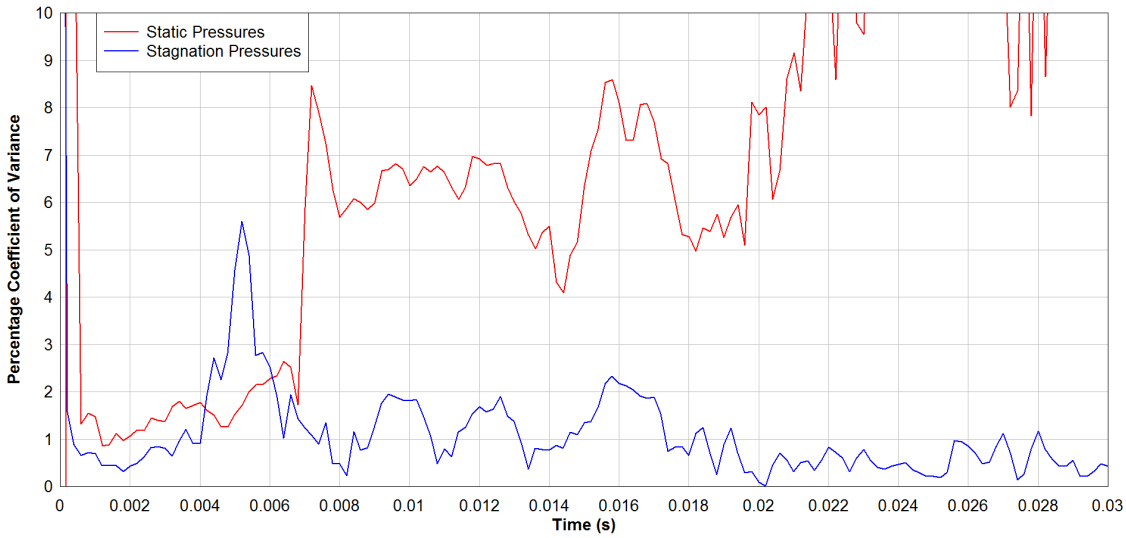


Figure 5.30: Initial Variability Tests; 8 bar driver pressure, Percentage Coefficient of Variation - Detail View

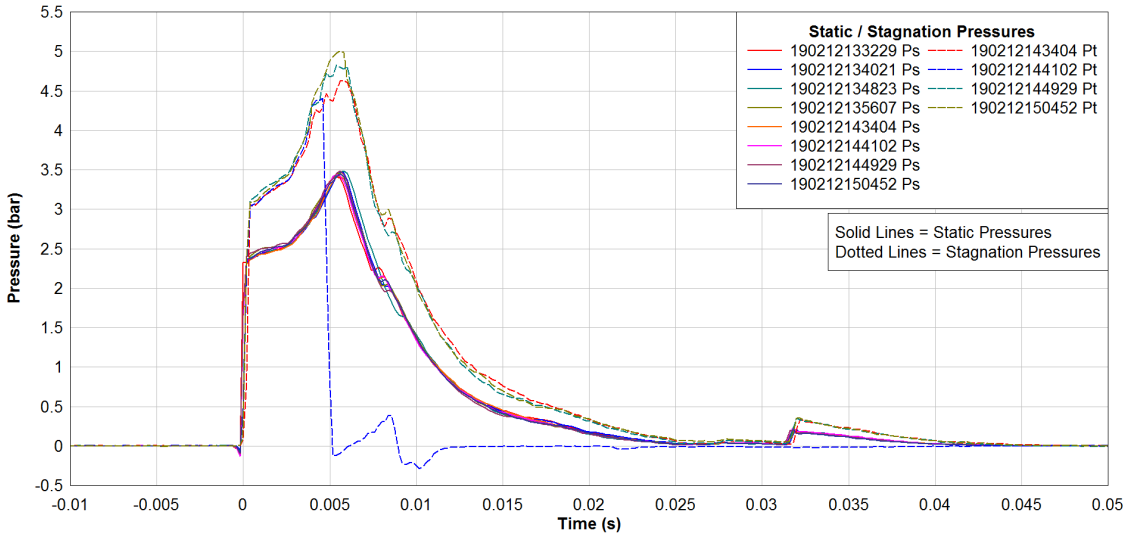


Figure 5.31: Initial Variability Tests; 10 bar driver pressure, 75μm Mylar® double diaphragm

Thus from these simple tests, using the shock tube in an open configuration with an unrestricted 60 mm bore, it can be seen that:

- The novel miniature gauges developed return usable signals in both static and stagnation pressure configurations.

- Higher driver pressures, with the double diaphragm technique, return a level of output precision that enables a reduced dataset to be used for the final analysis.

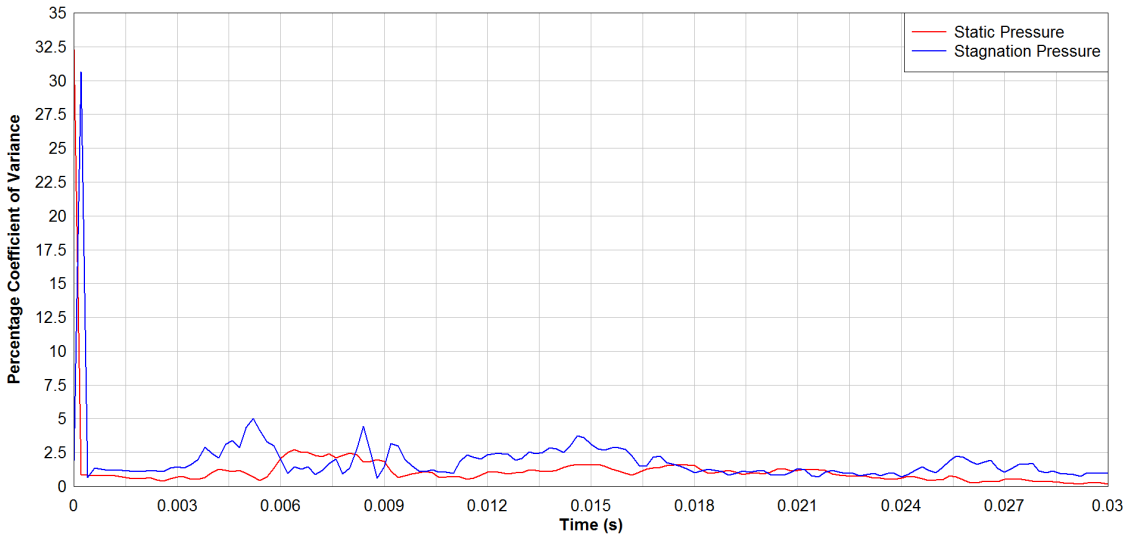


Figure 5.32: Initial Variability Tests; 10 bar driver pressure, Percentage Coefficient of Variation

5.2.4 Analogue to Digital Output Gauge Calibration

Each FISO Technologies Inc. Fabry-Perot sensor is factory calibrated prior to delivery to the customer. This calibration is National Institute of Standards and Technology (NIST) traceable and allows the signal conditioning unit to return precise pressure values with sub nanometre cavity length precision. The calibration data is held on a smart chip which forms part of the gauge connector to the signal conditioning unit and is therefore always available.

The FISO FPI-LS signal conditioning unit supplies both the initial laser signal to the sensor and the hardware required to convert the returned signal into a calibrated pressure output. This unit can be coupled to the FISO Technologies Inc. Evolution software package which allows the direct recording of digital pressure outputs up to a maximum acquisition rate of 5 kHz. The FISO FPI-LS signal conditioning unit can also be run in an analogue mode, coupled to a digital recording oscilloscope, at an acquisition rate of 15 kHz.

Before making use of the analogue output, and increased acquisition rate, it is necessary to use the Evolution software to set the analogue calibration factor. This is done

through the appropriate command window within the software interface and allows user determined minimum and maximum pressure settings to be allocated against the 0 V and 5 V upper and lower outputs of the sensor / FPI-LS unit combination.

A series of calibration experiments was conducted to determine the applicability and usability of the analogue output for this research programme, and also to determine the accuracy of the factory set calibration factor. The experiments were conducted using the unrestricted 60 mm bore open shock tube configuration, with two FISO FOP-LS-2FR-30 catheter pressure probes fielded to record static and stagnation pressures, as shown in Figure 5.33.

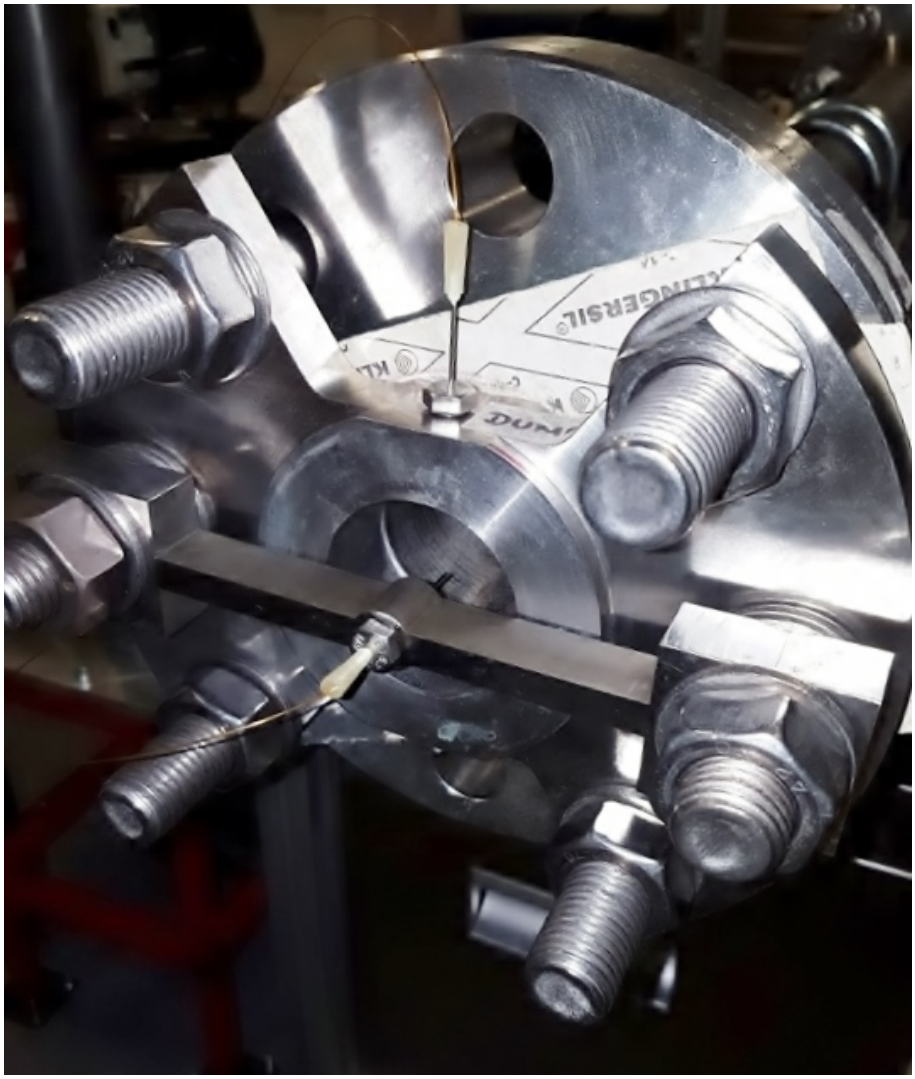


Figure 5.33: Static/Stagnation Probe Layout for Calibration Experiments

The static pressure probe was run using the digital output at the maximum acquisition

rate of 5 kHz (with the factory calibration setting), to give a check on the consistency of the driver conditions across all experiments. Experiments were conducted using a double diaphragm configuration of 75 μm Mylar® each, enabling high pressure air driver pressures of 8 bar and 10 bar to be consistently achieved. The output bore of the shock tube was kept at 60 mm, and the stagnation pressure probe was positioned along the longitudinal axis of the exit vent, as shown in Figure 5.33.

The stagnation probe was run in a combined digital and analogue output mode to enable a detailed data comparison to be conducted. The digital output was recorded directly in psi at the maximum acquisition rate of 5 kHz, while the 15 kHz acquisition rate analogue output was recorded on a Tektronix DPO 4104B digital phosphor oscilloscope, giving a signal in V.

The recorded curves for each driver pressure tested show a good agreement in shape between the digital and analogue outputs. This can be seen clearly in Figure 5.34 for the 8 bar driver pressure cases, and in Figure 5.35 for the 10 bar driver pressure experiments.

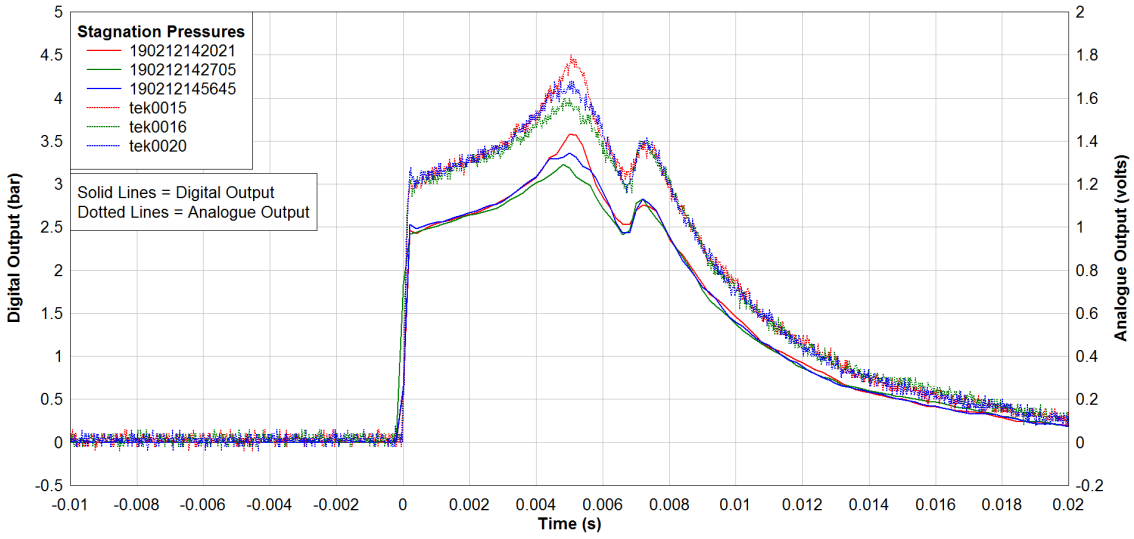


Figure 5.34: 8 bar Driver Pressure Digital / Analogue Output Comparison

A close inspection of the traces returned by 190212144102 and tek0018 show that even when the stagnation pressure gauge is blown out of the holding rig, the analogue and digital traces both show an excellent agreement in shape with time, save for the peak in analogue signal at the time of gauge removal which is not seen in the digital trace. This

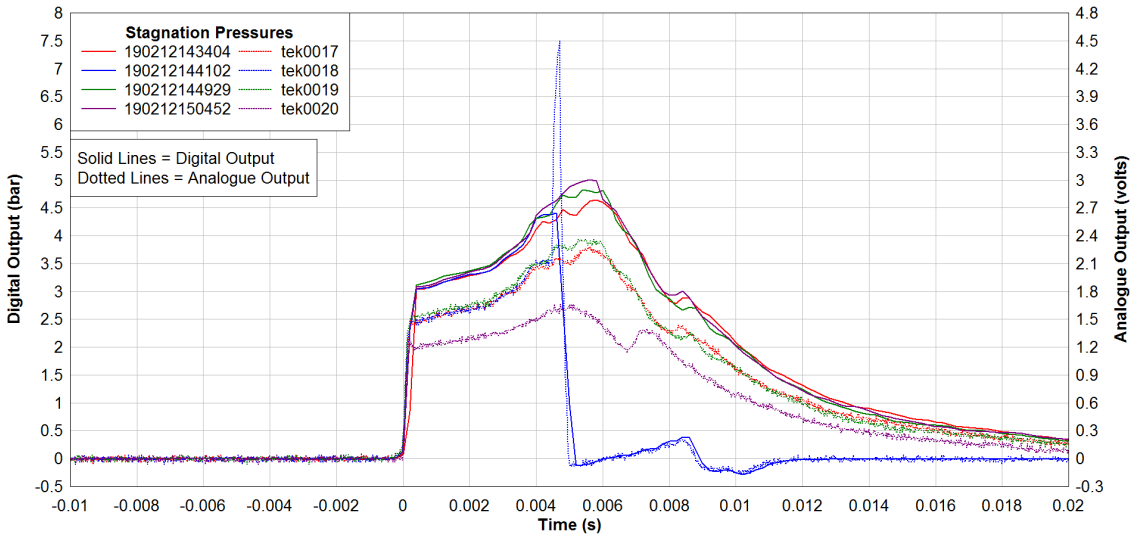


Figure 5.35: 10 bar Driver Pressure Digital / Analogue Output Comparison

is probably an artefact of the increased acquisition rate of the analogue signal enabling the capture of such a transient phenomenon which occurs too quickly for the digital output to capture. Although the analogue signal gives more detailed information in this case, it does not affect the overall usefulness of the digital output as both can be seen to return to a zero level signal within a very similar timeframe.

Taking the average signal for each case, 8 bar and 10 bar driver pressures in both digital and analogue modes, gives the four traces shown in Figure 5.36.

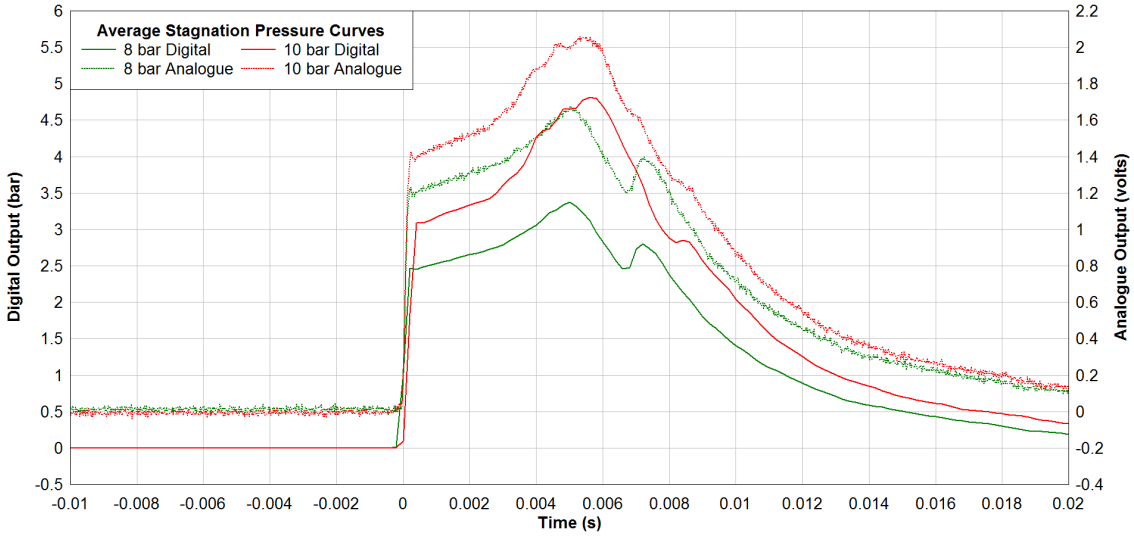


Figure 5.36: Digital And Analogue Output Comparisons - Average Traces

For the 10 bar driver pressure average traces, the results from 190212144102 and

tek0018 have not been included, as the dramatic deviation due to the gauge removal during the experiment would have an adverse effect on the average curves, thereby not giving a fair account of the combined results. Again inspection of Figure 5.36 clearly shows the agreement between the digital and analogue shapes with time for each driver pressure.

At this stage, the analogue output still has not been converted from V, and the agreement in shape with the digital output suggests a simple linear relationship exists to transform the analogue output from V directly to psi. Close inspection of the Figures clearly show the analogue outputs exhibit more noise within the overall signal, however this may possibly be removed by applying filtering or smoothing methods to the data if required. It is not clear how much benefit such smoothing of the analogue data would give and over-smoothing may remove any benefit from the increased acquisition rate. For the data recorded in these experiments, it can be seen that the increased acquisition rate does not offer any substantial increase in levels of detail within each trace, except for the details discussed above concerning the traces 190212144102 and tek0018.

Simple manipulation of the data traces in Figure 5.36 allows the linear calibration factor to be determined for each driver pressure tested, such that the simple relationship $P = k.V$ can be applied to give the calibration factor k $[psi\ V^{-1}]$ for each driver pressure. The two calculated calibration factors can be seen in Figure 5.37, along with an average of the two.

Close inspection of Figure 5.37 shows the measured analogue calibration factor to differ slightly between the two driver pressures tested, with more consistency shown for times less than 0.008 s (8 ms) giving a factor of approximately 29.5 $psi\ V^{-1}$. Although there is a large amount of noise within each trace due to slight variations in baseline values, this can be seen to very quickly reduce within the region of non-zero data values. It is not clear why the value of the calibration factor changes for the 8 bar driver pressure results after 8 ms, but it can be seen that for a driver pressure of 10 bar the calibration factor is very close to the 30.0 $psi\ V^{-1}$ pre-selected within the Evolution software. Allowing for

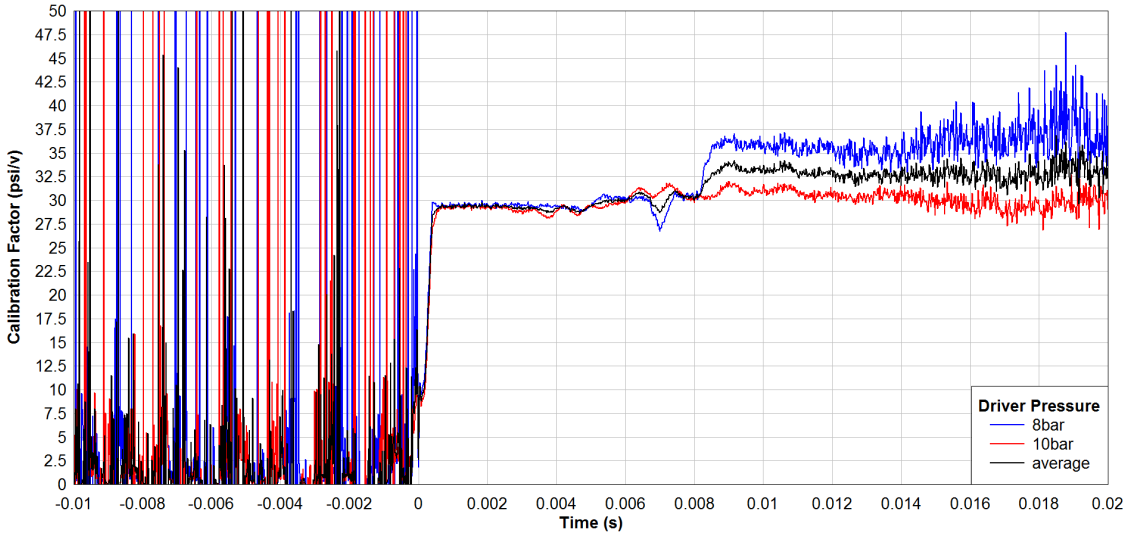


Figure 5.37: Experimental Calibration Factor ($psi\ V^{-1}$)

the rise time of approximately 0.7 ms shown in Figure 5.37, it can be seen that for the 10 bar driver pressure case, the average calibration factor (out to a time of approximately 20 ms) is 29.98 $psi\ V^{-1}$.

Application of the experimentally determined analogue calibration factor allows the development of the higher acquisition rate analogue pressure traces to be generated and compared directly with the digital output. These comparisons can be made in Figure 5.38 and Figure 5.39, showing the digital and converted analogue pressure signals for 8 bar and 10 bar driver pressures respectively.

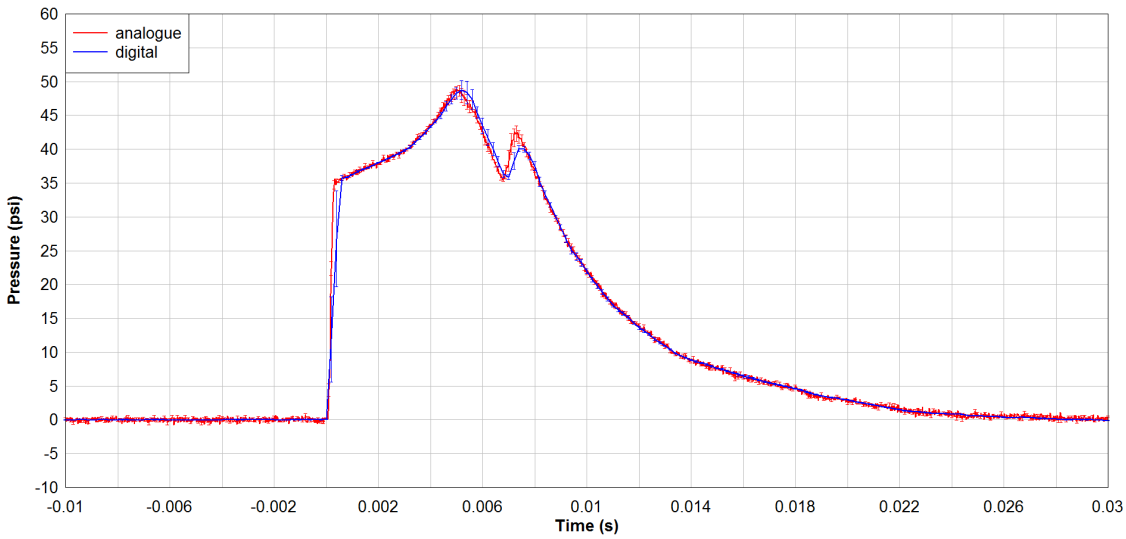


Figure 5.38: 8 bar Driver Pressure Digital / Analogue Pressure Comparison

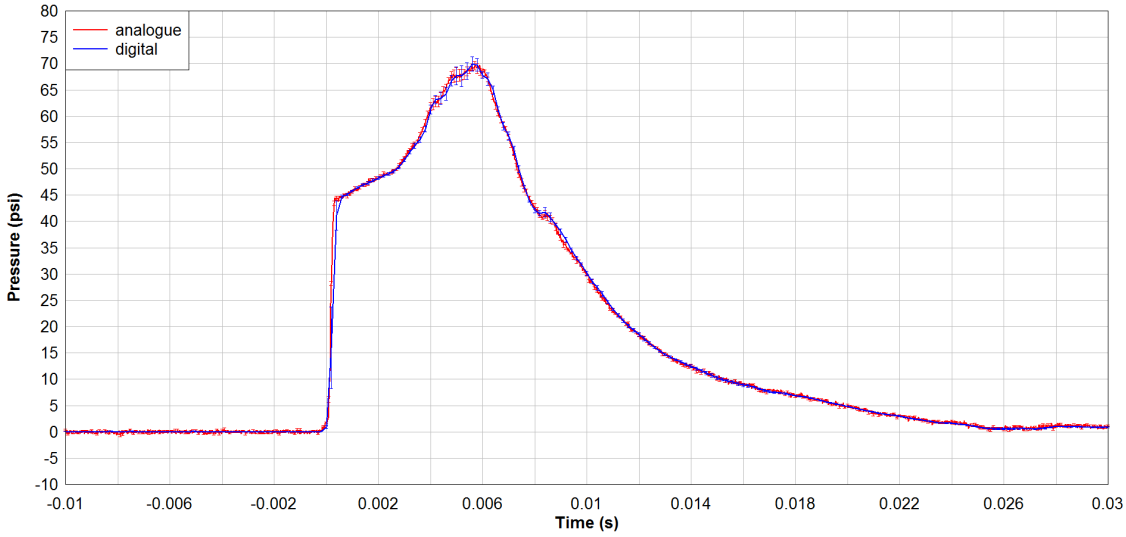


Figure 5.39: 10 bar Driver Pressure Digital / Analogue Pressure Comparison

From the comparison shown it can be seen that, in the configuration used, the higher acquisition rate of the analogue output does not capture any increased detail when compared to the digital output. This is most likely due to the physical size of the gauge being utilised within the development phase to ensure the reflected pressure experienced is reduced to the stagnation pressure quickly, thus removing it from the measured signal at these acquisition rates. Indeed, to enable the reflected pressure to be measured directly using these novel miniature gauges, a minimum acquisition rate of approximately 339 kHz is necessary to capture 1 data point within the reflected pressure zone and ideally the gauge would require at least double this or higher to capture any meaningful data within that regime. Should a gauge of this physical size be required to capture such a transient feature, additional research would be required to increase the signal rate of the laser conditioning unit; however, this is not of concern at this stage and the lower acquisition rates are ideally suited to capturing the steady state flow regimes of interest within the research topic of this thesis.

For the shock tube experimental campaign to be conducted during this research thesis, it was envisioned that the maximum 5 kHz acquisition rate of the digital output through the Evolution software would be sufficient to capture all the relevant features of both the static and stagnation pressure traces. Use of the same acquisition rate for the static

and stagnation pressure measurements simplified the analysis required to generate the dynamic pressure, and subsequent Mach number, against time data. Use would be made of the analogue output as a supplementary data source should any features be visible within the measured flow at the higher 15 kHz data acquisition rate.

5.2.5 Benchmarking of Novel Gauge Response

As mentioned in the preceding section, the sampling rate response of the novel optical gauge is 5 kHz for the digital output and 15 kHz for the analogue output. This makes the gauge suitable for sustained flow measurements, but not for rapidly fluctuating flow or for shockwave tracking. The gauge working pressure range is up to 10 bar (145 psi, 1000 kPa) with a precision of ± 1% full scale, and a resolution of ± 0.3 mmHg (± 0.006 psi, ± 0.04 kPa). As the working temperature range is between 10 °C and 50 °C, the gauge is suitable for shock tube experiments but not for explosively driven field tests.

Miniature pressure sensors are a specialised product with few manufacturers producing items of a truly miniature nature. Alternative commercial pressure sensors are available which use piezo crystals to generate recordable electrical outputs when pressure loadings are applied; piezoelectric transducers generate a direct electrical output on pressure loading whereas piezoresistive transducers produce a change in resistance on pressure loading which is converted into a useable voltage output via a wheatstone bridge or similar. Two such examples of alternative miniature transducers being PCB Piezotronics micro piezoelectric wind tunnel pressure sensor model 132B38 [116] and Millar Inc. piezoresistive SPR-1000 Mikrotip [117].

A brief comparison of some of the properties of these alternative gauges can be seen in Table 5.2.

Although it can be difficult to derive a true comparison between gauge types due to the difference in reporting specifications between manufacturers, the brief comparison shown in Table 5.2 shows that finding an alternative gauge of a higher sampling rate is possible;

Property	μ ICP 132B38	SPR 1000	FOP-LS-2FR-30
Max Pressure	50 psi (345 kPa)	4000 mmHg* (533 kPa)	10 bar (1000 kPa)
Sensitivity	20.3 mV/kPa	37.6 μV/V/kPa	–
Resolution	0.007 kPa	–	0.04 kPa
Low Frequency Response	11 kHz	–	–
Resonant Frequency	$\geq$ 1000 kHz	$\geq$ 10kHz	–
Sampling Rate	–	–	15 kHz analogue 5 kHz digital
Tip Diameter	3 mm	1F (0.33 mm)	2F (0.66 mm)

* Operating pressure range is up to 4000 mmHg (5.3 bar) but linear operating range is only up to 300 mmHg (0.4 bar)

Table 5.2: Comparison of available pressure gauges

however matching the operating pressure and physical gauge size requirements make the choice a little more limited.

5.2.6 Novelty of Miniature Stagnation Probe Design

A quick search of diagnostic equipment catalogues is likely to return a large number of stagnation probes, stagnation-pitot probes and small pressure probes for use across varying pressure ranges. The application required within this research imposed limitations, both pressure and physical dimension, making use of available commercial pressure gauges, and even specialised designs such as that of Josey *et al*, impractical. From this, a stagnation pressure gauge of original design was required, which included novel features:

- Miniature physical dimensions; overall diameter (including external protection) 1.1 mm with a sensing element diameter of 0.67 mm.
- Optical pressure sensing element; no electrical interference on recorded signal.
- Minimal reflected pressure signal; gauge design makes positive use of physical size to enable shock wave clearing to rapidly reduce the measured signal from a recorded pressure to the stagnation pressure. This can limit the potential for over-ranging

the gauge due to the initial shock peak.

Future improvements to the consistency and reproducibility of manufacturing should be made to move the research forward, including:

- Laser cutting, laser welding of components, ion beam milling
- Use of bespoke thin walled external protection; this may be non metallic if right material properties available
- Thin walled cylinder bending methods, to enable probe to be fixed off axis and reduce potential blockage effects from location hardware. This may also reduce whipping effects on the fibre optic.

5.3 Experimental Data Analysis

5.3.1 Shock Tube Blockage Effect Corrections

The measurement of the stagnation pressure within the venting flow is akin to common measurements made within wind tunnels during aerodynamic flow experiments. These aerodynamic measurements often require data correction factors to be applied to account for the effect of the test item or measurement gauge on the flow being measured; to minimise this effect the ratio of test item frontal area to the wind tunnel working section cross-sectional area is minimised where possible. In the experiments undertaken here, the test item frontal area is that of the stagnation gauge and the test section cross-sectional area is that of the venting gap under test, which for the majority of the experiments conducted gives a blockage factor, β,

$$\beta = \frac{\text{test item frontal area}}{\text{test section area}} = \frac{4\pi d_{gauge}^2}{4\pi d_{vent}^2} = \left(\frac{d_{gauge}}{d_{vent}}\right)^2 \tag{5.9}$$

where d_{gauge} and d_{vent} are the diameters of the stagnation pressure gauge and vent opening respectively.

For the case of a 1.1 mm diameter stagnation probe within a 6 mm diameter vent, it can be seen that

$$\beta = \left(\frac{1.1}{6}\right)^2 = 0.0336 \quad (3.36\%)$$

Using this simple method of calculating the blockage factor gives a value which is well below the maximum tolerable ratio of the model frontal area to tunnel cross sectional area of 7.5% [118] and is therefore not expected to produce a significant effect; however as shown in Figure 5.40 the physical hardware required to locate the stagnation pressure probe sits very close the outer face of the shock tube end plate and will undoubtedly cause some effect on the venting flow. Gould [119] showed an increase in the blockage factor, due to an increase in the ratio of projected areas, had an effect on the static pressure measured. From this, it was expected that the presence of the stagnation probe in the flow would lead to an over-estimation of the dynamic pressure in the vent opening.

Calculation of the blockage factor derived from a combination of the stagnation pressure probe frontal area and the probe location hardware sitting external to the venting gap is a somewhat more complex situation, and the effect is better quantified experimentally.

To this end a series of experiments were run measuring the static pressure both with and without the stagnation pressure probe and location hardware in position to enable a direct comparison to be made, and the subsequent effect on the static pressure due to the presence of the stagnation pressure probe (and associated hardware) to be quantified. The experiments were designed to keep the location of the stagnation pressure probe constant whilst enabling the distance between the location hardware and the end plate outer face to be varied. The results could then be used to determine the experimental setup which gave the minimal blockage effect on the static pressure; this setup was then employed for the remainder of the experimental campaign.

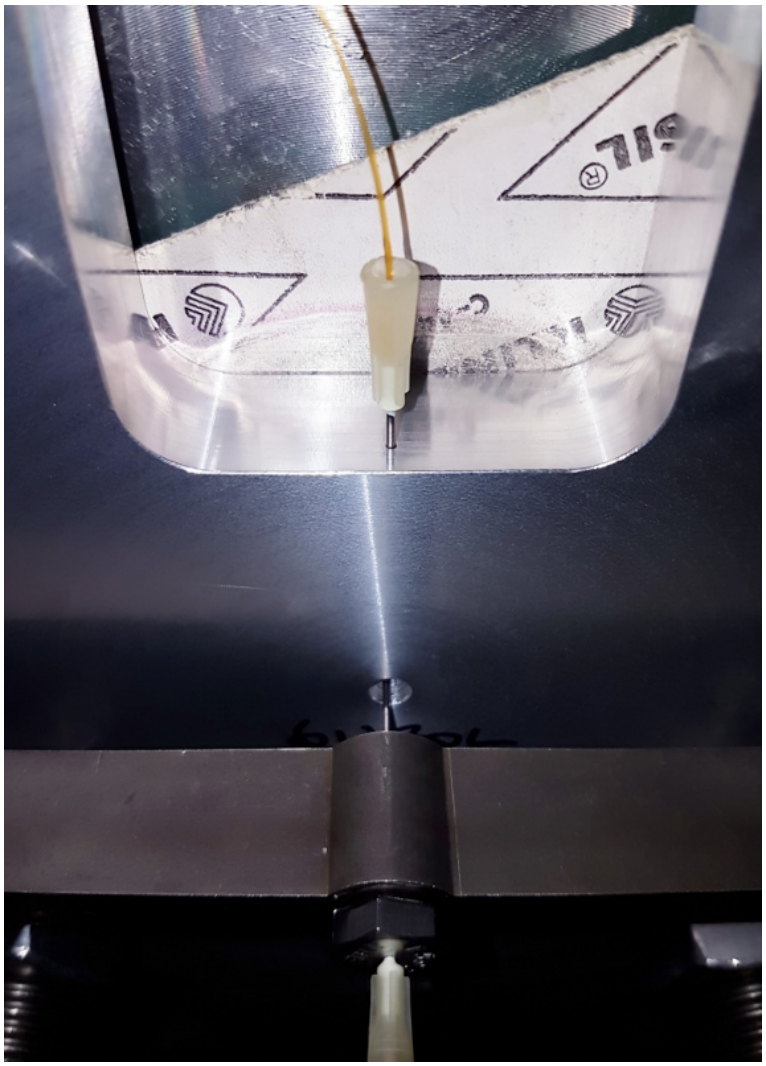


Figure 5.40: Stagnation Pressure Probe Location Hardware

Running these experiments with a driver pressure of 8 bar and 10 bar allowed the graphs in Figure 5.41 and Figure 5.42 to be constructed.

It may be possible to determine that there is a qualitative difference between the static pressure recorded for a 15 mm standoff and a 5 mm standoff between the stagnation probe location hardware and the outer face of the shock tube end plate; however due to the high levels of inconsistency between the static pressure results measured for the cases with a 5 mm standoff, it is not possible to determine any quantitative differences between the measured peak values. Given these levels of inconsistency, it was not feasible to use the 5 mm standoff setup to undertake any meaningful investigation of flow effects so the setup using the 15 mm standoff was used exclusively for the data capture phase of the

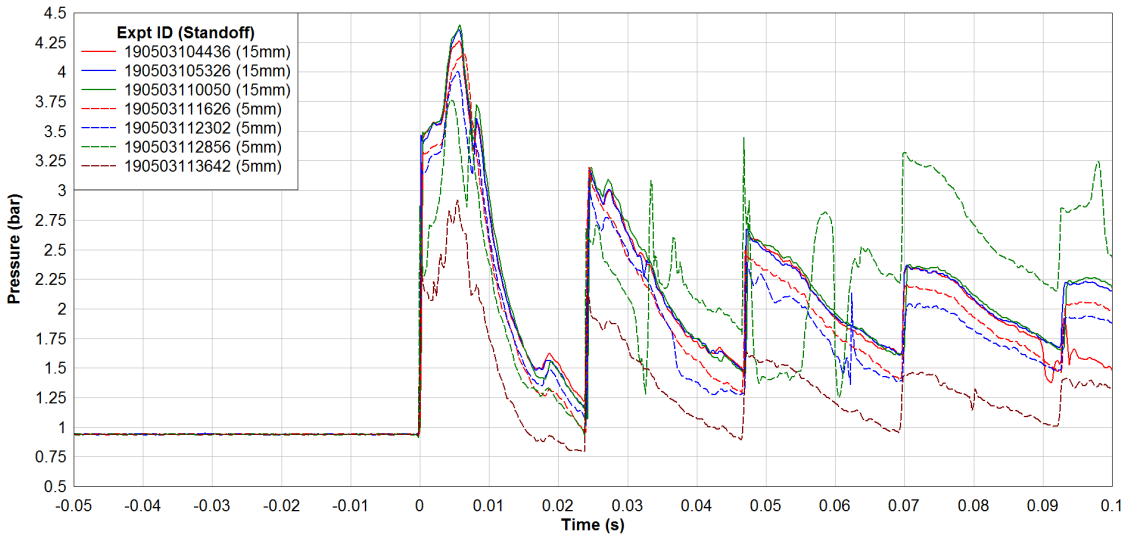


Figure 5.41: Stagnation Pressure Probe Hardware Effects - 8 bar Driver Pressure

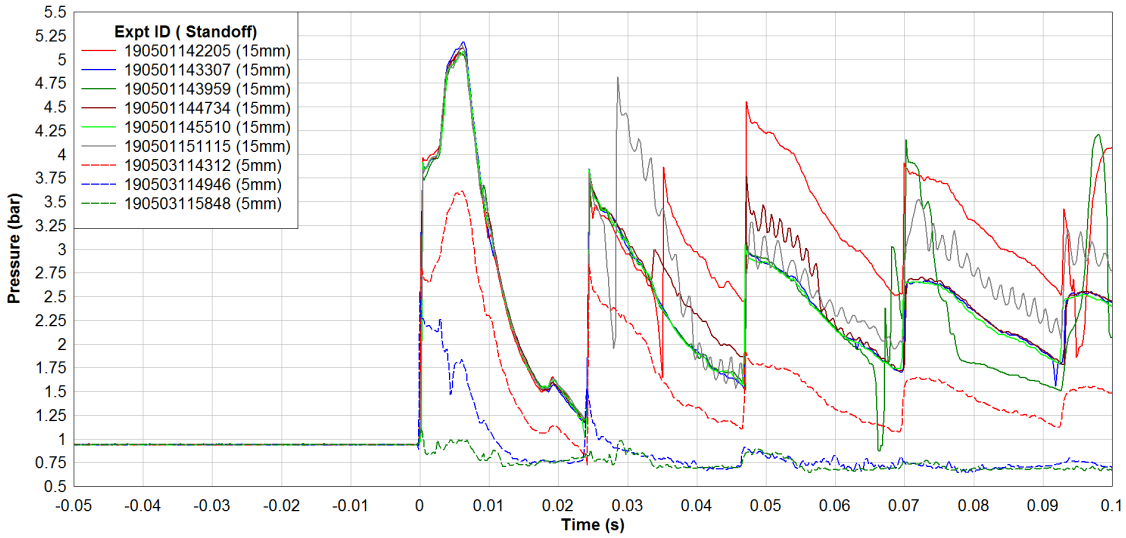


Figure 5.42: Stagnation Pressure Probe Hardware Effects - 10 bar Driver Pressure

experimental campaign.

The blockage correction factor was then calculated by the direct comparison of the measured static pressures recorded for the experiments run with only the static pressure gauge in place (i.e. no stagnation pressure probe or location hardware in position) and those experiments run with the stagnation pressure probe in position (probe end located 5 mm into the gap from the outer face of the end plate and the location hardware located at a 15 mm standoff from the same outer face).

Doing this with an 8 bar driver pressure gives the traces shown in Figure 5.43.

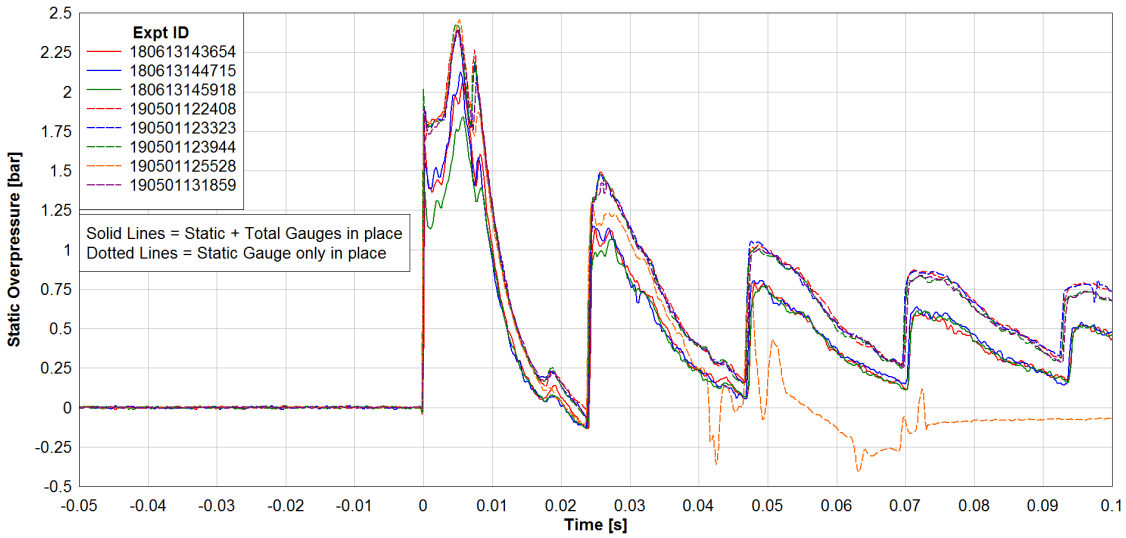


Figure 5.43: Static Pressure Measurements - 8 bar Driver Pressure

From this it can be seen that the static pressure measurements made with the stagnation pressure probe and location hardware in position are consistently lower than for an open 6mm vent gap with only the static pressure probe in place. Taking the averages of each curve set shown in Figure 5.43 allows the comparison shown in Figure 5.44 to be made.

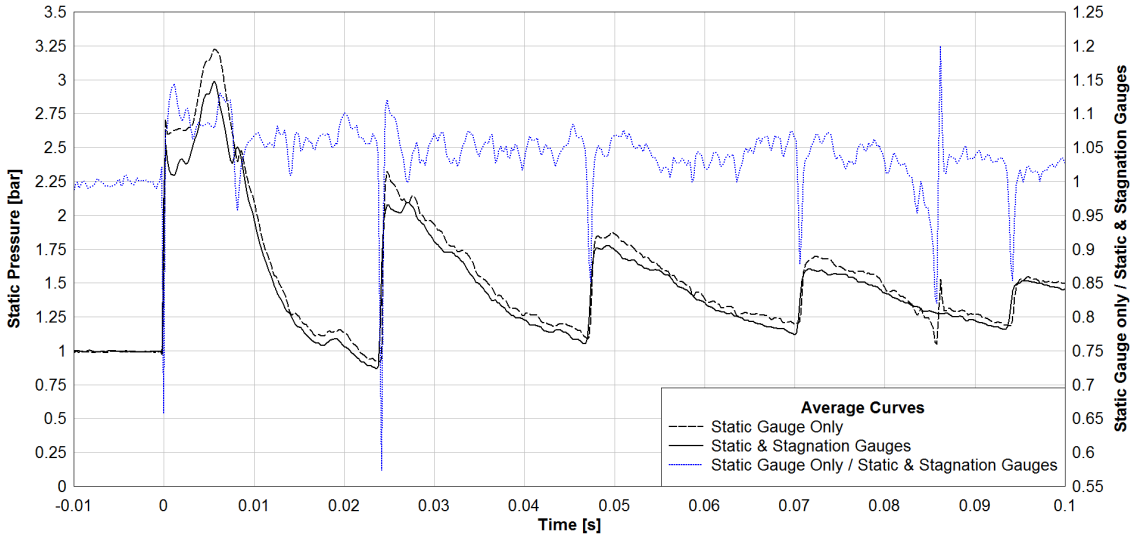


Figure 5.44: Blockage Correction Factor - 8 bar Driver Pressure, 6mm gap width

Here the ratio of static pressure with only the static pressure gauge in place against that with the stagnation pressure probe and location hardware in place can be seen plotted against the secondary ordinate axis; giving a value of approximately 1.1 for times less than

8 ms and 1.05 for times greater than 8 ms.

Similarly for a driver pressure of 10 bar, Figure 5.45 can be drawn where once again it can clearly be seen that the static pressure measured was higher for the experiments where the stagnation pressure probe and location hardware were not fielded.

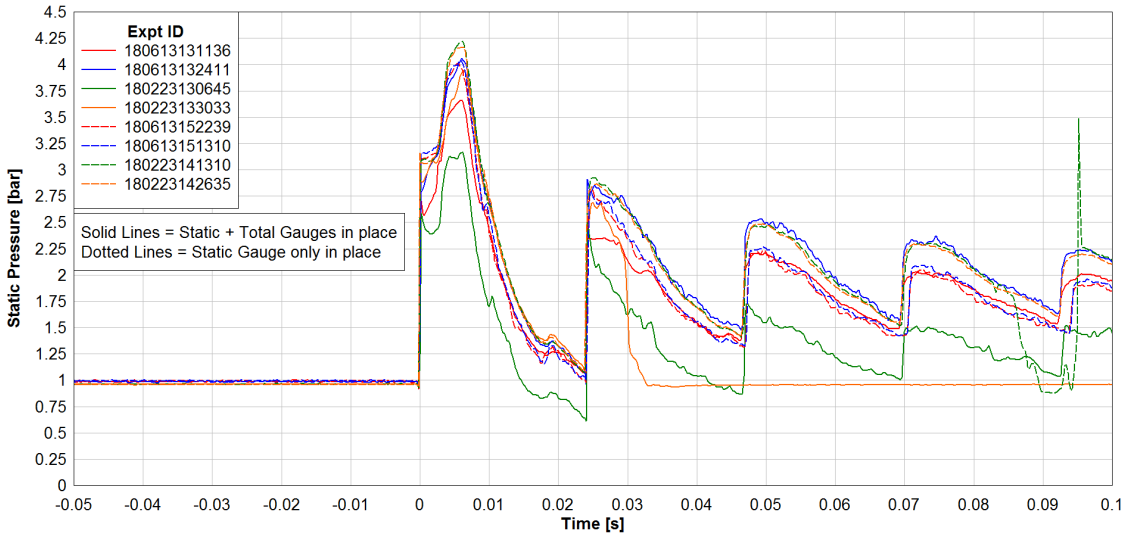


Figure 5.45: Static Pressure Measurements - 10 bar Driver Pressure

As before, it was possible to take an average of the traces for each setup case and plot them for comparison, as in Figure 5.46.

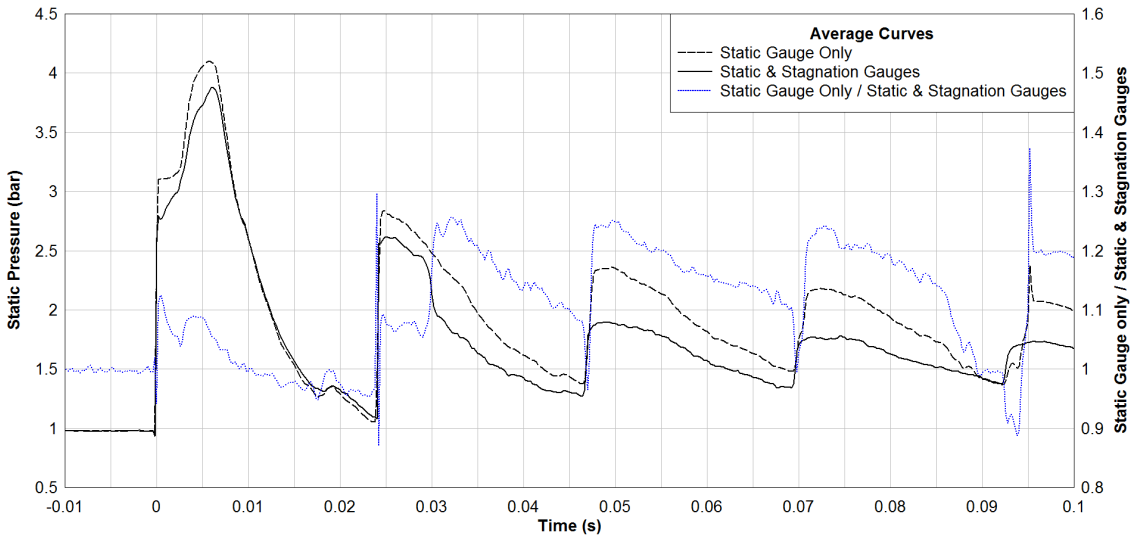


Figure 5.46: Blockage Correction Factor - 10 bar Driver Pressure, 6mm gap width

Again the ratio of static pressure with only the static pressure gauge in place against that with the stagnation pressure probe and location hardware in place can be seen plotted

against the secondary ordinate axis; however this time it is more difficult to ascertain any plateau values for the ratio as, except for an early peak, it is consistently decreasing with time for each shock tube pulse. For the pulse of interest it can be seen to decrease from approximately 1.1 to a fraction under unity. At this stage the cause of the dip before 0.5 ms is unknown but may be an artefact of the flow development along the gap. It may be possible to determine more details using the numerical simulation of this case.

Looking at the curves for the measured static pressures for both setups in Figure 5.44 and Figure 5.46, it can be seen that for both driver pressures tested the results agree with the statement made by Gould [119]. Use of the static pressure measured with the stagnation pressure probe and location hardware in place without any correction for the blockage effects would lead to a reduced static pressure value as thus an over estimation of the dynamic pressure.

Taking the curves for the ratio of pressures from Figure 5.44 and Figure 5.46 allows Figure 5.47 to be drawn for a more direct comparison of the results from the two driver pressure cases.

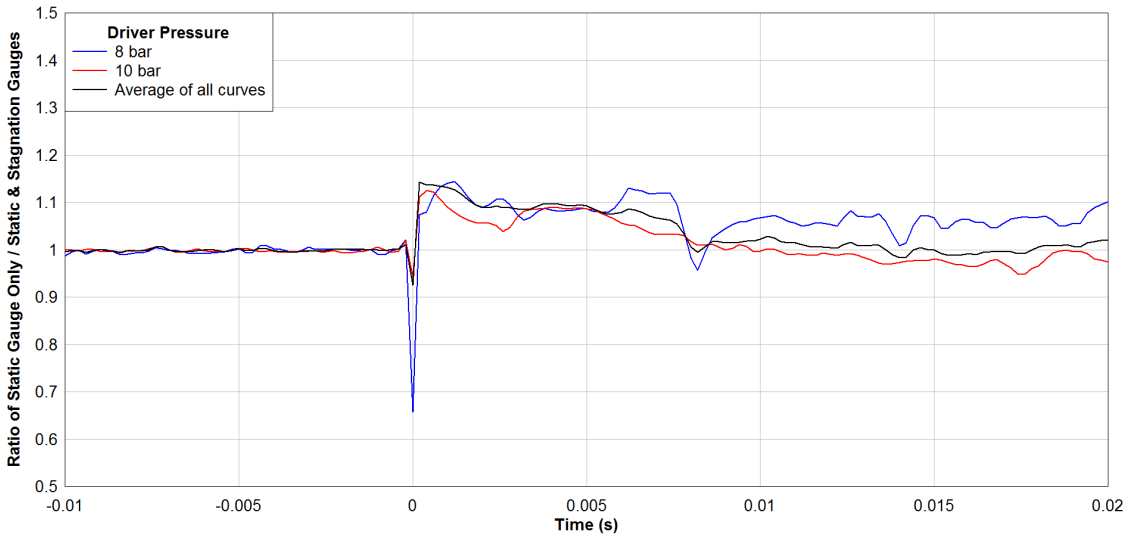


Figure 5.47: Blockage Effects - 6mm gap width

Concentrating on the initial flow pulse, lasting out to approximately 24 ms, shows that notwithstanding the artefact at approximately 8 ms the blockage effect for an 8 bar driver pressure is more consistent. The flow conditions developed from a 10 bar driver

pressure are such that the blockage effect varies slightly with time, with the actual value decreasing almost linearly with increasing time. The overall setup for the experiments does not give enough detail regarding the actual flow regimes to be able to experimentally determine the reason for this; however it may be possible to make use of some of the numerical modelling data generated, although it is likely that much higher fidelity numerical simulations including turbulent flow will be required for this.

At this stage, it is reasonable to apply an average set of correction factors to each of the experimentally measured static pressure results during the generation of the flow Mach number results. Taking the figures generated in Figure 5.47, it was possible to equate the experimental setup of static pressure gauge only in place as being the corrected value, whilst the experimental setup with the stagnation pressure gauge and location hardware in place was taken as the measured value. This gave a blockage correction of

$$\frac{P_{s_{corrected}}}{P_{s_{measured}}} = \begin{cases} 1.08 & \text{for t} < 8\text{ms} \\ 1.00 & \text{for t} > 8\text{ms} \end{cases} \tag{5.10}$$

which was applied before the local flow Mach number could be determined.

5.3.2 Local Flow Mach Number Determination

Once the static pressure measurements had been corrected for the blockage caused by the presence of the diagnostic hardware, the next stage of the analysis was to determine the local Mach number within the flow. From the pressure traces shown in the previous section, it could be seen that there was a small but finite time required for the flow to stabilise within the gap, signified by the time taken for the pressure rise within each measurement. The response of the gauges employed was not sufficient to detect any minor variations in the flow due to turbulence, however global variations between subsonic and supersonic flow were measurable. This meant that the flow characteristics must be

analysed such that both subsonic and supersonic flow could be determined.

For very low speed flow, usually limited to that with a Mach number less than 0.3, standard aerodynamic texts suggested the use of incompressible theory was acceptable. Above this limit of Mach 0.3, the changes in density with speed are large enough to invalidate the constant density assumption required for incompressible flow theory to hold. As the expected flow regime within the gap is one with a Mach number far in excess of the Mach 0.3 limit for incompressible flow, this theory was not applicable within the analysis required.

A relatively simple reorganisation of the Bernoulli theory could be used to determine the Mach number directly from the measured static and stagnation pressures. For this, it was seen that

$$q = (P_T - P_S) = \frac{\gamma}{2} p_S M^2 \tag{5.11}$$

thus

$$M = \sqrt{\frac{2}{\gamma}\left(\frac{P_T}{P_S} - 1\right)} \tag{5.12}$$

similarly

$$\frac{P_T}{P_S} = 1 + \frac{\gamma}{2} M^2 \tag{5.13}$$

This approach, however, was also only valid for very low Mach number flow.

A more appropriate flow model was that for compressible flow, which accounts for variations in density and is applicable across a much wider range of Mach numbers. From standard derivations, i.e. [105, 120], it was possible to describe compressible flow through the compressibility equation

$$\frac{\rho_T}{\rho_S} = \left(1 + \frac{\gamma - 1}{2} M^2\right)^{\frac{1}{\gamma - 1}} \tag{5.14}$$

which can be combined with the isentropic condition

$$\frac{P}{\rho^{\gamma}} = \text{constant} \tag{5.15}$$

to give a description of compressible flow theory as the ratio of the stagnation and static pressures

$$\frac{P_T}{P_S} = \left(1 + \frac{\gamma - 1}{2} M^2\right)^{\frac{\gamma}{\gamma - 1}} \tag{5.16}$$

The relatively simple form of the compressible flow equation allows it to be algebraically manipulated to give the Mach number directly against the ratio of the stagnation and static pressures, such that

$$M = \sqrt{\frac{2}{\gamma - 1}\left[\left(\frac{P_T}{P_S}\right)^{\frac{\gamma - 1}{\gamma}} - 1\right]} \tag{5.17}$$

The situation is made more complex by the potential for the flow to become supersonic, which may lead to the development of a detached bow shock ahead of the stagnation probe. Although the physical dimensions of the miniature stagnation probe have been kept small, the flat front end is capable of generating a bow shock which is effectively a normal shock upstream of the gauge on the stagnation streamline, thereby generating an area of subsonic flow immediately ahead of the probe tip. The analysis conducted must therefore determine and account for the presence of this bow shock. If one does exist in the experimental flow, the reduction in total pressure across the shock would mean that the stagnation pressure measured, p_{T_2}, was less than the expected isentropic stagnation pressure, p_{T_1}, as shown in Figure 5.48.

Using standard normal shock theory, i.e. [105], the flow immediately behind the shock can be determined.

$$\frac{P_{T_2}}{P_{S_2}} = \left(1 + \frac{\gamma - 1}{2} M^2\right)^{\frac{\gamma}{\gamma - 1}} \tag{5.18}$$

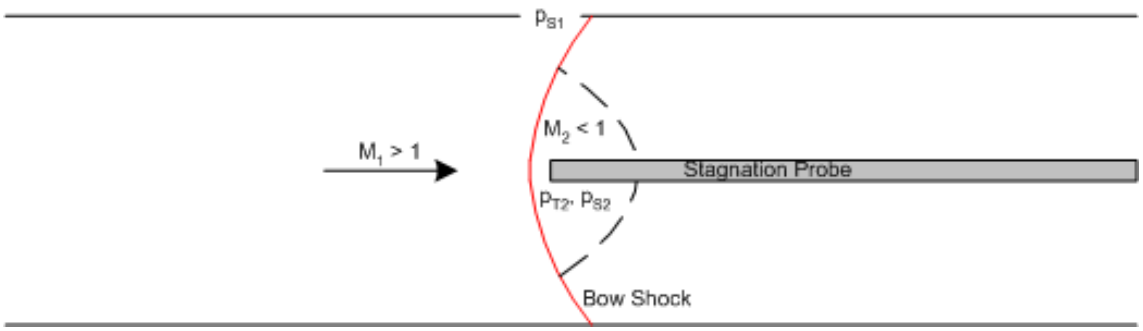


Figure 5.48: Schematic of Potential Bow Shock for Supersonic Flow in Experiments

However, as the analysis of the experimental data was concerned with the determination of the flow Mach number ahead of the bow shock, M_1, it was necessary to generate a relationship between M_1, and the measured pressures P_{T_2} and P_{S_1}.

$$\frac{P_{T_2}}{P_{S_1}} = \frac{P_{T_2}}{P_{S_2}} \frac{P_{S_2}}{P_{S_1}} \tag{5.19}$$

Within normal shock theory, conservation of momentum gives

$$P_{S_1} + \rho_1 U_1^2 = P_{S_2} + \rho_2 U_2^2 \tag{5.20}$$

Combining this with the definition of dynamic pressure, isentropic flow, and assuming ideal gas properties, it can be shown through

$$q = \frac{1}{2}\rho U^2 = \frac{\gamma}{2} P M^2$$

that

$$\rho_1 U_1^2 = \gamma P_{S_1} M_1^2 \quad ; \quad \rho_2 U_2^2 = \gamma P_{S_2} M_2^2 \tag{5.21}$$

and hence substituting Equation 5.21 into Equation 5.20 gives

$$P_{S_1} + \gamma P_{S_1} M_1^2 = P_{S_2} + \gamma P_{S_2} M_2^2$$

which can be rearranged to give

$$\frac{P_{S_2}}{P_{S_1}} = \frac{1 + \gamma M_1^2}{1 + \gamma M_2^2} \tag{5.22}$$

Using Prandtls relation for normal shock waves [105]

$$M_2^2 = \frac{1 + \left(\frac{\gamma-1}{2}\right) M_1^2}{\gamma M_1^2 - \left(\frac{\gamma-1}{2}\right)} \tag{5.23}$$

which can be rearranged to give

$$M_2^2 = \frac{2 + (\gamma - 1) M_1^2}{2\gamma M_1^2 - (\gamma - 1)}$$

and substituted into Equation 5.22 to give

$$\frac{P_{S_2}}{P_{S_1}} = \frac{1 + \gamma M_1^2}{1 + \gamma \left(\frac{2+(\gamma-1)M_1^2}{2\gamma M_1^2 - (\gamma-1)}\right)}$$

which can in turn be simplified

$$\frac{P_{S_2}}{P_{S_1}} = \frac{(1 + \gamma M_1^2)(2\gamma M_1^2 - (\gamma - 1))}{2\gamma M_1^2 - (\gamma - 1) + 2\gamma + \gamma(\gamma - 1) M_1^2}$$

$$\Rightarrow \frac{P_{S_2}}{P_{S_1}} = \frac{(1 + \gamma M_1^2)(2\gamma M_1^2 - (\gamma - 1))}{2\gamma M_1^2 + \gamma + 1 + \gamma(\gamma - 1) M_1^2}$$

$$\Rightarrow \frac{P_{S_2}}{P_{S_1}} = \frac{(1 + \gamma M_1^2)(2\gamma M_1^2 - (\gamma - 1))}{(\gamma + 1) + \gamma M_1^2 (\gamma + 1)}$$

$$\Rightarrow \frac{P_{S_2}}{P_{S_1}} = \frac{2\gamma M_1^2 - (\gamma - 1)}{(\gamma + 1)}$$

$$\Rightarrow \frac{P_{S_2}}{P_{S_1}} = \frac{\gamma + 1 + 2\gamma M_1^2 - 2\gamma}{\gamma + 1}$$

$$\Rightarrow \frac{P_{S_2}}{P_{S_1}} = 1 + \frac{2\gamma}{\gamma + 1}(M_1^2 - 1) \tag{5.24}$$

Combining this with Equation 5.18, and solving Equation 5.19 gives

$$\frac{P_{T_2}}{P_{S_1}} = \left(1 + \frac{\gamma - 1}{2} M_2^2\right)^{\frac{\gamma}{\gamma - 1}} \left(\frac{(1 - \gamma) + 2\gamma M_1^2}{\gamma + 1}\right) \tag{5.25}$$

Once again using Prandtl's Normal Shock relationship, Equation 5.23 allows the Rayleigh Supersonic Pitot Equation [121] to be derived

$$\frac{P_{T_2}}{P_{S_1}} = \left(\frac{(\gamma + 1)^2 M_1^2}{4\gamma M_1^2 - 2(\gamma - 1)}\right)^{\frac{\gamma}{\gamma - 1}} \left(\frac{(1 - \gamma) + 2\gamma M_1^2}{\gamma + 1}\right) \tag{5.26}$$

Unlike the equation for the compressible subsonic flow, the complexity of the Rayleigh Supersonic Pitot equation cannot be solved directly and numerical techniques need to be employed to determine M_1.

It can be noted that solving both Equation 5.17 and Equation 5.26 with a Mach number of unity returns a stagnation to static pressure ratio of 1.89; thus any value greater than this signifies supersonic flow and the potential for the generation of a detached bow shock by the stagnation probe hardware.

Plotting both models alongside that of the Bernoulli based model, as shown in Figure 5.49, showed an increasing divergence between the two equations for approximately Mach 0.5 and above. This shows the limitation of the Bernoulli model to very low Mach numbers, and its non-applicability in this situation.

A close up view of the similarity of the Compressible Theory and Rayleigh Supersonic

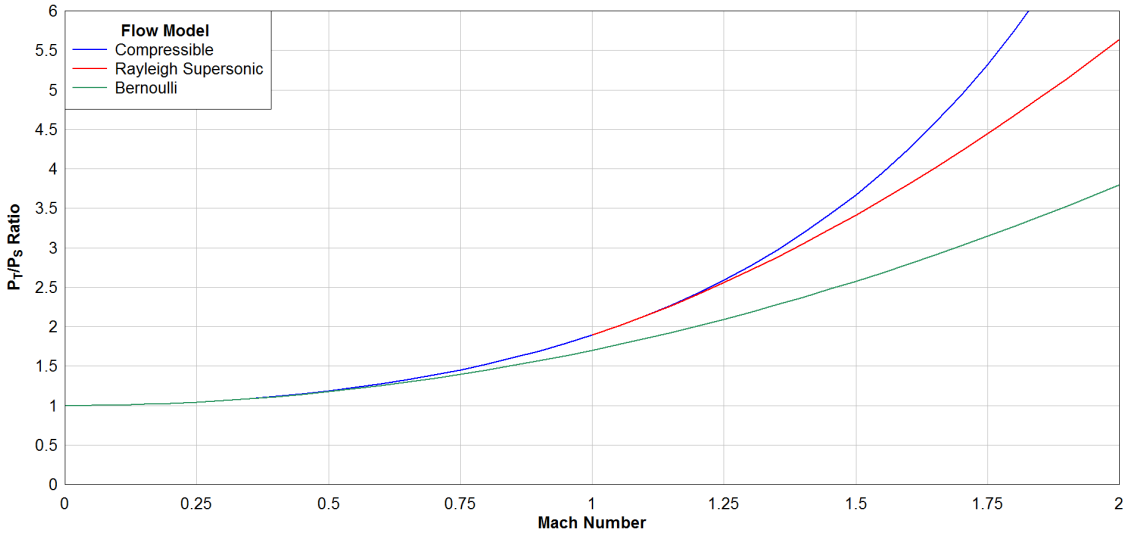


Figure 5.49: Flow Model Divergence with Mach Number

Pitot Models for the expected Mach number range of interest is shown in Figure 5.50, this also highlights the non-applicability of the Bernoulli model for this study.

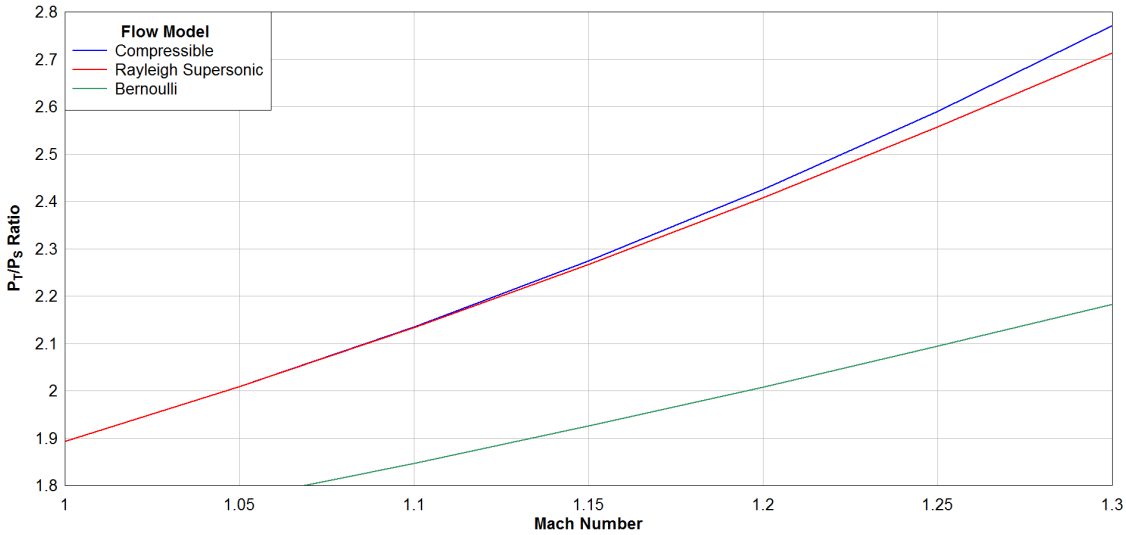


Figure 5.50: Close up of Flow Model Divergence with Mach Number

Before either of the flow models were employed within the analysis of the experimental data it was necessary to determine the potential for supersonic flow to exist; as the initial premise of the research was to establish the validity of the current assumption that ideal nozzle flow exists within the gap thus limiting the flow to a maximum Mach number of unity. If this assumption is backed by the experimental data, the ratio of stagnation to static pressures returned should plateau at a maximum value of 1.89.

Recapping, the measured pressures recorded during the experimental phase enabled Figure 5.51 and Figure 5.52 for 8 bar and 10 bar driver pressures respectively.

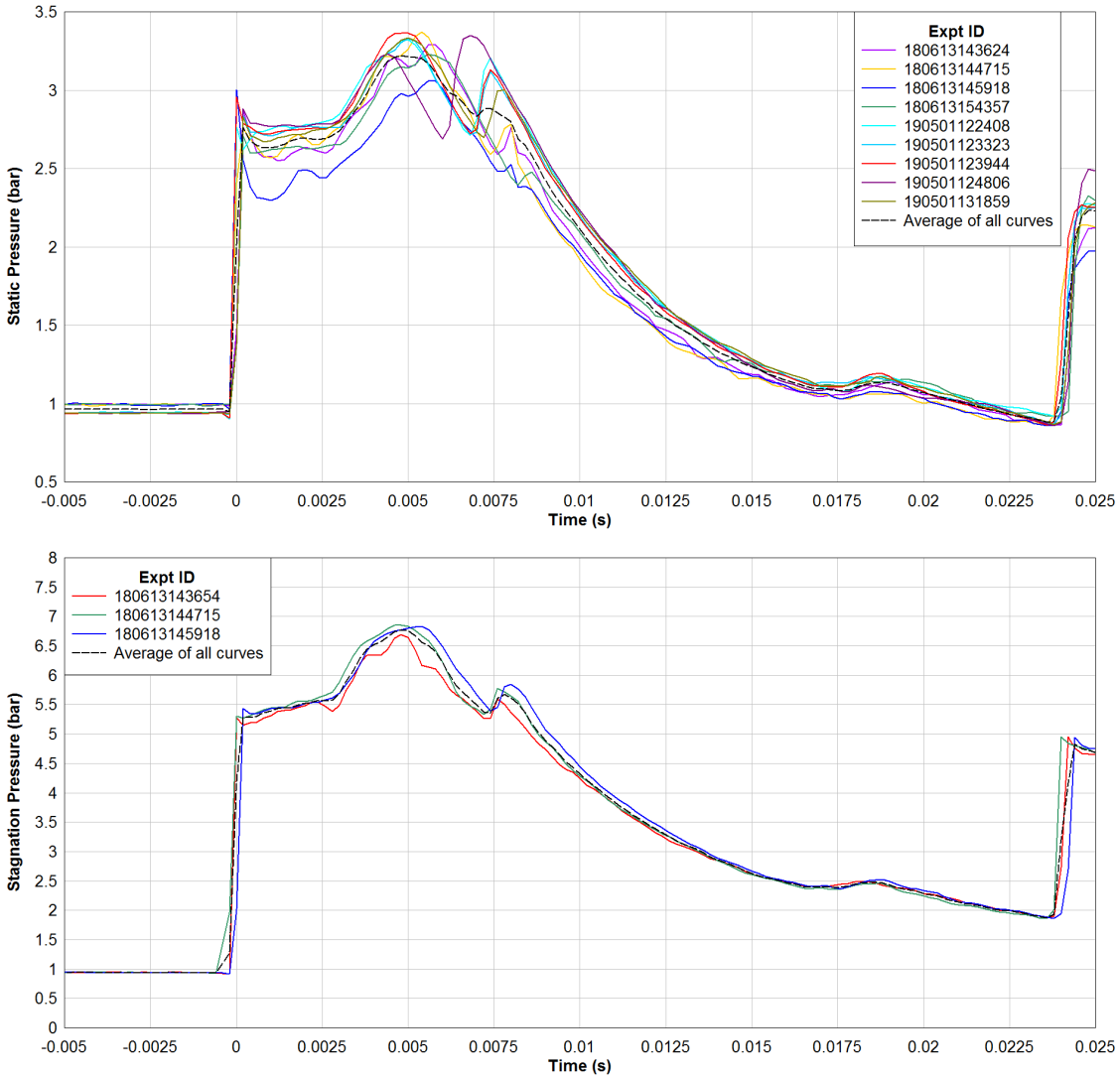


Figure 5.51: Experimental Pressure Data - 8 bar driver

Previously, it was shown that the variability of the measured results is small and thus the limited sample size available gave a usable representation of the larger population should identical experiments be repeated. Figure 5.52, however, showed a negative effect of using a small sample size whereby the effect of a single outlying trace was amplified. Within this Figure the loss of signal within the 180613134114 trace had a dramatic effect on the average trace, which would obviously be promulgated throughout the remaining analysis required.

Taking the average traces, with error bars based on standard deviation, for both

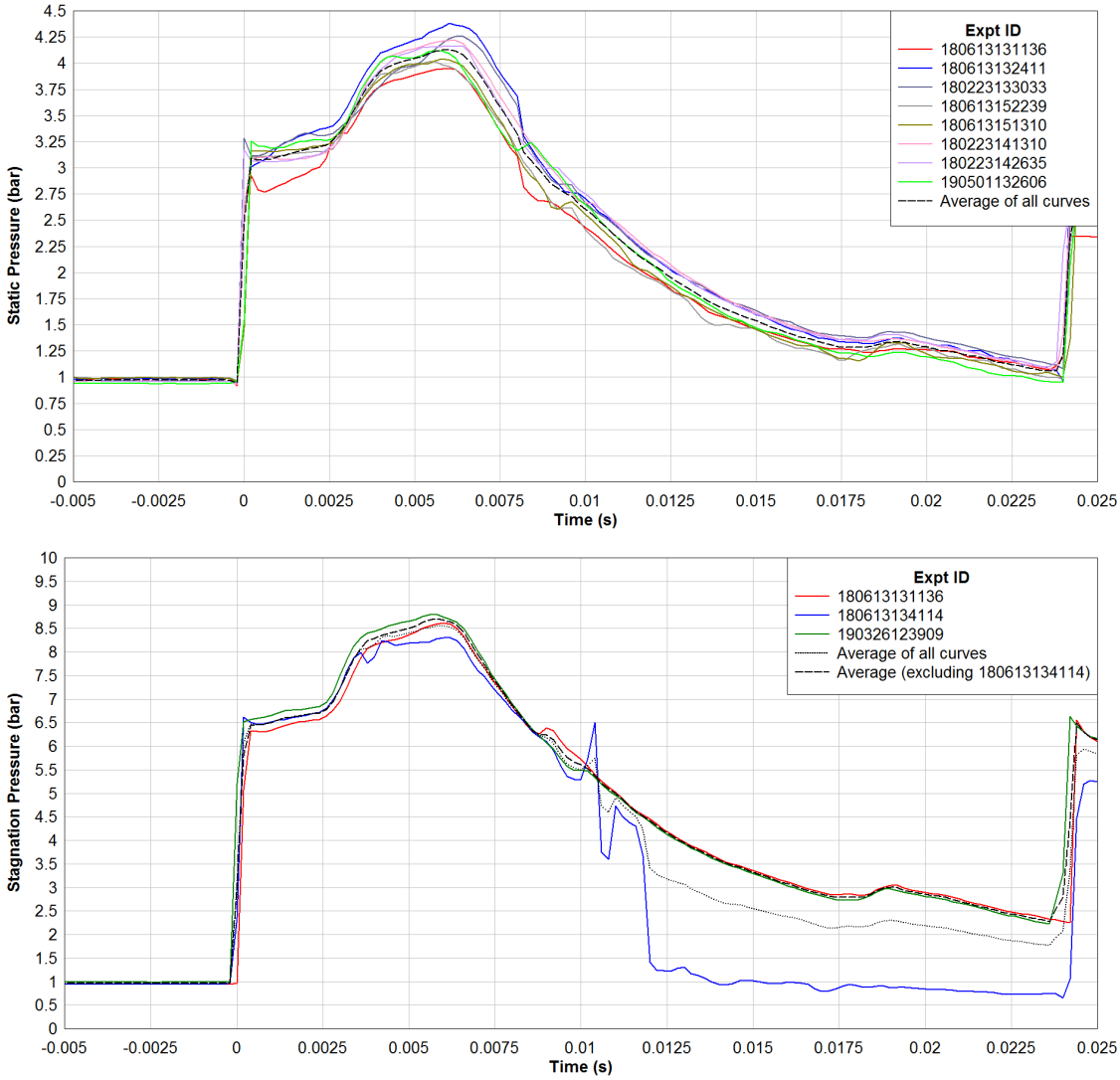


Figure 5.52: Experimental Pressure Data - 10 bar driver, static (upper) & stagnation (lower)

the static and stagnation pressures for each driver pressure allowed Figure 5.53 to be constructed.

The maximum and minimum curves for the stagnation and static pressure was combined to give the potential spread of P_T/P_S values for each driver pressure. As expected the maximum spread was seen to be between $P_{T_{max}}/P_{S_{min}}$ and $P_{T_{min}}/P_{S_{max}}$, which is highlighted by the shaded area within Figure 5.54.

The difference in shaded areas within the 10 bar driver pressure graph of Figure 5.54 shows the extent of the effect of the 180613134114 curve. This is highlighted more clearly in Figure 5.55 which shows only the ratio of stagnation to static pressure curves. The

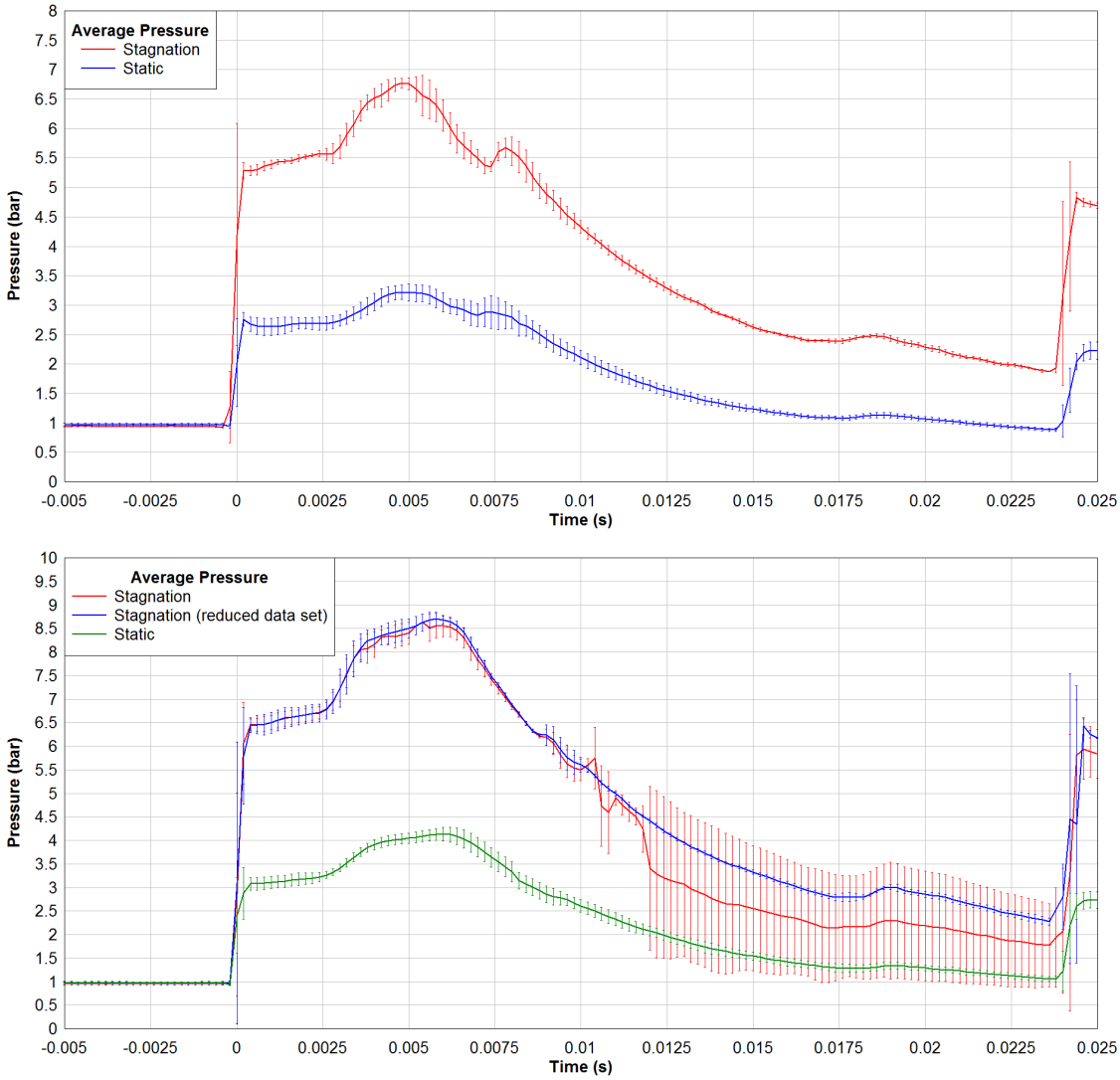


Figure 5.53: Experimental Data - Average Measured Pressures, 8 bar driver (upper) & 10 bar driver (lower)

reference line of $P_T/P_S = 1.89$ was included to show the extent of expected supersonic flow within the analysis.

Taking the highlighted areas for the 8 bar driver pressure and the reduced data set for the 10 bar driver pressure within Figure 5.55 shows a very similar spread in ratio values regardless of driver pressure. This allowed all the usable data curves to be included in the Mach number analysis regardless of driver pressure.

As the experimental data signified the expected presence of supersonic flow, it became necessary to attempt to establish whether a detached bow shock existed within the flow. The experimental setup was such that it was impossible to visualise the flow during

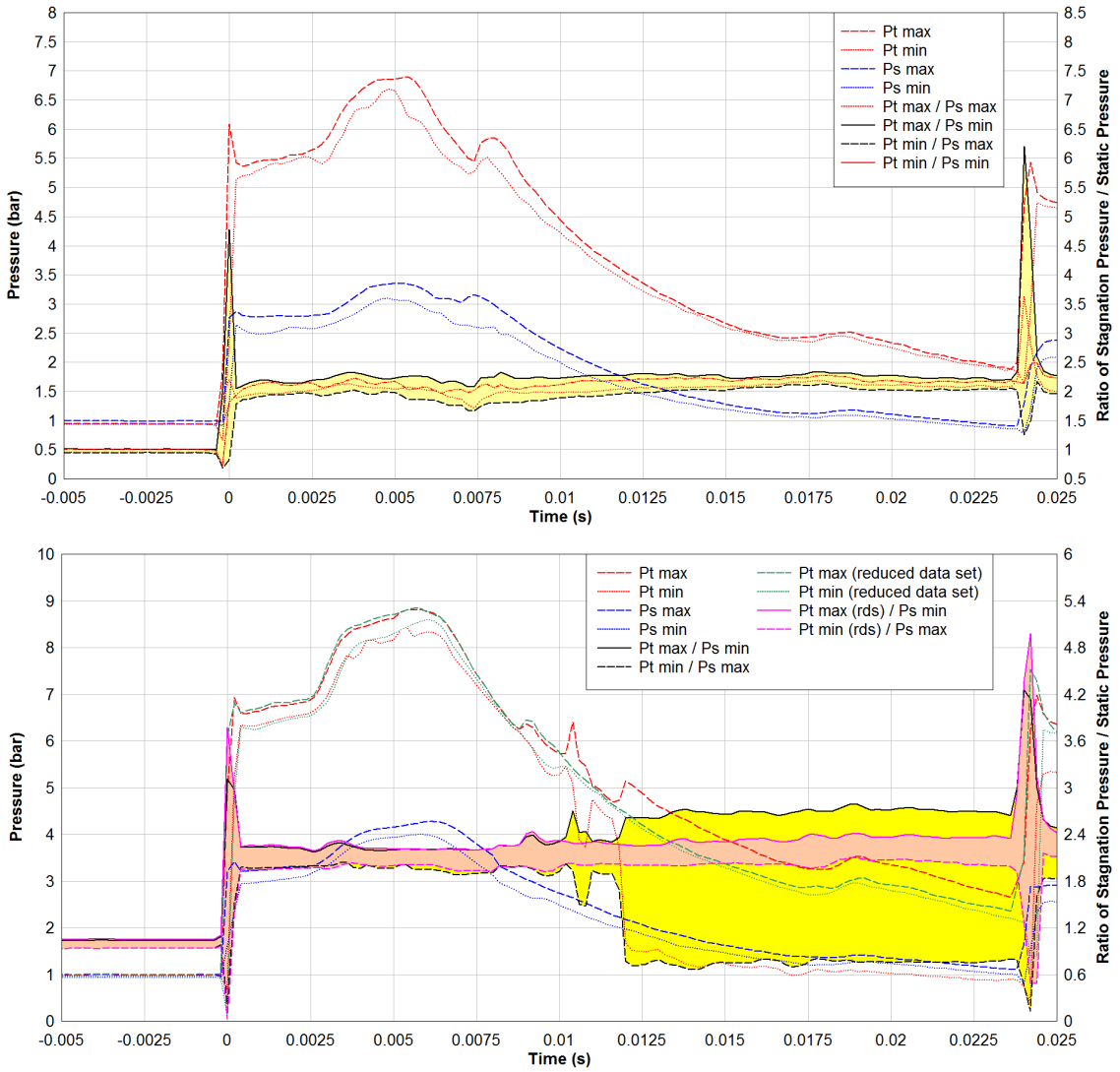


Figure 5.54: Experimental Data - Ratio of Stagnation over Static pressures, 8 bar driver (upper) & 10 bar driver (lower)

the data gathering, and this may be an area for development and improvement if the experiments are extended or repeated in the future. For now, however, it was necessary to rely on numerical modelling conducted. The model used was similar to those used during the previous sections to estimate the flow characteristics within the gap with a 6 mm gap width and a driver pressure of 10 bar; however, as signified by the shaded area within Figure 5.56, the stagnation probe hardware was removed from the Eulerian grid forming hard reflective boundaries which would not move during the analysis.

The numerical modelling was conducted using the ANSYS Student package which, as explained previously, limited the number of cells in the model to 32,000. Even using the

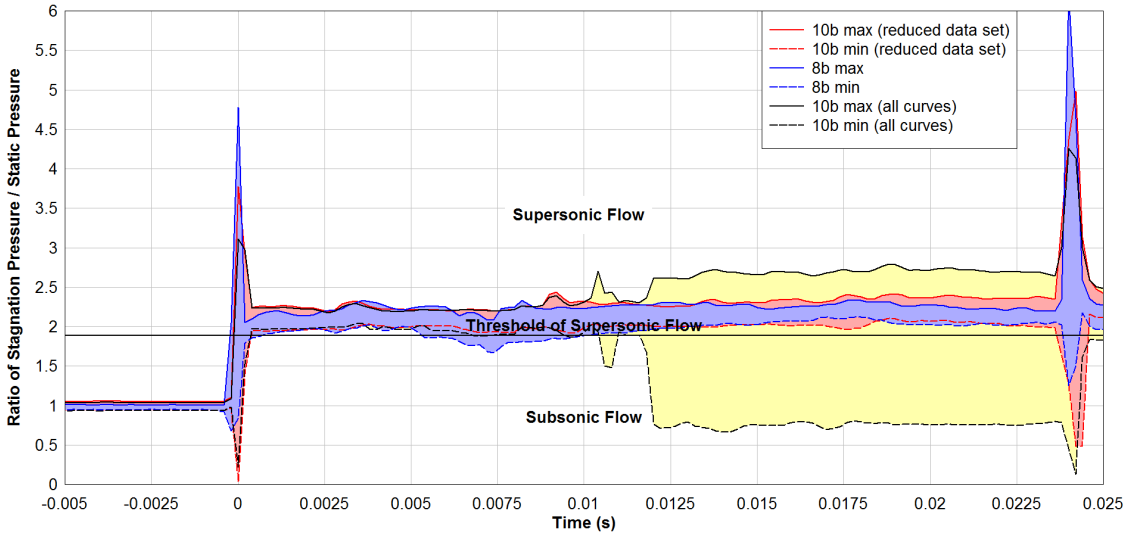


Figure 5.55: Experimental Data - Ratio of Stagnation over Static pressures

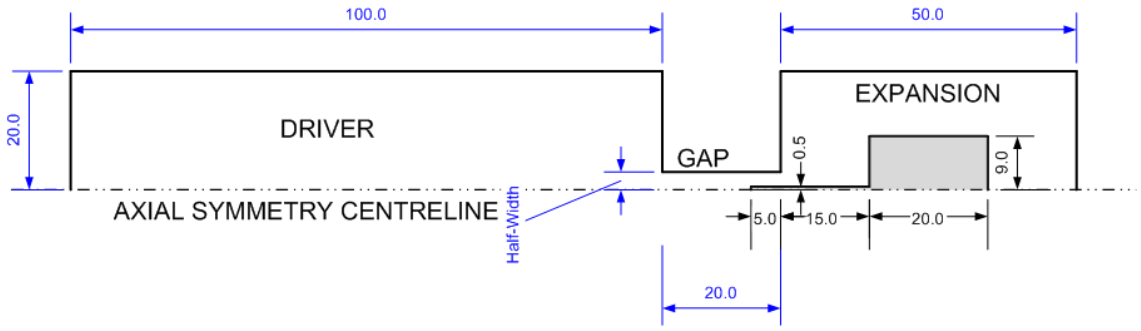
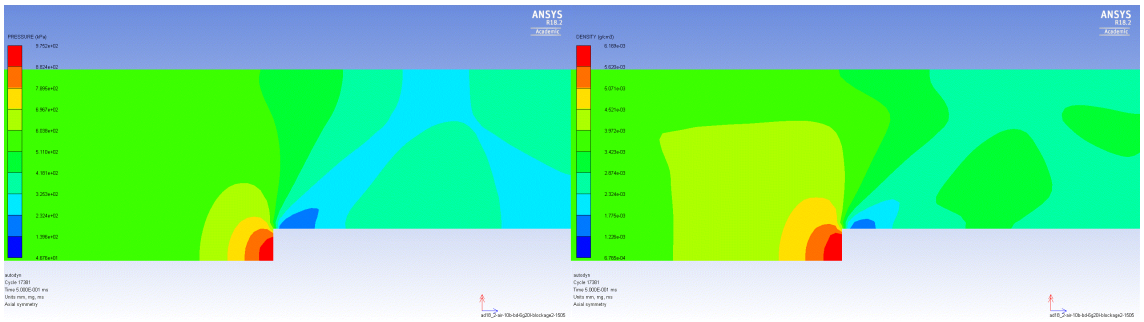


Figure 5.56: Schematic of AUTODYN Model Layout for Bow Shock Capture

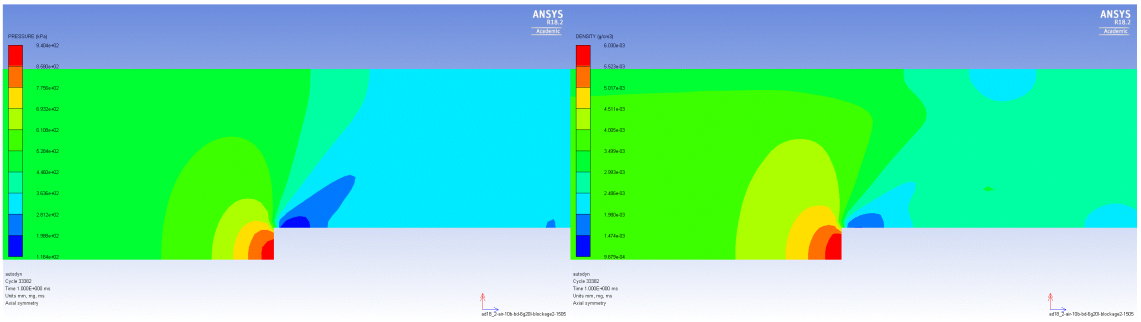
high resolution mesh from the previous numerical modelling set up gave approximately 26,000 cells within the model; this resolution may not be sufficient to see any potential bow shock definition in detail, as the resolution within the gap ahead of the stagnation probe area is only 0.1 mm in each direction.

The model was run to a calculated time of 2.0 ms, and Figure 5.57 shows the pressure and density output every 0.5 ms.

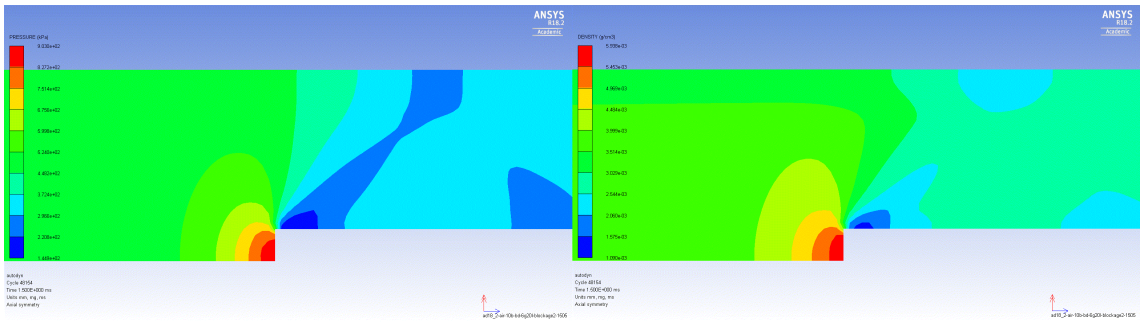
From Figure 5.57 it can be seen that a weak oblique shock wave seems to have formed near the leading corner of the stagnation probe; however, there is no evidence of a definitive strong shock wave with a distinct discontinuity in pressure and density, nor is there any evidence of a detached shock wave forming ahead of the flat face of the stagnation probe. This suggested that although the flow within the gap was supersonic, it was not of a



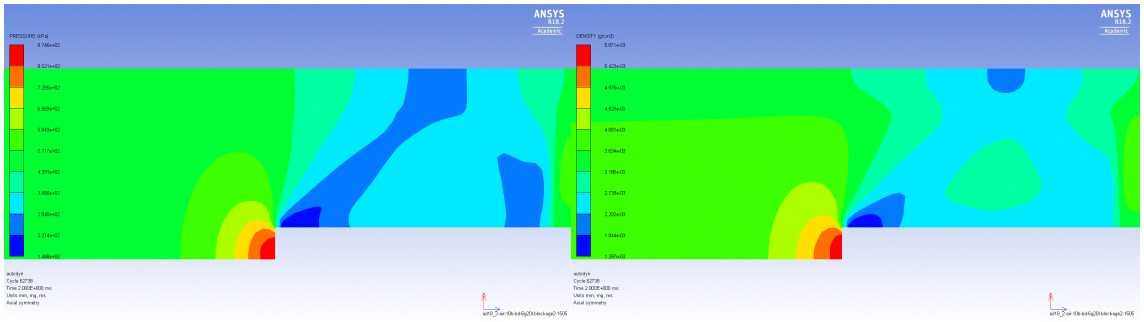
(a) Elapsed Time 0.5 ms



(b) Elapsed Time 1.0 ms



(c) Elapsed Time 1.5 ms



(d) Elapsed Time 2.0 ms

Figure 5.57: Pressure (left) and Density (right) Contour Plots for Stagnation Probe Bow Shock Analysis

high enough Mach number to form the bow shock which would make use of the Rayleigh Supersonic Pitot equation a necessity, at this stage. It should be noted here that although the numerical simulations point towards the lack of a bow shock, it is feasible that the lack

of resolution within the model has smeared the necessary detail making the final evidence ambiguous. For this reason, an investigation into the magnitude of any potential error introduced from using the inappropriate flow model (i.e. compressible flow model if a bow shock exists, or Rayleigh Supersonic Pitot model if no bow shock exists) was undertaken.

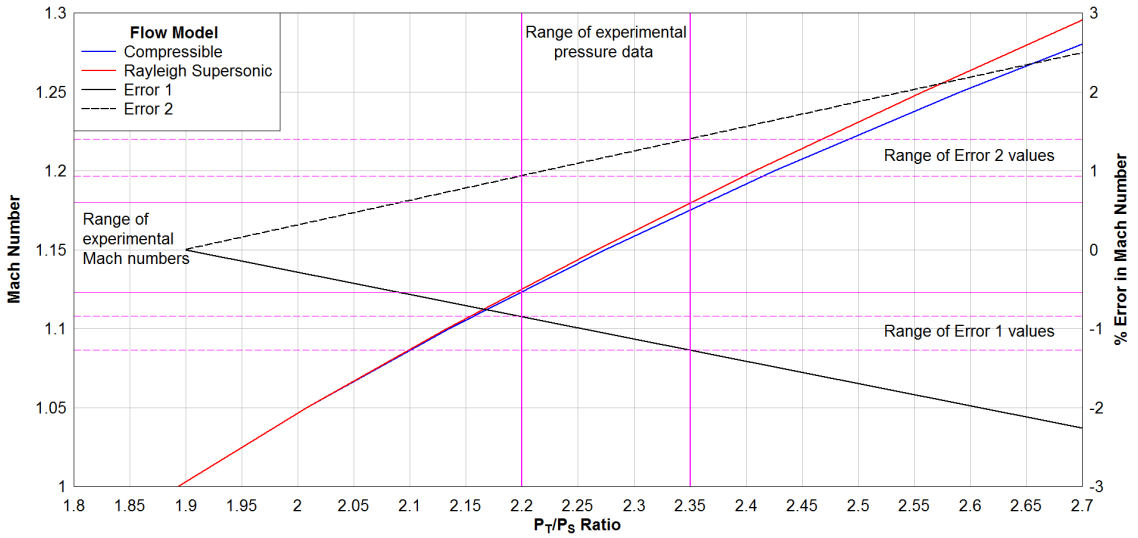


Figure 5.58: Experimental Analysis Errors due to Inappropriate Flow Model

Taking small increments in Mach number, and applying them to Equation 5.17 and Equation 5.26 it was possible to calculate the theoretical values of the stagnation to static pressure ratios for both flow models. These data were then plotted against the original Mach number, as shown in Figure 5.58, such that the Mach number was that of the upstream flow ahead of the stagnation probe and any bow shock that may or may not be present. The error lines in Figure 5.58 have been constructed to determine the uncertainty introduced by using the wrong flow model for the situation. By this, if the flow is supersonic and a detached bow shock exists ahead of the stagnation probe but the general compressible flow model is used

$$Error1(\%) = 100\left(\frac{M_{Compressible} - M_{Rayleigh}}{M_{Rayleigh}}\right) \tag{5.27}$$

Similarly if the flow is supersonic and the Rayleigh Supersonic Pitot model is used but no detached bow shock exists ahead of the stagnation probe

$$Error2(\%) = 100\left(\frac{M_{Rayleigh} - M_{Compressible}}{M_{Compressible}}\right) \tag{5.28}$$

Using the range of possible experimental values for the stagnation to static pressure ratio, p_T/p_S of between 2.2 and 2.35, estimated from Figure 5.55 and translated onto Figure 5.58, it was possible to estimate the range of Mach numbers for the flow based on the use of either flow model as being between 1.12 and 1.18. Within Figure 5.58 it was also possible to construct the reference lines giving the potential range of each error type described above, these being

$$Error1 = \begin{cases} -1.27\% & \max \\ -0.84\% & \min \end{cases} \tag{5.29}$$

$$Error2 = \begin{cases} 1.40\% & \max \\ 0.93\% & \min \end{cases} \tag{5.30}$$

which clearly shows the general trend for Error 1 to be an underestimation of the Mach number when the general compressible flow theory is applied in the presence of a detached bow shock.

Although there is evidence from the numerical modelling presented that there was no bow shock present, this underestimation of the Mach number means that use of the compressible theory in this situation was a conservative approach as any flow Mach number returned would potentially be lower than the actual flow Mach number seen within the experiment, and the final expanding weapon casing scenario. For this reason, the compressible flow theory from Equation 5.17 was applied during the final analysis of the experimental data to return the Mach number-time plot shown in Figure 5.59.

A more detailed view of the first oscillation of the shock tube shown in Figure 5.60.

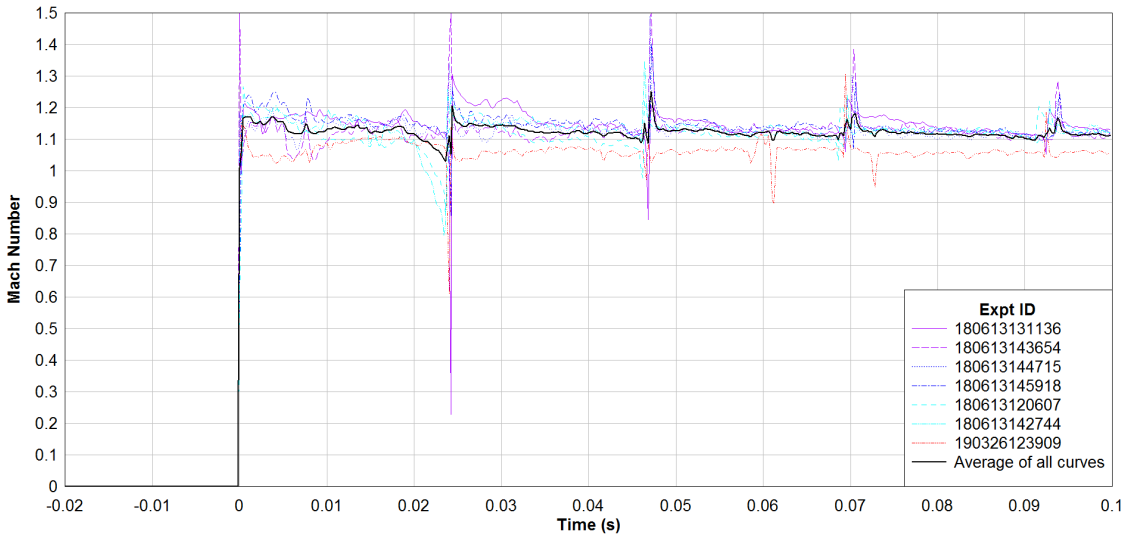


Figure 5.59: Experimentally Determined Mach Number for 6mm gap

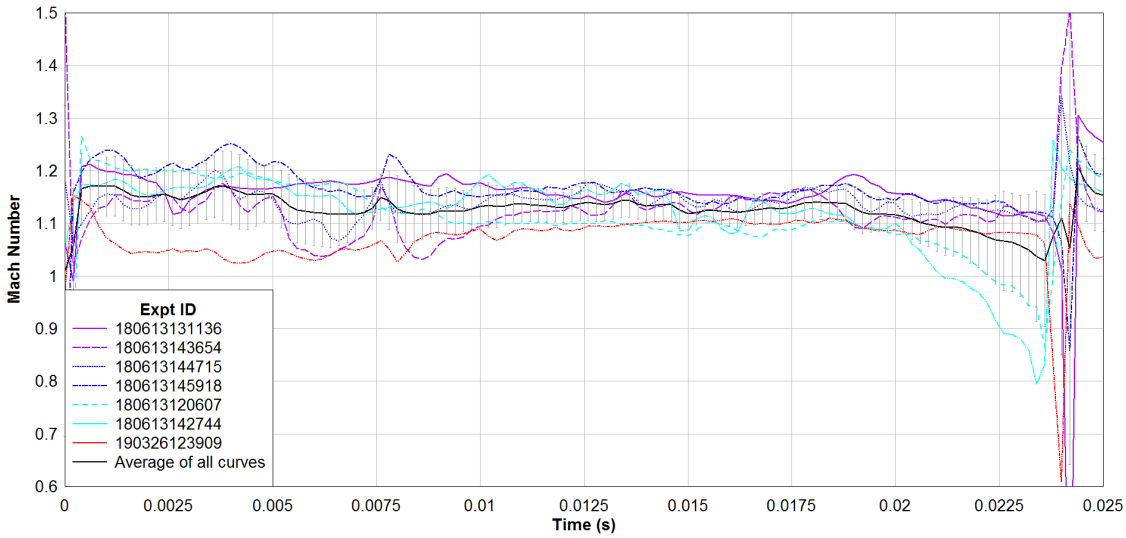


Figure 5.60: Experimentally Determined Mach Number for 6mm gap; Initial Shock Oscillation

Both Figure 5.59 and Figure 5.60 show the average local flow Mach number was in excess of Mach 1.1 for the majority of the experiment duration across the experiments reported. It can be seen that some individual experiments return flows in excess of Mach 1.2, however in general the results are in reasonable agreement with each other. Figure 5.61 shows the average Mach number trace along with an indication of how the standard deviation of the data varied with time as the experiment progressed.

Again a more detailed view of the initial oscillation of the shock tube is shown in Figure 5.62, which clearly shows the tightness of the standard deviation of the data around

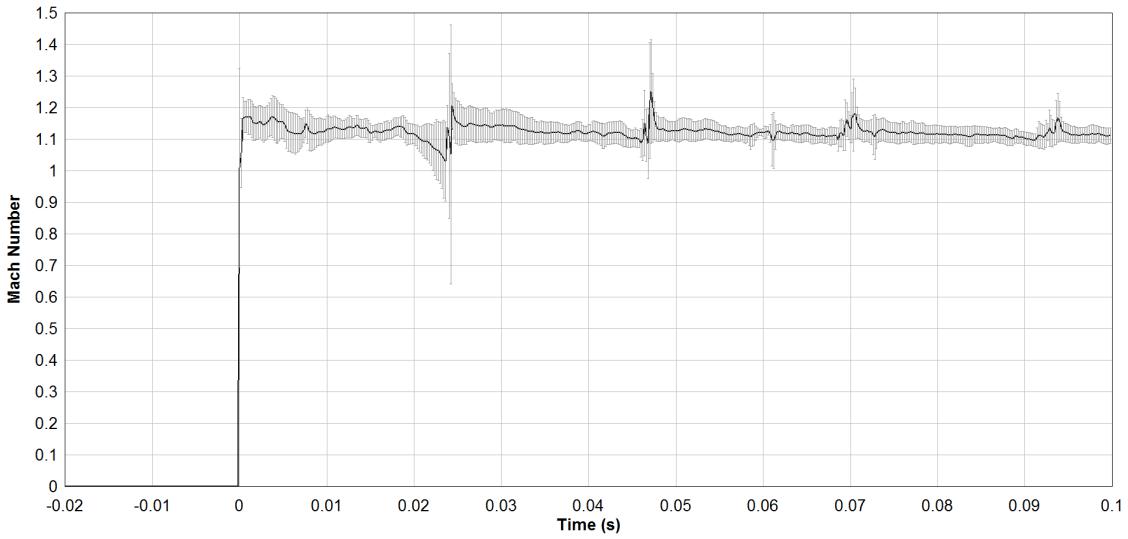


Figure 5.61: Average of Experimentally Determined Mach Number for 6mm gap with Standard Deviation

the mean value at each time, especially during the plateau phase around mid-oscillation.

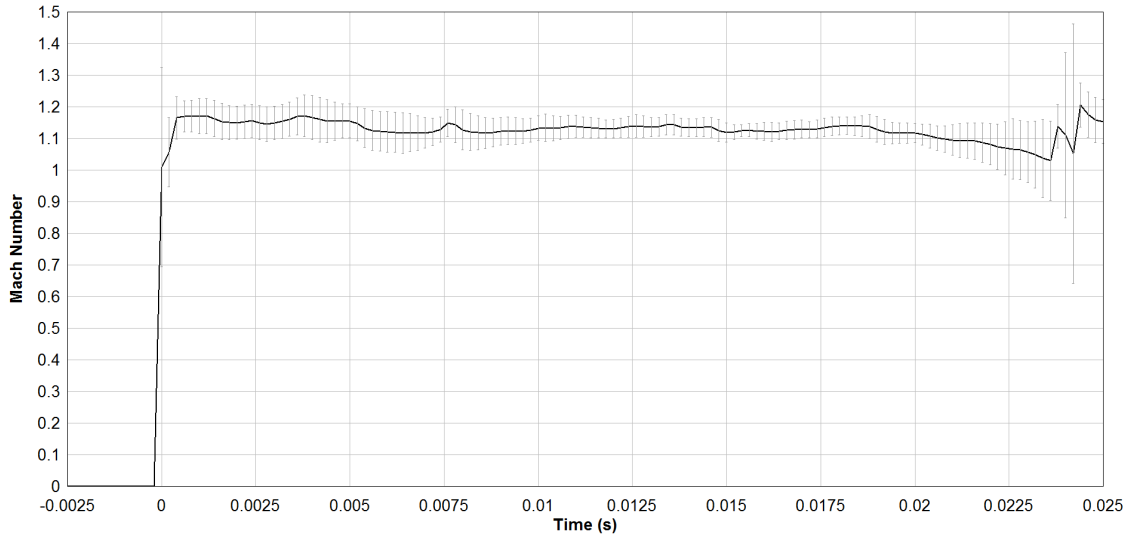


Figure 5.62: Average of Experimentally Determined Mach Number for 6mm gap with Standard Deviation; Initial Shock Oscillation

5.4 Summary

The experimental campaign conducted on The Royal British Legion Centre for Blast Injury Studies 60 mm bore shock tube produced a set of consistent results which support the previous numerical modelling.

To deliver these results several complex steps were conducted, these included

- Design of specific shock tube end plate hardware.
  - This hardware was required to enable the intent of the research without compromise whilst not presenting any safety hazard during the dynamic firing of the shock tube at the driver pressures required.
- Design, construction and calibration of a novel miniature pressure probe.
  - The probe was required to return accurate and repeatable pressures (both stagnation and static) whilst sitting within the end plate hardware. The probe in the stagnation pressure orientation had to obtain quality results without compromise due to excessive aerodynamic blockage effects.
  - Use was made of a 0.67 mm diameter fabry-perot optical pressure probe designed primarily as a rodent catheter probe for life sciences research. External protection was developed using a hypodermic needle to protect both the pressure sensing element and the optical fibre.
  - A numerical design optimisation exercise enabled the probe design to achieve repeatable measurements and removed potential ringing of the measured pressure trace due to any cavity effects ahead of the sensor. The small physical probe dimensions enabled the use of blast clearing theory to determine the response of the final probe design and ensured it was adequate for the measurements to be undertaken.
  - Aerodynamic blockage effects were accounted for with the appropriate correction factors being determined and applied during the analysis. The stagnation probe location hardware, which sat outside but close to the venting gap, complicated the blockage characteristics and an empirical study was conducted as part of the experimental campaign. The effect was minimal due to the physical dimensions of the probe and the maximised stand off to the location hardware.

Final analysis of the flow Mach number within the venting gap was conducted and returned a time averaged flow of Mach 1.15 at the point of measurement. Numerical modelling was used during the experimental analysis to predict the potential presence of a detached bow shock ahead of the stagnation probe. The final flow Mach number was within the transonic / low supersonic regime and thus a detached bow shock could not be definitively predicted, thus it was necessary to undertake an error analysis based on using an inappropriate analysis method.

The options being an error in the final Mach number based on

- using general compressible theory in the presence of a detached bow shock ahead of the probe. This returned a possible error in the Mach number of between -0.84% and -1.27% (an underestimation).
- using Rayleigh Supersonic Pitot theory with no detached bow shock present. This returned a possible error in the Mach number of between 0.93% and 1.40% (an overestimation).

From this, use of the general compressible flow theory was likely to be the most conservative (underestimation of the final flow Mach number) so it was used during the analysis. With this in mind the experimental outcome of a flow at Mach 1.15 corresponds well with the numeral modelling outcome of roughly Mach 1.3; both outcomes being measurably above unity and therefore supporting the research hypothesis that the current assumption regarding the applicability of ideal nozzle flow within early time cracks requires revisiting.

Chapter 6

New Model Hypothesis

The numerical and experimental data generated has shown the current assumption, of ideal nozzle flow throughout the venting of the products through casing fractures, is not wholly applicable. It is necessary to postulate an alternative hypothesis to enable a model to be developed which better reflects the physical processes. At this stage the postulated new model will act as a framework of possibility, however it is clear that more data (both experimental and high fidelity, high resolution numerical modelling) is required to assess the range of applicability.

6.1 Pseudo Convergent-Divergent Nozzle

Work conducted by Jankee and Ganapathisubramani [122] on flow through orifices in plates showed that the flow separated at the leading edge of the orifice; however under certain conditions the flow through the orifice reattached to the orifice wall. These conditions occur when a threshold aspect ratio (of orifice channel height, h_0, to orifice diameter, d_0) was exceeded, with the research conducted by Jankee and Ganapathisubramani highlighting the threshold aspect ratio being $h_0/d_0 = 0.75$. The situation is reproduced in Figure 6.1.

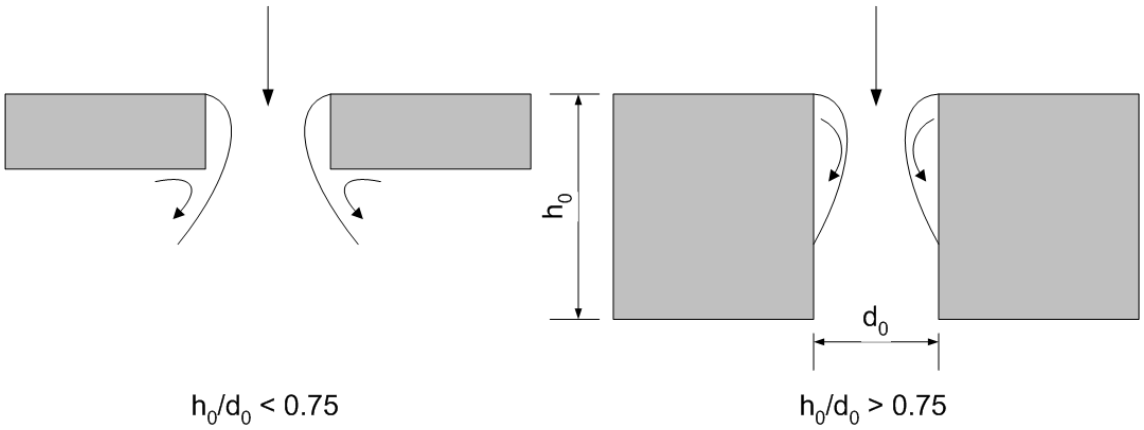


Figure 6.1: Schematic Representation of Flow Re-attachment Threshold [122]

Here, the height of the orifice channel, h_0, is equivalent to the casing thickness and the orifice diameter, d_0, is equivalent to the fracture (gap) width.

Building on this, it was possible to determine that the early time development and opening of the fractures related to the situation where the orifice aspect ratio was above the threshold value, and so flow re-attachment within the fracture length could be expected. Considering the existing model, and the work conducted by Hutchinson *et al*, it can be postulated that the ideal nozzle flow condition is most likely to be met at the *vena contracta* formed by the detached flow within the fracture.

This condition is similar to that which exists when a shock tube is used with a large area contraction at, or near to, the diaphragm as shown by historical work independently conducted by multiple researchers [123–125]. It is possible, therefore, to postulate the flow conditions within the fracture length as being similar to that shown in Figure 6.2, where the labelling convention has been adapted from that of Alpher and White [123].

Figure 6.2 shows the region of detached flow from the leading edge of the fracture generating a *vena contracta* within the fracture length. The flow reattachment point will vary along the length of the fracture, being dictated by phenomena such as the casing thickness, the fracture width, the local flow density, pressure, temperature, adiabatic index, and any turbulence generated within the flow. Other phenomena may undoubtedly contribute to the reattachment point and the local conditions, many of which will be time

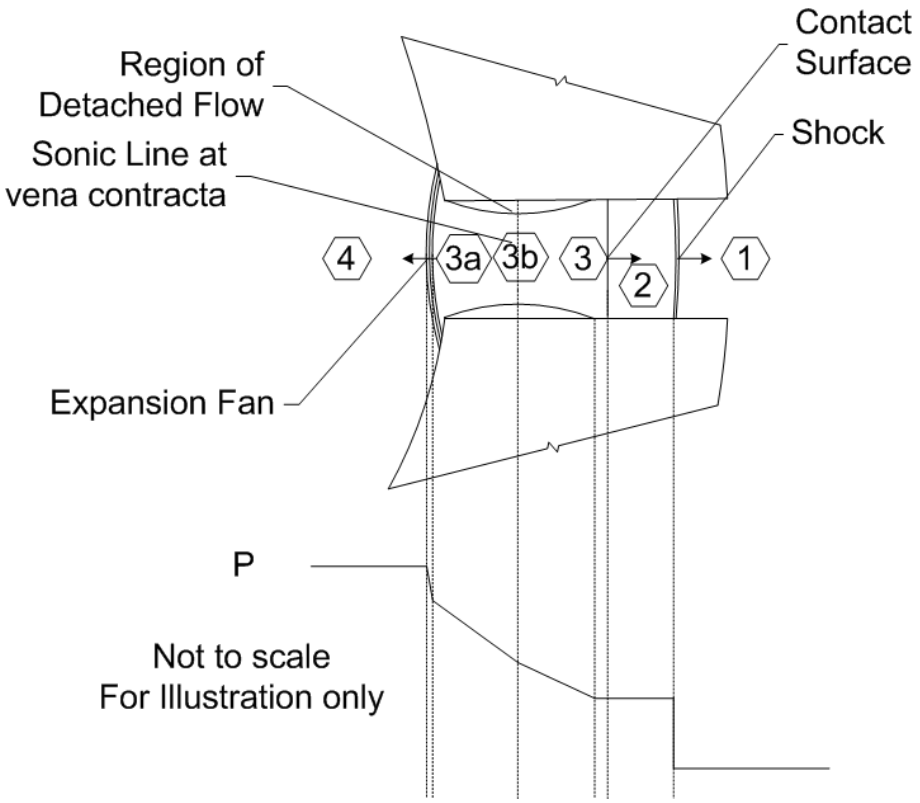


Figure 6.2: Schematic Representation of Pseudo Convergent-Divergent Flow Model - Early Time

varying.

It can be considered that once the fracture begins to form, an expansion fan will be generated akin to that formed by the rupturing of the diaphragm within a shock tube, and the flow will be accelerated from effectively stationary at region 4 to some sub sonic value in region 3a. The detached flow then acts as a convergent-divergent nozzle, as per the current model, accelerating the flow further until it is just sonic at region 3b (the *vena contracta*) which results in a supersonic flow at region 3 (behind the contact surface).

Very quickly the fracture will be fully opened and the initial shock and contact surface will exit the fracture leading to a relatively stable regime of venting as shown in Figure 6.3. The expansion of the vented region 3c will depend on the opening rate of the fracture and also the location of surrounding fractures and their opening rates. The physical conditions in this region will be extremely complex and are beyond the simple model update suggested here, which is concerned with the flow within the fracture.

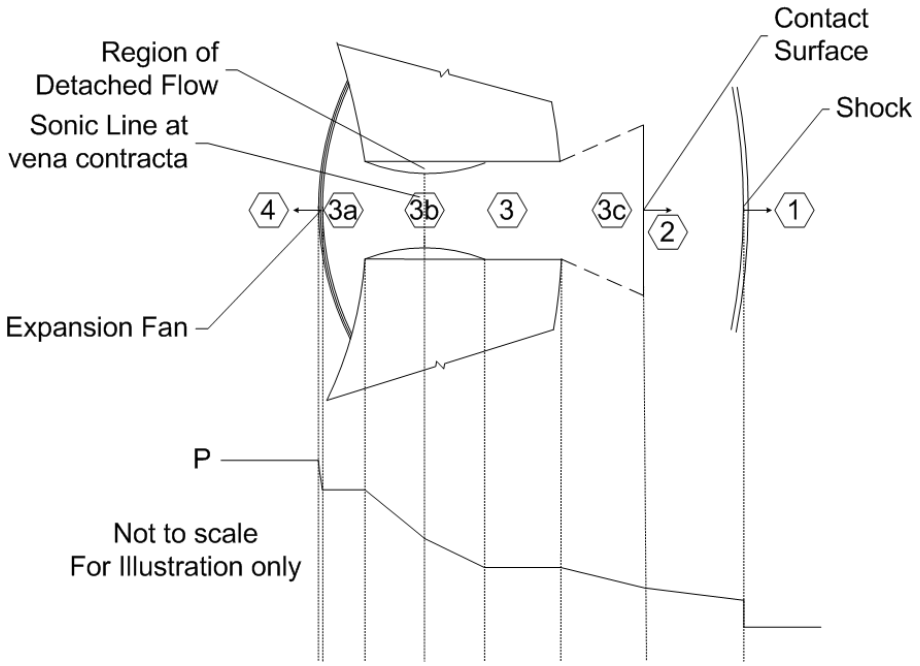


Figure 6.3: Schematic Representation of Pseudo Convergent-Divergent Flow Model - Late Time

From the experimental campaign conducted during this research it is possible to use standard theory to determine the flow characteristics at each region 4, 3a, 3b and 3. As mentioned, the flow in region 3c will be complex and is beyond the concern of the model update here, but it and the characteristics within region 2 should be determinable, given any specific information required. Likewise with more detailed data about the flow, and the fracture opening conditions, the time varying position of the *vena contracta* should be observable.

Starting with region 3, as measured experimentally, and applying the assumption of sonic flow at the *vena contracta*, it was possible to use the convergent-divergent nozzle equations to determine the Mach number of the sub-sonic flow at region 3a. Knowing the experimentally determined Mach number in region 3 allowed the area of the *vena contracta* at region 3b to be determined using Equation 6.1.

$$\frac{A_3}{A_{3b}} = \left(\frac{\gamma+1}{2}\right)^{-\frac{(\gamma+1)}{2(\gamma-1)}} \frac{\left(1+\frac{\gamma+1}{2}M_3^2\right)^{\frac{\gamma+1}{2(\gamma-1)}}}{M_3} \tag{6.1}$$

Taking the area at region 3a to be that of the fracture, equal to the area at region 3, the area at region 3b can then be used to estimate the Mach number of the flow at region 3a.

$$\frac{A_{3a}}{A_{3b}} = \left(\frac{\gamma+1}{2}\right)^{-\frac{(\gamma+1)}{2(\gamma-1)}} \frac{\left(1+\frac{\gamma+1}{2}M_{3a}^2\right)^{\frac{\gamma+1}{2(\gamma-1)}}}{M_{3a}} \tag{6.2}$$

Equation 6.2 is not easily manipulated to give the Mach number at region 3a, M_{3a}, however it can be solved using numerical methods or by constructing a look up table of adequate resolution.

Once M_{3a} has been determined, it can be combined with the essentially stationary flow in region 4 ($M_4 = 0$) to determine the pressure ratio across the expansion fan generated.

$$\frac{P_{3a}}{P_4} = \left(\frac{1}{1+\left(\frac{\gamma-1}{2}\right)M_{3a}^2}\right)^{\frac{\gamma}{\gamma-1}} \tag{6.3}$$

This pressure ratio can then be applied to the known pressure in region 4, being either the experimental driver pressure or the calculated pressure driving the pre-fracture casing expansion, to give the pressure at the leading edge of the fracture.

Similarly the isentropic flow equation used in Equation 6.3 can be used to determine the pressures at regions 3b and 3. The equation is given in a generalised form in Equation 6.4, where region 4 is the stagnation condition.

$$\frac{P_x}{P_4} = \left(\frac{1}{1+\left(\frac{\gamma-1}{2}\right)M_x^2}\right)^{\frac{\gamma}{\gamma-1}} \tag{6.4}$$

The generation of the pressure profile along the fracture from the leading edge is beyond this model update as it will require the dynamic calculation of the position of both the *vena contracta* and the flow reattachment point.

Once the local flow pressure has been determined, for each region, the density at these regions can be calculated by applying

$$\frac{P}{P_0} = \left(\frac{\rho}{\rho_0}\right)^{\gamma} \tag{6.5}$$

It is then a simple case of using the local pressure and density, along with the adiabatic index, to determine the local speed of sound at each region, and then the local flow velocity. The mass flow rate through the fracture can be estimated by equating the parameters at each region (3a, 3b and 3) through

$$\dot{m} = \rho A u \tag{6.6}$$

Starting with the experimental conditions of driver pressure, $P_4 = 10$ bar, with a vent diameter of 6 mm, along with the assumption that M_{3b} is sonic, allows Equation 6.1 to Equation 6.6 to be applied to generate Table 6.1 , where the starting figures are given in **bold**.

It should be noted that the pressure in region 3 is estimated at 4.40 bar for this example which compares reasonably well with the experimentally determined value of 4.11 $\pm$ 0.1 bar, with the uncertainty based on the standard deviation of the experimental results about the mean value of the maximum static pressure recorded. The upper bound of the maximum static pressure recorded was 4.21 bar. Should the calculations be run to match the pressure within region 3 against the experimentally measured maximum static pressure, this returns a Mach number for the flow in region 3 of Mach 1.2, which is within the standard deviation error bounds of the experimentally determined Mach number.

From the initial application of the experimentally determined values, the alternative model using a pseudo convergent-divergent nozzle within the fracture appears to fit. It should be remembered, however, that the experimental data gathered is limited to a

	Region			
Parameter	**4:Driver**	**3a:Inlet**	**3b:Vena Contracta**	**3:Outlet**
Adiabatic Index, γ	1.4	1.4	1.4	1.4
Pressure, P [bar]	**10**	6.16	5.28	4.40
P_x/P_4	1	0.616	0.528	0.440
Density, ρ [kg/m^3]	6.6285	4.447	3.985	3.496
ρ_x/ρ_4	1	0.707	0.634	0.556
Speed of sound, a [m/s]	471.95	440.39	430.83	419.70
Local Flow Speed, u [m/s]	0	379.42	430.83	482.65
Mach Number	0	0.86	**1**	**1.15**
Gap Diameter, d [mm]		6	5.948	6
Vent Area, A [mm^2]		28.274	27.789	28.274
A_x/A_{3b}		1.0174	1	1.0174
Mass Flow Rate, $\dot{m}$ [kg/s]		0.0477	0.0477	0.0477

Table 6.1: Pseudo Convergent-Divergent Nozzle Model - Experimental Flow Parameters

single case only and before the model can be taken forward it is necessary to generate more experimental data spanning different gap widths and pressure regimes.

6.2 Moving Centred Rarefaction Wave

Historical work has been conducted to investigate the effects of a sudden large area reduction within a shock tube, both along the driven section and also at, or near, the diaphragm [123–127]. The approximation that the opening of the fracture in the expanding case acts like a shock tube diaphragm releasing high pressure gas along the fracture length is analogous to the latter scenario. Use can therefore be made of some of this historical work to inform a potential alternative to the pseudo convergent-divergent nozzle model in the previous section.

It is well known [126] that a sudden decrease in the diameter of the shock tube causes

an increase in the transmitted shock Mach number, which leads to a similar increase in the pressure, temperature and Mach number of the flow behind this transmitted shock. The situation is somewhat more complicated when the area contraction is coincident with the diaphragm, but solvable nonetheless.

Within a standard shock tube of constant diameter, once the diaphragm ruptures the usual scenario is that of a shock wave running into the driven section followed by the contact surface separating the expanding driver and the driven gases. The Mach number of the flow behind the contact surface is subsonic. At the same time as this, there is an expansion wave travelling into the driver section, bridging the pressure difference between the remaining unexpanded and expanding driver gas. The explanatory diagram for this is available in many reference texts (i.e. [105, 126]) and is reproduced in Figure 6.4.

The introduction of the area change at the diaphragm location changes these standard shock tube conditions by varying degrees depending on whether the flow at the inlet to the contracted area is subsonic, sonic or supersonic. Earlier work by Falcovitz and Igra [125] concentrated on the former two conditions, with later work by Falcovitz *et al* [127] covering all three conditions. Given the experimental evidence for supersonic flow behind the contact surface generated during this research, it is clear that the subsonic case is not applicable and can be discounted. This supersonic flow can, however, be generated by introducing either sonic or supersonic flow at the contraction / diaphragm.

Falcovitz *et al* [127] introduced the need for a centred rarefaction wave at the contraction which bridged the pressure difference between states p_3 and $p_{3'}$, as reproduced in Figure 6.5. Alongside the usual expansion fan running into the driver gas to bridge the pressure difference between states $p_{3'}$ and p_4, there exists a centred rarefaction wave which sits stationary at the area contraction or moves upstream into the driven section with velocity u_3 - c_3 (> 0) in the case of sonic and supersonic flow at the contraction respectively.

As with the pseudo convergent-divergent nozzle flow model, it is possible to set the

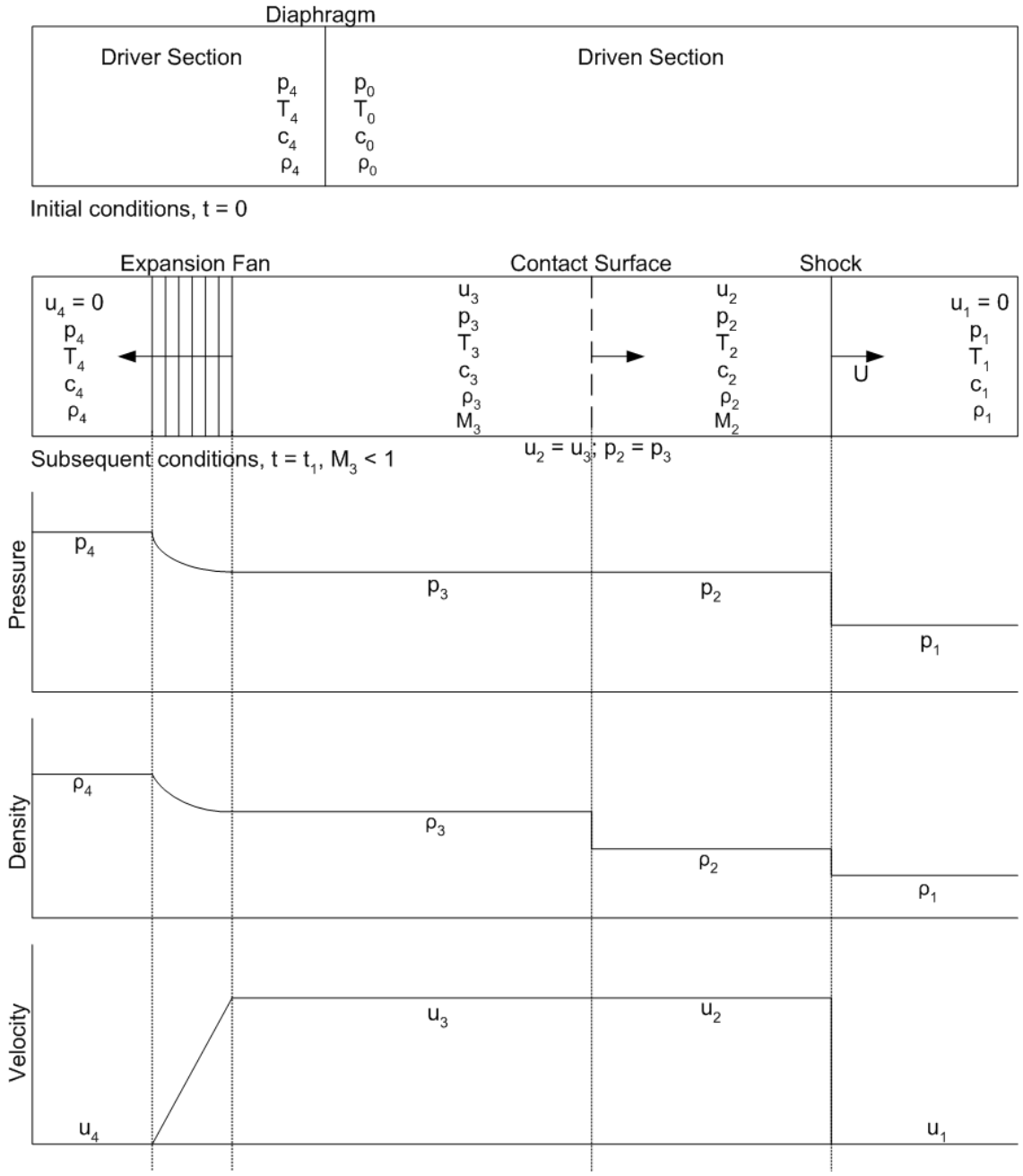


Figure 6.4: Schematic Representation of Shock Tube Flow Development

Mach number at the contraction to be just sonic and use Equation 6.4 and Equation 6.5 to calculate the flow properties for region 3' and 3. As with the pseudo convergent-divergent nozzle model, applying flow speeds of Mach 1.0 at region 3' and Mach 1.15 at region 3 returns pressure values of 4.40 bar within region 3. Running the calculations with the experimentally determined maximum static pressure in region 3 returns a flow Mach number of 1.2 within this region.

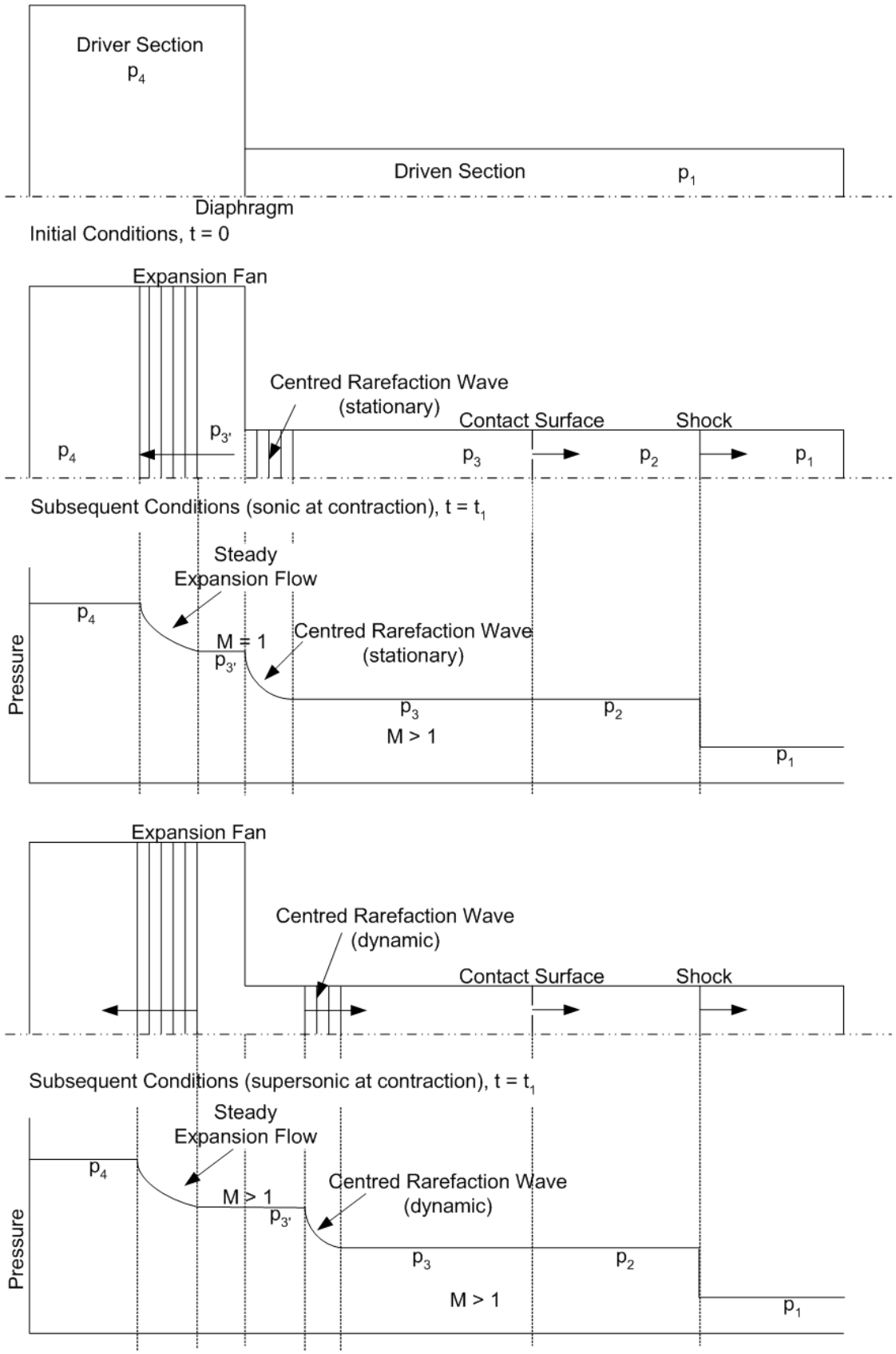


Figure 6.5: Schematic Representation of Centred Rarefaction Wave Development

From this initial application of the experimental results, the alternative model with a stationary centred rarefaction wave at the diaphragm location also appears to fit. However, if the shape of the experimental traces generated during the research is examined closely, it can be seen that certain artefacts of the trace may fit better with the dynamic centred rarefaction wave theory. Examples of the experimental traces for 10 bar driver pressure are shown in Figure 6.6.

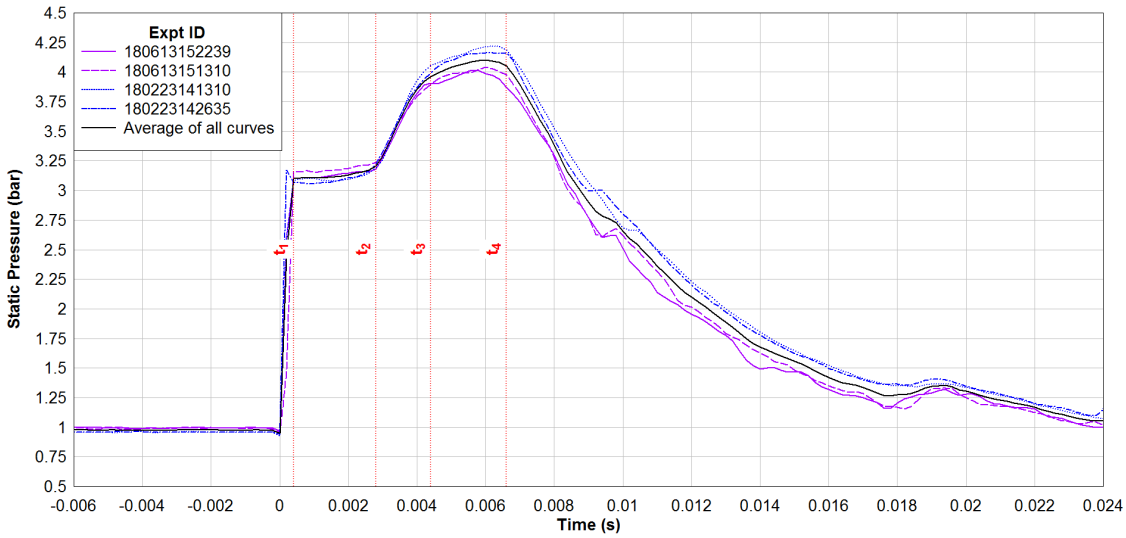


Figure 6.6: Experimental Pressure Trace Breakdown

Close inspection off these traces allows the reference time lines to be constructed where it is possible that:

- Time zero to t_1 is the rise time related to the arrival of the shock and the increase in pressure from P_1 (atmospheric) to $P_2 = P_3$.
- t_1 to t_2 is the pressure plateau for regions 2 and 3, ending with the arrival of the centred rarefaction wave at t_2
- t_2 to t_3 dynamic centred rarefaction wave, bridging the pressure difference between P_3 and $P_{3'}$
- t_3 to t_4 is the pressure plateau for region 3'

At this stage it has not been possible to match the experimental timings for t_2 - t_1 with the motion of the centred rarefaction wave behind the shock; however, the length of

the dynamic centred rarefaction wave ($t_3 - t_2$) is found to match the calculations closely depending on the ratio of Mach numbers chosen between regions 3' and 3 (and thus the ratio of the pressures within each region). Holding the Mach number of the flow in region 3' at unity, the difference between the experimental and calculated lengths of the centred rarefaction wave is approximately 15% with region 3 at Mach 1.15 but this quickly reduces to a difference of slightly less than 2.5% when region 3 is set to Mach 1.13. Both of these values are within the experimental spread of results. Alternatively, with the pressure in region 3 matched to that of the experimental results, 4.12 bar, it can be found that setting the flow to be Mach 1.08 and Mach 1.2 in regions 3' and 3 respectively gives a difference between the experimental and calculated length of the centred rarefaction wave of approximately 3%.

6.3 Summary

Future models could be developed to describe the whole scenario, although a modular approach breaking the problem into manageable sections can be more beneficial. A modular approach would allow the very early time to be modelled using specialist or bespoke software, looking at the microscale shock interactions, before the expansion and fragmentation mechanisms are modelled using alternative software.

This methodology would allow calculation of the gas flow through casing fractures, feeding back into the expansion phase. The model would need to include fracture mechanics for the dynamic opening of the venting area, and the surface properties of the fracture. Alongside the fracture mechanics, the model would need to consider the properties of transonic, or low supersonic, flow and the interaction of the flow with the surface properties of the venting fracture. To accurately model the flow, the dominant parameters need to be incorporated including the adiabatic constant, the density and flow speed along with the vent width. Variations in each of these parameters has a profound effect on the Mach number recorded within the flow, however parameters such as the internal

driver pressure and gap length (for gap widths below 3 mm) do not influence the flow Mach number to the same extent. Once the venting fracture width expands to greater than 3 mm the venting gap length, akin to the casing thickness, becomes more influential.

The two hypotheses presented within this chapter both fit the experimental data gathered during the research, however the limited dataset doesn't allow either the pseudo convergent-divergent nozzle or the centred rarefaction wave to be taken forward into a definitive model. To enable this a comprehensive experimental campaign, complemented with detailed high fidelity numerical modelling, could isolate further parameter effects and allow the applicability of either hypothesis to be validated beyond the initial dataset presented.

Allowing either hypothesis to be taken forwards would develop on the original application of either theory.

- For the pseudo convergent-divergent nozzle; the original application of detached flow reattaching to form a slipstream nozzle, with the *vena contracta* acting as the throat, could be extended to look at 3-dimensional effects within the vent. Extension of the original simple model to include 3-dimensional surface artefacts feeding back into the flow, without requiring high capacity computational facilities, would increase the complexity of the model and require an enormous dataset of experimental and high fidelity numerical evidence.

- For the centred rarefaction wave; the original application of existing shock tube theory, with a dramatic area constriction at the diaphragm, to the development of the flow through a compete thickness fracture could again be extended to include 3-dimensional and surface artefact effects. As with the alternative model, this extension of the original hypothesis would require extensive supporting evidence to determine the full range of applicability.

Chapter 7

Conclusions and Future Considerations

7.1 Summary of Thesis

The majority of current fragmentation models used in response to the requirements of the UK explosives regulations are based on data gathered at distances well beyond the extent of the fireball and the expanded detonation products. This is acceptable when the models are applied to scenarios at these same distances; however, issues may arise in certain scenarios where the distances involved are much shorter. These scenarios may include blast and fragment impact on explosive storehouse walls from the outer layer of weapons in a stack configuration, and weapon to weapon sympathetic detonation propagation within a stack configuration, amongst others. At these much reduced distances, the need for physically accurate models of the gas flow through fractures generated by expanding casings cannot be overlooked.

The initial scope of the thesis was to determine the acceleration profile of the generated fragmentation through the close in regime dominated by the fireball and the interaction with the expanding cloud of detonation products. The scope narrowed to look at the

flow of the gasses through the opening fractures when the application of the current flow model failed to replicate historical experimental data for both the motion of the gas front and generated fragments post casing break up.

The research conducted simplified the scenario greatly; however this enabled the details of the flow within the stylised fracture to be isolated in a manner that allowed both a numerical and experimental investigation of the flow to be conducted. Regarding the initial model used for replication of the historical experiments, and the AUTODYN numerical model used to look at the gas flow in more detail, it can be seen that:

- The current flow model is limited in applicability.
- The AUTODYN numerical modelling showed good agreement with the historical experimental data for the gas flow expansion outside of the casing; however it did not agree with the current assumption that the flow in the fracture gap would be limited to sonic velocities.
- The AUTODYN numerical modelling showed a consistent increase in flow Mach number from 1.2 at a fracture width of 1 mm to approximately Mach 1.35 at a 3 mm fracture width after which it appeared to level off being unaffected by the fracture width (up to the 6 mm maximum width investigated). This held for all driver pressures calculated between 18 and 200 bar, with the Mach number curve for the 10 bar case following a similar trend but consistently lower by approximately Mach 0.05 across all fracture widths.
- The AUTODYN numerical modelling used was bounded by the limitations of the student version of the software package.
  - Full access to all material models and numerical solvers, but a limit of 32,000 cells per calculation.
  - This drove the simplification of the scenario to a 2 dimensional representation, concentrating on static fracture diameters of a circular nature. This was easily replicated in the experimental campaign.

Replicating the modelled geometry in an experimental set up enabled direct comparison of the numerical and experimental results to be conducted, as well as enabling the modelling to inform the experimental expectations. The CBIS shock tube used for the experimental campaign was extremely well characterised, giving consistent output for a given driver pressure / diaphragm combination. Before testing could begin, it was necessary to determine applicable diagnostics for the measurement of the flow properties. Given the small diameter of the test fracture, even when testing at the 6 mm largest diameter, it was necessary to use diagnostics that would not unduly affect the measurements and invalidate any analysis conducted. Conventional optical based flow measurement techniques were not applicable given the solid end plate arrangement and the small diameter of the fracture vent precluded techniques using particles to measure the flow dynamics.

To enable the experimental campaign to be conducted:

- A miniature stagnation pressure probe was specifically designed and manufactured using a 0.67 mm diameter small rodent catheter fabry-perot pressure probe .
  - Standard hypodermic needle hardware was adapted to provide stability and external protection for the delicate optical components and fibre.
  - Numerical modelling was used to optimise the straight probe, zero cavity design before initial manufacture. The final design also allowed the gauge to be used for static pressure measurements at the wall of the fracture gap.
  - Use was made of the physical size of the probe, blast clearing theory and the available response frequency of the data capture hardware to filter the expected reflected shock pressure.
  - Further external protection for the optical fibre was required for a length immediately external to the shock tube to prevent damage from fibre whip.
  - The output of the miniature pressure gauge was recorded using the proprietary software available on purchase of the catheter probes, and proved to be consistent and reliable, returning a percentage coefficient of variation around 2.5%

across the timeframe of interest. This gave confidence to base any findings on a limited number of test cases.

  - The upper limit of measurable pressure from the miniature probe was 10 bar, due to the FISO Technologies Inc. FOP-LS-2FR-30 catheter probe used.
  - Alternative FISO Technologies Inc. catheter probes were available with a smaller working diameter; however these were limited to maximum measurable pressures too low to be of practical use in this investigation. Alternative catheter probe manufacturers were investigated; however at the time of the research the catheter probe chosen had the best compromise of probe diameter, sensor placement (end rather than side facing), and maximum pressure.

- The CBIS shock tube was reliable and gave consistent output as characterised by Nguyen [108].
  - Use of the double diaphragm set up provided extremely accurate driver pressure control, and removed any burst pressure variations due to diaphragm material properties.
  - The stagnation probe location hardware was bulky but achieved consistent alignment of the stagnation probe along the centreline of the fracture gap. Tests conducted to determine the level of flow blockage caused by the stagnation probe and external location hardware concluded that minimal effect on the flow could be seen. The correction factor determined was applied during the analysis.
  - Use of the higher data acquisition rate for the pressure probes (15 kHz analogue cf 5 kHz digital) was not necessary as calibration testing showed no extra features were discernible within the measured traces given the higher acquisition rate.

With the expectation of supersonic flow within the fracture gap, it was necessary to account for this within the analysis methodology employed.

- Standard Bernoulli and incompressible flow methods were not applicable.
- High speed compressible flow analysis was conducted including use of the Rayleigh Supersonic Pitot equation to account for the presence of a detached bow shock ahead of the stagnation pressure probe, and the effect this has on the measured flow.
  - Although the physical size of the stagnation gauge may not create a detached bow shock at the Mach numbers being tested, the analysis methodology must account for any bow shock potentially created.
  - Use of the numerical modelling conducted can assist in the assessment of the existence of any detached bow shock. The AUTODYN modelling conducted showed the production of a shock wave from the leading shoulder of the stagnation pressure probe however it was unclear at the cell resolution used whether a detached bow shock was generated.
  - Due to the uncertainty of the presence of a detached bow shock, the analysis employed an error estimation based on the effects of either not accounting for a detached shock or accounting for the presence of one when none exists. The final analysis erred on the conservative side by using the case giving the lowest flow Mach number.

Use of a combined numerical and experimental based approach allowed aspects of the investigation to be optimised, with the numerical analysis enabling design change impacts to be quickly determined prior to the more time consuming experimental campaign. Comparison of the results generated by both methods show:

- The numerical modelling and experimental campaign conducted show a reasonable agreement in the Mach number of the flow within the fracture gap. Both numerical and experimental results show a flow Mach number greater than unity (Mach 1.3 numerical cf Mach 1.15 experimental).

Recapping the aims and objectives of the thesis, it can be seen that the research has

successfully fulfilled these objectives and contributed to the understanding of the topic.

- Determine the limits of applicability of the current gas leakage model.
  - This objective was completed within the research. Numerical evidence shows the current gas leakage model to not be applicable for fracture openings greater than 1 mm diameter; experimental evidence at a larger 6 mm opening diameter corroborates this.
- Conduct original shock tube experiments to investigate gas flow through small openings.
  - This objective was completed within the research. The novelty of the diagnostic developed for the measurement of the stagnation pressure within the flow lies within the design using a rodent catheter optical probe and physical miniature size to determine gauge response.
- Propose new gas leakage model based on original experimental data.
  - This objective was partially completed within the research. New models were proposed with novel applications of theory, however not enough evidence could be gathered to predict the limits of applicability of either hypothesis.

Completion of the aims and objectives of this thesis has progressed the understanding of the flow within venting fractures.

- The lack of applicability of an ideal nozzle flow model using the full venting fracture diameter has been shown; the potential of alternative hypotheses has been shown although not fully established.
- A novel miniature stagnation pressure gauge has been designed and developed which can be used to progress shock tube research within this and related topics.

7.2 Future Work

The numerical and experimental work conducted during this research has shown the limitations on the current assumption, and has enabled the suggestion of alternative models to be hypothesised. To drive the research forward and determine the best alternative model to be used, thus giving more realistic gas and fragment expansion profiles within the close in regime, it is necessary to initiate work to improve the numerical and experimental set ups as well as generate data across a wider series of scenarios.

Although not employed to any where near full capability within the research at this stage, high fidelity numerical modelling packages, such as ABAQUS or AUTODYN, could allow a detailed study of the processes and interactions at all stages of the cylinder expansion. Complete material models would be required for all materials used to ensure full and accurate representation of these processes and interactions across all regimes.

As mentioned previously, high fidelity modelling could be run as either a single end to end simulation, which would require a large computational effort, or the model could be split into several more computationally efficient simulations requiring meshing and parameter mapping to progress through the timeline. Use of automatic Adaptive Mesh Refinement (AMR) should be investigated to enable the number of cells to be reduced in non critical areas, with the area of maximum mesh resolution constantly tracking the parameter of interest. This method is often used in applications such as shock wave tracking.

The modelling could be expanded from 2 dimensional ring expansion and fragmentation simulations to 3 dimensional simulations looking at details such as the effects of any surface artefacts within the venting fracture. This would be more efficient than trying to include such details within the full simulation due to the mesh resolution required to distinguish such features. A series of 2 dimensional and 3 dimensional simulations could be used to investigate edge effects on the flow within the venting fracture, as well as determining any improvements to the experimental set up.

The determination of the surface artefact effects could be investigated experimentally, incorporating any set up improvements identified, however this would require further development of novel diagnostics to measure, or visualise, the flow within the venting fracture including the detachment and reattachment of the flow within the fracture.

For this it is suggested that:

- Numerical modelling be conducted on the full version of AUTODYN such that a much higher cell resolution can be employed. This would especially increase the confidence in the determination of any detached bow shock generated during the experimental campaign.
  - Confirmation of full material models across all expected regimes.
  - 2 dimensional ring expansion / fragmentation modelling with high resolution mesh.
  - 3 dimensional high resolution modelling to investigate surface artefact effects on flow in venting fracture.
  - Structured 3 dimensional end to end modelling, broken into detailed sub models with parameter mapping between sections. This will maximise available mesh resolution by limiting the physical aspects simulated.
  - Alternatively, use could be made of more specialised fluid dynamics software, such as Fluent or Star CCM+, which would enable the effects of turbulence, boundary layer growth, and surface roughness to be better investigated.
- Numerical models could be used to investigate the effects of the dynamic opening rate of the fracture, linked to the casing expansion rate, to compliment experimental campaigns conducted with static venting fracture opening values.
- Experimental campaigns should be conducted to isolate different aspects of the fracture.
  - Venting fracture opening width

  - Venting fracture opening shape
  - Venting fracture opening area
  - Venting fracture dynamic opening rate
  - Venting fracture opening wall surface roughness

- Experimental diagnostics will need to be adjusted / improved.
  - Smaller diameter stagnation probe designs will be necessary.
  - Smaller external location hardware will be necessary to prevent excessive blockage effects when testing smaller fracture gap sizes.
  - Alternative catheter probe designs and data capture methods will need investigation.
  - Flow visualisation methods need to be investigated for use within the venting fracture opening, to determine flow detachment / reattachment phenomena.

- Experimental layout and stagnation pressure probe protection will need improving.
  - During the campaign conducted the majority of stagnation pressure probe damage was caused by impact of sections of shock tube diaphragm material. This caused the sensor to overpressure resulting in non-repairable damage. Examples of this are shown in Figure 7.1.

- Potential protection schemes could include:
  - use of granular beds or perforated screens to both remove the initial shock front and also stop fragments of the ruptured diaphragm.
  - use of the radial consistency of the shock tube output to enable the vent opening to be located off axis.

The combination of the detailed high fidelity modelling and improved experimentation methods may return the evidence required to determine the applicability of either, or both new model hypothesis.

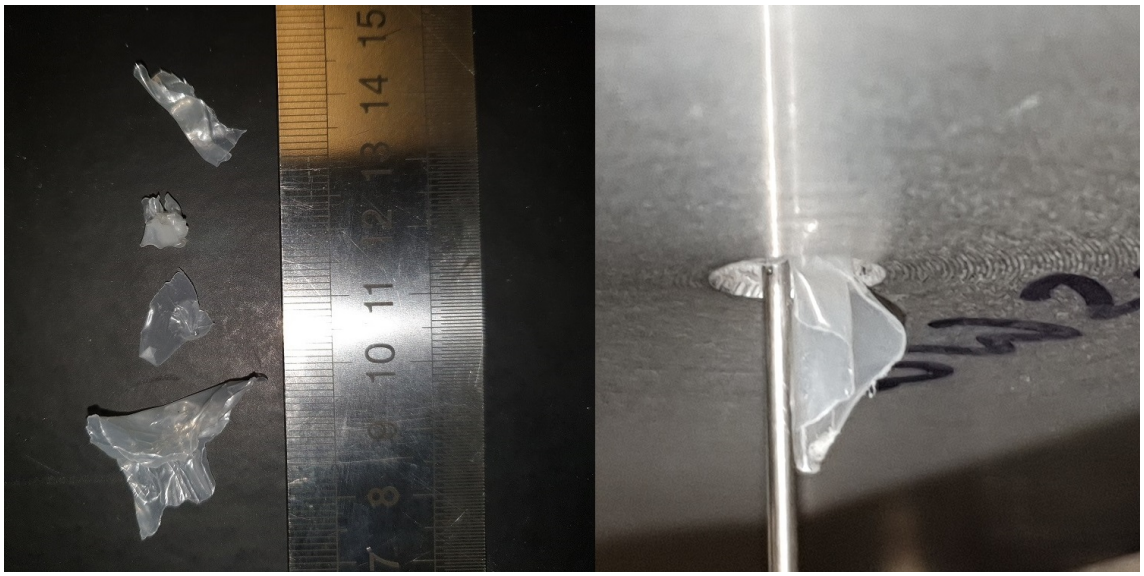


Figure 7.1: Debris from Ruptured Diaphragm

7.3 Exploitation Routes

The applicability of the research can be foreseen in the following areas:

- Improvement of the underlying physics within the weapon fragmentation and structural debris models for close in fragment interactions, giving more robust output from the UK Ministry of Defence (MOD) quantitative risk analysis software tool supporting the regulation of explosives storage across the Defence Estate.

- Future fast running engineering model development and advances under an international collaborative programme on explosive, fragmentation and far field effects in complex threat scenarios.

- Removal of crude assumptions applied within the currently available models. These render the modelling inaccurate for fragment / target interactions, either within or close to the edge of the fireball region, such as internal detonations, sympathetic reaction and near field warhead lethality considerations.

- Support to operational aspects such as the modelling of collateral damage from nearby weapon detonations.

- Development of improved arena trials analyses methods required by MOD to deter-

mine the performance of fragmentation for new weapons brought into service.

- Development of accurate early time fragment speed profiles which can be used to remove some of the conservatism required in the design of:
  - Armour and protection scheme designs.
  - Mitigation and unitisation barriers and barricades
  - Sympathetic reaction impact velocity threshold values
- Development of accurate early time fragment rotational motion profiles, including the initial distance to onset of rotational motion and an initial assessment of the primary factors required for the onset of rotational motion.
  - This would initially cover rotational motion along the plane of linear travel (pitch) but could eventually be expanded to include rotational motion about all planes of motion (roll and yaw).
- Development of improved models for fragmentation impact effects from an accidental initiation within a storehouse, either UK based masonry storehouse or expeditionary field storage, or a deliberate initiation of a device in a crowded place.
  - This development could potentially be used for the development of mitigation and protection schemes required for the conduct of cased experiments within containment systems or sealed bomb chambers.

Bibliography

[1] Defence Safety Authority. *Ministry of Defence explosives regulations.* Technical report, JSP482, 2013.

[2] US Army. *GE/UK/US static testing of high explosive munitions for obtaining fragment spatial distribution.* Technical report, ITOP 4-2-813, US Army Test and Evaluation Command, 1993.

[3] Bo Janzon. *Retardation of fragments in air (translated from Swedish report "Splitters luftmotstand").* Technical report, RAE LT1681, 1972.

[4] John Pearson. *A fragmentation model for cylindrical warheads.* Technical report, Naval Weapons Center, China Lake, 1990.

[5] Sam Waggener. *The performance of axially initiated cylindrical warheads.* In Proceedings of the international symposium on ballistics, 1978.

[6] John HS Lee. *The detonation phenomenon.* Cambridge University Press, ISBN 978-0-521-89723-5, 2008.

[7] Siavouche Nemat-Nasser and Soon Nam Chang. *Compression-induced high strain rate void collapse, tensile cracking, and recrystallization in ductile single and polycrystals.* Mechanics of materials, 10(1-2):1–17, 1990.

[8] M. Lanari and A. Fakhimi. *Numerical study of contributions of shock wave and gas penetration toward induced rock damage during blasting.* Computational particle mechanics, 2(2):197–208, 2015.

[9] J R Brinkmann. *An experimental study on the effects of shock and gas penetration in blasting.* In Fragblast, Brisbane, 1990.

[10] M M D Banadaki. *Stress-wave induced fracture in rock due to explosive action.* PhD thesis, University of Toronto, 2010.

[11] Dr.ir. P J G Schreurs. *Fracture mechanics.* Eindhoven University of Technology, Course 4A7 lecture notes, 2014.

[12] N F Mott. *A theory of the fragmentation of shells and bombs.* Technical report, Advisory Council on Scientific Research and Technical Development, Ministry of Supply, 1943.

[13] N F Mott. *Fragmentation of shell casings and the theory of rupture in metals.* Technical report, Advisory Council on Scientific Research and Technical Development, Ministry of Supply, 1943.

[14] N F Mott. *Fragmentation of HE shells; a theoretical formula for the distribution of weights of fragments.* Technical report, Advisory Council on Scientific Research and Technical Development, Ministry of Supply, 1943.

[15] N F Mott and E H Linfoot. *A theory of fragmentation.* Technical report, Advisory Council on Scientific Research and Technical Development, Ministry of Supply, 1943.

[16] Geoffrey Ingram Taylor. *Analysis of the explosion of a long cylindrical bomb detonated at one end.* In G K Batchelor, editor, Scientific Papers of Sir Geoffrey Ingram Taylor, volume III. University Press, Cambridge, 1963.

[17] F. E. Allison and J. Thomas Schriempf. *Explosively loaded metallic cylinders. II.* Journal of applied physics, 31(5):846, 1960.

[18] R W Gurney. *The initial velocities of fragments from bombs, shells, grenades.* Technical report, Ballistics Research Laboratories, 1943.

[19] Paul W Cooper and Stanley R Kurowski. *Introduction to the technology of explosives.* Wiley-VCH, ISBN 0-471-18635-X, 1996.

[20] Paul W Cooper. *Explosives engineering.* Wiley-VCH, ISBN 0-471-18636-8, 1996.

[21] P H Denny, D J James, and H R James. *Blast and fragments from steel cylinders containing RDX/wax explosive with varying aluminium content. Part 2: The initial velocity of the casing.* Technical report, UKAEA, 1970.

[22] S T S Al-Hassani and W Johnson. *The dynamics of the fragmentation process for spherical shells containing explosives.* International journal of mechanical sciences, 11:811–823, 1969.

[23] S.T.S. Al-Hassani, H G Hopkins, and W Johnson. *A note on the fragmentation of tubular bombs.* International journal of mechanical sciences, 11:545–549, 1969.

[24] H M Sternberg. *Computation of weight, velocity and angular distributions of fragments from naturally fragmenting weapons.* Technical report, Naval Ordnance Laboratory, 1974.

[25] S T Surzhikov. *Two-component radiation-gasdynamic model of a turbulent fireball.* Journal of engineering physics and thermophysics, 73(1):29–35, 2000.

[26] V Novozhilov. *Some aspects of the mathematical modelling of fireballs.* Proceedings of the institute of mechanical engineers, Part E, Journal of process mechanical engineering, 217(2):103–121, 2003.

[27] Bryan J Steward. *Reproducibility, distinguishability and correlation of fireball and shockwave dynamics in explosive munitions detonations.* Air Force Institute of Technology (US), MSc thesis, 2006.

[28] Kaushik Balakrishnan, Franklin Genin, Doug V. Nance, and Suresh Menon. *Numerical study of blast characteristics from detonation of homogeneous explosives.* Shock Waves, 20(2):147–162, 2009.

[29] Mina Reda Mankbadi, S Balachandar, and Alexander L Brown. *Compressible instability of rapidly expanding spherical material interfaces.* Technical report, Sandia National Laboratories, 2012.

[30] Harold L Brode. *Weapons effects for protective design.* Technical report, The RAND Corporation, Santa Monica, CA, 1951.

[31] Francis B Porzel. *Rate of growth of atomic fireballs.* Technical report, Los Alamos Scientific Laboratory of the University of California, Los Alamos, 1951.

[32] Hans A Bethe. *Theory of the fireball.* Technical report, Los Alamos Scientific Laboratory of the University of California, Los Alamos, 1964.

[33] Harold L Brode. *Fireball phenomenology.* Technical report, The RAND Corporation, Santa Monica, CA, 1964.

[34] NATO. *Manual of NATO safety principles for the storage of military ammunition and explosives.* Allied Ammunition Storage and Transport Publication, AASTP-1, 2010.

[35] NATO. *Manual on explosives safety risk analysis.* Allied Ammunition Storage and Transport Publication, AASTP-4, 2011.

[36] D R Stull. *Fundamentals of fire and explosion.* American Institute of Chemical Engineers, ISBN 978-0816900404, New York, 1977.

[37] J B Gayle and J W Bransford. *Size and duration of fireballs.* Technical report, NASA TM X-53314, George C Marshall Space Flight Center, Huntsville, AL, 1975.

[38] B G Laidlaw, F H Winfield, and J S Watson. *NATO DRESTC trial series.* Technical report, Defence Research Establishment Suffield, 1975.

[39] A M Patterson, C N Kingery, R D Rowe, J Petes, and J M Dewey. *TTCP Panel N-2: Fireball and shock wave anomalies.* Technical report, The Technical Cooperation Program, 1970.

[40] Jay A Orson, William F Bagby, and Glen P Perram. *Infrared signatures from bomb detonations.* Infrared physics and technology, 44:101–107, 2003.

[41] Kevin C. Gross and Glen P. Perram. *The phenomenology of high explosive fireballs from fielded spectroscopic and imaging sensors for event classification.* International journal of high speed electronics and systems, 18(01):19–29, 2008.

[42] Y Kato, N Mori, H Sakai, T Sakurai, and T Hikita. *Detonation temperature of some liquid and solid explosives.* In Proceedings of the ninth international symposium on detonation, 1989.

[43] Jon D Koch, Joel Carney, James Lightstone, and Scott Piecuch. *Use of a fast near-infrared spectrometer for absorption and emission measurements within the expanding blast wave of a high explosive.* AIP conference proceedings, 1426:386–389, 2012.

[44] W K Lewis, C G Rumchik, P B Broughton, and C M Lindsay. *Time-resolved spectroscopic studies of aluminized explosives : Chemical dynamics and apparent temperatures.* Journal of applied physics, 111:014903, 2012.

[45] Luke S. Lebel, Patrick Brousseau, Lorne Erhardt, and William S Andrews. *Measurements of the temperature inside an explosive fireball.* Journal of applied mechanics, 80, 2013.

[46] W R Porter. *Radially expanding fragmentation warhead study.* Technical report, Air Force System Command, 1965.

[47] M Kornhauser. *An improved approximate model of explosive casing expansion.* In Proceedings of the seventh international symposium on detonation, 1981.

[48] K I Kozorezov and V V Sergeev. *Calculation of the Parameters of a Shock Wave Near a High Explosive Charge.* Translated from Fizika goreniya i vzryva, 11(6):928–938, 1975.

[49] O S Popel', O A Sinkevich, and A L Shevchenko. *Shock damping during high explosive detonation product dispersion into a gas.* Translated from Fizika goreniya i vzryva, 13(4):936–939, 1977.

[50] James T Dehn. *Models of explosively driven metal.* Technical report, Ballistic Research Laboratories, 1984.

[51] A V Kashirskii, Yu V Korovin, and L A Chudov. *Motion of the detonation products of a point ignited charge in a cylindrical shell.* Translated from Zhurnal prikladnoi mekhaniki i tekhnicheskoi fizika, (6):170–172, 1974.

[52] Predrag M Elek, Vesna V Dzingalasevic, Slobodan S Jaramaz, and Dejan M Mickovic. *Determination of detonation products equation of state from cylinder test: Analytical model and numerical analysis.* International journal of thermal sciences, 2013.

[53] E L Lee, H C Hornig, and J W Kury. *Adiabatic expansion of high explosive detonation products.* Technical report, Lawrence Radiation Laboratory, University of California, 1968.

[54] Ho-Young Kwak, Ki-Moon Kang, Ilgon Ko, and Jae-Hoon Kang. *Fire-ball expansion and subsequent shock wave propagation from explosives detonation.* International journal of thermal sciences, 59:9–16, 2012.

[55] Kunihito Nagayama and Shiro Kubota. *Equation of state for detonation product gases.* Journal of applied physics, 93(5):2583–2589, 2003.

[56] Peter Huson, Robert J. Asaro, Lauren Stewart, and Gilbert A. Hegemier. *Non-explosive methods for simulating blast loading of structures with complex geometries.* International journal of impact engineering, 38(7):546–557, 2011.

[57] John F Polk. *Determination of the equation of state of explosive detonation products from the cylinder expansion test.* Technical report, US Army Armament Research and Development Center Ballistic Research Laboratory, 1984.

[58] Khaled Alhussan, K.L. Stepanov, Y.A. Stankevich, A.S. Smetannikov, and S.A. Zhdanok. *Hydrodynamics of the initial phase of explosion.* International journal of heat and mass transfer, 54(7-8):1627–1640, 2011.

[59] Michael D. Hutchinson and David W. Price. *On the continued acceleration of bomb casing fragments following casing fracture.* Defence technology, 10(2):211–218, 2014.

[60] K Nagayama and S Kubota. *Equation of state for detonation product gases.* Journal of physics: conference series, 500(19), 2014.

[61] Steven B Segletes. *An examination of the JWL equation of state.* Technical report, US Army Research Laboratory, 2018.

[62] Ralph Menikoff. *JWL equation of state.* Technical report, Los Alamos National Laboratory, 2017.

[63] B M Dobratz. *LLNL explosives handbook: properties of chemical explosives and explosives and explosive simulants.* Technical report, Lawrence Livermore National Laboratory, 1981.

[64] L G Hill. *Detonation product equation of state directly from the cylinder test.* Technical report, Los Alamos National Laboratory, 1997.

[65] B. D. Sutton, J. W. Ferguson, and A. N. Hodgson. *An analytical approach to obtaining JWL parameters from cylinder tests.* AIP conference proceedings, 1793, 2017.

[66] A White, F J Zerilli, and H D Jones. *Ab initio calculation of intermolecular potential parameters for gaseous decomposition products of energetic materials.* Technical report, Defence Science and Technology Organisation, 2000.

[67] F. Charlet, M. L. Turkel, J. F. Danel, and L. Kazandjian. *Evaluation of various theoretical equations of state used in calculation of detonation properties.* Journal of applied physics, 84(8):4227–4238, 1998.

[68] P C Souers and J W Kury. *Comparison of cylinder data and code calculations for homogeneous explosives.* Propellants, explosives, pyrotechnics, 18(175), 1993.

[69] Charles L Mader. *FORTRAN BKW: A code for computing the detonation properties of explosives.* Technical report, Los Alamos Scientific Laboratory of the University of California, 1967.

[70] Mohammad Hossein Keshavarz, Hadi Motamedoshariati, Reza Moghayadnia, Hamid Reza Nazari, and Jamshid Azarniamehraban. *A new computer code to evaluate detonation performance of high explosives and their thermochemical properties, part I.* Journal of hazardous materials, 172:1218–28, 2009.

[71] L E Fried, W M Howard, P C Souers, and L Haselman. *Adding kinetics and hydrodynamics to the CHEETAH thermochemical code.* Technical report, Lawrence Livermore National Laboratory, UCRL-ID-125794, 1997.

[72] Jing Ping Lu. *Evaluation of the thermochemical code - CHEETAH 2.0 for modelling explosives performance.* Technical report, Defence Science and Technology Organisation, DSTO-TR-1199, 2001.

[73] Raymond Chirat and Gerard Pittion-Rossillon. *A theoretical equation of state for detonation products: Application to twelve CHNO explosives.* Combustion and flame, 45:147–159, 1982.

[74] Jean-Philippe Dionne. *Chapman-Jouguet properties of heterogeneous explosives.* McGill University, MEng thesis, 1996.

[75] Mohammad Hossein Keshavarz and Abolfazl Semnani. *The simplest method for calculating energy output and Gurney velocity of explosives.* Journal of hazardous materials, 131(1-3):1–5, 2006.

[76] V. P. Kopyshev, A. B. Medvedev, and V. V. Khrustalev. *Equation of state of explosion products on the basis of a modified Van der Waals model.* Combustion, explosion and shock waves, 42(1):76–87, 2006.

[77] M-L Turkel and F Charlet. *Carbon in detonation products. A "three-phase" modelisation.* Journal of physics IV, 5(Colloque C4):407–416, 1995.

[78] Capt. Yves J Charron. *Estimation of velocity distribution of fragmenting warheads using a modified Gurney method.* Air Force Institute of Technology (Canada), MSc thesis, 1979.

[79] Donald C Tucker and Chester R Hoggatt. *Prediction of the theoretical behavior and energy transfer when solids are subjected to explosive loading - summary report 1.* Technical report, Denver Research Institute, 1965.

[80] Robert R Karpp and William W. Predebon. *Calculations of fragment velocities from naturally fragmenting munitions.* Technical report, Ballistic Research Laboratories, 1975.

[81] William W. Predebon, Walter G Smothers, and Charles E. Anderson. *Missile warhead modeling: computations and experiments.* Technical report, Ballistic Research Laboratory, BRL Memo Report No . 2796, 1977.

[82] Padraic E. O'Donoghue, William W. Predebon, and Charles E. Anderson. *Dynamic launch process of performed fragments.* Journal of applied physics, 63(2), 1988.

[83] V S Trofimov. *Elementary technique for estimating the parameters of a high explosive charge for the plane acceleration of a metal plate.* Translated from Fizika goreniya i vzryva, 12(1):96–104, 1976.

[84] Tan Bing-Sheng and Jing Fu-Qian. *The planar flyer plate driven by detonation product convergent flow.* In Proceedings of the seventh international symposium on detonation, 1981.

[85] N E Hoskin and B D Lambourn. *The acceleration of two metal plates in an HE-metal sandwich.* In Proceedings of the seventh international symposium on detonation, 1981.

[86] W Chen, X Li, F Lu, Z Li, and Z Zhang. *Parallel control to fragments of a cylindrical structure driven by explosive inside.* Mathematical problems in engineering, Volume 2015, Article ID 723463, 2015.

[87] Andreas Helte, Olof Andersson, and Patrik Lundberg. *Deformation, fragmentation and acceleration of a controlled fragmentation charge casing.* Defence technology, 15:1974–1977, 2019.

[88] Marinko Ugrčić. *Numerical simulation of the fragmentation process of high explosive projectiles.* Scientific technical review, 63(2):47–57, 2013.

[89] Valerie J Bishop and D J James. *Blast and fragments from steel cylinders containing RDX/wax explosives. Part 1: The blast wave parameters.* Technical report, AWRE, 1970.

[90] Valerie J Bishop and D J James. *Blast and fragments from steel cylinders containing RDX/wax explosives with varying aluminium content. Part 3: fragment distribution.* Technical report, AWRE, 1971.

[91] DJ James. *Blast and fragments from steel cylinders containing RDX/wax explosives with varying aluminium content. Part 4: Partition of energy.* Technical report, AWRE, 1972.

[92] D J James. *Blast and fragments from steel cylinders containing RDX/wax explosives with varying aluminium content. Part 5: Further analysis of blast parameters.* Technical report, AWRE, 1973.

[93] Muhamed Suceska. *Explo5: Computer program for calculation of detonation parameters.* Proceedings of the thirty second international annual conference on ICT, (110):1–13, 2001.

[94] N. S. Brar and Z. Rosenberg. *Shock hugoniot of 1215 steel.* AIP conference proceedings, 370:101–104, 1996.

[95] William Flis. *A Lagrangian approach to modeling the acceleration of metal by explosives.* In Proceedings of the seventeenth southeast conference on theoretical and applied mechanics, Hot Springs, AK, 1994.

[96] Predrag Elek, Slobodan Jaramaz, and Dejan Mickovic. *Modeling of expansion dynamics of explosively driven metal cylinders.* In Proceedings of the international symposium on ballistics, 2013.

[97] Predrag Elek, Slobodan Jaramaz, and Dejan Mickovic. *Modeling of the metal cylinder acceleration under explosive loading.* Scientific technical review, Vol 63(2):39–46, 2013.

[98] Rodney A White and Larry H Hollier. *Vascular surgery : basic science and clinical correlations.* Wiley-Blackwell, ISBN 978-1405122023, 2005.

[99] Amanda R. Lawrence and Keith J. Gooch. *Differences in transmural pressure and axial loading ex vivo affect arterial remodeling and material properties.* Journal of biomechanical engineering, 131(10):101009, 2009.

[100] Peter R Greene. *Scaling laws for vascular buckling, axial and circumferential: Applications to pulse wave velocity.* Journal of vascular medicine and surgery, 05(03):3–6, 2017.

[101] Amanda R Lawrence and Keith J Gooch. *Transmural pressure and axial loading interactively regulate arterial remodeling ex vivo.* American journal of physiology-heart and circulatory physiology, 297:H475–H484, 2009.

[102] Isaac Newton. *The mathematical principles of natural philosophy.* Translated into English by Andrew Motte, 1729.

[103] Mikell P. Groover. *Fundamentals of modern manufacturing: materials, processes, and systems.* John Wiley & Sons, Inc. ISBN 978-470467008, fourth edition, 2010.

[104] Michael D. Hutchinson. *Replacing the equations of Fano and Fisher for cased charge blast impulse - III - yield stress method.* Propellants, explosives and pyrotechnics, 39(4):586–589, 2014.

[105] J D Anderson. *Modern compressible flow: with historical perspective.* McGraw-Hill Education, ISBN 0-07-100665-6, second edition, 1990.

[106] L W Longdon (editor). *Textbook of ballistics and gunnery, volume 1: part II applications and design*. Her Majesty's Stationery Office, London, England, 1987.

[107] Jon Chrostowski, Wenshui Gan, and Li Cao. *TRAJ_CAN White Paper*. Technical report, ACTA report 14-873/03 for submission to DDESB, 2014.

[108] Thuy-tien Ngoc Nguyen. *Characterisation of a shock tube for blast injury studies*. PhD thesis, Imperial College London, 2012.

[109] W. C. Young and R. G. Budynas. *Roark's formulas for stress and strain*. McGraw-Hill, ISBN 0-07-072542-X, seventh edition, 2002.

[110] US Department of Defense. *Structures to resist the effects of accidental explosions*. Technical report, UFC 3-340-02, 2008.

[111] T Josey, D V Ritzel, and T W Sawyer. *Development of a miniature double pitot-static probe and its application to calibrating blast flow conditions*. In Proceedings of the international symposium on the military aspects of blast and shock, 2016.

[112] FISO Technologies Inc. *Multiple-use pre-clinical pressure catheter for small animal physiological testing*. FISO datasheet life sciences pressure sensor MC-00257, 2017.

[113] GF Kinney and KJ Graham. *Explosive shocks in air*. Springer-Verlag Berlin Heidelberg, ISBN 978-3-642-86684-5, second edition, 1985.

[114] Sam Rigby. *Blast wave clearing effects on finite-sized targets subjected to explosive loads*. PhD thesis, University of Sheffield, 2014.

[115] Wonsik Ahn, Jae-Hyon Bahk, and Young-Jin Lim. *The gauge system for the medical use*. Anesthesia and analgesia, 95(4):1125, 2002.

[116] PCB Piezotronics. *Product datasheet: Micro ICP® pressure sensor model 132B38*, 2019.

[117] Millar Inc. *Mikro-Tip® catheter pressure transducer (animal use only) instructions for use*, 2013.

[118] JB Barlow, WH Rae, and A Pope. *Low speed wind tunnel testing.* John Wiley & Sons, Inc., ISBN 978-0-471-55774-6, third edition, 1999.

[119] R W F Gould. *Wake blockage corrections in a closed wind tunnel for one or two wall-mounted models subject to separated flow.* Technical report, Ministry of Technology Aeronautical Research Council reports and memoranda 3649, 1970.

[120] N Curle and HJ Davies. *Modern fluid dynamics, volume 1: incompressible flow.* D van Nostrand Company Ltd, ISBN 978-0442017972, students' paperback edition, 1968.

[121] D A Caughey. *Review of compressible flow topics.* Lecture notes, MAE3050, Cornell University, 2008.

[122] Girish K Jankee and Bharathram Ganapathisubramani. *Influence of internal orifice geometry on synthetic jet performance.* Experiments in fluids, 60(51):1–11, 2019.

[123] R. A. Alpher and D. R. White. *Flow in shock tubes with area change at the diaphragm section.* Journal of fluid mechanics, 3(5):457–470, 1958.

[124] G H Trengrouse and M M Soliman. *Effect of sudden changes in flow area on pressure waves of finite amplitude.* Journal of mechanical engineering science, 8(2):198–206, 1966.

[125] J Falcovitz and O Igra. *Model for shock interaction with sharp area reduction.* Proceedings of the institution of mechanical engineers, part G: Journal of aerospace engineering, 222:789–800, 2008.

[126] George Emanuel, U S Satyanand, and Frank K Lu. *Performance of a shock tube with a large-area Contraction.* American institute of aeronautics and astronautics journal, 43(9):1995–1999, 2005.

[127] J Falcovitz, D Igra, and O Igra. *Analysis of wide driver shock tube flow with sharp area transition.* In G Ben Dor, O Sadot, and O Igra, editors, Proceedings of the

thirtieth international symposium on shock waves 1. Springer, ISBN 978-3-319-46213-4 (online), 978-3-319-46211-0 (print), 2017.

Appendix A

MATLAB Function for Simple Cylindrical Case Expansion

```
function [sa_cc,a_M, sa_C, vol_C,vol_M,m_C,m_M,m_GP,sa_I,P_IN,f_I,a_M_IN,mbar_F,lbar_F,
vol_SP,v,r_X,R_FIN, P_4] = FOULNESS1_SIunits_chunky_1DE_INF_v5()
    % Calculate the motion of the casing from an expanding cylinder includes gas leakage
after critical expansion ratio gas leakage mass flow rate based on Ideal Nozzle Flow
    %PARAMETERS and SYMBOLS.    UNITS - kg, m, s, Pa
    % _C relates to charge; _M relates to metal; _F relates to fragment; _cc relates to
within the crack; _HE relates to HE charge; _GP relates to gaseous detonation products
    % _SP relates to solid detonation products; _CJ relates to Chapman Jouget conditions;
_IN relates to initial conditions, _I relates to internal; _E relates to external; _X relates
to expansion; _R relates to Denny/James reports; _1,_2,_3,_4 relate to gas within each
section of flow (shock tube notation adopted): 1 = ambient ahead of outgoing shock; 2
= preshocked ambient behind outgoing shock; 3 = products ahead of fragments behind
contact surface; 4 = initial charge region and region behind fragments
    % lower case letters relate to individual parameters; UPPER case letters relate to
ratios of parameters (with numerator subscript first i.e. P_21 = p_2/p_1)
    % r = radius, thk = thickness, t = time, h = height, vol = volume, v = velocity
(speed), rho = density, m = mass, sa = surface area, mw = molecular weight, mols =
number of moles, mbar = average mass, n = number, lbar = average length, p = pressure,
a = acceleration, c = sound speed, f = force
    %start from empty arrays and figures
close all
clear all
    % max time to calculate to (in s)
max_time = 100E-6;   %1E-6 = us, 1E-3 = ms
    % external conditions
rho_1 = 1.225;   %kg/m^ 3
gamma_1 = 1.4;
P_1 = 101325;   %Pa
```

```
    %GEOMETRY - Calculate physical geometry attributes of charge and case
r_C = 0.040;  %m
thk_M = 0.003175;  %m h_C = 0.381;    %m
    % Enter densities of charge and case material
rho_C = 1636.6;  %kg/m^ 3
rho_M = 7850;  %kg/m^ 3
    % Calculate charge and case volumes and masses
vol_C = (h_C*pi*(r_C).^ 2);  %m^ 3
vol_M = h_C*pi*((r_C+thk_M).^ 2 - (r_C).^ 2);  %m^ 3 m_C = vol_C*rho_C;  %kg
m_M = vol_M*rho_M;  %kg
sa_C = 2*pi*r_C*h_C;  %m^ 2
sa_E = 2*pi*(r_C + thk_M)*h_C;  %m^ 2
    % Need to account for EM converting to both gas and solid products therefore not all
mass of charge becomes mass of gas
mw_HE = 0.19373;    %kg/mol
mols_HE = m_C/mw_HE;
molGPpermolHE = 6.629;    %from Explo5
mols_GP = molGPpermolHE*mols_HE;
mw_GP = 0.023143;  %kg/mol
m_GP = mols_GP*mw_GP;  %kg
molSPpermolHE = 3.356;    %from Explo5
mols_SP = molSPpermolHE*mols_HE;
mw_SP = 0.012001;    %kg/mol from Explo5 - probably Carbon
m_SP = mols_SP*mw_SP;    %kg
rho_SP = 2250;  %kg/m^ 3 - based on Carbon
vol_SP = m_SP/rho_SP;  %m^ 3
    %Calculate average mass of fragments based on total number of fragments reported
and casing mass: N_F is total number of fragments - 219 from Foulness report
n_F = 219;
mbar_F = m_M/n_F;  %kg


    %assume frag square in planform, lbar_frag is length of side of average fragment
lbar_F = (mbar_F/(rho_M*thk_M)).^ (0.5);  %m
    % Calculate initial conditions based on geometry and detonation properties of charge.
Enter detonation properties of charge used (RDX/wax 88/12)
P_CJ = 23.531*1E9;  %Pa - 23.531E9 for 98%TMD; 24.72E9 for 100%TMD
P_IN = 0.42*P_CJ;    %Pa
gamma_4 = 3.325;  % from Explo5 run
D = 7885.7;  %m/s
    % Calculate internal Force acting on casing post detonation and associated acceleration
P_atm = 101325;  %Pa
f_I = P_IN*sa_C - P_atm*sa_E - P_IN*(0.5*(2*r_C+thk_M))*h_C;  % N
a_M_IN = (f_I/m_M);  % m/s^ 2
    %Calculate distance moved under Newtonian motion and effect of motion on internal
pressure. Decide timestep (s) and initial speed from shock interaction with casing
timestep = 0.1E-6;  % s
P_3 = 101325;  % Pa
    %initial internal radius
```

```
r_I_IN = r_C;   %m
r_E_IN = r_C + thk_M;    % external radius in m
    %cut off expansion ratio for casing rupture
R_0Xcrit = 1.98;
r_Ecrit = r_E_IN*R_0Xcrit;   %m
r_Icrit = sqrt((r_Ecrit).^ 2 - m_M/(rho_M*pi*h_C));   %m
sa_F_I = h_C*2*pi*r_Icrit/n_F;   %m^ 2 - internal surface area of individual average fragment, based on internal cylinder area at rupture
sa_F_E = h_C*2*pi*r_Ecrit/n_F;   %m^ 2 - external surface area of individual average fragment, based on external cylinder area at rupture
sa_Fcrit = m_M/(n_F*rho_M*(r_Ecrit-r_Icrit));   %m^ 2
    % Initiating output vectors
v(1) = 990;    %(m/s): 990 for 98%TMD, 1030 for 100%TMD - by hugoniot calculations
r_I(1) = r_I_IN;   %m
r_E(1) = r_E_IN;   %m
vol(1) = (h_C*pi*r_I(1).^ 2) - vol_SP;   %m^ 3
sa_I(1) = h_C*2*pi*r_I(1);   %m^ 2
sa_E(1) = h_C*2*pi*r_E(1);   %m^ 2
V(1) = 1;
P_4(1) = 0.42*P_CJ;   %Pa
f_I(1) = P_4(1)*sa_I(1) - P_3*sa_E(1) - P_4(1)*(0.5*(r_I(1)+r_E(1)))*h_C;   %N
a_M(1) = a_M_IN;   %m/s^ 2
R_FIN(1) = r_E(1)/r_E_IN;
m_4(1) = m_GP;   %kg
mdot(1) = 0;   %kg/s
mdot_total(1) = 0;   %kg/s
m_4_lost(1) = 0;   %kg
m_4_lost_total(1) = 0;   %kg
rho_GP(1) = m_GP/vol(1);   %kg/m^ 3
CS(1) = r_I(1);
S(1) = r_I(1);
v_S_staticframe(1) = 0;
    % calculated the maximum number of iterations to compute (length of vector)
t = 0:timestep:max_time;
[~, maxits] = size(t);
        % Forward marching timesteps
        %Logic to be followed = current timestep parameter values only derived from last time step values (or current timestep values of their parameters). This means that value returned is the value at the end of the last timestep that is carried through (values change at end of step not start??)
    for i = 2:maxits
current_time = (i-1)*timestep;
r_E(i) = r_E(i-1) + v(i-1)*timestep;   %m
r_X(i) = r_E(i) - r_E_IN;   %m

    if r_E(i) < r_Ecrit    %casing expanding before rupture
r_I(i) = sqrt((r_E(i)).^ 2 - m_M/(rho_M*pi*h_C));   %m
vol(i) = (h_C*pi*r_I(i).^ 2) - vol_SP;   %m^ 3
```

```
m_4(i) = m_4(i-1);   %kg
V(i) = (vol(i))/(vol(1));
P_4(i) = P_4(i-1)*(vol(i-1)/vol(i))^ gamma_4;   % x1E12 Pa
sa_I(i) = h_C*2*pi*r_I(i);   %m^ 2
sa_E(i) = h_C*2*pi*r_E(i);   %m^ 2
f_I(i) = P_4(i)*sa_I(i) - P_3*sa_E(i) - P_4(i)*(0.5*(r_I(i)+r_E(i)))*h_C;
a_M(i) = f_I(i)/m_M;   %m/s^ 2
v(i) = v(i-1) + a_M(i-1)*timestep;    %m/s
mdot(i) = mdot(i-1);   %kg/s
m_4_lost(i) = mdot(i)*timestep;   %kg
m_4_lost_total(i) = m_4_lost(i) + m_4_lost_total(i-1);   %kg
m_3(i) = m_4_lost_total(i);   %kg
rho_4(i) = m_4(i)/vol(i);   %kg/m^ 3
v_4(i) = v(i);
v_3(i) = v(i);
CS(i) = r_I(i);
CS_X(i) = r_X(i);
CS_X_staticframe(i) = CS_X(i) - r_X(i);
R_FIN(i) = r_E(i)/r_E_IN;
S(i) = r_I(i);
S_X(i) = r_X(i);
v_S(i) = v(i);
v_S_staticframe(i) = 0;
S_X_staticframe(i) = S_X(i) - r_X(i);

    else    %rupture occurs, gas leakage starts
r_E(i) = r_E(i-1) + v(i-1)*timestep + 0.5*a_M(i-1)*(timestep^ 2);   %m
r_I(i) = sqrt((r_E(i)).^ 2 - m_M/(rho_M*pi*h_C));   %m
vol(i) = (h_C*pi*r_I(i).^ 2) - vol_SP;   %m^ 3
sa_I(i) = h_C*2*pi*r_I(i);   %m^ 2
sa_cc(i) = sa_I(i) - (sa_Fcrit*n_F);   %m^ 2
m_Fcrit = sa_Fcrit*(r_Ecrit-r_Icrit)*rho_M;
mdot(i) = sa_cc(i)*sqrt(gamma_4*rho_4(i-1)*P_4(i-1))*(2/(gamma_4+1)) ^
((gamma_4+1)/(2*(gamma_4-1)));   %kg/s

    %Karpp and Predebon mass flow rate - assumes maximum flow of M=1 through crack
m_4_lost(i) = mdot(i)*timestep;   %kg
m_4(i) = m_4(i-1) - m_4_lost(i);   %kg
rho_4(i) = m_4(i)/vol(i);   %kg/m^ 3
m_4_lost_total(i) = m_4_lost(i) + m_4_lost_total(i-1);   %kg
m_3(i) = m_4_lost_total(i);   %kg
n_F_h = h_C/sqrt(sa_Fcrit);   % number of fragments along length
n_F_r = n_F/n_F_h;   % number of fragments around radius
width_cc(i) = sa_cc(i)/(n_F_h * sqrt(sa_Fcrit));   %m width of axial cracks
    %no gaps between axial fragments due to lack of expansion in axial direction. pressure drop due to mass loss through cracks based on change in mass with constant volume. Pressure drop due to expansion based on ratio of densities rho_0/rho
V(i) = (m_4(i)*rho_GP(1))/(rho_4(i)*m_GP);
```

```
P_4(i) = P_4(i-1)*(m_4(i)/m_4(i-1)*(V(i-1)/V(i)))^ gamma_4;
a_4(i) = P_4(i)*sa_Fcrit/m_Fcrit;
    %fragment velocity
v(i) = v(i-1) + a_M(i-1)*timestep;    %m/s
    % flow velocities: v_4 = fragment velocity + local sound speed of products in crack
c_4(i) = sqrt(gamma_4*P_4(i)/rho_4(i));
v_4(i) = v(i) + c_4(i);
    %calculate v_4 based on mass flow rate - solve shock tube equation to find P2/P1
P_1 = 101325;   %Pa - pressure in air ahead of shockwave
P_41(i) = P_4(i)/P_1;   %ratio of P_4 / P_1
c_1 = 340;   %speed of sound in air ahead of shockwave
problem.objective = @(x) x*(1-((gamma_4 -1)*(c_1/c_4(i))*(x -1)/(sqrt(2*gamma_1*
(2*gamma_1+(gamma_1+1)*(x-1))))))^ (-2*gamma_4/(gamma_4 -1)) - P_41(i);
    if (r_E(i) - r_Ecrit) < 1.5e-4    % if we are on the first loop after fracture guess a value
problem.x0=5;
    else
problem.x0=P_21(i-1);    % otherwise set the guess at the previous value: P_21 = pressure
ratio across shockwave P_2 / P_1
    end
problem.solver = 'fzero';
problem.options = optimset(@fzero);
x(i) = fzero(problem);
P_21(i) = x(i);
P_3(i) = P_1*P_21(i);
    %shock tube equation for v_3.
v_3(i) = ((2*c_4(i))/(gamma_4 -1))*(1-(P_3(i)/P_4(i))^ ((gamma_4-1)/(2*gamma_4)));
rho_3(i) = rho_4(i)*(P_3(i)/P_4(i))^(1/gamma_4);
c_3(i) = sqrt(gamma_4*P_3(i)/rho_3(i));
P_2(i) = P_3(i);
v_2(i) = v_3(i);
rho_2(i) = rho_1*(P_21(i))^ (1/gamma_1);
c_2(i) = sqrt(gamma_1*P_2(i)/rho_2(i));
c_1 = sqrt(gamma_1*P_1/rho_1);
    %drag curve points for tumbling cube - from Traj_Can
M = [0 0.1 0.75 1.5 2.5 100];
CD = [0.681 0.681 0.881 1.331 1.181 1.181];
    %M_4 = Mach number of frag in local flow region 4 (v_4 flow)
M_4(i) = v(i)/c_4(i);
    %M_3 = mach number of frag in local flow region 3
M_3(i) = v(i)/c_3(i);
    %M_2 = mach number of frag in local flow region 2
M_2(i) = v(i)/c_2(i);
      %M_1 = mach number of frag in local flow region 1
M_1(i) = v(i)/c_1;
CD_4(i) = interp1(M,CD,M_4(i));
CD_3(i) = interp1(M,CD,M_3(i));
CD_2(i) = interp1(M,CD,M_2(i));
CD_1(i) = interp1(M,CD,M_1(i));
```

```
alpha_3(i) = (v_3(i) - v(i))/v(i);
alpha_2(i) = (v_2(i) - v(i))/v(i);
    %point mass model a_4 = acceleration from products drive; a_3 = deceleration from
motion into region 3
a_drag4(i) = ((pi*rho_4(i)*sa_F_I)/(8*mbar_F))*CD_4(i)*v(i)*(c_4(i));
a_drag3(i) = ((-pi*rho_3(i)*sa_F_E)/(8*mbar_F))*CD_3(i)*v(i)*v(i)*(1-alpha_3(i));
a_drag2(i) = ((-pi*rho_2(i)*sa_F_E)/(8*mbar_F))*CD_2(i)*v(i)*v(i)*(1-alpha_2(i));
a_drag1(i) = ((-pi*rho_1*sa_F_E)/(8*mbar_F))*CD_1(i)*v(i)*v(i);   % assume no wind
CS_X_staticframe(i) = CS_X_staticframe(i-1) + v_3(i)*timestep;
v_S_staticframe(i) = c_1*sqrt(((gamma_1 + 1)/(2*gamma_1))*(P_21(i) - 1));

    if real(v_S_staticframe(i)) > 10
v_S(i) = v_S_staticframe(i);
    else
v_S(i) = c_1;
    end
S_X_staticframe(i) = S_X_staticframe(i-1) + v_S(i)*timestep;
    %change to moving fragment frame of reference
CS_X(i) = r_X(i) + CS_X_staticframe(i);
S_X(i) = r_X(i) + S_X_staticframe(i);
    %total acceleration is sum of accelerations acting on fragment
    if r_X(i) < CS_X(i)   % fragment within region 3
a_M(i) = a_4(i) + a_drag4(i) + a_drag3(i);   %m/s^ 2
    elseif CS_X(i) < r_X(i) < S_X(i)   % fragment ahead of contact surface but behind
shock
a_M(i) = a_drag2(i);   % m/s^ 2
    elseif r_X(i) > S_X(i)   % fragment ahead of shock
a_M(i) = a_drag1(i);   % m/s^ 2
    end
v_CS(i) = (CS_X(i) - CS_X(i-1))/timestep;
R_FIN(i) = r_E(i)/r_E_IN;
P_42(i) = P_41(i)/P_21(i);
    end
    end
    %Plot curves from FOULNESS Report
t = 0:timestep:max_time;
[~, maxits] = size(t);
    %Report gas curve starts at rupture ( 20.9 us) - Time at which the regime changes
cut_off=20.9E-6;   %s
    for i=1:maxits
r_R(i) = 1.46E7*(t(i))^ 2 + 1760*t(i) + 2.67E-6;   %m
    if t(i)<=cut_off
r_GP_R(i) = 1.46E7*(t(i))^ 2 + 1760*t(i) + 2.67E-6;   %m
    else
r_GP_R(i) = 3180*t(i) - 0.0233;   %m
    end
    end
    %Plot some graphs to track what's happening
```

```
subplot(5,2,1)
plot(t*1E6,r_GP_R*1E3,'–r',t*1E6,r_R*1E3,'r',t*1E6,r_X*1E3,'b');
xlabel('Time (us)')
ylabel('Expansion (mm)')
legend('Report - Gas','Report','Calculation')
grid on
subplot(5,2,2)
plot(R_FIN,r_GP_R*1E3,'–r',R_FIN,r_R*1E3,'r',R_FIN,r_X*1E3,'b');
xlabel('Expansion Ratio (R/R0)')
ylabel('Expansion (mm)')
legend('Report - Gas','Report','Calculation')
grid on
subplot(5,2,3)
plot(t*1E6,v/1E3);
xlabel('Time (us)')
ylabel('Velocity (mm/us)')
grid on
subplot(5,2,4)
plot(R_FIN,v/1E3);
xlabel('Expansion Ratio (R/R0)')
ylabel('Velocity (mm/us)')
grid on
subplot(5,2,5)
plot(t*1E6,P_4/1E9);
xlabel('Time (us)')
ylabel('Pressure (GPa)')
grid on
subplot(5,2,6)
plot(R_FIN,P_4/1E9);
xlabel('Expansion Ratio (R/R0)')
ylabel('Pressure (GPa)')
grid on
subplot(5,2,7)
plot(t*1E6,a_M/1E9);
xlabel('Time (us)')
ylabel('acceleration (mm/us2̂)')
grid on
subplot(5,2,8)
plot(R_FIN,a_M/1E9);
xlabel('Expansion Ratio (R/R0)')
ylabel('acceleration (mm/us^ 2)')
grid on
subplot(5,2,9)
plot(t*1E6, mdot);
xlabel('Time (us)')
ylabel('Gas Mass Flow (kg/s)')
grid on
subplot(5,2,10)
```

```
plot(R_FIN, mdot);
xlabel('Expansion Ratio (R/R0)')
ylabel('Gas Mass Flow (kg/s)')
grid on

figure;
plot(t*1E6,r_GP_R*1E3,'–r',t*1E6,r_R*1E3,'r',t*1e6,CS_X*1E3,'–',t*1E6,r_X*1E3,'b');
xlabel('Time (us)')
ylabel('Expansion (mm)')
legend('Report - Gas','Report - Case','Calculation - Gas', 'Calculation - Case',
'Location','Northwest')
grid on
figure;
plot(t*1E6,S_X,t*1E6,CS_X,'r',t*1E6,r_X,'b')
xlabel('Time (us)')
ylabel('Expansion (m)')
legend('Shock','Contact Surface','Fragment','Location','northwest')
grid on
figure;
plot(t*1E6,a_M);
xlabel('Time (us)')
ylabel('acceleration (m/s^ 2)')
grid on
    noindent figure;
plot(t*1E6,width_cc*1E3)
xlabel('Time (us)')
ylabel('Crack width (mm)')
grid on
figure;
plot(t*1E6,v/1E3);
xlabel('Time (us)')
ylabel('Velocity (mm/us)')
grid on

    end
```

Appendix B

EXPLO5_V6.02 Data for RDX/Wax(88/12)

B.1 Brief Description of Explo5 v6.02

Explo5 v6.02 from OZM is a software package for the thermochemical prediction of ideal and non-ideal high explosive, propellant and pyrotechnic mixture performance. The calculation engine is based on data for the chemical formula, density and heat of formation for the reactants. It calculates the chemical composition at equilibrium as well as the thermodynamic properties of state for the products species generated at a given volume, density and temperature state.

Explo5 v6.02 uses the Becker-Kistiakowsky-Wilson equation of state for the gaseous detonation products, and a choice of other equations of state for the combustion and the products in a condensed phase state. The software uses the Gowan and Fickett equation of state for the solid carbon products. As before, the BKW EoS is often given in the form

$$\frac{PV}{RT} = 1 + xe^{\beta x}$$

$$x = \frac{\kappa \Sigma X_i k_i}{[V(T+\theta)]^{\alpha}}$$

with X_i being the molar fraction of the i^{th} gas product, k_i being the molar covolume of the i^{th} gas product and α, β, κ, θ are empirical constants.

The Gowan and Fickett EoS is given by

$$P = P_1(V) + a(V)T + b(V)T$$

with polynomial constants according to Gowan and Fickett being used to calculate the parameters $P_1(V)$, $a(V)$, and $b(V)$.

B.2 Results of Calculation for RDX/Wax 88/12

Composition of Reactants

Reactant	**Amount %**
Hexogen (RDX)	88
Wax	12

Chemical Parameters of Reactants

Reactant Density	1.6366	gcm^{-3}
Reactant Brutto Formula	C(3.958)H(7.948)N(4.605)O(4.605)	
Oxygen Balance	-60.156	%
Energy of Formation (at 298.15K)	234.95	$kJkg^{-1}$
Enthalpy of Formation (at 298.15K)	125.18	$kJkg^{-1}$
Relative Molar Mass	193.73	

Detonation Parameters at Chapman-Jouget Point

Parameter	**98% TMD**	**100% TMD**	
Heat of Detonation	-5605.46	-5618.09	$kJkg^{-1}$
Detonation Temperature	3511.77	3499.74	K
Detonation Pressure	23.531	24.72	GPa
Detonation Velocity	7885.72	8030.75	ms^{-1}
Particle Velocity	1823.29	1843.21	ms^{-1}
Sound Velocity	6062.43	6187.55	ms^{-1}
Density of Products	2.129	2.167	gcm^{-3}
Specific Volume of Products	0.47	0.461	cm^3g^{-1}
Exponent 'Gamma'	3.325	3.357	
Moles of Gaseous Products	6.629	6.607	$mol(molEM)^{-1}$
Moles of Condensed Products	3.356	3.377	$mol(molEM)^{-1}$
Mean Mw of Gas	23.143	23.182	$gmol^{-1}$
Mean Mw of Condensed Products	12.011	12.011	$gmol^{-1}$
Mean Mw of All Products	19.402	19.403	$gmol^{-1}$
Volume of Gas at STP	836.832	834.057	$dm^3(kgEM)^{-1}$
Internal Energy of Products	7267.66	7316.8	$kJkg^{-1}$
Compression Energy	1662.2	1698.71	$kJkg^{-1}$
Entropy of Products	7.452	7.405	$kJkg^{-1}$

Composition of Detonation Products

	98% TMD			100% TMD		
Product	**per mol EM**	**per kg EM**	**Mol %**	**per mol EM**	**per kg EM**	**Mol %**
H_2O	3.635147095	18.76371193	36.4052	3.649016857	18.83530426	36.5474
N_2	2.284493685	11.79197979	22.8787	2.287075281	11.80530548	22.9066
$C(s,d)$	1.840546966	9.50043869	18.4327	1.888590336	9.748426437	18.9155
$C(s,gr)$	1.515577793	7.823029995	15.1782	1.488611698	7.683837414	14.9095
CO	0.22289528	1.150529146	2.2322	0.19700858	1.016908526	1.9732
CH_2O_2	0.208306283	1.0752244	2.0861	0.215620995	1.112981081	2.1596
CO_2	0.165181071	0.852622986	1.6543	0.163887635	0.84594661	1.6414
H_2	0.074356332	0.383808613	0.7447	0.061604414	0.317986429	0.617
NH_3	0.033270411	0.171733454	0.3332	0.028686579	0.148072883	0.2873
HCN	0.002788279	0.014392395	0.0279	0.002226328	0.01149174	0.0223
CH_4	0.002224573	0.011482685	0.0223	0.001648584	0.008509577	0.0165
H	0.000144345	0.000745074	0.0014	0.000115039	0.000593803	0.0012
NO	8.85138E-05	0.000456886	0.0009	8.11531E-05	0.000418892	0.0008
C_2H_4	5.75605E-05	0.000297113	0.0006	3.90069E-05	0.000201344	0.0004
CH_3OH	4.48181E-05	0.000231339	0.0004	3.26773E-05	0.000168672	0.0003
N_2H_4	3.59603E-05	0.000185618	0.0004	3.12245E-05	0.000161173	0.0003
C_2H_6	3.48561E-05	0.000179918	0.0003	2.32639E-05	0.000120082	0.0002
OH	2.57266E-05	0.000132794	0.0003	2.04334E-05	0.000105472	0.0002
O	1.03728E-05	5.35416E-05	0.0001	1.00744E-05	5.20017E-05	0.0001
O_2	9.42579E-06	4.86535E-05	0.0001	9.83034E-06	5.07417E-05	0.0001
CH_2O	2.84252E-06	1.46724E-05	0	1.81926E-06	9.39054E-06	0
CNO	2.599E-06	1.34154E-05	0	2.18551E-06	1.1281E-05	0
N	1.25717E-06	6.48919E-06	0	1.14617E-06	5.91623E-06	0
N_2O	9.9156E-08	5.11818E-07	0	8.41374E-08	4.34296E-07	0
$C(l)$	1.70954E-11	8.82421E-11	0	1.65743E-11	8.55525E-11	0
NO_2	1.18234E-13	6.10295E-13	0	6.95051E-14	3.58768E-13	0
$H_2O(l)$	1.0168E-13	5.24846E-13	0	1.0476E-13	5.40746E-13	0

Shock Hugoniot of Detonation Products

98% TMD		100% TMD	
Pressure $[GPa]$	**Particle Velocity** $[ms^{-1}]$	**Pressure** $[GPa]$	**Particle Velocity** $[ms^{-1}]$
19.6429	1499.1391	20.6766	1519.8969
21.9112	1694.3878	23.0896	1718.7657
22.8455	1769.6663	24.0843	1795.5059
23.2127	1798.5612	24.4753	1824.9707
23.4432	1816.4835	24.6265	1836.2562
23.4976	1820.7089	24.6849	1840.5844
23.5185	1822.3257	24.7068	1842.2218
23.5269	1822.9605	24.7158	1842.8688
23.5292	1823.1667	24.7188	1843.1036
23.5302	1823.2333	24.7196	1843.1772
23.5299	1823.2388	24.7197	1843.2081
23.531	1823.3088	24.721	1843.2737
23.5326	1823.4133	24.7215	1843.3207
23.5345	1823.5595	24.7237	1843.4796
23.539	1823.9276	24.7286	1843.8558
23.5519	1824.9234	24.7423	1844.8716
23.5859	1827.5478	24.7777	1847.5205
23.6745	1834.3895	24.8728	1854.5339
23.8199	1845.5197	25.1226	1872.8864
24.4427	1892.7295	25.7854	1921.0208
26.1517	2017.702	27.6068	2048.5709
34.598	2563.3054	36.7394	2612.8705

Appendix C

AUTODYN Modelling Results: Graphs of Local Flow Mach Number

This Appendix shows graphs of

- local flow Mach Number against time with each driver pressure for a gap length of 20 mm and gap widths of 1 to 6 mm in 1 mm steps
  - 10 bar (Figure C.1 and Figure C.2)
  - 18 bar (Figure C.3 and Figure C.4)
  - 50 bar (Figure C.5 and Figure C.6)
  - 200 bar (Figure C.7 and Figure C.8)
- local flow Mach Number against time for 18 bar driver pressure for a gap length of 5 mm and 10 mm and gap widths of 1 mm to 6 mm in 1 mm steps
  - 5 mm gap length (Figure C.9 and Figure C.10)
  - 10 mm gap length (Figure C.11 and Figure C.12)
- local flow Mach Number against proportion along opening to show driver pressure and gap width effects
  - 10 bar and 18 bar driver pressure (Figure C.13)

  - 50 bar and 200 bar driver pressure (Figure C.14)

- time averaged Mach Number against proportion along opening for 18 bar driver pressure to show gap length effects

  - 1 mm, 2 mm and 3 mm gap widths (Figure C.15)

  - 4 mm, 5 mm and 6 mm gap widths (Figure C.16)

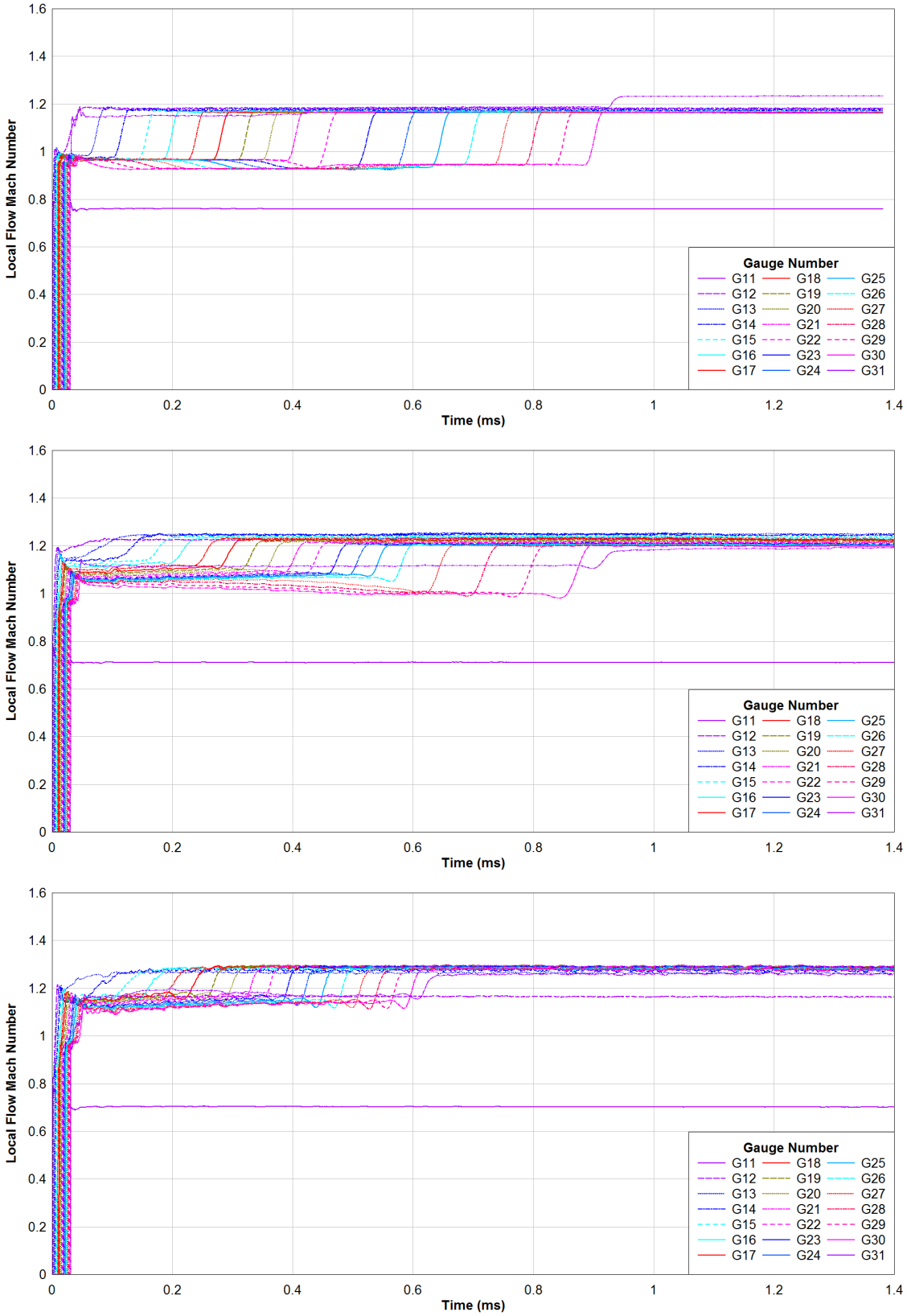


Figure C.1: 10 bar driver pressure, 20 mm gap length: 1 mm gap width (upper), 2 mm gap width (middle), 3 mm gap width (lower)

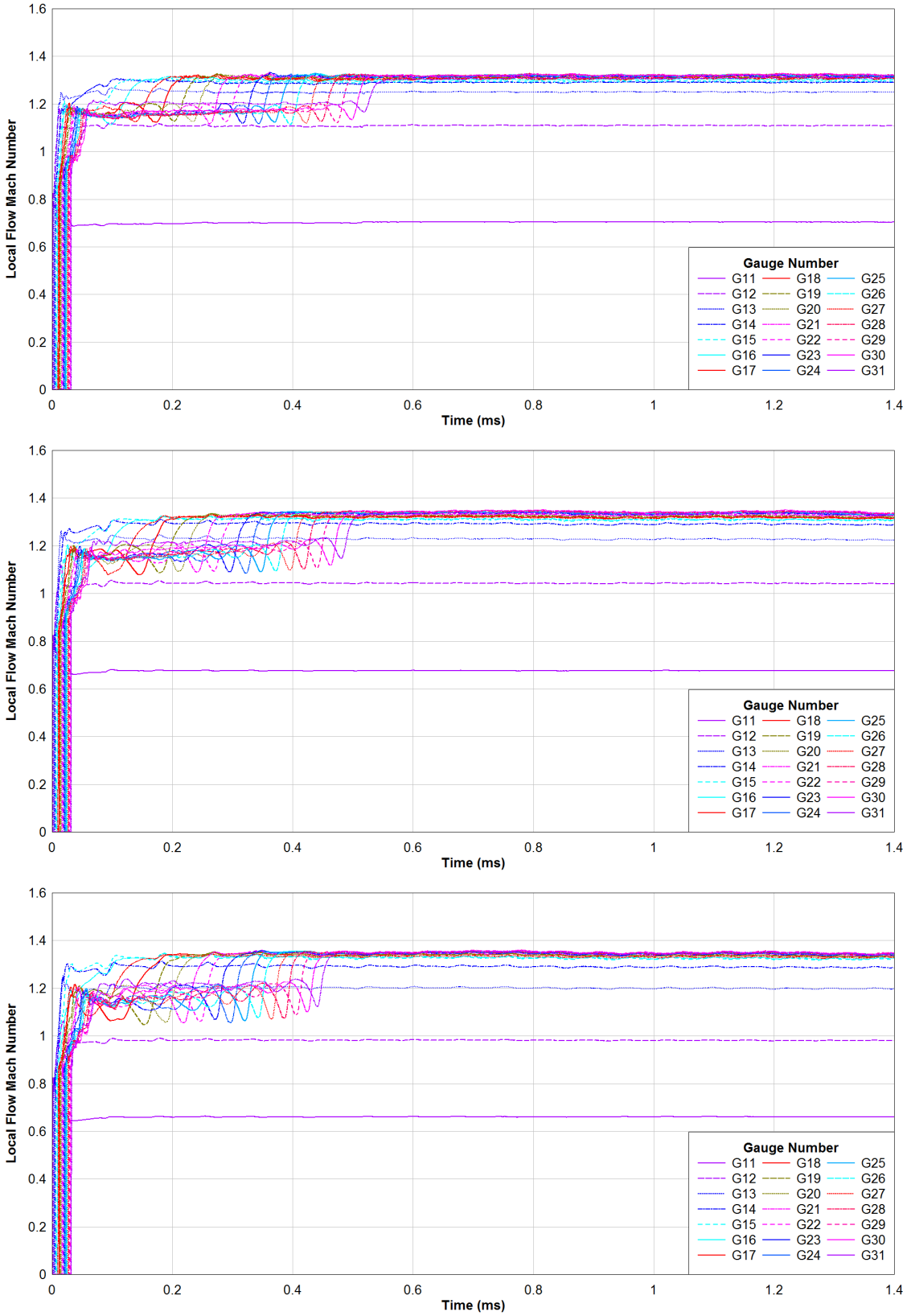


Figure C.2: 10 bar driver pressure, 20 mm gap length: 4 mm gap width (upper), 5 mm gap width (middle), 6 mm gap width (lower)

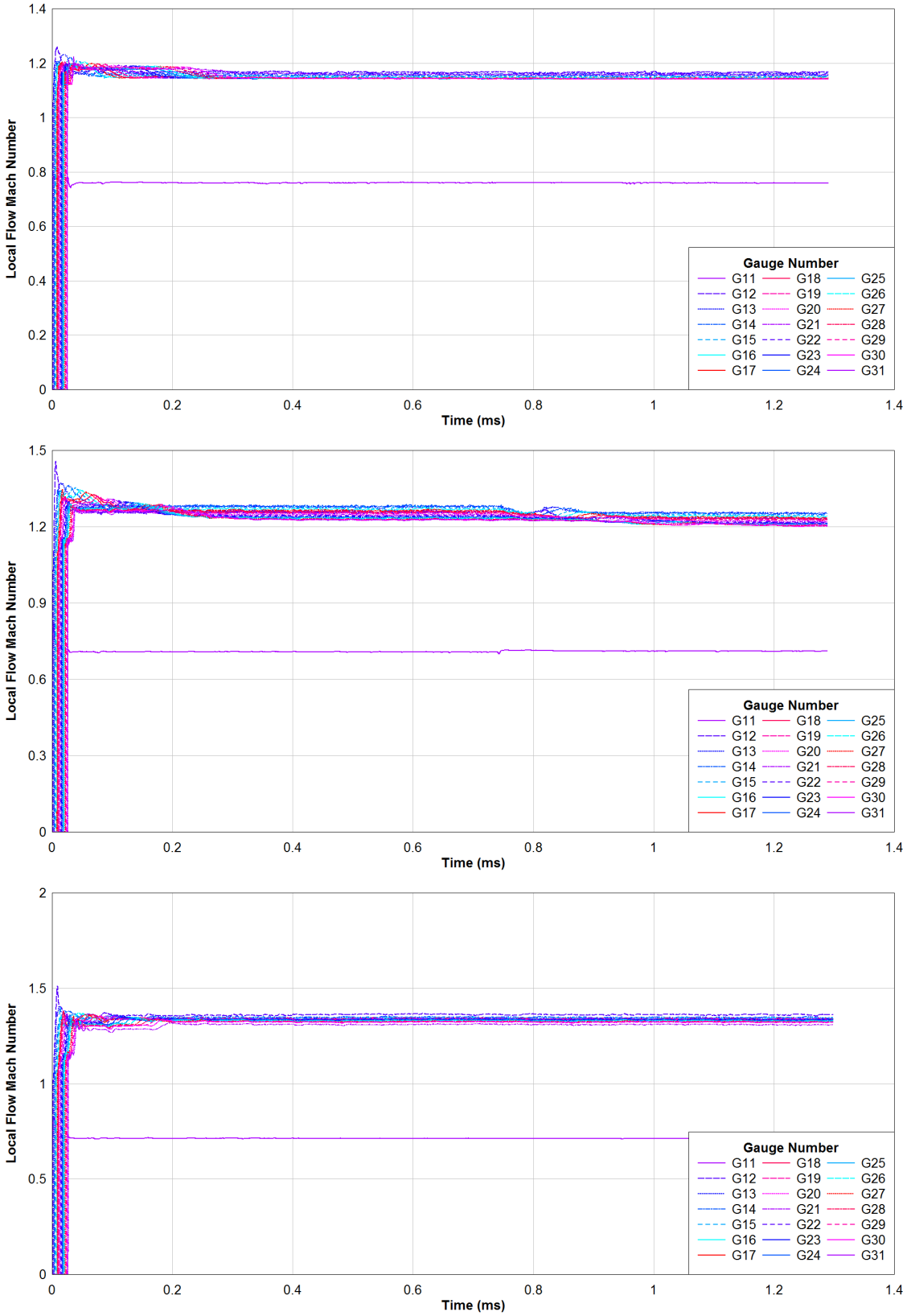


Figure C.3: 18 bar driver pressure, 20 mm gap length: 1 mm gap width (upper), 2 mm gap width (middle), 3 mm gap width (lower)

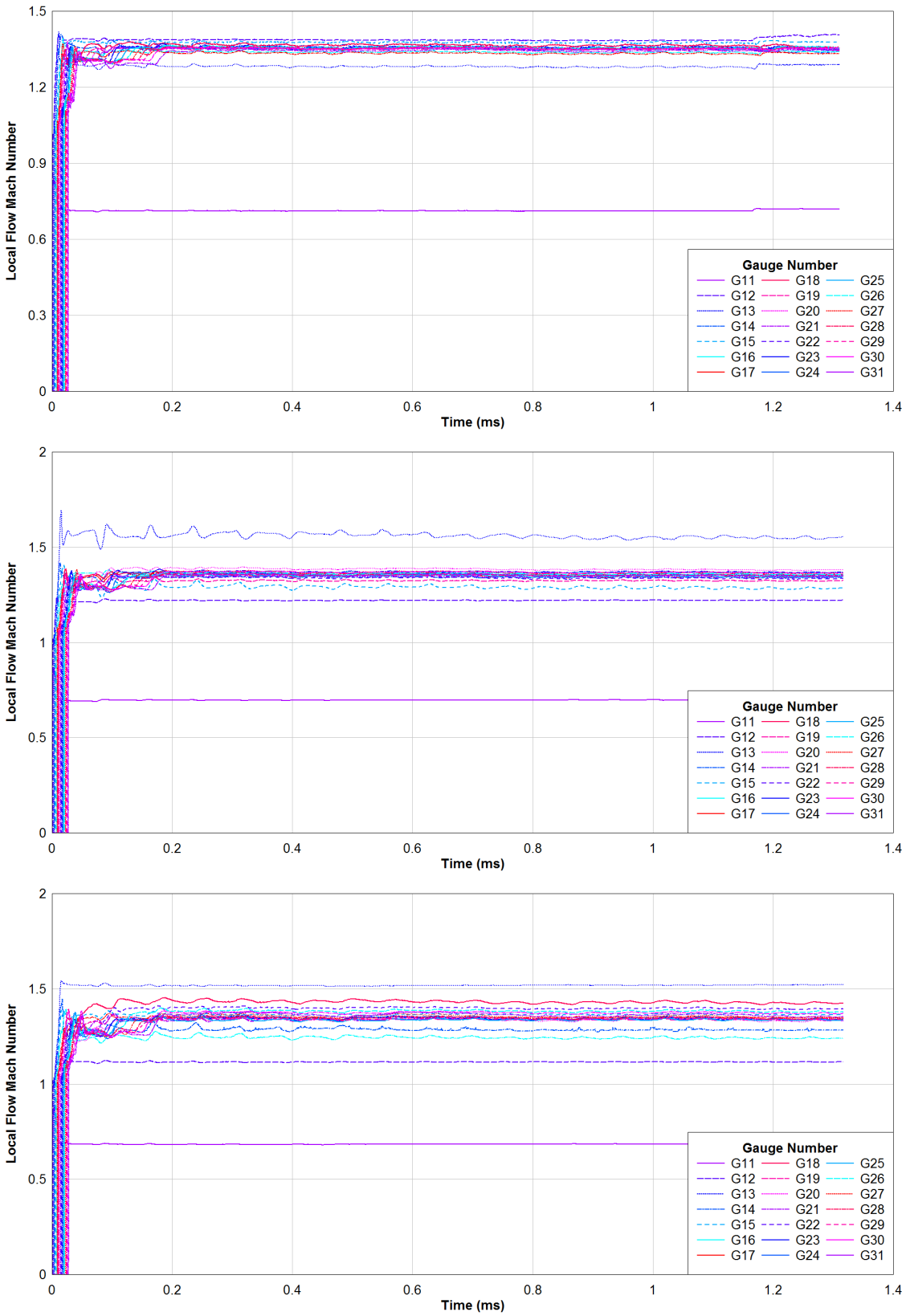


Figure C.4: 18 bar driver pressure, 20 mm gap length: 4 mm gap width (upper), 5 mm gap width (middle), 6 mm gap width (lower)

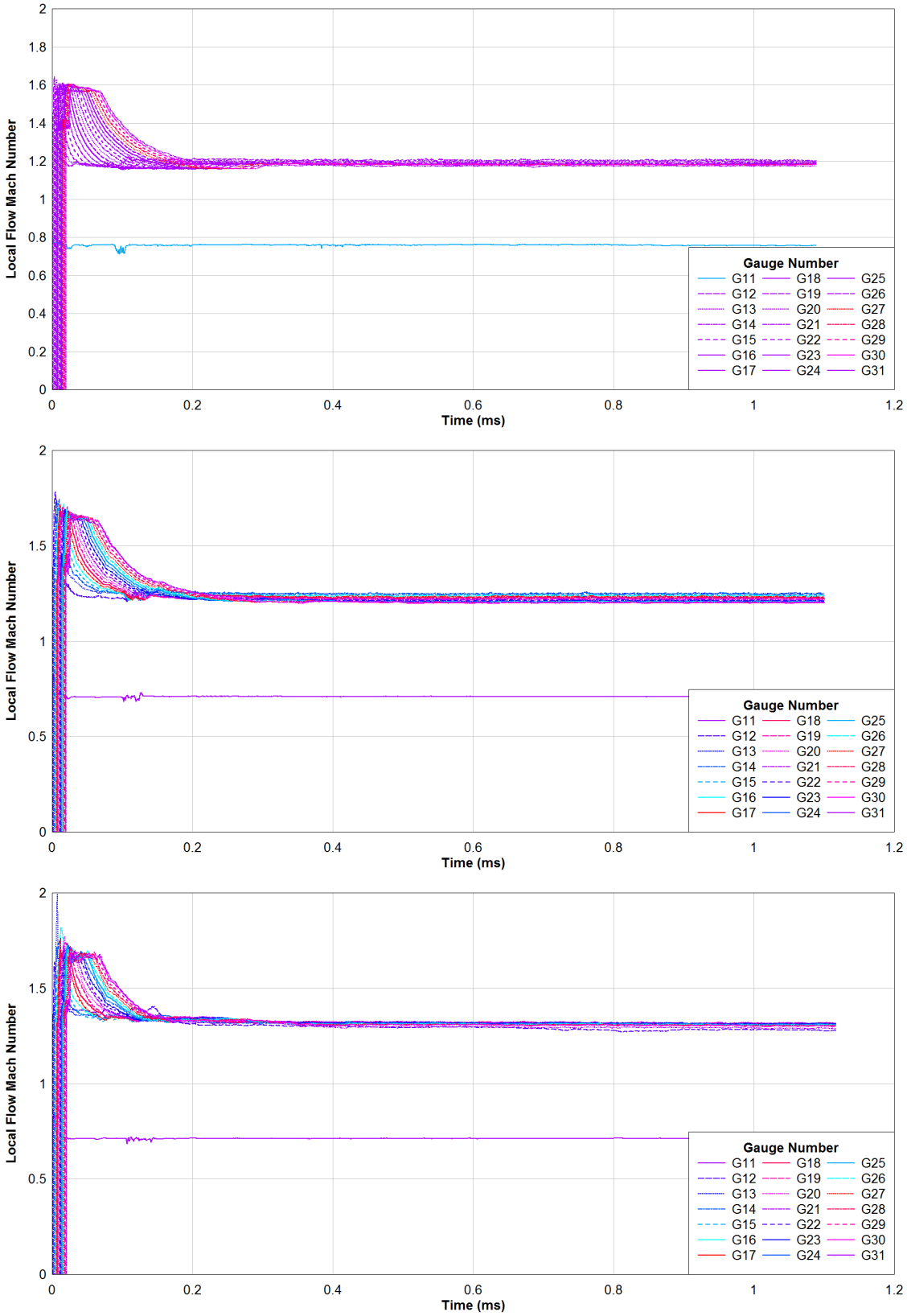


Figure C.5: 50 bar driver pressure, 20 mm gap length: 1 mm gap width (upper), 2 mm gap width (middle), 3 mm gap width (lower)

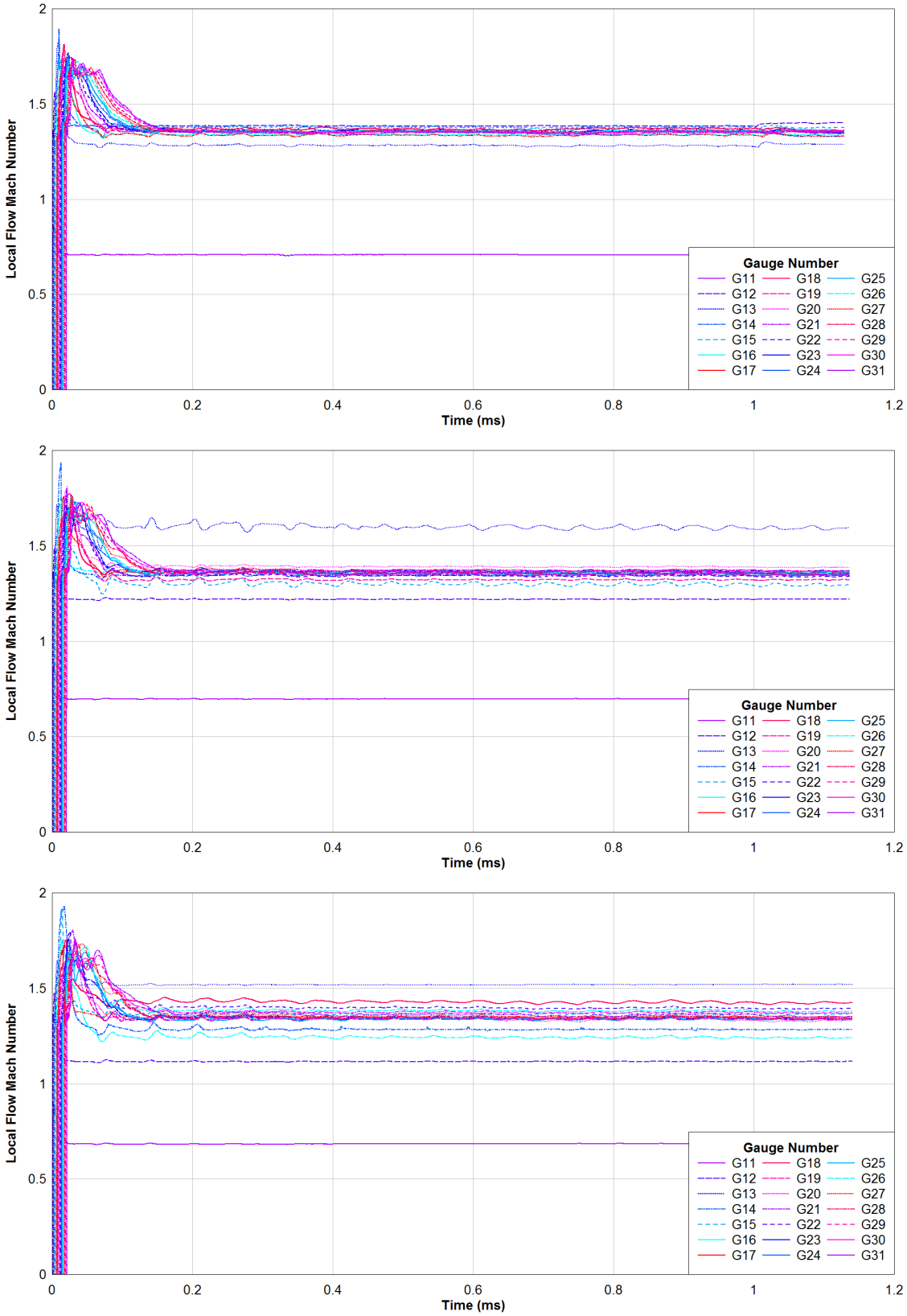


Figure C.6: 50 bar driver pressure, 20 mm gap length: 4 mm gap width (upper), 5 mm gap width (middle), 6 mm gap width (lower)

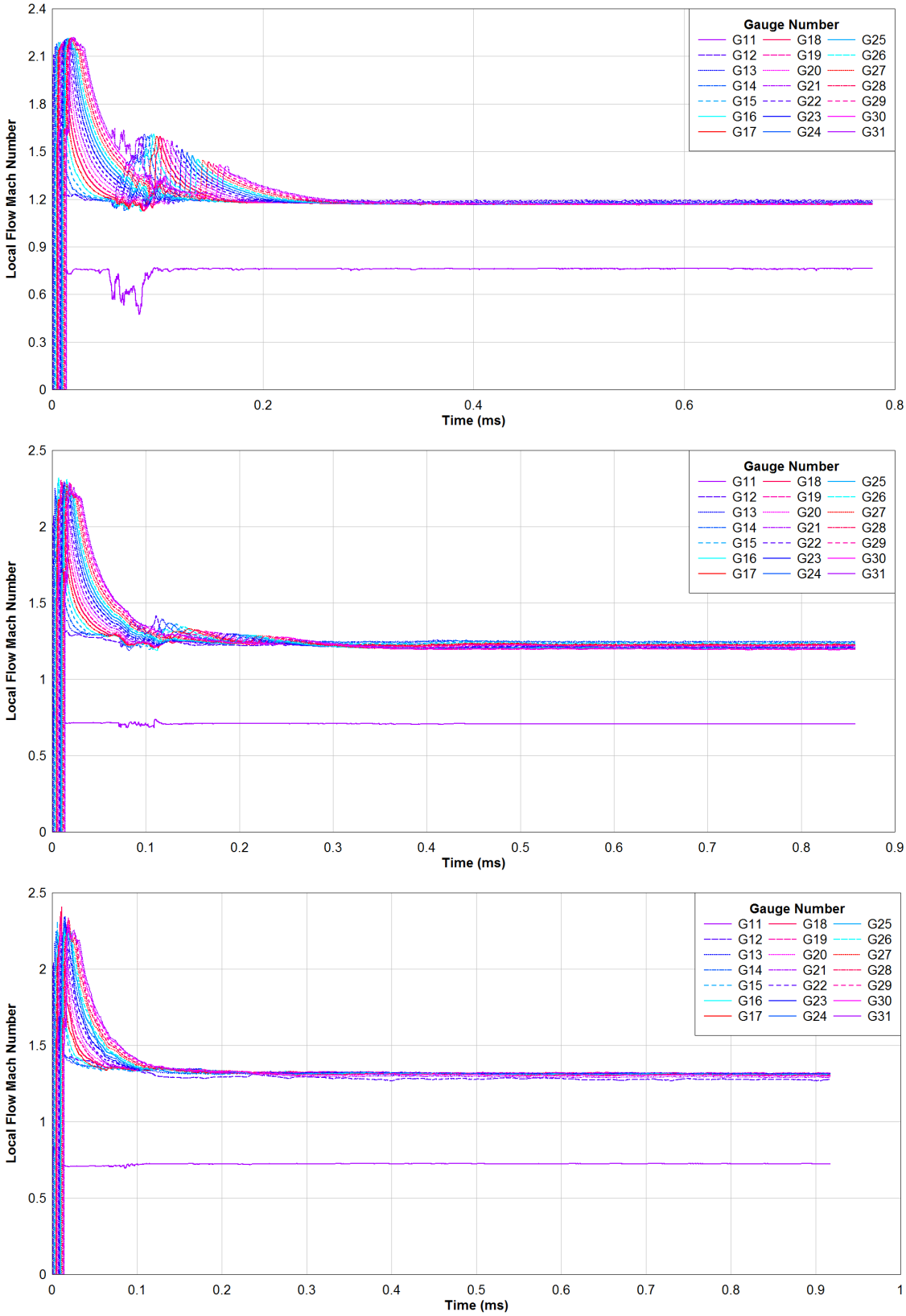


Figure C.7: 200 bar driver pressure, 20 mm gap length: 1 mm gap width (upper), 2 mm gap width (middle), 3 mm gap width (lower)

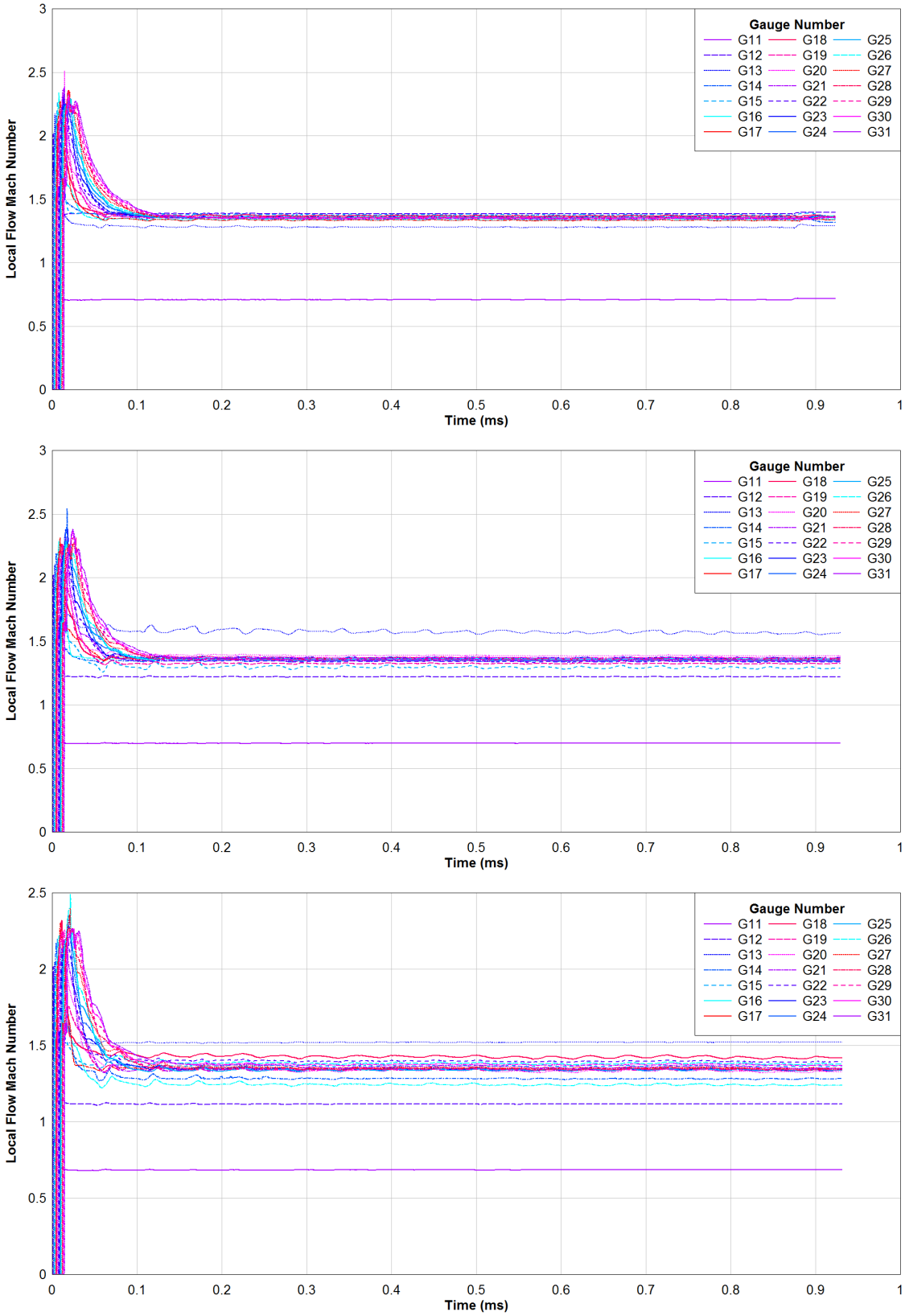


Figure C.8: 200 bar driver pressure, 20 mm gap length: 4 mm gap width (upper), 5 mm gap width (middle), 6 mm gap width (lower)

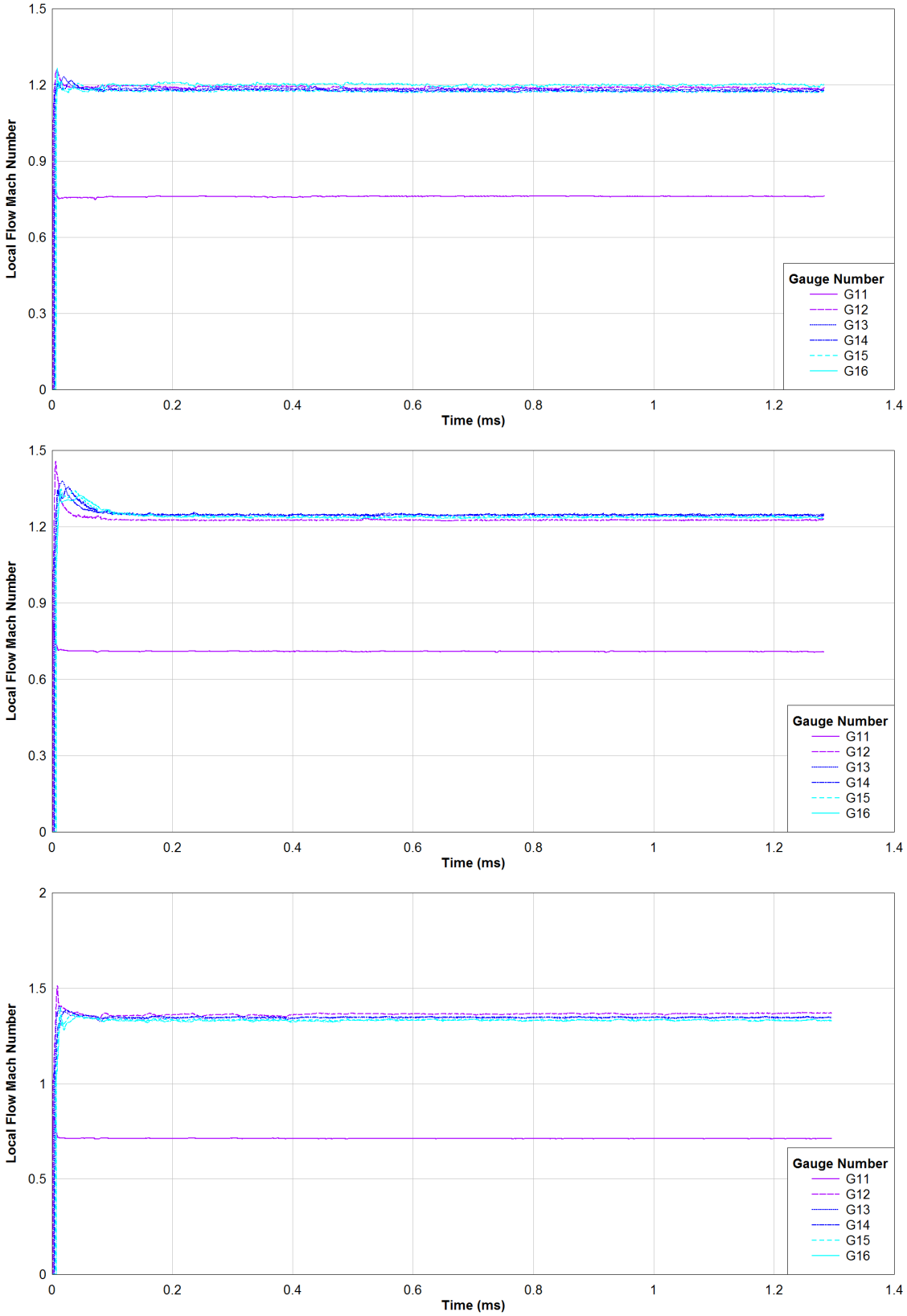


Figure C.9: 18 bar driver pressure, 5 mm gap length: 1 mm gap width (upper), 2 mm gap width (middle), 3 mm gap width (lower)

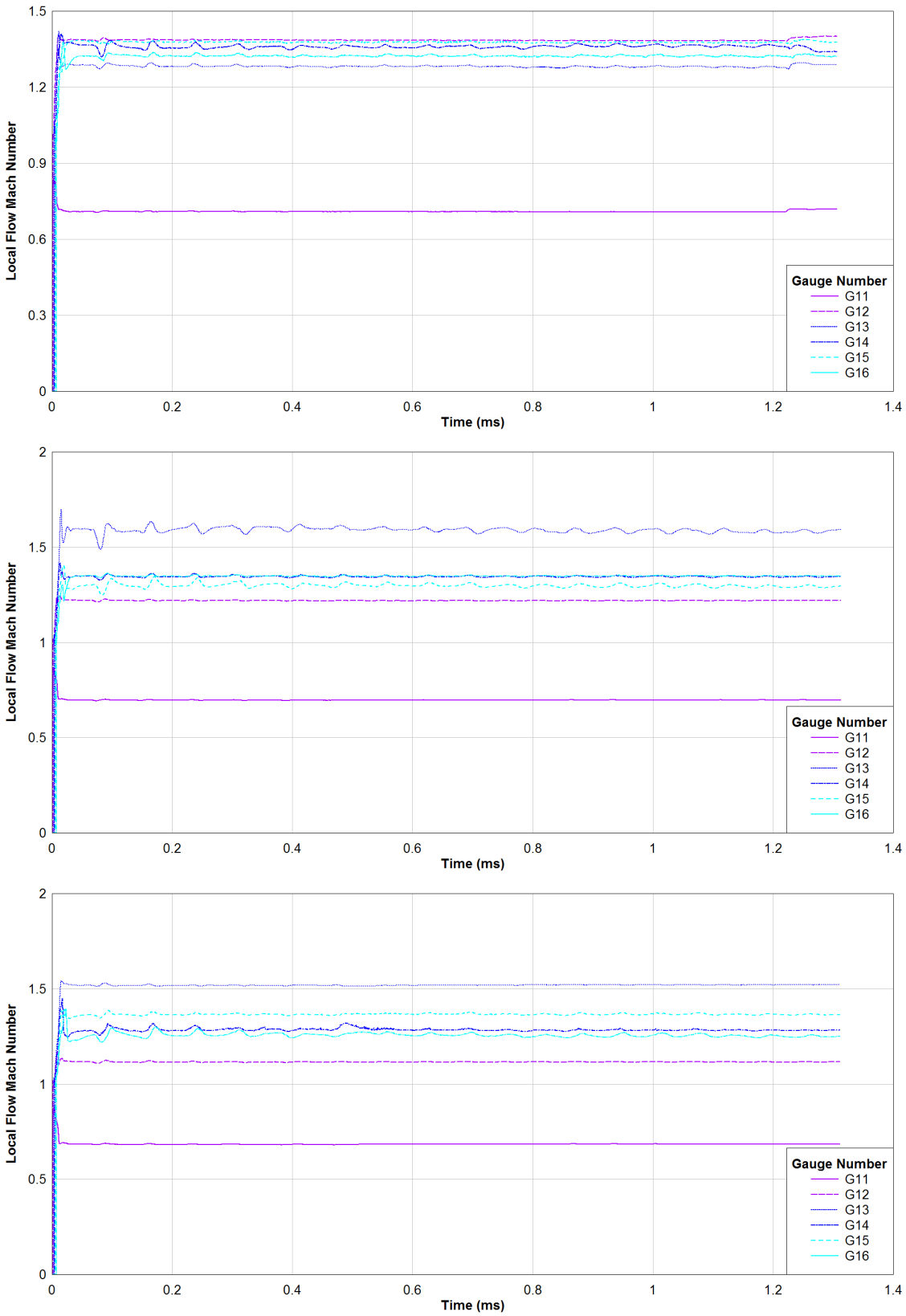


Figure C.10: 18 bar driver pressure, 5 mm gap length: 4 mm gap width (upper), 5 mm gap width (middle), 6 mm gap width (lower)

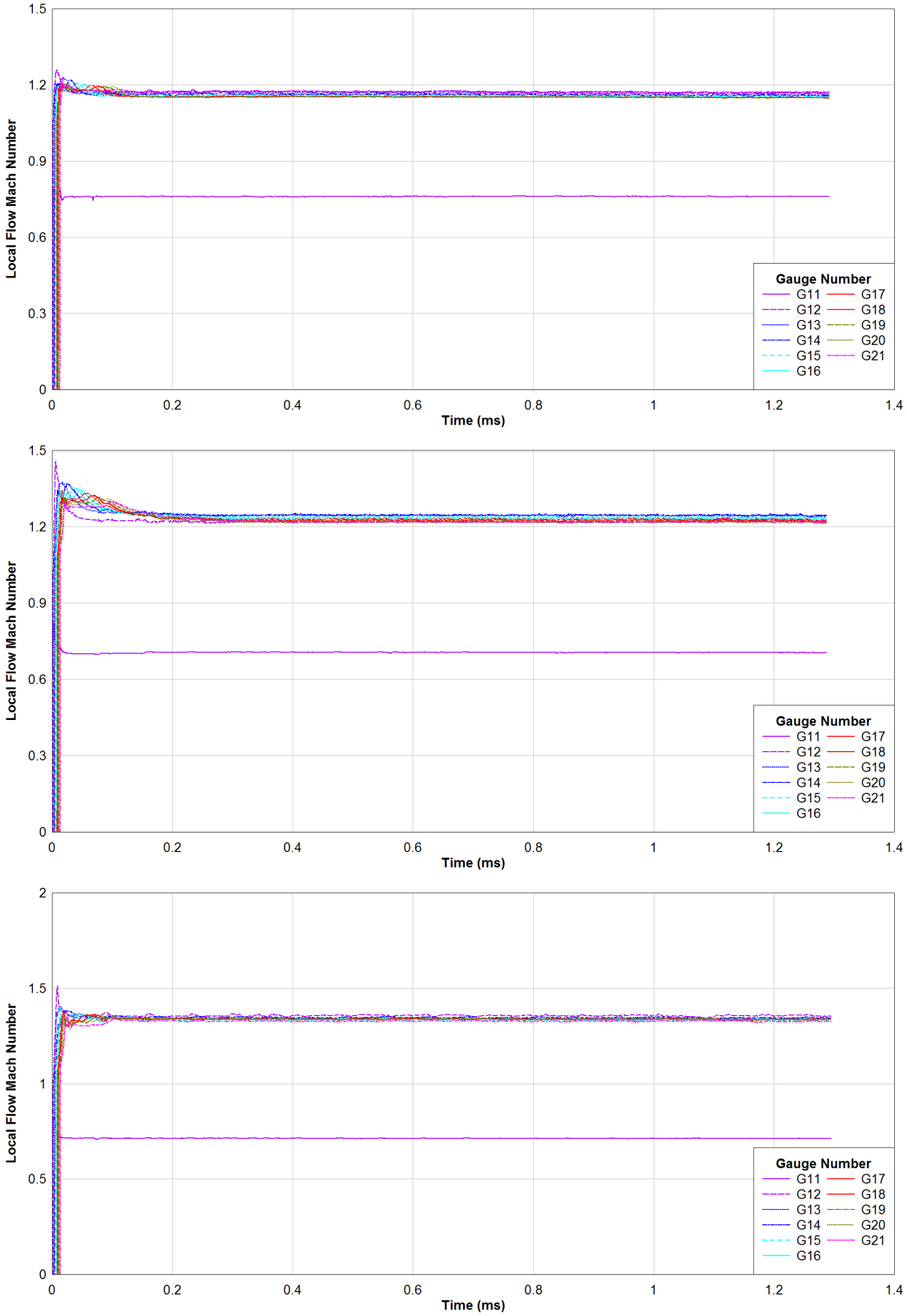


Figure C.11: 18 bar driver pressure, 10 mm gap length: 1 mm gap width (upper), 2 mm gap width (middle), 3 mm gap width (lower)

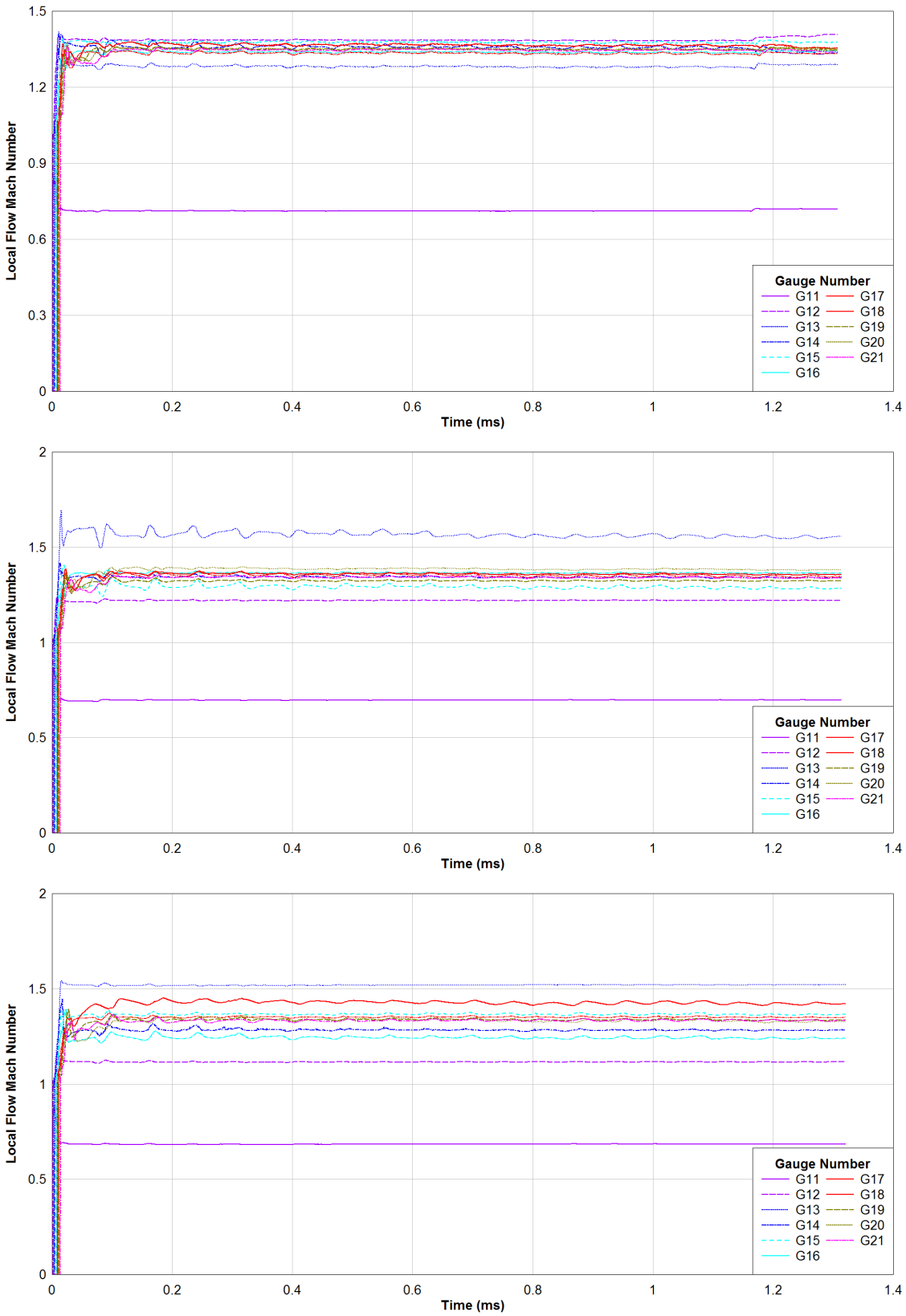


Figure C.12: 18 bar driver pressure, 10 mm gap length: 4 mm gap width (upper), 5 mm gap width (middle), 6 mm gap width (lower)

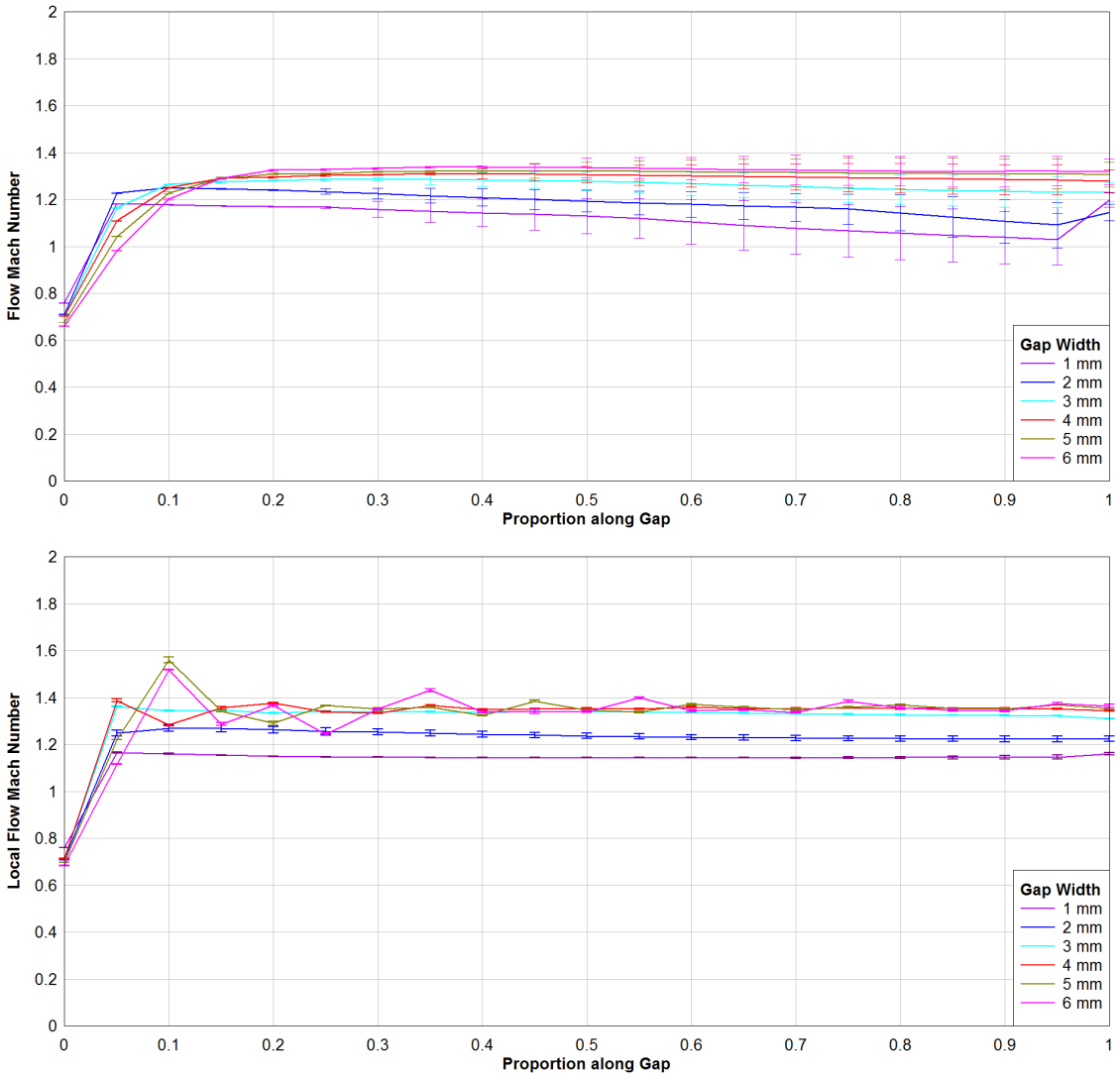


Figure C.13: Gap width effects: 10 bar driver pressure (upper), 18 bar driver pressure (lower)

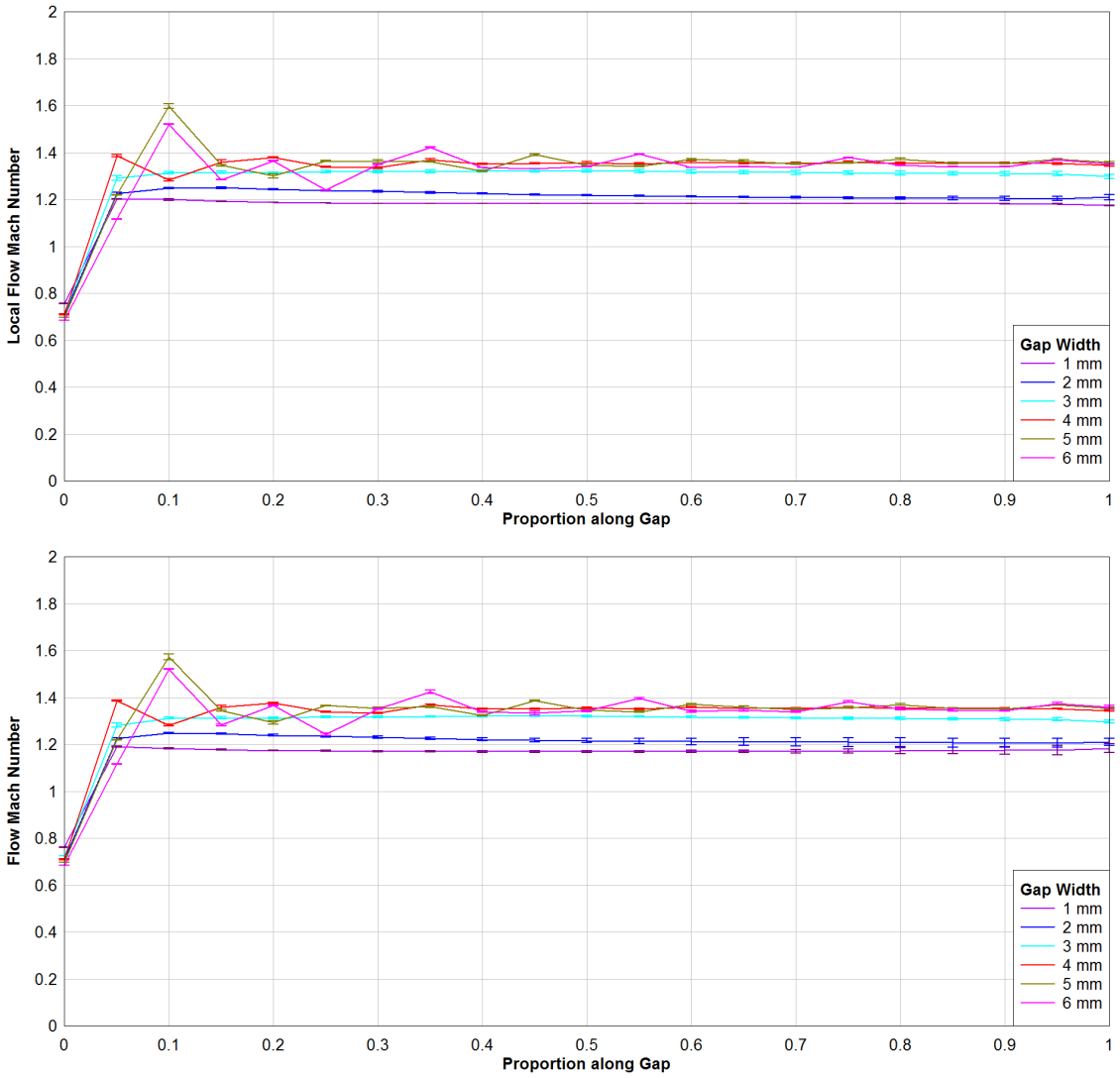


Figure C.14: Gap width effects: 50 bar driver pressure (upper), 200 bar driver pressure (lower)

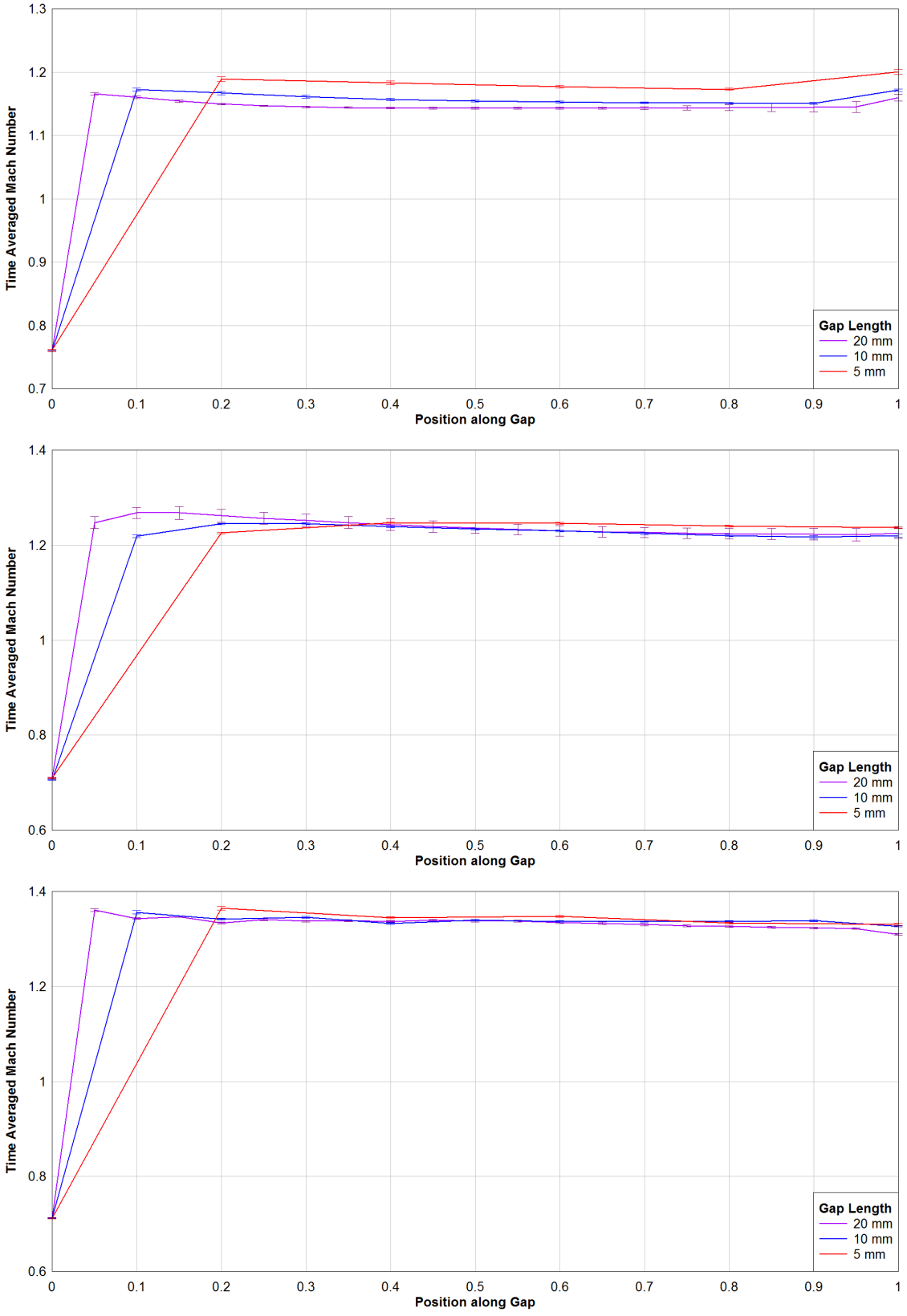


Figure C.15: Gap length effects: 1 mm gap width (upper), 2 mm gap width (middle), 3 mm gap width (lower)

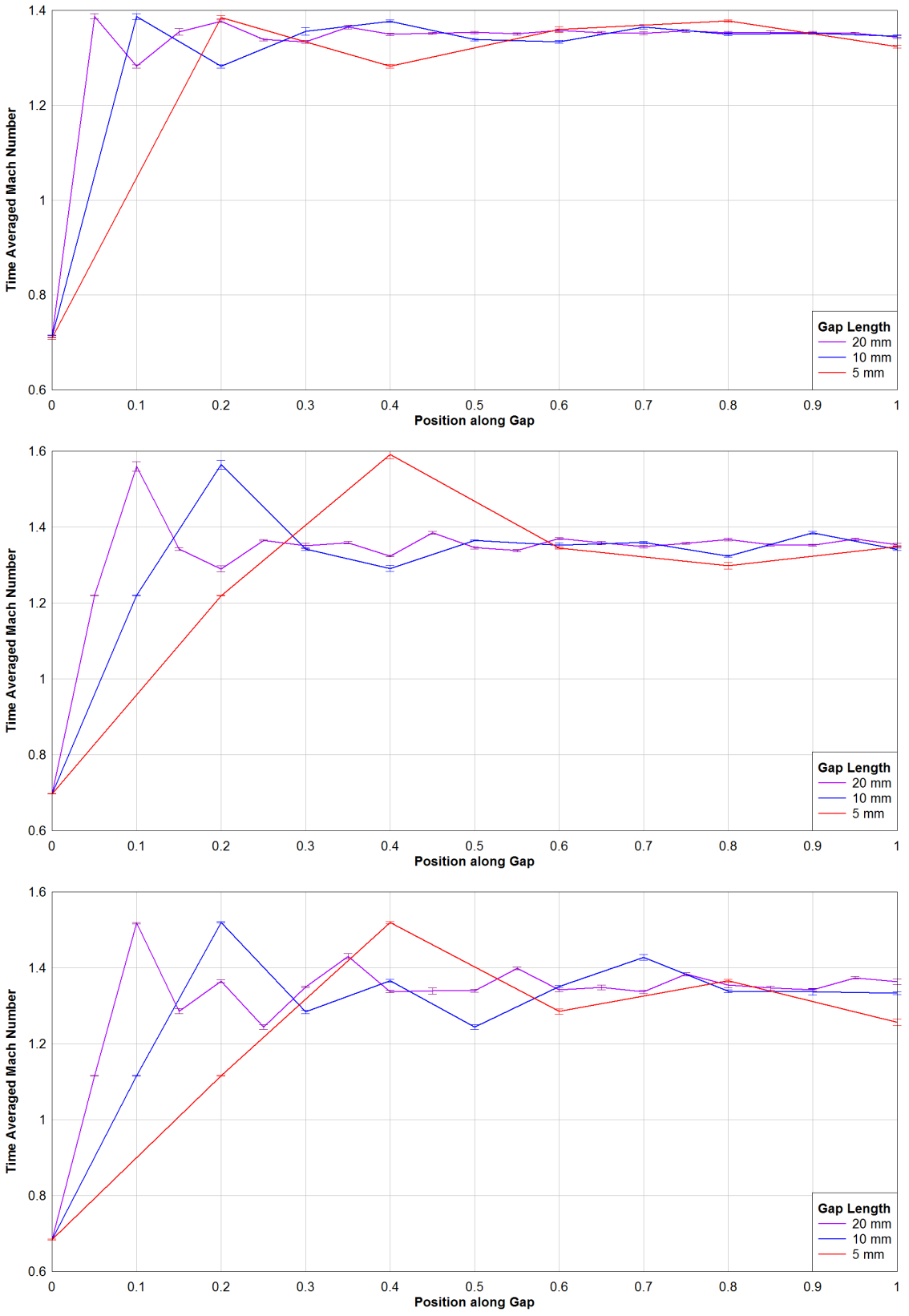


Figure C.16: Gap length effects: 4 mm gap width (upper), 5 mm gap width (middle), 6 mm gap width (lower)